University of Bath

PHD

Non-Destructive Testing and Structural Health Monitoring Systems for Damage Assessment in Aerospace Structures
(Alternate Format Thesis)

Andreades, Christos

Award date:
2021

Awarding institution:
University of Bath

Link to publication

Alternative formats
If you require this document in an alternative format, please contact:
openaccess@bath.ac.uk

General rights
Copyright and moral rights for the publications made accessible in the public portal are retained by the authors and/or other copyright owners and it is a condition of accessing publications that users recognise and abide by the legal requirements associated with these rights.

- Users may download and print one copy of any publication from the public portal for the purpose of private study or research.
- You may not further distribute the material or use it for any profit-making activity or commercial gain
- You may freely distribute the URL identifying the publication in the public portal ?

Take down policy
If you believe that this document breaches copyright please contact us providing details, and we will remove access to the work immediately and investigate your claim.

Download date: 22. Jun. 2021

University of Bath

PHD

Non-Destructive Testing and Structural Health Monitoring Systems for Damage Assessment in Aerospace Structures
(Alternate Format Thesis)

Andreades, Christos

Award date:
2021

Awarding institution:
University of Bath

Link to publication

Alternative formats
If you require this document in an alternative format, please contact:
openaccess@bath.ac.uk

General rights
Copyright and moral rights for the publications made accessible in the public portal are retained by the authors and/or other copyright owners and it is a condition of accessing publications that users recognise and abide by the legal requirements associated with these rights.

- Users may download and print one copy of any publication from the public portal for the purpose of private study or research.
- You may not further distribute the material or use it for any profit-making activity or commercial gain
- You may freely distribute the URL identifying the publication in the public portal ?

Take down policy
If you believe that this document breaches copyright please contact us providing details, and we will remove access to the work immediately and investigate your claim.

Download date: 04. Mar. 2021

Non-Destructive Testing and Structural Health Monitoring Systems for Damage Assessment in Aerospace Structures

Christos Andreades

A thesis submitted for the degree of
Doctor of Philosophy

University of Bath
Department of Mechanical Engineering

October 2020

Copyright

Attention is drawn to the fact that copyright of this thesis rests with the author and copyright of any previously published materials included may rest with third parties. A copy of this thesis has been supplied on condition that anyone who consults it understands that they must not copy it or use material from it except as licenced, permitted by law or with the consent of the author or other copyright owners, as applicable.

Christos Andreades

Acknowledgements

First and foremost, I would like to express my great appreciation to my supervisor Professor Michele Meo for kindly sharing his knowledge, giving valuable advice at every step, providing constructive suggestions when necessary and monitoring closely the progress of my work. His integrity and professionalism have been worthy of admiration.

Equally, I am very grateful to my former supervisor and mentor Dr Francesco Ciampa for giving me the opportunity to undertake this PhD, and most importantly for his strong support, guidance and encouragement from the beginning until the end of this research project.

In addition, I am truly thankful to Dr Gian Piero Malfense Fierro for generously sharing his time and expertise with me. His assistance was critical for the achievement of several milestones throughout my PhD research.

A special thank you goes to my colleagues and friends Marco Boccaccio, Salvatore Boccardi, Fabrizio Bucciarelli, Harry Chu, Stefano Cuomo, Mario De Simone, Francesco Flora, Kostas Myronidis, Mario Rapisarda and Francesco Rizzo for the invaluable help, excellent cooperation and unique memories.

Finally, I would like to take this opportunity to express my deep and sincere gratitude to my family. I owe everything to my beloved parents, Antonis and Andrie. They have always believed in me, supported my choices and provided everything I needed. Their unconditional love and never ending humour have been a great source of strength, especially during this long period. My brother Paris, my first and forever best friend, has also been there for me through the good and the bad times. His encouragement and advice were truly essential.

Abstract

Advanced engineering structures, particularly in the aerospace field, are expected to operate in harsh environments for extended periods while maintaining the highest possible efficiency. This is achieved with continuous optimisation of the structural design combined with the use of materials that are both lightweight and strong, such as metal alloys and fibre reinforced plastic (FRP) composites. Since the integrity and durability of structures is dependent on the material condition, the existence of structural damage must be identified immediately using various non-destructive evaluation (NDE) methods and structural health monitoring (SHM) systems. These methodologies often involve the transmission and reception of ultrasonic waves through the material using transducers, thus enabling effective, practical and reliable ultrasonic inspection. The damaged interfaces inside a material can interact with the propagating waves, and this can give rise to recognisable linear and nonlinear ultrasonic effects. In general, inspection methods have been found to offer earlier detection of flaws when assessing the nonlinear than the linear features in the acoustic/ultrasonic response of the material.

The research study outlined in this thesis aimed at proposing innovative designs of SHM systems and alternative NDE procedures based on nonlinear ultrasound, for the enhancement of sensitivity and accuracy in the detection of defects in metallic and FRP materials. This work focused on three main SHM/NDE research topics associated with specific challenges currently existing in aerospace applications.

Firstly, a new design of “smart” carbon fibre reinforced plastic (CFRP) laminate containing internal piezoelectric lead zirconate titanate (PZT) transducers was proposed, which could be utilised in the development of on-board SHM systems without exposing the sensors to extreme operating conditions. The novelty is on the methodology used for the electrical insulation of the embedded sensors from the conductive carbon fibres. Specifically, sensors were covered with a thin glass fibre patch to enable enhanced adhesion with the epoxy matrix of the composite plies. This prevents the formation of internal delamination which is usually the case for conventional insulation techniques involving the use of polymeric films and coatings. Experimental mechanical tests proved that this layout of internal sensors had no impact on the tensile, compressive, fatigue, flexural and interlaminar shear strength of CFRP composite samples. In addition, the

results from several ultrasonic experiments confirmed that such embedded transducers could detect defects of different type and size in CFRP plates, and monitor the growth of impact damage in composite samples subject to repeated tensile loading. Both delamination and impact damage were assessed using two nonlinear ultrasonic techniques.

In the second research topic, an SHM method involving the transmission and reception of ultrasonic waves within a surface-attached array of PZT transducers was developed for the detection and localisation of barely visible impact damage (BVID) in composite panels. In contrast to most of the available ultrasonic SHM methods, the accuracy of the developed algorithm did not rely on the recording of signals at the original state of the material (baseline data) or a priori knowledge of the wave velocity. In addition, the reliability of the method was enhanced by adding some initial steps to the algorithm for the identification of malfunctioning transducers. Moreover, the method included a simple process for the selection of a suitable frequency for signal transmission through the material. The signals recorded between all pairs of PZTs in the array were used to evaluate the level of material nonlinearity in each sensor-to-sensor path based on the received amplitude at the fundamental and second harmonic frequencies. Thus, a surface plot was generated showing the variation of material nonlinearity in the area enclosed by the transducers, with the peak amplitude being the position of damage. The proposed method was experimentally tested on three CFRP panels with different dimensions and shape, and the results verified the correct localisation of BVID, as well as the identification of a partially damaged transducer.

Regarding the last proposed SHM/NDE topic, an ultrasonic phased array method was optimised for the improvement of signal-to-noise ratio (SNR) in the acoustic response recorded in pulse-echo testing experiments. The aim was to achieve higher effectiveness in the detection of contact-type defects (e.g. closed crack and delamination) at several depths in metallic and laminated composite structures. The presented technique involved the processing of single-frequency and dual-frequency signals that were acquired with four different firing orders of the piezoelectric elements in the phased array probe. This allowed the filtering of unwanted linear and nonlinear acoustic features resulting in the extraction of the nonlinear response corresponding only to the response of damaged surfaces under excitation. Experiments were performed on piles of aluminium disks and CFRP laminates representing samples with several horizontal interfaces of contact

defects. The obtained nonlinear ultrasonic response of the material was compared with the linear response acquired under standard phased array inspection. In all cases, the results proved that the defect-related peaks exhibited in the nonlinear response were characterised by higher SNR and their positions indicated the locations of contact interfaces with a smaller error, relative to the linear peaks.

Therefore, the individual designs and methods proposed by this research study could potentially be utilised in the relevant SHM and NDE applications for improved detection and localisation of defects in metallic and composite materials.

Contents

Chapter 1. Introduction 1

1.1 Motivation 1

1.2 Research Aim and Objectives 6

1.3 Thesis Outline 7

Chapter 2. Background and Literature Review 11

2.1 Ultrasonic Wave Inspection of Materials 12

2.2 Linear Ultrasonic Methods 15

2.3 Nonlinear Ultrasonic Methods 18

2.4 Smart Composite Materials with Embedded Sensors 31

Chapter 3. Development of Smart CFRP Composites with Embedded PZT Transducers 34

Chapter 4. Nonlinear Ultrasonic Detection of Damage in Smart CFRP Composites 67

Chapter 5. Tensile-Mode Fatigue of Smart CFRP Composites and Nonlinear Ultrasonic Monitoring of Damage 91

Chapter 6. A Nonlinear Ultrasonic Method for In-Plane Localisation of Impact Damage 117

Chapter 7. A Nonlinear Ultrasonic Approach for Through-Thickness Localisation of Contact Defects 141

Chapter 8. Conclusions and Recommendations for Future Work 164

8.1 Concluding Remarks 164

8.2 Future Work 170

References 172

List of Figures

Chapter 1. Introduction

Figure 1: Typical stacking sequence of prepreg layers for the fabrication of composite laminates. 1

Figure 2: Common defects in composite laminates. 2

Figure 3: Example of experimental set-up used for ultrasonic structural health monitoring of materials. 3

Chapter 2. Background and Literature Review

Figure 1: Schematic of pulse-echo (a), through-transmission (b) and pitch-catch (c) ultrasonic testing. 13

Figure 2: Cross-sectional view of plate during near-surface propagation of Rayleigh waves (a) and when excited at symmetric (a) and antisymmetric (b) modes of Lamb waves. Not to scale. 14

Figure 3: Phase (a) and group velocities (b) of symmetric and antisymmetric Lamb wave modes in A606 steel plate [26]. 15

Figure 4: Stress-strain behaviour of linear undamaged materials (a) and their expected ultrasonic response under single frequency excitation (b). 16

Figure 5: Illustration of a dislocation line at the original equilibrium position (a) and the new equilibrium position (bowing) due to internal shear stress. 19

Figure 6: Stress-strain behaviour of materials with classical nonlinearity (a) and their expected ultrasonic response under single frequency excitation (b). 19

Figure 7: Stress-strain behaviour of materials with non-classical (hysteretic) nonlinearity (a) and their expected ultrasonic response under single frequency excitation (b). 21

Figure 8: Schematic of opening-closing crack in materials with non-classical (contact) nonlinearity (a) and the resultant bi-linear stress-strain behaviour (b). 22

Figure 9: Schematic of slipping crack in materials with non-classical (contact) nonlinearity (a) and the resultant stress-strain behaviour in micro-slip (b) and stick-slip (c) modes. 23

Figure 10: Ultrasonic response of undamaged (linear) materials (a) and damaged (nonlinear) materials (b) under single-frequency excitation. 25

Figure 11: Ultrasonic response of undamaged (linear) materials (a) and damaged (nonlinear) materials (b) under dual-frequency excitation. 28

Figure 12: Sensor embedment in composites using the cut-out (a), interlaying (b) and direct (c) techniques. 32

Chapter 3. Development of Smart CFRP Composites with Embedded PZT Transducers

Figure 1: Cross-sectional view of CFRP laminate with directly embedded PZT transducer. 34

Figure 2: Configuration of embedded PZTs in CFRP laminates. 39

Figure 3: Illustration of the geometry used for the numerical FE short beam three point bending test (a) and a zoom of the section view of the numerical model with the PZT inserted between layers 4 & 5 (b). 44

Figure 4: Contour plot of Hashin's damage index values on the CFRP Layer under the PZT (top view). The PZT and glass fibre layer were inserted between layers 8 & 9. 46

Figure 5: Contour plot of Hashin's damage index values on the glass fibre layer above the PZT (top view). The PZT and glass fibre layer were inserted between layers 8 & 9. 46

Figure 6: Dimensions of short-beam specimens (a) and long-beam specimens (b) used in bending tests. 47

Figure 7: Dimensions of specimens used in compression tests. 48

Figure 8: Schematic of short-beam (a) and long-beam (b) three-point-bending configurations. 49

Figure 9: Schematic of compression test fixture. 49

Figure 10: Long-beam specimen - section view. 50

Figure 11: Short-beam specimens - cross-sectional view of damaged P-specimen (a), G-specimen (b) and K-specimen (c). 53

Figure 12: Short-beam specimens - closer view of specimen ends in the control P-specimen (a), damaged P-specimen (b), control G-specimen (c), damaged G-specimen (d), control K-specimen (e) and damaged K-specimen (f). 54

Figure 13: Long-beam specimens - cross-sectional view of P-specimen (a), G-specimen (b) and K-specimen (c). 55

Figure 14: Long-beam specimens - closer view of damage area (a) and PZT area (b). 56

Figure 15: Compression specimens - closer view of un-tabbed section in the control P-specimen (a) damaged P-specimen (b), control G-specimen (c), damaged G-specimen (d), control K-specimen (e) and damaged K-specimen (f). 57

Figure 16: Composite specimens used in NEWS experiment with embedded PZTs (a) and their lay-up (b). 58

Figure 17: Illustration of set-up used in NEWS experiment. 59

Figure 18: Illustration of the damaged area scanned by the laser Doppler vibrometer (a) and 3D representation of the out-of-plane vibrational velocity on the specimen 1 surface at the second harmonic frequency of 30 kHz. 60

Figure 19: Amplitude of the received signal in time domain (a) and its associated spectrum (b) - case of 100V input signal at 15 kHz. 62

Chapter 4. Nonlinear Ultrasonic Detection of Damage in Smart CFRP Composites

Figure 1: Design of undamaged CFRP plate - top view (a) and stacking sequence (b). Dimensions in mm. Not to scale. 76

Figure 2: Design of artificially damaged plate (a) and impact damaged plate (b). Dimensions in mm. Not to scale. 76

Figure 3: Ultrasonic C-scan of the small (a) and the big (b) artificial damage in AD-laminate and the associated B-scans (c), (d) - Images not to scale. 77

Figure 4: Ultrasonic C-scan of the 10 J (a) and the 15 J (b) impact damage in ID-laminate and the 78

Figure 5: Illustration of the set-up used in NEWS experiments. 78

Figure 6: Illustration of the set-up used in LV experiments. 81

Figure 7: Frequency spectrum of the received signal in the UD-laminate and in the AD-laminate - Input signal of 60 V at 184.7 kHz. 81

Figure 8: Amplitude of the received signal in AD-laminate at the fundamental (a) and second (b) harmonic frequencies - Input signals of 60, 70, 80, 90, and 100 V at 104.5 and 184.7 kHz. 82

Figure 9: Amplitude of the received signal in ID-laminate at the fundamental (a) and second (b) harmonic frequencies - Input signals of 60, 70, 80, 90, and 100 V at 128 and 310 kHz. 82

Figure 10: 3D representation of the out-of-plane vibrational velocity around the location of the small (a) and the big (b) artificial damage at the fundamental and second harmonic frequencies. 83

Figure 11: 3D representation of the out-of-plane vibrational velocity around the location of the 10 J (a) and the 15 J (b) impact damage at the fundamental and second harmonic frequencies. 83

Figure 12: Amplitude of the received signal in the UD-laminate and the ID-laminate at f_1 (a) and at f_2 and $f_2 \pm f_1$ (b) - Input signal voltage to PZT2 = 50 V and to PZT1 = 60 V. 85

Figure 13: Amplitude of the received signal in the ID-laminate at f_1 & f_2 (a) and at $f_2 \pm f_1$ (b) - Input signal voltage to PZT2 = 50 V and to PZT1 = 60, 70, 80, 90 and 100 V. 85

Figure 14: 3D representation of the out-of-plane vibrational velocity at the location of the impact damage at f_1, f_2 and $f_2 \pm f_1$ 86

Chapter 5. Tensile-Mode Fatigue of Smart CFRP Composites and Nonlinear Ultrasonic Monitoring of Damage

Figure 1: Illustration of the SCODD system (a) and the arrangement of sensors around the impact monitoring grid (b) [198]. 92

Figure 2: Illustration of the set-up used to test the MA method (a) and the arrangement of sensors around the impact monitoring grid (b) [199]. 93

Figure 3: Illustration of P-specimen (a) and G-specimen (b) used in this study. 98

Figure 4: Design of test specimens. 100

Figure 5: BVID on top (b) and bottom (c) specimen surfaces from 3 J impact, and the associated C-scan (c) and B-scan (d). 101

Figure 6: Illustration of the set-up used in the nonlinear ultrasonic experiments. .. 103

Figure 7: Received signal amplitude in frequency spectrum of G-specimen after 120k fatigue cycles - case of 100 V input signal between 200-250 kHz. 103

Figure 8: Tensile failure of specimens without BVID. Top view (a) and side view (b) of P-specimen, and top view (c) and side view (d) of G-specimen. 104

Figure 9: Tensile failure of specimens with BVID. Top view (a) and side view (b) of P-specimen, and top view (c) and side view (d) of G-specimen. 104

Figure 10: Tension-tension fatigue failure of specimens without BVID. Top view (a) and side view (b) of P-specimen, and top view (c) and side view (d) of G-specimen. 105

Figure 11: Tension-tension fatigue failure of specimens with BVID. Top view (a) and side view (b) of P-specimen, and top view (c) and side view (d) of G-specimen. 105

Figure 12: Capacitance of transmitting (a) and receiving (b) sensors in G-specimens. 108

Figure 13: Change in nonlinear parameter β with increasing number of fatigue cycles for G-specimen 1 (a), G-specimen 2 (b) and G-specimen 3 (c) - Input signal of 100V at 200-220 kHz. 110

Figure 14: Peak value of nonlinear parameter β at each state of G-specimens 1, 2 and 3 during fatigue testing - Input signal of 100V at ~210 kHz. 111

Chapter 6. A Nonlinear Ultrasonic Method for In-Plane Localisation of Impact Damage

Figure 1: Example of functionality check of sensor S2 based on the correlation coefficients r_{12} and r_{23} of the time signals in directions d_{12}, d_{21} and d_{23}, d_{32} respectively. 126

Figure 2: Illustration of nonlinear parameter β amplitude assigned to four sensor-to-sensor paths in the form of ellipses. 127

Figure 3: Illustration of CFRP panel 1 (a), 2 (b) and 3 (c) - Dimensions in mm. Not to scale. 128

Figure 4: C-scan around the location of BVID on CFRP panels 1 (a), 2 (b) and 3 (c). 129

Figure 5: Illustration of the set-up used in the nonlinear ultrasonic experiments. ..130

Figure 6: Positioning of sensor array around the location of BVID on CFRP panel 1 (a), 2 (b) and 3 (c). 131

Figure 7: Average plot of the received signals spectrum captured in all paths of CFRP panel 2 under ultrasonic excitation from 100 kHz to 500 kHz. 132

Figure 8: Frequency spectrum of the signal received by (a) sensor S1 and (b) sensor S5 on CFRP panel 2 under ultrasonic excitation of sensor S3 at f_s = 357.9 kHz. 133

Figure 9: Plot of correlation coefficients between the forward and backward signals in outer sensor-to-sensor paths using eight functional sensors (a) and after replacing S6 with a partially damaged sensor (b). 135

Figure 10: Normalised map of nonlinear parameter β in CFRP panel 1 - array position 1 (a), panel 1 - array position 2 (b), panel 2 (c) and panel 3 (d). The ellipses represent the actual size of internal delamination. 135

Figure 11: Normalised map with threshold of nonlinear parameter β in CFRP panel 1 - array position 1 (a), panel 1 - array position 2 (b), panel 2 (c) and panel 3 (d). The ellipses represent the actual size of internal delamination. 136

Chapter 7. A Nonlinear Ultrasonic Approach for Through-Thickness Localisation of Contact Defects

Figure 1: Longitudinal wave propagation through contact interface between two material layers held under pressure. 147

Figure 2: Frequency order of phased array elements in signal u_{f1} (a), signal u_{f2} (b), signal u_{f12} (b) and signal u_{f21} (d). The numerical superscripts indicate the 0º and 180º phase angles respectively. 149

Figure 3: Illustration of the frequency spectrum resulting from signal summation $u_{f1}^{0} + u_{f2}^{0}$ (a), $u_{f12}^{0} + u_{f21}^{0}$ (b), $u_{f1}^{0} + u_{f1}^{180}$ (c), $u_{f2}^{0} + u_{f2}^{180}$ (d), $u_{f12}^{0} + u_{f12}^{180}$ (e) and $u_{f21}^{0} + u_{f21}^{180}$ (f). 151

Figure 4: Size of aluminium disks (a) and their stacking sequence in test sample AL1 (b) and AL2 (c). Dimensions in mm. Not to scale. 153

Figure 5: Size of composite laminates (a) and their stacking sequence in test sample CFRP1 (b) and CFRP2 (c). Dimensions in mm. Not to scale. 153

Figure 6: Hilbert transform of linear response against absolute nonlinear modulated response of sample AL1. Normalised plot showing the contact interfaces and back surface (a), and normalised plot around interface 1 (b), interface 2 (c) and back surface (d). 156

Figure 7: Hilbert transform of linear response against absolute nonlinear modulated response of sample CFRP1. Normalised plot showing the contact interfaces and back surface (a), and normalised plot around interface 1 (b), interface 2 (c) and back surface (d). 157

List of Tables

Chapter 1. Introduction

Table 1: Peer-reviewed journal papers.....10

Table 2: Conference papers.....10

Chapter 3. Development of Smart CFRP Composites with Embedded PZT Transducers

Table 1: Properties of CFRP layer and woven E-glass fibre fabric layer. 43

Table 2: Properties of PZT and resin. 43

Table 3: Summary of Hashin's Failure Values. 46

Table 4: Summary of mechanical testing results. 52

Table 5: Summary of damage measurements in short-beam specimens. 54

Table 6: Summary of damage measurements in long-beam specimens. 56

Table 7: Summary of results from NEWS experiment. 62

Chapter 4. Nonlinear Ultrasonic Detection of Damage in Smart CFRP Composites

Table 1: Input signal frequencies and voltages used in NEWS experiments for second harmonic generation. 79

Table 2: Input signal frequencies and voltages used in NEWS experiments for nonlinear wave modulation. 80

Chapter 5. Tensile-Mode Fatigue of Smart CFRP Composites and Nonlinear Ultrasonic Monitoring of Damage

Table 1: Summary of tensile and fatigue testing results. 107

Chapter 6. A Nonlinear Ultrasonic Method for In-Plane Localisation of Impact Damage

Table 1: Coordinates of sensors and damage on CFRP panels 1, 2 and 3. 131

Chapter 7. A Nonlinear Ultrasonic Approach for Through-Thickness Localisation of Contact Defects

Table 1: *SNR*, w_h and ε_p of the peaks in R_{f1} and $R_{\beta s+\beta d}$ responses of aluminium and CFRP samples. 158

List of Acronyms

AE	Acoustic Emission
ANOVA	Analysis of Variance
BVID	Barely Visible Damage
CAN	Contact Acoustic Nonlinearity
CFRP	Carbon Fibre Reinforced Plastic
CT	Computerised Tomography
CZM	Cohesive Zone Model
FE	Finite Element (analysis or model)
FEP	Fluorinated Ethylene Propylene (polymeric film)
FRP	Fibre Reinforced Plastic
GFRP	Glass Fibre Reinforced Plastic
IR	Infrared
LDR	Local Defect/Damage Resonance
LV	Laser (Doppler) Vibrometer
MA	Minimum Average (method)
MMOD	Micrometeoroids and Orbital Debris
MRI	Magnetic Resonance Imaging
NDE	Non-Destructive Evaluation
NEWS	Nonlinear Elastic Wave Spectroscopy
PVDF	Polyvinylidene Fluoride (piezoelectric film transducers)
PZT	Lead Zirconate Titanate (piezoelectric ceramic transducers)
SCODD	Smart Composite Orbital Debris Detector
SEM	Scanning Electron Microscopy
SHM	Structural Health Monitoring
SNR	Signal-to-Noise Ratio
TR	Time Reversal (method)
UT	Ultrasonic Testing
VI	Visual Inspection

Chapter 1

Introduction

1.1 Motivation

The continuous development of engineering structures with more complex geometries, improved performance and higher efficiency is directly related to the use of advanced materials with enhanced properties. This is common in many engineering fields such as the automotive, marine and civil, but most importantly the aerospace industry where a large percentage of metallic parts have been replaced with fibre-reinforced polymer (FRP) composite components during the past few decades. The advantages of FRP materials are numerous with some of the most important being their low weight, high resistance to corrosion and great durability under repeated loading [1]. Briefly, the term FRP refers to the class of materials that are composed of polymeric matrix (typically epoxy resin) with integrated high-strength fibres for reinforcement. Examples of FRP materials include those made from glass fibres (GFRP), aramid fibres (Kevlar) and carbon fibres (CFRP), with the last one offering the highest strength-to-weight ratio. One of the most convenient and widely applicable methods for the fabrication of FRP composites involves the use of layers (plies) of unidirectional fibres which have been pre-impregnated with resin, known as "prepreg" layers. As illustrated in Figure 1, multiple layers are stacked with specific sequence (lay-up) of fibre orientation and cured in a pressure/thermal chamber resulting in the finished composite material which has the form of a laminated panel.

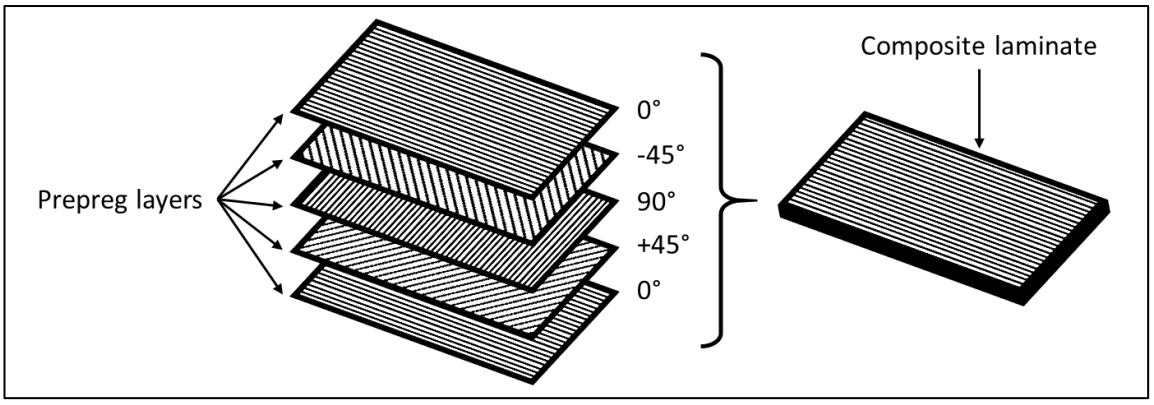

Figure 1: Typical stacking sequence of prepreg layers for the fabrication of composite laminates.

Despite the advantages that composite materials have over metals, their failure tends to be more unpredictable due to their high brittleness and their ability to contain internal defects or damage with minor visual signs (Figure 2). Damaging of composite parts on aircrafts and spacecrafts can occur at different stages throughout their life cycle. The typical defects attributed to manufacturing errors are porosity, ply waviness and delamination due to inclusions or contaminants [2]. In addition, fibre breakage, matrix cracking, debonding and delamination at several interfaces can be caused from applied loads and in many cases after low-energy or high-energy impacts from moving objects. For example, these can be impacts from accidental tool drops during maintenance-related activities, or impacts from hail storms, flying birds, orbital space debris and runway debris during in-service operations. Degradation of composites can also occur, especially in the form of matrix aging, as a result of over-exposure to high temperatures and UV radiation [2].

Among the above, low-energy impacts are considered particularly dangerous because they can lead to multi-mode internal damaging while leaving almost invisible dents or bumps on the surface, which are often referred to as barely visible impact damage (BVID). Apart from the aforementioned defects concerning the use of composite materials, damage such as plastic deformation, corrosion, fatigue cracks and thermal aging are common types of damage found in metallic parts due to mechanical stresses and environmental conditions [3]. These can also affect the integrity of a structure, meaning that their detection is of utmost importance.

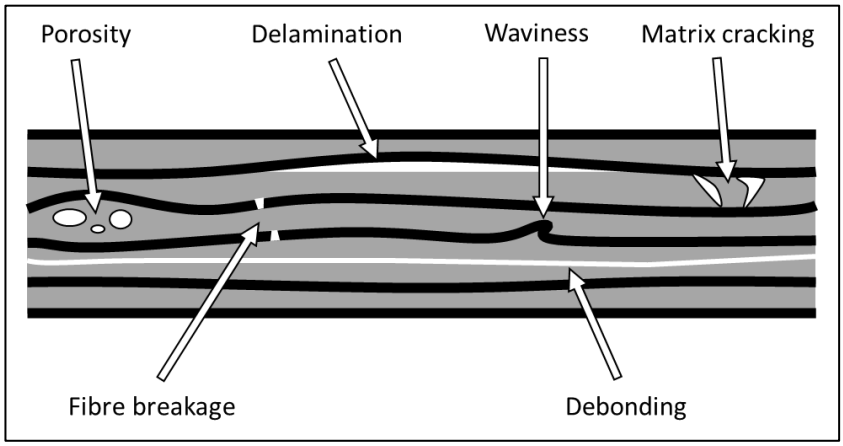

Figure 2: Common defects in composite laminates.

Therefore, the operation of critical structures demands rigorous inspections, which can be performed with various methods of non-destructive evaluation (NDE) namely visual testing (VT), acoustic emission (AE) testing, infrared (IR) and thermal scanning, electromagnetic (X-ray) testing, magnetic resonance imaging (MRI), computerised tomography (CT), scanning electron microscopy (SEM) and ultrasonic testing (UT) [4]. These are all recognised as reliable inspection methods, and the benefits and drawbacks between them can vary depending on the application. In most cases though, the inspection cannot be performed without taking the structure out of service, including all the associated delays, expenses and needs for facilities and experienced operators. Alternatively, the standard equipment required for ultrasonic NDE (e.g. transducers, waveform generators and oscilloscopes) can be permanently attached to the structure to create an on-board structural health monitoring (SHM) system. In general, ultrasonic SHM involves the installation of sensors at different locations across the structure for the transmission and reception of ultrasonic waves, enabling the identification of changes in the acoustic response of material that are indicative of defect or damage existence (Figure 3). The effectiveness and versatility of ultrasonic SHM techniques attracted the interest of many researches in both academia and industry. The ultrasonic methods can be divided into two main categories, the linear and the nonlinear [5]. In the first category, flaws can be detected based on the linear ultrasonic effects occurring in the inspected material from the interaction between the propagating waves and the flaws. Reflections, scattering and attenuation of waves are examples of such effects.

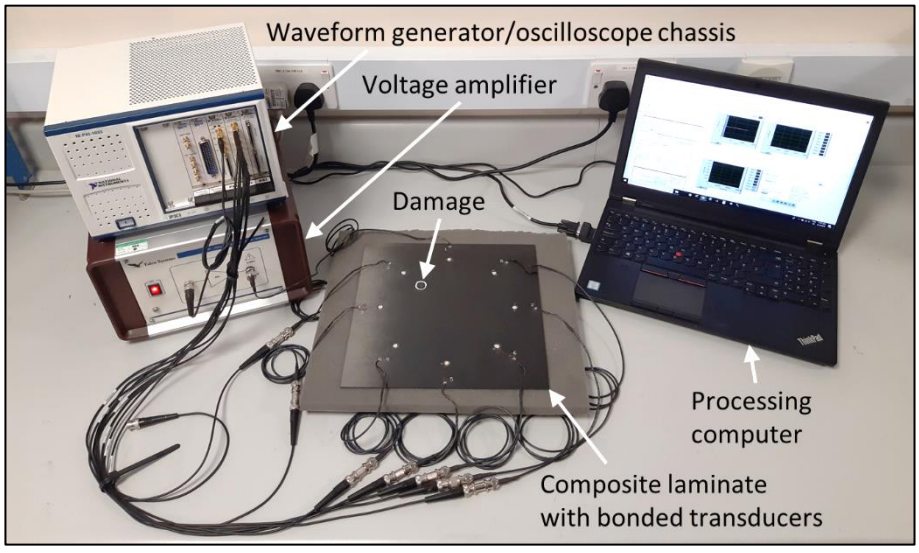

Figure 3: Example of experimental set-up used for ultrasonic structural health monitoring of materials.

In the second category, damage detection relies on the identification and quantification of effects associated with the presence of nonlinear waves generated from the excitation of the damaged interfaces, after their interaction with the incident propagating waves. In the acoustic response of the material, the nonlinear waves are characterised by unique features such as the presence of higher order harmonics, sub-harmonics and modulation sidebands in the spectrum of the detected signals. In contrast to linear ultrasonic methods, the nonlinear techniques have demonstrated higher sensitivity and accuracy in the detection of defects, especially at the initial stages of micro-damage formation [5]. Additional information is provided in Chapter 2.

According to the above, a number of nonlinear ultrasonic SHM methods have been developed by many researches over the last years, with some great advances in the detection, localisation, imaging and monitoring of damage in metallic and composite structures [6]. However, this is a continuously growing field, and most of the existing methods and systems are far from being optimised. Depending on the application, there is always space for improvement in relation to the complexity of implementation and the efficiency of data acquisition and processing.

For instance, some aircraft and spacecraft applications can benefit from the placement of sensors inside the composite materials instead of attaching them to the surface [7]. This will prevent the transducers from direct exposure to humidity, radiation and external impacts while maintaining smooth (aerodynamic) surfaces on the structure. Only a limited number of studies though proposed designs of such “smart” CFRP laminates with embedded piezoelectric transducers, because of the challenges associated with the electrical insulation of the sensors from the conductive carbon fibres. In those studies, insulation was achieved using polymeric films or coatings, but these are known to impede the adhesion between the composite layers with the risk of causing delamination [8]. In addition, the detection and monitoring of damage in CFRP composites based on nonlinear ultrasonic techniques combined with the use of embedded sensors has never been attempted in the past. Hence, the introduction of a novel method for the electrical insulation of embedded piezoelectric sensors with no impact on the strength of CFRP laminates will be a significant contribution to the design of “smart” materials. This is one of the areas this research focuses on, as well as the suitability of these embedded sensors for nonlinear ultrasonic testing.

In other SHM applications, the use of externally mounted transducers is preferred for easier access and replacement of any malfunctioning or damaged sensors. With regard to the localisation of impact damage and delamination in composite panels using sparse arrays of sensors, the available ultrasonic methods (linear and nonlinear) often rely on measurements of the arrival time of the signals [9, 10]. This can be very difficult and time consuming in the case of composite materials as the wave velocity changes in different directions depending on the lay-up (i.e. fibre orientation) of the laminate. Moreover, the techniques usually depend on the correlation between the captured signals and baseline data recorded at the pristine state of the structure, as well as on the assumption that the sensors forming the array are all functional [11, 12]. However, it is hardly possible for future inspections to be carried out under the same conditions (environmental, boundary, etc.) that existed during the acquisition of baseline data, and it is very likely for the external sensors to be subject to impact damage, corrosion and degradation. Hence, the effectiveness of these methods can be significantly affected. Furthermore, there is often lack of explanation regarding the selection of the frequency used for the transmission of waves through the material, which is very critical for the excitation and detection of defects. Based on the above, there is a need for nonlinear ultrasonic SHM methods that will not rely on baseline data or the time-of-flight of signals, will follow some simple steps for the choice of the frequency of signals and at the same time will be capable of identifying any malfunctioning transducers in the array. In this way, the localisation of impact damage in composite laminates will be more practical and reliable, and this is another research topic of this PhD.

Except for the localisation of damage across the surface area (in-plane) of structures, there are several applications where metallic and composite thin-walled structures need to be inspected through their thickness. This is important for the estimation of the depth at which contact type defects such as kissing bond, closed crack, delamination and debonding may be present. These flaws are characterised by an interface of plastic contact between two layers (zones) of the material, meaning that there is lack of mechanical strength at the interface [13]. Ultrasonic pulse-echo methods are broadly utilised for through-thickness inspections as they require access only to one side of the material. Typically, longitudinal waves are generated from an ultrasonic source which can also be used for the capturing of echoes. The ultrasonic source can be represented by a transducer containing a single piezoelectric element, or a single probe housing an array of elements.

The second option is becoming more desirable as the elements can be excited individually based on a programmed pattern of delay laws. This difference in the excitation phase of the elements enables focusing or steering of the transmitted wave beam for more accurate localisation of damage [14]. Nevertheless, in many cases, such defects remain "transparent" under linear ultrasonic inspection because when the material is compressed the waves can propagate through the closed interface with nearly negligible amount of reflection or attenuation [15]. For this reason, few recent studies proposed phased array methods for nonlinear ultrasonic identification of contact defects. However, the majority of these experiments were conducted on samples containing a single interface of damage, and in many cases on samples containing a vertical crack [16, 17]. The localisation of multiple horizontal contact interfaces of damage remains particularly challenging. This is because the generation of detectable nonlinear acoustic effects from deeper defects requires the transmission of high-voltage signals with long duration, which is often a limitation for the equipment of conventional phased array systems. Hence, the last area of this research focuses on the optimisation of a nonlinear ultrasonic phased array technique, for the reduction of noise in the recorded acoustic response. As a result, the detection of nonlinear ultrasonic features can be improved, enabling more sensitive and accurate identification of contact flaws in the material.

1.2 Research Aim and Objectives

The main aim of this research project is to propose novel designs of SHM systems and improved NDE methods based on ultrasonic wave propagation, for enhanced sensitivity and accuracy in the detection and localisation of structural damage in metallic and composite materials. The objectives for the achievement of this aim are directly related to the research opportunities arising from the challenges in the specific applications of NDE mentioned in Section 1.1. Below is a list of the three primary objectives (•) along with their associated tasks (−).

- Fabrication of "smart" CFRP laminates with embedded piezoelectric transducers which are electrically insulated using an alternative technique.
  - Selection of sensor type and insulating material for strong adhesion with the resin matrix of the laminates.

  - Determination of sensor position through the thickness of the composite plates with the least impact on interlaminar properties, using numerical simulations.
  - Evaluation of the structural integrity of the "smart" CFRP samples through static and dynamic mechanical tests.
  - Assessment of the ultrasonic capabilities of the embedded sensors by conducting experiments for the detection and monitoring of material damage.

- Development of a practical and reliable SHM method, for the identification and positioning of impact damage in composite laminates using a sparse array of sensors.
  - Creation of an algorithm for the evaluation of acoustic nonlinearities in the sensor-to-sensor paths without using baseline data or the arrival time of signals.
  - Establishment of a plan for the identification of any malfunctioning transducers in the array.
  - Implementation of a procedure for the choice of an appropriate signal transmission frequency to achieve damage excitation.
  - Testing of the algorithm performance on different composite laminates.

- Introduction of a phased array method with improved signal-to-noise ratio (SNR) to enable more sensitive and precise localisation of contact defects at various levels through the thickness of the material.
  - Decision about the nonlinear ultrasonic effect to be utilised for the identification of defect existence.
  - Optimisation of a signal processing technique for the extraction of the acoustic nonlinearities associated with the contact defects.
  - Programming of the firing sequences of the piezoelectric elements for the generation of the different signals to be processed.
  - Verification of the method effectiveness by performing tests on metallic and composite samples.

1.3 Thesis Outline

The outline of this thesis follows the "PhD by publication" format, and thus the peer-reviewed journal papers listed in Table 1 are integrated as chapters. The objectives

mentioned in the previous section are completed through the work presented in the papers. Table 2 summarises the papers published in conference proceedings, for reference only. In Chapter 2, the theoretical background and literature related to this research work are covered. More specifically, different ultrasonic testing methods and designs of composites with internal sensors are explained and compared with reference to their advantages and disadvantages. In addition, a review of the state-of-the-art literature is provided highlighting the existing limitations and challenges associated with the ultrasonic detection and localisation of damage in materials, and the development of "smart" composite materials.

Chapter 3 to Chapter 7 refer to the journal publications from Paper I to Paper V respectively. Every chapter begins with a summary of the scope, process and outcome of the work completed in the corresponding publication, followed by the accepted manuscript. It must be noted that some descriptions and definitions are repeated throughout this thesis since each article has self-contained sections such as the introduction, theoretical background and conclusions.

Chapter 3 represents the initial study on the development of an alternative design of "smart" CFRP laminates using a novel method for the electrical insulation of embedded piezoelectric transducers. This chapter provides the numerical simulations conducted for the determination of the least destructive position of the sensors through the thickness of the laminates. In addition, it covers the mechanical tests performed for the assessment of the compressive, flexural and interlaminar shear strength of the "smart" CFRP specimens, along with the post-test fractographic inspection of the samples. Moreover, this chapter presents the nonlinear ultrasonic experiments regarding the functionality of the embedded sensors and their sensitivity to the detection of delamination.

Moving to Chapter 4, the layout of embedded sensors introduced in Chapter 3 is employed for the detection of multiple types of damage with different size in CFRP plates, using two separate nonlinear ultrasonic techniques. This chapter includes the experiments performed on a laminate containing two areas of delamination, and a laminate with impact damage caused by two different levels of impact energy.

Chapter 5 investigates how the tensile strength and fatigue endurance of "smart" CFRP laminates is affected by the inclusion of piezoelectric transducers using the same embedding configuration as in Chapter 3 and Chapter 4. This chapter summarises the results from the mechanical tests performed using undamaged and impact damaged

"smart" specimens. Also, this chapter examines the durability of the internal sensors under cyclic loading conditions, and their capability of monitoring the growth of impact damage with regard to nonlinear ultrasonic wave propagation.

About Chapter 6, this is related to the second research topic of this PhD and introduces a novel nonlinear ultrasonic SHM method for the localisation of impact damage in CFRP laminates using a circular array of externally attached piezoelectric transducers. This chapter explains how an appropriate signal transmission frequency is chosen, and demonstrates how the accuracy of the proposed technique is not reliant on the recording of baseline data or the measurement of the arrival time of the signals. Moreover, this chapter shows how the proposed technique can be used for the identification of malfunctioning transducers using the signals recorded only in the peripheral paths of the array. Application of this method is demonstrated on three CFRP panels with BVID.

The last topic of this research work which concerns the requirement for more effective detection of multiple horizontal contact interfaces through the thickness of the material is explored in Chapter 7. In fact, this chapter describes how a phased array method associated with the nonlinear mixing of waves with two different frequencies can be optimised to offer reduced levels of noise in the received signal response, and eventually improve the sensitivity and accuracy of pulse-echo inspection. Based on this, the chapter explains how the signals generated from a phased array probe using different firing combinations of the piezoelectric elements can be processed to extract the acoustic nonlinearities corresponding only the excitation of defects. This alternative phased array method is tested on two aluminium and two CFRP samples with contact interfaces at various depths.

Finally, the conclusions of this thesis along with the recommendations for possible future work on the basis of this research study are discussed in Chapter 8.

Table 1: Peer-reviewed journal papers.

Paper	Publication Details (Reference)
I	Andreades, C., Mahmoodi, P., & Ciampa, F. (2018). Characterisation of smart CFRP composites with embedded PZT transducers for nonlinear ultrasonic applications. *Composite Structures*, 206(1), 456-466.
II	Andreades, C., Malfense Fierro, G. P., Meo, M., & Ciampa, F. (2019). Nonlinear ultrasonic inspection of smart carbon fibre reinforced plastic composites with embedded piezoelectric lead zirconate titanate transducers for space applications. *Journal of Intelligent Material Systems and Structures*, 30(20), 2995-3007.
III	Andreades, C., Meo, M., & Ciampa, F. (2020). Tensile and fatigue testing of impacted smart CFRP composites with embedded PZT transducers for nonlinear ultrasonic monitoring of damage evolution. *Smart Materials and Structures*, 29(5), 055034.
IV	Andreades, C., Fierro, G. P. M., & Meo, M. (2020). A Nonlinear ultrasonic SHM method for impact damage localisation in composite panels using a sparse array of piezoelectric PZT transducers. *Ultrasonics*, 108(1), 106181.
V	Andreades, C., Fierro, G. P. M., & Meo, M. A Nonlinear Ultrasonic Modulation Approach for the Detection and Localisation of Contact Defects. *Mechanical Systems and Signal Processing*, (Submitted).

Table 2: Conference papers.

Paper	Publication Details (Reference)
I	Andreades, C., & Ciampa, F. (2017). Embedded piezoelectric transducers in carbon fibre composites for nonlinear ultrasonic applications. In *Proceedings of the 11th International Workshop on Structural Health Monitoring IWSHM 2017* (Vol. 1, p. 739-746). DEStech Publications.
II	Andreades, C., & Ciampa, F. (2018). CFRP Composites with Embedded PZT Transducers for Nonlinear Ultrasonic Inspection of Space Structures. In *Proceedings of the 9th European Workshop on Structural Health Monitoring EWSHM 2018* (Vol.1, p. 0133). Elsevier.
III	Andreades, C., Meo, M., & Ciampa, F. (2020). Fatigue testing and damage evaluation using smart CFRP composites with embedded PZT transducers. In *Materials Today: Proceedings of the 12th International Conference on Composite Science and Technology ICCST 2019* (DOI: 10.1016/j.matpr.2020.03.081). Elsevier.

Chapter 2

Background and Literature Review

This chapter provides an overview of the background information and the previous studies related to the work presented in this thesis. Emphasis is given to the nonlinear ultrasonic techniques for NDE and SHM of metallic and composite structures used in engineering applications (mainly in aerospace), as well as to the development of "smart" composite materials with integrated piezoelectric sensors. The details reported in the following sections of this chapter can be combined with the literature review included in the Introduction section of each individual chapter (journal paper) to clarify the challenges and gaps this research project aims at making a contribution.

Section 2.1 introduces the concept of ultrasonic wave propagation as an inspection tool for NDE of materials, and explains the fundamental configurations of ultrasonic testing. The basic principles of linear ultrasonic methods are described in Section 2.2 along with a general review of their applications and limitations in the characterisation of damage in material. Section 2.3 introduces the mechanisms of material nonlinearities and the associated nonlinear ultrasonic effects. Attention is focused on two of the most popular effects which are also exploited in the work of this thesis; (i) the generation of second-order frequency harmonics and (ii) the modulation of waves with two different frequencies. Two sub-sections are devoted to their explanation together with a review of their use in nonlinear ultrasonic methods for the detection, localisation and imaging of structural defects. The fabrication of "smart" composite laminates with embedded piezoelectric transducers for in-service ultrasonic SHM of materials is discussed in Section 2.4. A review of the previous studies highlights the challenges related to (i) the different techniques for sensor embedment and (ii) the need for electrical insulation of sensors when inserted in CFRP plates.

2.1 Ultrasonic Wave Inspection of Materials

The idea of using ultrasonic waves for the detection of flaws in solids was originally studied and proposed by Sokolov in the late 1920s, and this was inspired from high-frequency underwater inspection systems employed in submarine applications during World War I. The development of technology enabled Mulhauser to obtain a patent in 1931 for ultrasonic identification of defects using two probes (transmitter-receiver) [18]. In 1940, Firestone (in United States) and Sproule (in Great Britain) achieved the detection of flaws by transmitting pulses and receiving reflected echoes on the same side of the material. They both registered several patents in the 1940s [19]. In 1949 the first commercial ultrasonic flaw detecting machines were developed by Krautkramer brothers in Germany and by Mitsubishi in Japan [20]. By 1960s piezoelectric ceramic transducers were already available and well-understood, and the first portable battery-operated ultrasonic inspection systems were introduced. Panametrics released the first generation of digital detecting devices in the early 1980s. The continuous improvements in technology over the following decades allowed the production of the compact ultrasonic systems that are available today for NDE of materials [20].

In aerospace and other industries, ultrasonic inspection refers to the NDE methods involving the use of actuating and sensing devices for the transmission and reception of elastic sound waves (mechanical vibrations) through the material, which are propagating at frequencies above the range of human hearing (i.e. > 20 kHz). The captured waves can be then analysed to reveal any changes to their characteristics (e.g. frequency, amplitude, phase, velocity etc.) that are directly related to alterations of the material properties due to the presence of surface/sub-surface defects. In most cases, the pulsing and receiving devices are transducers instrumented with piezoelectric elements that are capable of generating sound waves when supplied with voltage (electric charge), and inversely to convert any received wave into an electric charge based on the principle of piezoelectricity. Piezoelectric ceramic sensors made from lead zirconate titanate (PZT) compound are widely preferred for their high sensitivity and signal-to-noise ratio, great physical strength, low weight, chemical inertness, heat resistance and low cost [21]. The propagation of ultrasonic waves in solids and their characteristics are analysed comprehensively in the text books of Krautkramer J. and Krautkramer H. [22] and Rose [23], with particular focus on applications of NDE.

The two general configurations of ultrasonic testing are the pulse-echo and the transmission-reception (or pitch-catch). In the first one, a single-element or multi-element (array) ultrasonic transducer is coupled to the surface of the material for both the generation of longitudinal elastic waves and the recording of reflected echoes as the incident waves interact with internal flaws and the boundaries of the material such as the opposite surface (Figure 1a). This is typically utilised for the inspection of parts through their thickness, and it is particularly useful in applications where only one side of the material is accessible. In the transmission-reception layout, two or more transducers are placed at different locations on the structure. The pulser and the receiver can be used on opposite surfaces on the material to perform through-transmission (Figure 1b) detection of ultrasonic waves with the advantage of having reduced attenuation of wave energy relative to the pulse-echo approach. In addition, by using guided ultrasonic waves, the actuation and sensing process can be carried out over relatively long distances between the transducers on the surface of the material (Figure 1c). This enables faster inspection of structures with large surface area.

According to Rose [24], the term "guided waves" refers to the propagation of ultrasonic waves along a material, where the waves are repeatedly reflected and refracted at various angles by the boundaries or other interfaces between two zones of different

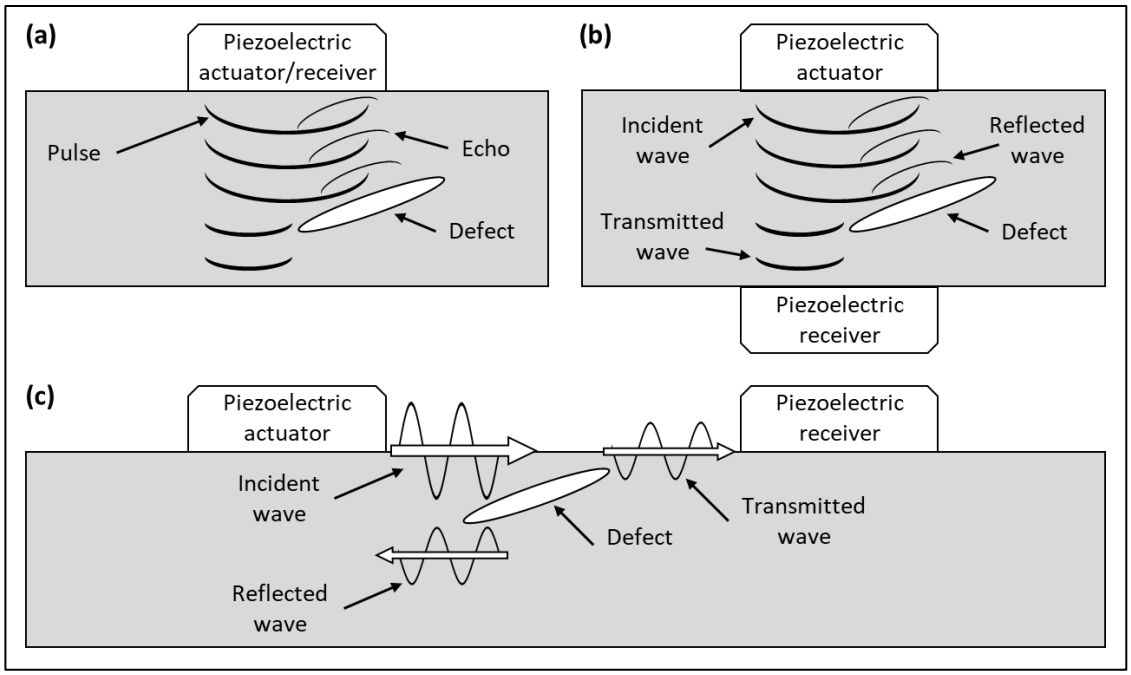

Figure 1: Schematic of pulse-echo (a), through-transmission (b) and pitch-catch (c) ultrasonic testing.

acoustic impedance. This causes the conversion of waves to additional modes (e.g. from longitudinal to shear/transverse wave), leading to regions of constructive and destructive interference based on the principle of superposition [24]. As a result, wave packets are formed that are propagating along the material and guided by the boundaries. Therefore, guided waves can follow the profile of the surface, meaning that they are suitable for the inspection of parts with more complex shapes. In addition, they offer long-distance propagation and high sensitivity to defects existing in their path. Two of the most popular types of guided waves are the Rayleigh and Lamb waves.

Briefly, Rayleigh waves (or surface waves) propagate on the surface of materials and include both longitudinal and shear modes that together result in an elliptical motion of the material particles perpendicular to the wave direction, as illustrated in Figure 2a [25]. This motion has a penetration depth from the level of surface of around one wavelength. Theoretically, in homogenous, isotropic and linear elastic materials the velocity of these waves is not a function of the frequency (i.e. non-dispersive waves) [25]. Regarding Lamb waves (or plate waves), these are typically propagating inside structures such as plates or shells with a thickness of the order of the wavelength. The waves are guided by the top and bottom surfaces of the material, and their direction of propagation is parallel to the plane of the surface. These are complex waves that exhibit multiple wave modes with the two principal being the symmetric (*S*) and the anti-symmetric (*A*), as shown in Figure 2.

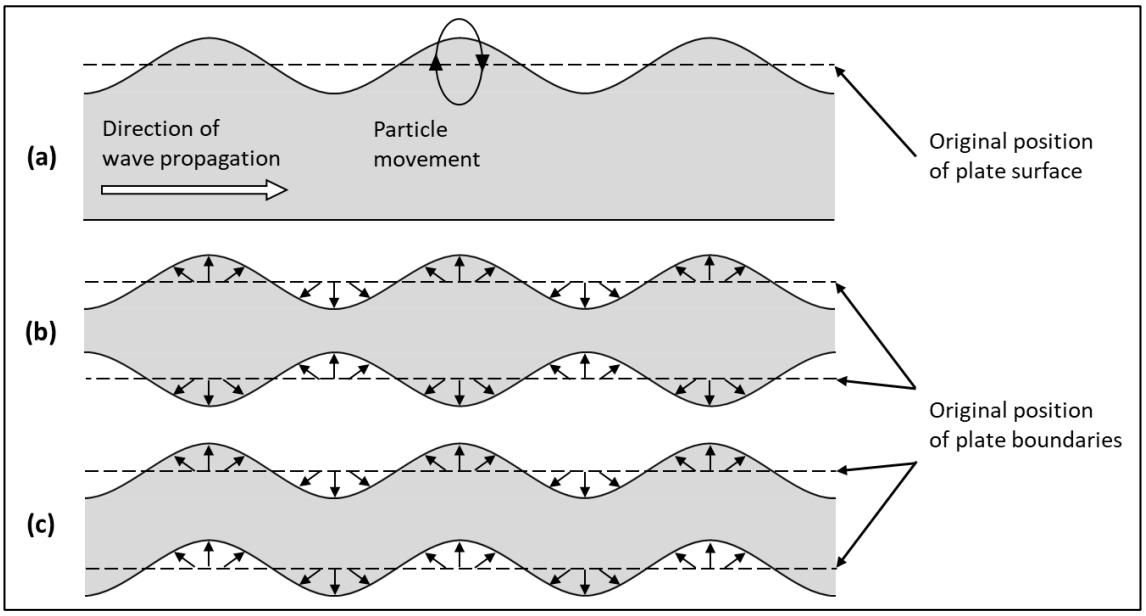

Figure 2: Cross-sectional view of plate during near-surface propagation of Rayleigh waves (a) and when excited at symmetric (a) and antisymmetric (b) modes of Lamb waves. Not to scale.

Each of these modes comprises of fundamental and higher-order components (S_i and A_i with $i = 0, 1, 2, ...$) and, unlike Rayleigh waves, their phase and group velocities are dependent on the product of the excitation frequency multiplied by the thickness of the plate (i.e. dispersive waves) [26]. As an example, the dispersion curves of S_i and A_i modes in an A606 steel plate are shown in Figure 3. Additional information about the calculation of these phase and group velocities are provided in [26].

A great number of NDE and SHM techniques have been developed around the concept of ultrasonic wave propagation that enable the identification of structural flaws, and in many cases the determination of the location and size of damage (i.e. damage imaging). These can be divided into two main categories; the linear and nonlinear ultrasonic methods. An overview of these two categories is provided in the following sections with closer attention to the nonlinear methods which are relevant to the research study presented in this thesis.

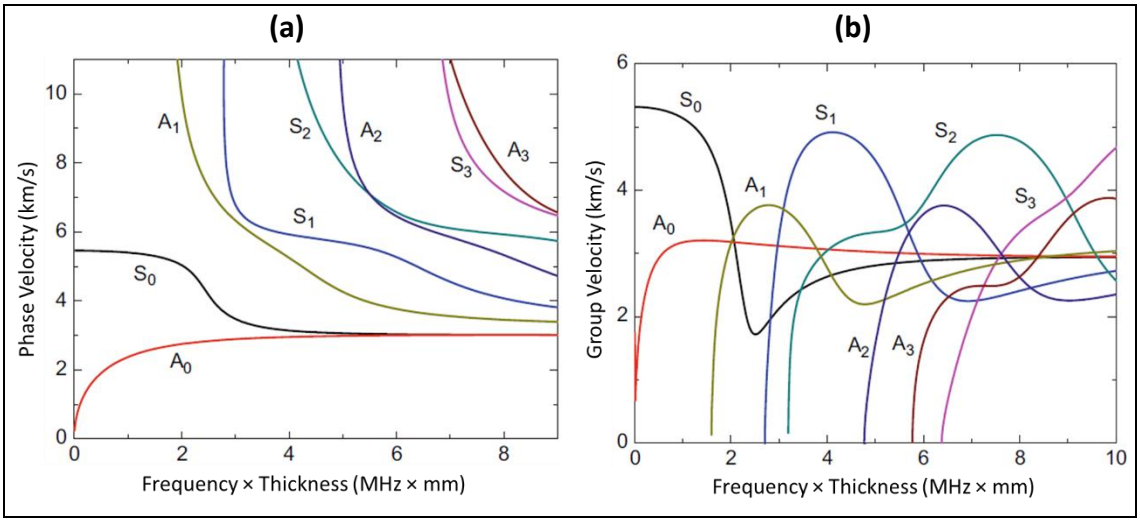

Figure 3: Phase (a) and group velocities (b) of symmetric and antisymmetric Lamb wave modes in A606 steel plate [26].

2.2 Linear Ultrasonic Methods

Traditional ultrasonic testing methods rely on the assumption that intact materials have perfectly linear elastic behaviour (Figure 4a), as described by the Hooke's stress-strain equation

$$\sigma = E\varepsilon \tag{1}$$

where E is the elastic (Young's) modulus of the material and ε is the strain at any given value of applied stress σ. Theoretically, if the material is undamaged, the frequency spectrum of the received signal contains only a single harmonic corresponding to the fundamental signal frequency (e.g. f_1), as shown in Figure 4b. These methods examine how the transmitted waves are affected by the defects relative to the case of wave propagation inside a pristine solid with linear elastic properties. For example, the waves passing over an anomalous region may be scattered or refracted. Also, internal cracks and voids containing trapped air can reflect partially or totally the incident waves towards the excitation source or another sensing device. These are common linear ultrasonic phenomena. By measuring the changes in the phase, amplitude and arrival time of waves, or by processing their scattering effects or even by evaluating their coefficients of transmission and reflection it is possible to estimate the elastic properties of the material (Young's modulus) as well as to localise and visualise the defects. It is important to be noticed that the frequency of the transmitted and received waves remains unchanged, and this is a characteristic of linear ultrasonic methods.

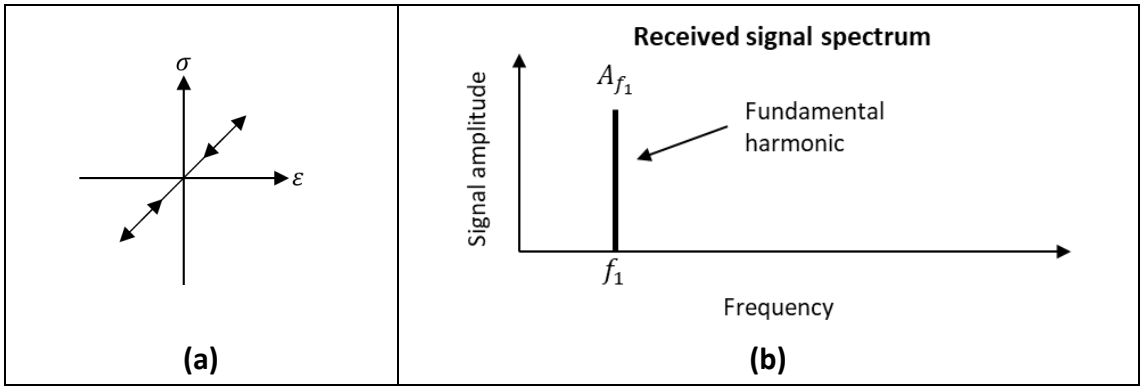

Figure 4: Stress-strain behaviour of linear undamaged materials (a) and their expected ultrasonic response under single frequency excitation (b).

2.2.1 Applications of Linear Ultrasonic Methods

Conventional linear ultrasonic methods rely on the transmission of bulk longitudinal or shear waves at low-amplitude and high-frequency for the detection of imperfections or flaws that exist in their propagation path. Under pulse-echo inspection, defects can be recognised in the captured response as echoes (reflections) of the incident wave. In through-transmission testing, dispersion and energy loss of the waves arrived at the receiving transducer indicate the propagation of waves through a flaw. According to Blitz

and Simpson [27] and Bond [28] these two testing layouts can be used for the characterisation of inclusions, cavities, cracks, delaminations, disbonds, bursts and other discontinuities in metals and composites.

As previously explained, pulse-echo is often the preferred layout for inspections through the thickness of thin-walled structures as it requires access only to one side of the material. A recent review from Felice and Fan [29] provides a good summary of the available pulse-echo techniques enabling the detection and sizing of defects, which are categorised as amplitude, temporal, imaging (e.g. delay-and-sum and super-resolution) and inversion (e.g. time-reversal and scattering matrix) techniques. However, the transducers in both configurations of pulse-echo and through-transmission testing must be moved along the surface until the entire structure is scanned. This is usually carried out manually which is not only time consuming but it also involves the risk of missing a defect, especially those oriented perpendicularly to the surface (e.g. vertical cracks) which have minimal interaction with the incident wavefront.

Alternatively, quick interrogation of large structural components with localised flaws can be achieved using guided Rayleigh and Lamb waves. Early studies on the application of such guided waves for ultrasonic NDE were published by Worlton [30, 31], Viktorov [32], Achenbach [33] and Graff [34]. The review studies of Rose [35], Su [36] and Guan [37] summarise the use of guided waves over the years based on different techniques for the detection and imaging of various types of defects including cracks, holes, aging and welding-induced voids in metallic parts (e.g. pipes, plates, turbine blades etc.) as well as impact and thermal damage, fibre fracture, delamination and transverse cracks in composite parts (e.g. laminated and sandwich structures, panels with lap-splice joints etc.). However, Rayleigh waves are mainly sensitive to imperfections near the surface of the material, and the multi-modal and dispersive nature of Lamb waves can make the analysis of captured signals very complicated [38].

In addition to these challenges, the major drawback of linear ultrasonic methods regardless of bulk or guided wave propagation is that their sensitivity is limited to defects with size similar to the wavelength or bigger (i.e. gross defects and open cracks). It is hardly possible for smaller defects to cause detectable changes to linear parameters such as the wave speed or the damping parameter [39]. In the case of multi-layered composite structures with anisotropic and viscoelastic properties, attenuation of waves is greater leading to even lower sensitivity. This is not always acceptable, especially in aerospace

applications, because gross defects can evolve rapidly to a size that is not safe for the integrity of the structure.

2.3 Nonlinear Ultrasonic Methods

Nonlinear ultrasonic testing methods, also referred to as nonlinear elastic wave spectroscopy (NEWS) techniques, are considered a powerful NDE and SHM tool because they are sensitive to flaws with size in the micro-scale, thus enabling damage detection much earlier than the traditional linear ultrasonic techniques [39]. NEWS methods focus on a number of different ultrasonic effects observed in the recorded response due to the nonlinear elastic behaviour of damaged solids.

2.3.1 Classical Nonlinearities

In the "classical" nonlinear theory of elasticity, ultrasonic nonlinearities in isotropic solids are the cause of distortions in the shape of propagating waves, leading to the generation of harmonic waves [40]. It is assumed that there are two primary sources for wave distortion. The first one is the anharmonicity of the lattice crystalline (i.e. nonlinear lattice elasticity), which is commonly referred to as inherent or intrinsic nonlinearity [40]. Imperfections in the atomic lattice can be exhibited in undamaged materials and they require relatively high internal stresses in order to produce detectable nonlinearities. Since the stresses induced by the propagating waves are usually low, intrinsic nonlinearities can have nearly negligible effects on the ultrasonic response of the material. The second source is related to the microstructural changes taking place in isotropic solids at the initial stages of material degradation, prior to crack initiation. These changes result in the formation of dislocations at localised regions which are arranged in patterns such as dislocation veins and persistent slip bands [41]. According to the model of Koehler [42], a single dislocation line can be considered as a straight string pinned at the two ends with the pins being represented by impurity atoms, as illustrated in Figure 5a. Further degradation of the material accompanied by microscopic plastic deformation introduces internal stresses (e.g. shear stress σ_τ) that cause the dislocation line to bow out forming an arc (Figure 5b) [43]. The displacement of the dislocation from this new equilibrium position is expected to be different under the application of equal magnitudes of positive and negative stress. Clearly this marks a deviation from the Hooke's law (i.e. linear stress-strain relationship), as shown in Figure 6a.

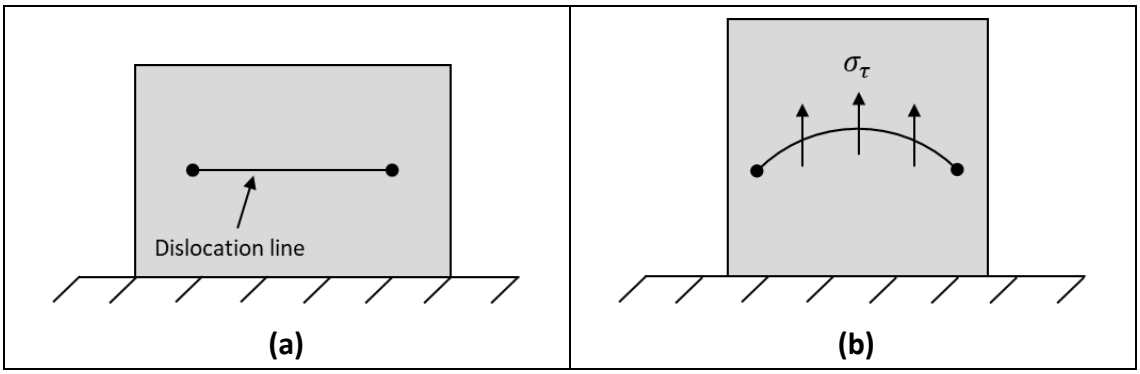

Figure 5: Illustration of a dislocation line at the original equilibrium position (a) and the new equilibrium position (bowing) due to internal shear stress.

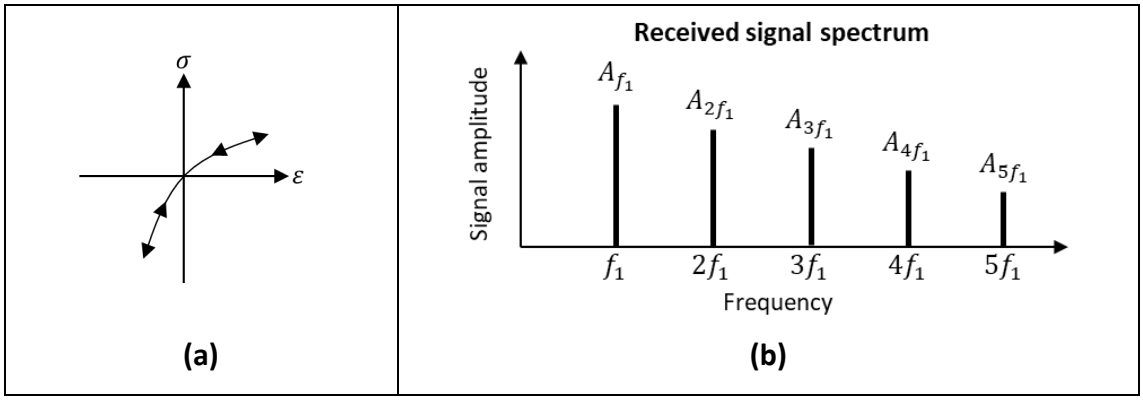

Figure 6: Stress-strain behaviour of materials with classical nonlinearity (a) and their expected ultrasonic response under single frequency excitation (b).

Therefore, when ultrasonic sinusoidal waves of sufficient stress amplitude pass through the medium, the oscillation of the bowed dislocation is nonlinear because of the asymmetric displacement caused by the tensile and compressive parts of the waves. As a result, the propagating waves are distorted leading to the generation of higher harmonics in the form of even and odd multiples of the fundamental excitation frequency (Figure 6b). This is the principal nonlinear phenomenon and it is usually modelled based on the "classical" nonlinear theory of elasticity [44, 45], where the elastic coefficients in the stress-strain equation of the solid describe the stress dependence on strain as a power series

$$\sigma = E\varepsilon(1 + \beta\varepsilon + \delta\varepsilon^2 + \cdots) \tag{2}$$

where $\varepsilon = \partial u(x,t)/\partial x$ is the strain and β and δ are the second and third order nonlinear coefficients (parameters) respectively. Equation (2) can be substituted into the following

equation which describes the propagation of one-dimensional longitudinal waves in the x-direction of the solid

$$\rho \frac{\partial^2 u(x,t)}{\partial t^2} = \frac{\partial \sigma}{\partial x}\,, \tag{3}$$

with ρ being the material density and $u(x,t)$ is the displacement. The resulting expression up to the second order term is

$$\frac{\partial^2 u(x,t)}{\partial t^2} - c^2 \frac{\partial^2 u(x,t)}{\partial x^2} = 2\beta c^2 \left(\frac{\partial u(x,t)}{\partial x}\right)\left(\frac{\partial^2 u(x,t)}{\partial x^2}\right) \tag{4}$$

where $c = \sqrt{E/\rho}$ is the longitudinal wave speed [46]. Perturbation theory can be used to solve equation (4), and based on this, the displacement $u(x,t)$ can be expressed as

$$u(x,t) = u^{(1)}(x,t) + u^{(2)}(x,t), \tag{5}$$

where $u^{(1)}(x,t)$ corresponds to the solution of the linear equation the input wave and $u^{(2)}(x,t)$ represents the first-order perturbation solution [46]. Assuming that the driving wave has the following format

$$u^{(1)}(x,t) = A_1 \sin(kx - 2\pi f t), \tag{6}$$

then the perturbation solution is

$$u(x,t) = A_1 \sin(kx - 2\pi f t) - \frac{\beta k^2 A_1^2}{8} x \cos[2(kx - 2\pi f t)], \tag{7}$$

where A_1 is the amplitude of the fundamental frequency harmonic, $A_2 = \frac{\beta k^2 A_1^2}{8} x$ is the amplitude of the second harmonic, x is the propagation distance from the source of nonlinearity and k is the wave number [46]. This analysis proves the generation of second-order harmonics as a result of the nonlinear behaviour of the material. Additional harmonics can be included (third, fourth and so on) by expanding the above equations to higher orders.

2.3.2 Non-Classical Nonlinearities

Damaged solids with cracks, voids, delamination and other major defects manifest highly nonlinear behaviour associated with more complicated effects. These can only be analysed with "non-classical" nonlinear models which are typically relying on the mechanisms of (i) mesoscopic (hysteretic) nonlinearity and (ii) contact acoustic nonlinearity.

2.3.2.1 Hysteretic Nonlinearity

Mesoscopic models are mainly used to describe heterogeneous materials with nonlinearities arising from the bonding system of internal cracks, grain contacts, dislocations, etc. The stress-strain curve of such materials is characterised by strong elastic nonlinearity and hysteresis which can be accompanied by discrete (end-point) memory [47, 48]. More specifically, a material is considered hysteretic when its stress-strain curve (Figure 7a) follows different paths during loading and unloading phases, and a loop of discrete memory can be created if a small change in stress takes place during the loading phase [49]. The area enclosed by the hysteresis loop represents the amount of dissipated energy.

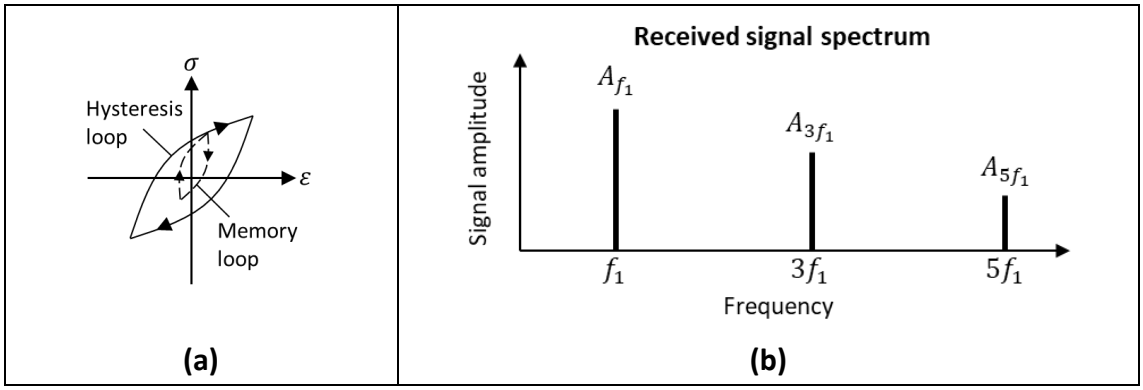

Figure 7: Stress-strain behaviour of materials with non-classical (hysteretic) nonlinearity (a) and their expected ultrasonic response under single frequency excitation (b).

The stress-strain expression that applies to hysteretic nonlinear materials is

$$\sigma = \int E(\varepsilon, \dot{\varepsilon}) d\varepsilon \tag{8}$$

with $$E(\varepsilon, \dot{\varepsilon}) = E_0\{1 - \beta\varepsilon - \delta\varepsilon^2 - \alpha[\Delta\varepsilon + \varepsilon(t)sign(\dot{\varepsilon})] + \cdots\} \tag{9}$$

where E is the elastic modulus, E_0 is the linear elastic modulus, α is a measure of the material hysteresis, $\Delta\varepsilon$ is the local strain amplitude, $\dot{\varepsilon}$ is the derivative of strain and $sign(\dot{\varepsilon})$ is equal to 1 or -1 for $\varepsilon > 0$ or $\varepsilon < 0$ respectively [50]. Equation (8) can be substituted into (3) similarly to the case of classical nonlinearity, to obtain a general solution verifying the generation of higher-order harmonics in the ultrasonic spectrum of the material. Ideally, when a sinusoidal wave propagates through a pure hysteretic medium, the discontinuities existing in the stress-strain behaviour (due to the changes in loading and unloading phases) convert it to a triangular wave. As a result, only odd higher harmonics of the driving frequency are generated (Figure 7b). In reality, mesoscopic

materials are rarely characterised by pure hysteretic nature. Instead, they also present classical nonlinear behaviour to some extent, meaning that higher harmonics can be generated at even multiples of the fundamental frequency as well.

2.3.2.2 Contact Acoustic Nonlinearity

The models related to contact acoustic nonlinearities apply to a wider range of materials and concern the mechanical constrain between the fractured surfaces at the plane of damage, causing their excitation to be strongly nonlinear. This is common for contact-type defects including closed fatigue cracks, delamination and debonding. The excitation of the defects can be categorised based on the movement of the surfaces at the damaged interface when interacting with the propagating ultrasonic waves.

The first category is related to the open-closing motion of the crack, known as the "clapping" mechanism (Figure 8a). In this case, the material is expected to exhibit a bi-linear stress-strain behaviour (Figure 8b) as its stiffness changes during the interaction of the pre-stressed crack (static stress σ^0 and strain ε^0) with longitudinal waves [51]. In particular, the tensile and compressive parts of the incident wave tend to open and close the damaged surfaces, respectively. Consequently, the material stiffness during the tensile phase is lower than in the compressive phase, because the crack is only supported by the stress acting on its edges.

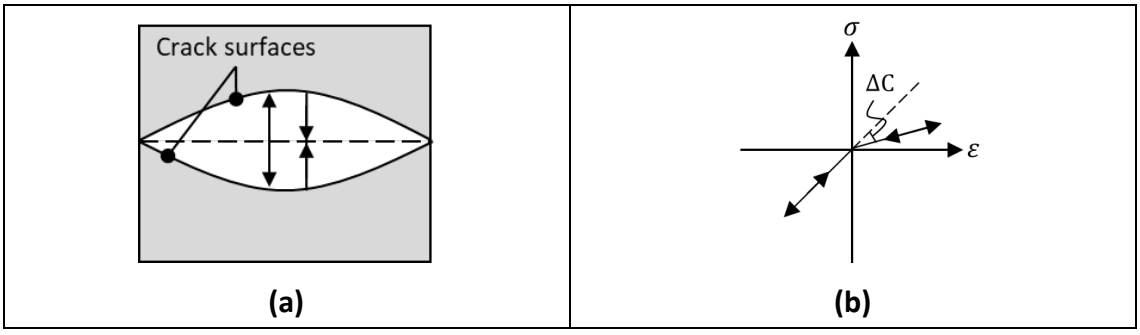

Figure 8: Schematic of opening-closing crack in materials with non-classical (contact) nonlinearity (a) and the resultant bi-linear stress-strain behaviour (b).

This bi-linear character of the material can be expressed with the following piece-wise stress-strain relation

$$\sigma = \varepsilon C[1 - H(\varepsilon)(\Delta C/C)], \tag{10}$$

where C is the linear stiffness at pristine material condition, $H(\varepsilon)$ is the Heaviside unit-step function and $\Delta C = [C - (d\sigma/d\varepsilon)]$ for $\varepsilon > 0$ [51]. The opening-closing motion of the crack acts as a half-wave rectifier which allows only the compressive part of the input wave to be transmitted through the contact interface. This wave distortion (nonlinearity) combined with the pulse-type material stiffness results in the generation of n higher harmonics (both even and odd) in the signal spectrum, and their amplitude is modulated by the $sinc$ envelope function

$$A_n = \varepsilon_0 \Delta C \Delta\tau [sinc((n+1)\Delta\tau) - 2\cos(\pi\Delta\tau) sinc(n\Delta\tau) + sinc((n-1)\Delta\tau)], \quad (11)$$

where ε_0 is the strain amplitude of the fundamental wave, $\Delta\tau = \tau/T$ is the normalised modulation pulse length with $\tau = (T/\pi) Arc\cos(\varepsilon^0/\varepsilon_0)$, $T = 2\pi/f_1$ and $\tau = 0$ if $\varepsilon_0 > \varepsilon^0$ [52].

The second category is associated with the relative frictional movement of the contact surfaces, which is referred to as the "slipping" or "rubbing" mechanism (Figure 9a). When the crack interacts with shear waves of relatively low amplitude, the roughness of the mated surfaces can be high enough to prevent their in-plane motion, which is finally limited to micro-slipping [52]. This interaction between the surface asperities does not rely on the direction of wave motion, and introduces a step-wise change in the material stiffness which occurs twice in every cycle of the driving signal. Thus, as illustrated in Figure 9b, the micro-slip mode leads to a symmetrical stress-strain relation (symmetrical nonlinearity) characterised by the generation of odd harmonics. Again, the pulse-type change in stiffness causes the modulation of harmonic amplitude based on the following $sinc$ function [52]:

$$A_{2n+1} = 2\varepsilon_0 \Delta C \left(\frac{\tau}{T}\right) \left[sinc\left(\frac{2n\tau}{T}\right) + sinc\left(\frac{2(n+1)\tau}{T}\right)\right]. \quad (12)$$

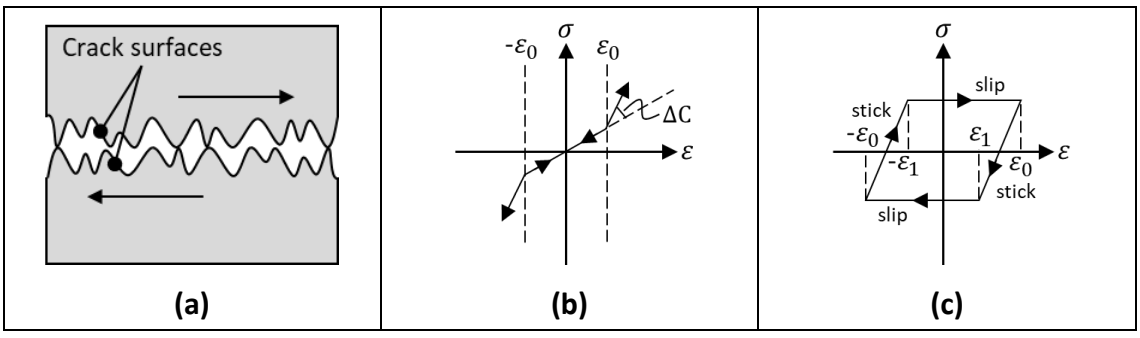

Figure 9: Schematic of slipping crack in materials with non-classical (contact) nonlinearity (a) and the resultant stress-strain behaviour in micro-slip (b) and stick-slip (c) modes.

Finally, for shear waves of higher amplitude, the in-plane excitation of the contact interface can switch from micro-slipping to sliding. The oscillation of the contact interface can be described as a periodic change between static and kinematic friction (i.e. stick-slip mode), resulting in a hysteretic stress-strain curve as shown in (Figure 9c) [53]. This type of surface interaction is also independent of wave direction, and the value of material stiffness changes symmetrically between C_S (at stick phase) and zero (at slip phase), twice per wave period. Again, for such a symmetrical material nonlinearity, the received signal spectrum exhibits higher odd harmonics characterised by the following $sinc$-modulated amplitude [53]:

$$A_N = \varepsilon_0 C_S\{\Delta\tau[sinc((N-1)\Delta\tau) + sinc(N+1)\Delta\tau) - 2\Delta\varepsilon\ sinc(N\Delta\tau)] \\ -0.5(1-\Delta\varepsilon)\ sinc(N/2)\}, \quad N = 2n+1. \tag{13}$$

Realistically, as previously explained, damaged materials also manifest classical nonlinearities. Hence, higher even harmonics are likely to be detected for both the micro-slip and the stick-slip modes of contact acoustic nonlinearities.

At this point it is important to be mentioned that except for the generation of higher-order harmonics, non-classical nonlinearities are associated with additional effects, depending on the process followed for the acoustic excitation of the material (e.g. single or dual frequency transmission, variation of signal amplitude, excitation at natural modes of vibration etc.). Although different non-classical nonlinear ultrasonic phenomena are well-known and widely-used as indicators of material degradation, their physical explanation is not completely understood. Nonetheless, according to the review studies of Jhang [46] and Broda et al. [49], experimental works involving different arrangements of wave transmission, types of defects and boundary conditions revealed that the most common non-classical nonlinear ultrasonic effects are:

- Generation of higher harmonics [50, 54-57] and sub-harmonics [51, 58-63] of the fundamental signal frequency.
- Modulation and frequency mixing of two waveforms transmitted at different frequencies [50, 54, 64, 65].
- Shifting of resonance frequency when increasing the amplitude of excitation signal [66-70].

- Slow restoration (few minutes) of original material properties that are temporarily altered due to ultrasonic excitation; known as the "slow dynamics" effect [71-74].
- Localised resonant activation of a defective region, referred to as local defect/damage resonance (LDR) effect [75-78].
- Dissipation of wave energy that depends on the amplitude of excitation [79, 80].

Among the above, the generation of higher harmonics, especially second-order harmonics, and the modulation of ultrasonic waves with different frequency are the two primary phenomena analysed by the majority of NEWS methods for the characterisation of material nonlinearities. This is further explained in the following sections.

2.3.3 Applications of Second Harmonic Generation Effect

As already mentioned in the previous paragraphs, when a nonlinear solid is excited by a sinusoidal forcing with a single frequency (e.g. f_1), higher-order harmonics ($2f_1$, $3f_1$, $4f_1$, …) will be present in the recorded frequency spectrum of the material because of wave distortion by internal discontinuities and/or due to excitation of the damaged surfaces leading to the generation of new waves (Figure 10).

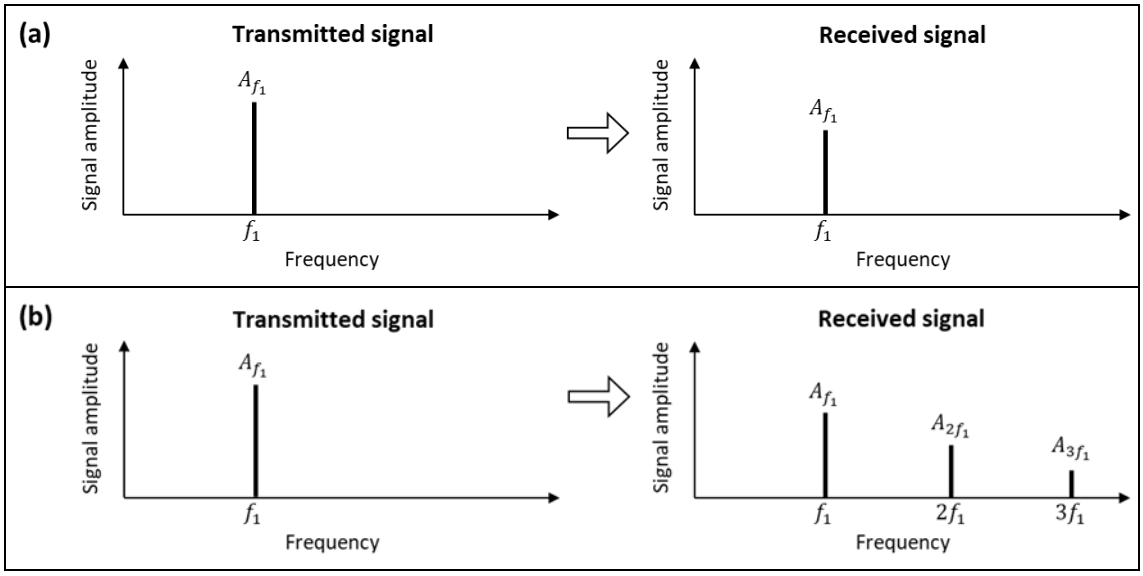

Figure 10: Ultrasonic response of undamaged (linear) materials (a) and damaged (nonlinear) materials (b) under single-frequency excitation.

The second-order harmonic ($2f_1$) has the highest content of elastic energy making it the principal indicator of acoustic nonlinearities. At the same time, the recorded responses must be closely analysed because part of the amplitude of second harmonics can be correlated to other sources of nonlinearities such as noise from the power instruments (e.g. waveform generators and amplifiers) or improper contact between the transducer and the material. The initial experiments around the concept of second harmonic generation are reported in the early studies of Breazeale et al. [81, 82], Hikata et al. [83, 84] and Gedroits et al. [85, 86]. These along with the majority of studies associated with this effect aim at characterising the material nonlinearity based on the nonlinear acoustic coefficient β, which is often referred to as the acoustic nonlinearity parameter β. There is a number of available theoretical and experimental works, including those of Yost and Cantrell [87], and Kim [88], which are in agreement with the solution described by equation (7) and show that the parameter β can be expressed as

$$\beta = \frac{8A_2}{{A_1}^2 x\, k^2}\,. \tag{13}$$

Since equation (13) is valid only for bulk longitudinal elastic waves travelling in one-direction of a solid with nonlinear stress-strain behaviour, the common practice in literature is to approximate β to the following ratio

$$\beta \propto \frac{A_2}{{A_1}^2}\,. \tag{14}$$

According to Matlack et. [89], the ratio expressed by equation (14) is applicable to wave propagation in the three dimensions, and also using guided Rayleigh or Lamb waves. This ratio is known as the relative acoustic nonlinearity parameter (often denoted by β').

Previous research studies exploited the effect of second harmonic generation for the inspection of metal and composite parts using piezoelectric actuators and sensors, and investigated the contribution of material nonlinearities to the magnitude of the acoustic nonlinearity parameter β (mainly in the relative format of ${A_2}/{{A_1}^2}$).

A large amount of experimental tests on metal components proved that the increase in the value of parameter β could be used to monitor the level of material degradation for different types of damage including fatigue, thermal aging, creep, and radiation damage. A comprehensive review of the relevant studies up to 2015 is provided in the review study of Matlack et al. [89]. Similar tests have been carried out by more recent studies. Examples include the measurement of β for the evaluation of fatigue-induced damage such as the formation of precipitates and dislocations [90, 91], propagation of cracks [92,

93] and weakening of adhesively bonded joints [94, 95]. In addition, the value of β was used for the monitoring of thermal aging [96-98], corrosion [99, 100] and creep [101-103].

In the case of composite parts, the number of available studies was considerably smaller. In fact, the correlation between the magnitude of parameter β and the severity of damage was predominantly demonstrated with tests on multi-layered CFRP plates that were impacted at different levels of energy [104-107], or subject to fatigue loading at ambient [108-110] and fluctuating temperature [111].

In addition to the detection of defects and the relative monitoring of damage growth, recent studies focused on the localisation of structural flaws and the visualisation of the shape and size of damage. Although different tomographic techniques (and algorithms) have been proposed based on the measurement of second-to-fundamental harmonic ratio, the number of research works that achieved the imaging of defects using only a surface-mounted network of piezoelectric transducers is still limited. These studies performed tests on aluminium plates with fatigue cracks [112, 113], pitting corrosion from hypervelocity impact events [113, 114] and chemical corrosion [115, 116], and on CFRP plates with damage from low-energy impacts [117-119]. However, in most cases, experimental validation of the methods was shown on a single sample (i.e. lack of repeatability) [112, 114, 115, 117-119], and in some tests the damage was positioned at the centre of the array which is the point with the maximum number of intersecting sensor-to-sensor paths (i.e. higher sensitivity to defects) [114, 116, 119]. Therefore, the development of additional methods and their application to more realistic scenarios of damage would be significantly important, because such techniques could be utilised for on-board inspections where scanning of the structural parts with laser instruments or thermal/infrared cameras would not be practically possible.

2.3.4 Applications of Nonlinear Wave Modulation Effect

This nonlinear effect occurs when a solid is excited simultaneously by two waveforms with distinctive frequencies (e.g. f_1 and f_2), referred to as the low-frequency (high-energy) pumping wave and the high-frequency (low-energy) probing wave. As previously mentioned, if the material is undamaged with perfectly linear elastic properties, the monitored frequency spectrum contains only the fundamental harmonics at f_1 and f_2 (Figure 11a). For a damaged material, with either classical or non-classical nonlinearities,

the f_2 wave interacts with the defect similarly to the case of single-frequency excitation, but it also interacts with the f_1 wave. Consider a crack that opens and closes periodically during the tensile and compressive phases of the f_1 wave. When the crack is open, the f_2 wave travelling inside the material is partially decoupled [120]. However, during the closed phase of the crack, the shape of f_2 wave remains almost unaffected and its amplitude increases. In other words, the high-frequency wave is subject to amplitude and/or frequency modulation by the low-frequency wave [120]. Amplitude modulation is attributed to the vibrational energy added to the system by the low-frequency wave, and frequency modulation occurs as a result of the mixing and multiplication of the two waves at the damaged interface. Consequently, apart from the higher-order harmonics at nf_1 and nf_2 ($n = 1, 2, 3, ...$), the spectrum of the modulated response includes additional nonlinear frequency components (spectral sidebands) at the sum-frequency ($f_s = f_2 + nf_1$) and the difference-frequency ($f_d = f_2 - nf_1$), as illustrated in Figure 11b.

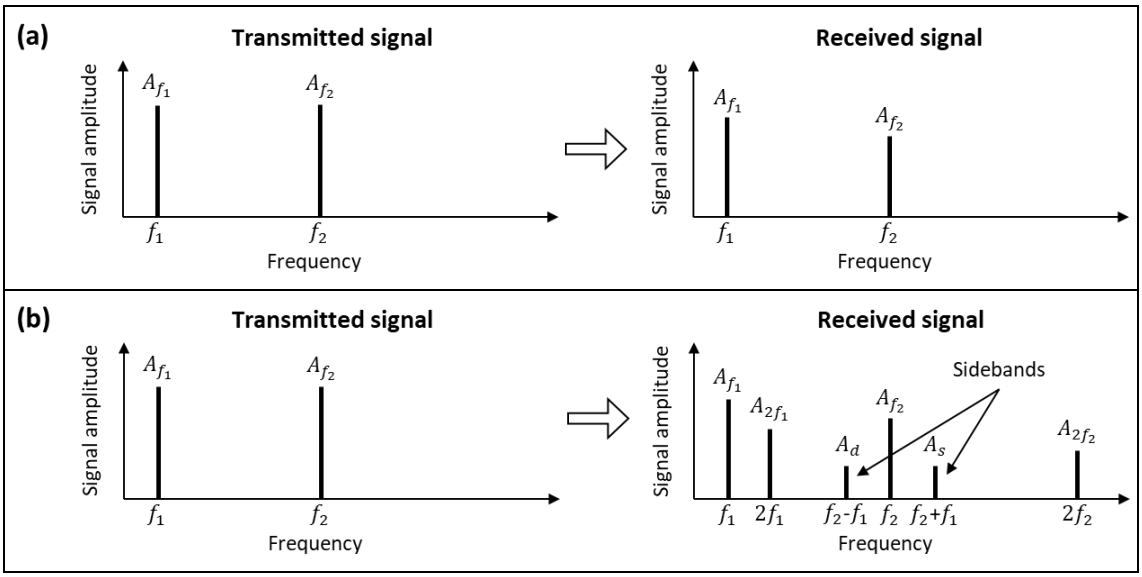

Figure 11: Ultrasonic response of undamaged (linear) materials (a) and damaged (nonlinear) materials (b) under dual-frequency excitation.

Although the amplitude of sidebands is usually lower than that of second-order harmonics, their presence is indeed attributed to the mixing of waves at the location of damage (i.e. independent of induced noise). The fact that the nonlinearities induced by the set-up do not normally generate sidebands is a major advantage of the methods based

on the nonlinear modulation of waves over those relying on the generation of second harmonics.

The first applications of this phenomenon in the field of NDE are presented in the publications of Korotkov et al. [121, 122], Sutin and Nazarov [123], and Zaitsev et al. [124] concerning the identification of cracks in metal parts. These are followed by the studies of Donsky and Sutin [125], Zaitsev and Sas [126], and Van Den Abelee et al. [50] for the detection of fatigue cracks, corrosion and adhesion flaws in structural components (e.g. pipes and plates) made from steel, aluminium, titanium, thermoplastic, concrete and sandstone. Since then, numerous methods associated with the modulation of elastic waves have been developed which, together with those in the early studies, are known as the vibro-acoustic modulation (VAM) techniques or nonlinear ultrasonic modulation techniques or even nonlinear wave modulation spectroscopy (NWMS) methods.

It has been repeatedly shown that the amplitudes of the sideband products (A_s and A_d) at f_s and f_d are proportional to the driving amplitudes (A_1 and A_2) at f_1 and f_2 in the following format

$$A_s \propto \beta_s A_{f_1} A_{f_2} \quad \rightarrow \quad \beta_s \propto \frac{A_s}{A_{f_1} A_{f_2}} \tag{6}$$

$$A_d \propto \beta_d A_{f_1} A_{f_2} \quad \rightarrow \quad \beta_d \propto \frac{A_d}{A_{f_1} A_{f_2}} \tag{7}$$

where β_s and β_d are the nonlinear modulation parameters describing the acoustic nonlinearities. Therefore, in many studies, the level of material nonlinearity (i.e. damage/degradation severity) is evaluated based on the sideband amplitude (sum or mean of A_s and A_d) divided by the driving amplitudes, and the resulting ratio is called the damage index [127, 128] or modulation index/intensity [129, 130].

According to the literature, NWMS methods could be divided into the impact-modulation and the vibro-modulation methods. In both categories, the transmission of high-frequency (probing) waves through the structural parts was commonly achieved with the use of surface-attached piezoelectric actuators. In the case of impact-modulation techniques, the structural parts were subject to low-frequency decaying vibration (pumping vibration) using a modal/impact hammer or another object with the aim to excite the structure at its natural modes of vibration. Impact-modulation techniques were exploited for the assessment of cracks in sandstone, acrylic and metals [50, 130-132], bolt loosening at the joint between aluminium plates [133, 134], bonding flaws in composite plates [125] and cracks in carbon filament wound canisters from impact events [135].

In the case of vibro-modulation methods, low-frequency excitation of the components was carried out with steady-state forced vibrations typically from an electrodynamic shaker. Such methods were successfully applied to the detection of fatigue-induced cracks in steel [136, 137] and aluminium [129, 138-141] parts, stress-corrosion cracks in aluminium and steel components [142], impact damage on composite laminates [143-145], bonding defects in sandwich panels and stiffened composite plates [146, 147], and contact loosening at metal-metal and composite-composite bolted joints [148, 149].

Vibro-modulation tests were also performed using externally mounted piezoelectric actuators (mainly PZT transducers) for the transmission of both low-frequency and high-frequency waves through the material. This would be more suitable for on-board SHM applications rather than using shakers, or modal hammers in the case of impact-modulation. Again, the detected modulation products were analysed for the identification and monitoring of fatigue damage in steel [150, 151] and aluminium samples [127, 152-154], bolt loosening on aluminium [155] and steel [156] structures and BVID on carbon/epoxy composite plates [54, 157-161].

More recently, ultrasonic phased array probes were employed for the localisation and imagining of closed fatigue cracks oriented vertically in steel [162, 163] and aluminium [164] samples based on the nonlinear mixing of waves. In particular, a linear array of piezoelectric elements enclosed in an ultrasonic probe was programmed to transmit waves at two different frequencies in specific firing orders of the elements. The probe served both as the pulser and the receiver on one side of the sample (pulse-echo layout), and the elements were triggered with different patterns of signal phase to enable steering or focusing of the transmitted wave beams. In the same way, Fierro and Meo showed suppression of the “near field” noise when tested an impacted composite plate [164]. Moreover, Alston et al. [165], used an ultrasonic phased array to record the shear waves generated from two transducers on the opposite side of an aluminium sample (through-transmission configuration), and measured the nonlinear mixing of the waves due to the presence of a horizontal contact interface inside the sample. As can be seen, only few studies have investigated the application of NWMS methods with phased array probes, and those were limited to the localisation of a single contact-type defect. In the case of horizontally oriented defects, the transmission of wave beams through multiple contact interfaces would be very low due to attenuation and, as a result, the defect-related

nonlinearities could be covered by the noise in the signal. Therefore, it would be interesting to explore ways for the improvement of the performance of phased array techniques based on the nonlinear modulation of waves, in order to achieve accurate positioning of defects at several depths inside the material.

2.4 Smart Composite Materials with Embedded Sensors

The studies referenced in the previous paragraphs proposed different NEWS techniques and experimental layouts for the identification and characterisation of structural damage. In several cases this was achieved by using surface-mounted sensors with the intention to provide alternative ideas that could help in the development of on-board SHM systems. The installation of sensing devices on the surface of engineering structures though, is not always desired. In aerospace applications, for example, external transducers can be detached due to vibrations or be exposed to extreme temperatures, high levels of humidity and radiation, high-velocity impacts (e.g. hailstorms or orbital space debris) and interplanetary vacuum [166]. Such conditions can affect the sensing capabilities of the transducers or damage them permanently. Composite panels are usually fabricated by stacking multiple FRP layers, meaning that the sensors can be placed inside the material during the manufacturing process. Apart from protection to the transducers, this also enables the manufacture of "smart" composite parts with smooth surfaces which is important for the aerodynamic performance of structures. In addition, the insertion of sensors can lead to enhanced ultrasonic sensitivity because of stronger coupling to the material [167].

Based on the above and according to a recent review study from Meyer et al. [168], there is a number of published studies related to the manufacture of GFRP [169-179] and CFRP [180-195] plate-like structures with embedded piezoelectric sensors. Except for PZT transducers, piezoelectric polyvinylidene fluoride (PVDF) film sensors [171], piezoelectric patches [172, 195] and the piezoelectric Stanford Multi-Actuator-Receiver Transduction (SMART) layers [182, 188] were also used as sensors.

According to the literature, the transducers are typically embedded in the material using one of the three techniques shown in Figure 12. In the first one (Figure 12a), the sensor is placed into a pocket which is created after removing the required volume of material [169, 172, 178-180, 183-187, 192-195]. However, cutting of the fibres causes localised decrease in the strength of the material.

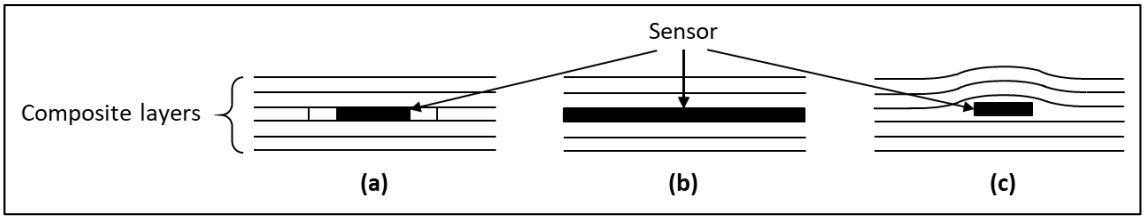

Figure 12: Sensor embedment in composites using the cut-out (a), interlaying (b) and direct (c) techniques.

The second technique (Figure 12b) involves the fabrication of a sensor network in the form of polymeric layer, in order to allow its insertion as an additional ply [170, 177, 181, 182, 188]. Although this maintains better distribution of internal stresses, there is a risk for complete delamination in the case of poor adhesion between the sensor and the composite layers. In the last method (Figure 12c), the transducer is directly interlaid between the composite plies [171, 173-176, 189-191]. Depending on the geometry of the sensor, this method can have lower impact on the interlaminar properties of the material relative to the first two techniques.

Besides the choice of an embedding method, the inclusion of transducers in CFRP plates has an additional level of difficulty relative to the case of GFRP laminates. The conductive carbon fibres will electrically short-circuit the transducer if they come in contact with the electrodes or the soldered joints. To avoid this, PZT sensors and patches are typically covered or completely wrapped with polyimide (Kapton) film [180, 183-186, 190, 193-195]. In the case of SMART layer the sensing network is printed on a Kapton substrate [182, 188]. Kapton is a polymeric material with different elastic and bonding properties than those of the matrix on the composite layers, and thus, it can introduce delamination to the plates in the same way as the release (Teflon) patches used in experimental samples to create bonding defects [196]. Other examples involve the insertion of sensors between GFRP layers, and the cured laminate is in turn embedded in a CFRP laminate [189, 192]. However, this is considered a hybrid composite (i.e. separate category), and there is still a great possibility for weak adhesion at the GFRP-CFRP interfaces as the two materials are often cured individually due to differences in their curing conditions (e.g. temperature, pressure, time etc.).

Regarding the standard CFRP plates, some studies concluded that the properties of the material were not affected by the inclusion of Kapton insulated sensors [182-186, 188, 193]. However, the majority of them referred to the results from static and cyclic tensile

tests, and compression tests [183-186] without performing any bending tests which focus on the flexural and interlaminar properties. Furthermore, only few of the previous research works examined the capabilities of embedded transducers to detect flaws in CFRP laminates based on ultrasonic wave propagation, and that was demonstrated only with linear ultrasonic techniques [182, 188, 190, 194].

Chapter 3

Development of Smart CFRP Composites with Embedded PZT Transducers

The main goal of the journal article (Paper I) presented in this chapter, was that of proposing a novel method for the electrical insulation of piezoelectric transducers embedded in CFRP composite laminates. The layout included thin piezoelectric PZT disks (PI Ceramic PIC255-00004137) directly placed between the layers of cross-ply CFRP laminates without cutting any fibres. This type of sensor was not only chosen because of its broadband frequency response and its low-power requirements, but also for its design. In fact, the small size of this transducer (6 mm diameter and 0.3 mm thickness) should cause negligible distortion of the surrounding material, and its circular shape would allow the interlaminar stresses to be distributed more evenly around its periphery. The top surface of the transducers, which featured both the positive and the negative electrodes, was covered with a square patch made from a single layer of dry woven E-glass fibre fabric Figure 1. This idea was inspired from studies on the development of fibre reinforced metal-matrix composites such as CFRP-Aluminium hybrid structures, which included glass fibres to stop the direct contact between the two materials and eventually to prevent the corrosion of their surfaces [197].

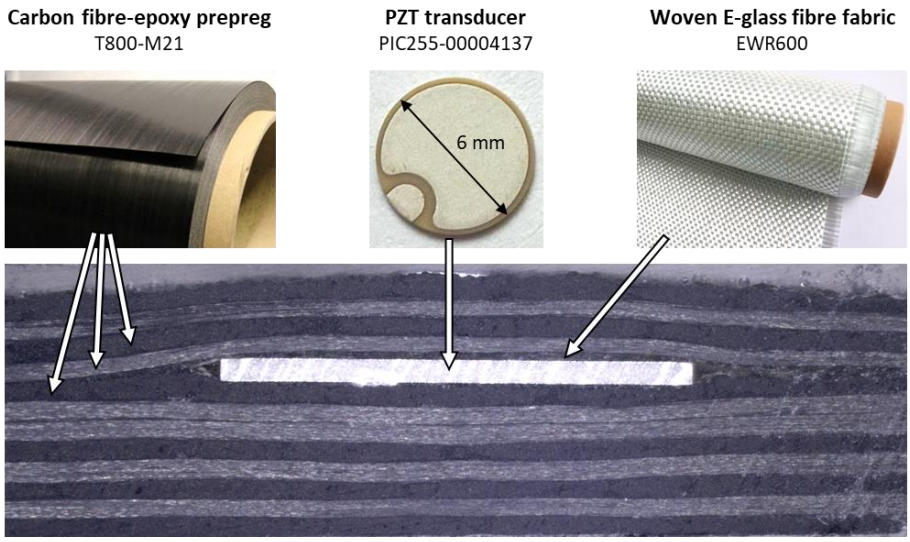

Figure 1: Cross-sectional view of CFRP laminate with directly embedded PZT transducer.

In this work, numerical simulations were initially conducted using finite element models of CFRP composites and suggested that the sensor should be placed above the middle plane of the laminate, so that interlaminar shear failure would be less likely to occur at the interface between the sensor and the composite.

Then, the mechanical performance of the CFRP specimens containing glass fibre insulated PZTs (G-specimens) was assessed by performing bending tests (short-beam and long-beam) and compression tests. For comparison, the same tests were repeated using plain laminates (P-specimens) and plates in which the embedded transducers were insulated with the standard method involving the use of a Kapton layer (K-specimens). The type of failure in each specimen group was studied with the use of an optical microscope, and the size of the damage length and opening inside the samples was recorded. The results from the mechanical tests and fractographic inspections were subject to a statistical analysis which revealed that the mean values corresponding to P-specimens were equal to those of G-specimens but significantly different from the values of K-specimens.

Finally ultrasonic NEWS experiments were conducted using pairs of sensors in CFRP laminates containing an area of delamination which was represented by a double-layered patch of fluorinated ethylene propylene (FEP). These experiments proved that the proposed embedding method achieved the electrical insulation of the PZT disks. Most importantly though, the sensitivity of the internal sensors to the detection of damage was found to be significantly higher than that of surface-bonded transducers, based on measurements of the relative acoustic nonlinearity parameter β (i.e. ratio of $A_2/{A_1}^2$).

The “Statement of Authorship” form and Paper I are provided on the following pages.

This declaration concerns the article entitled:			
Characterisation of Smart CFRP Composites with Embedded PZT Transducers for Nonlinear Ultrasonic Applications			
Publication status			
Draft manuscript ☐ Submitted ☐ Accepted ☐ Published ☒			
Publication details (reference)			
Andreades, C., Mahmoodi, P., & Ciampa, F. (2018). Characterisation of smart CFRP composites with embedded PZT transducers for nonlinear ultrasonic applications. *Composite Structures*, 206(1), 456-466.			
Candidate's contribution to the paper (detailed, and also given as a percentage)			
Formulation of ideas: 40% The idea of using a layer of glass fibres for the electrical insulation of embedded PZT transducers from the conductive carbon fibres was proposed by my former supervisor Dr Francesco Ciampa and finalised with my help.			
Design of methodology: 70% I chose the design, lay-up and material for the manufacture of the composite samples. The type of PZT transducers embedded in the samples was suggested by Dr Francesco Ciampa.			
Experimental work: 85% I manufactured the composite specimens, performed the mechanical and ultrasonic tests, conducted the fractographic examination, collected the data and provided the material properties used in the development of the finite element models. The numerical finite element simulations were completed by my co-author Dr Pooya Mahmoodi.			
Presentation of data in journal format: 90% I processed the experimental and numerical data, created the figures, chose the structure of the paper and wrote the manuscript. Dr Pooya Mahmoodi provided the screen-shots from the numerical finite element simulations. Dr Francesco Ciampa provided feedback on the above and supported the process of submission and review.			
Statement from Candidate			
This paper reports on original research I conducted during the period of my Higher Degree by Research candidature.			
Signed		**Date**	02/10/2020

Characterisation of Smart CFRP Composites with Embedded PZT Transducers for Nonlinear Ultrasonic Applications

Christos Andreades[1], Pooya Mahmoodi[2], Francesco Ciampa[1]

[1]Materials and Structures Centre (MAST), Department of Mechanical Engineering, University of Bath, Bath, BA2 7AY, UK.

[2]Engineering Central (Innovation Hub), Swansea University Bay Campus, Fabian Way, Crymlyn Burrows Swansea, SA1 8EN, UK.

Abstract

Embedded piezoelectric lead zirconate titanate (PZT) transducers in carbon fibre reinforced plastic (CFRP) composites are typically electrically insulated by interlaying materials such as polyimide Kapton films between the PZT and the laminate ply. However, the presence of polymeric films may cause debonding at the layer interface and an increase of material distortion around the PZT, thus reducing the structural performance. This paper proposes an alternative insulation technique in which PZTs are covered by a thin layer of woven E-glass fibre fabric for enhanced adhesion with the surrounding epoxy matrix. An analysis of variance on experimental test results showed that the compressive, flexural and interlaminar shear strengths of plain CFRP specimens were equal to the means of the smart CFRP composite ($0.41<p<0.58$), but significantly higher from the means of Kapton specimens ($0.0001<p<0.05$). Thus, the proposed insulation technique had no impact on the mechanical properties of the laminate. Moreover, a post-test fractographic analysis indicated that at least one damage parameter (damage opening) in Kapton specimens was significantly larger ($p=0.03$) than in plain specimens, but the damage length and opening in the proposed woven E-glass fibre samples were equal to those in plain composites. Also, the brooming failure under compression was the same for the smart CFRP composite and the plain samples, whereas the Kapton specimens failed by through-thickness shear. Finally, nonlinear ultrasonic experiments were conducted on CFRP laminates with artificial in-plane delamination using glass fibre insulated PZTs. The effect of second harmonic generation was found to be nearly two times higher than conventionally surface-bonded PZTs.

1 Introduction

With growing demand from aerospace industry for next-generation lightweight, safe and technologically advanced structures, there is a strong need to develop fibre reinforced plastic (FRP) composites with integrated sensing capabilities. Surface-mounted piezoelectric lead zirconate titanate (PZT) transducers are typically used to sense the monitored component and provide real-time information about structural health conditions. PZT sensors have balanced actuation and sensing constants, as well as good thermal stability and resistance to high temperatures [1]. PZTs are able to convert changes in strain, pressure, force and acceleration into electrical signals, based on the piezoelectric effect [2]. The signals can then be processed with dedicated ultrasonic algorithms to provide information about the health status of components. However, the external exposure of PZTs to the surrounding environment (e.g. moisture and corrosion) makes them susceptible to failure [3]. Protection systems of externally mounted PZTs would dramatically increase manufacturing costs and weight. Hence, in order to improve the efficiency of smart composites with sensing features, PZT transducers have been inserted into layers of both glass and carbon fibre reinforced plastic (GFRP and CFRP) laminates [4-11]. The use of embedded PZT sensors has, therefore, led to the development of smart composites for ultrasonic structural health monitoring (SHM) applications.

However, one of the biggest challenges in the development of smart CFRP laminates is the need for insulation of embedded PZTs from the electrically conductive carbon fibres. According to the literature, polyimide (Kapton) film is commonly used as an interlayer material between the sensor and the laminate plies due to its high temperature resistance [4-9]. A number of studies such as those by Mall and Coleman [4], Paget and Levin [5] and Arellano et al. [3] proved that the tensile and compressive strength as well as the fatigue endurance of CFRP laminates were negligibly affected by the embodiment of PZTs insulated by Kapton film layers. However, to the best of authors' knowledge, only few studies analysed both flexural and interlaminar properties of smart composites with embedded PZT insulated by polymer layers. Lin and Chang [7], for example, investigated the interlaminar behaviour of their SMART Layer inserted into the laminate of a CFRP composite. Double lap shear and short beam shear tests revealed that the interlaminar properties of the CFRP laminate were not significantly affected by the presence of an additional phase within the composite. Nevertheless, it is well known that

polymeric films made of Kapton and Teflon are typically used during the manufacturing process to generate controlled “artificial” delamination in composites [12]. Indeed, the presence of polymeric films within the laminate causes poor adhesion and debonding between plies, thus weakening the whole composite structure and creating interlaminar stresses surrounding the PZT sensor [13]. These stresses may even dramatically reduce the sensing ability of embedded transducers. Hence there is a need for alternative materials and processes to insulate embedded PZTs in CFRP composites.

This study proposes a novel material processing technique for the electrical insulation of circular PZTs inserted between the plies of CFRP laminates. In particular, a thin layer of woven E-glass fibre fabric was placed over the top (conductive) surface of the embedded PZT transducer, as illustrated in Figure 2. This novel smart composite was inspired from CFRP-Aluminium hybrid (CARALL) laminates in which glass fibres were integrated between the two materials to avoid corrosive degradation of the surfaces [14].

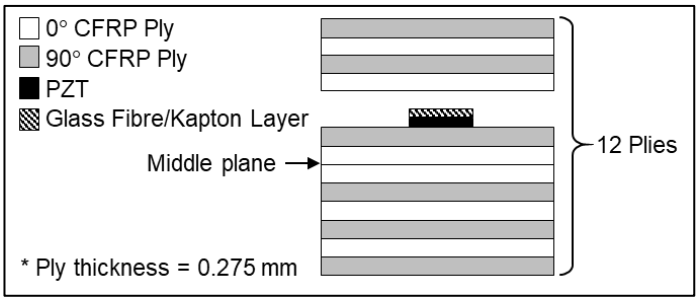

Figure 2: Configuration of embedded PZTs in CFRP laminates.

The effect of the proposed embedding technique on the mechanical properties of the laminate was experimentally studied and compared with the effect of the conventional embedding technique using Kapton layers. This study was supported by a numerical finite element (FE) model, which was developed to provide initial information about the optimal position of the PZT and glass fibre along the thickness of the CFRP composite. The interlaminar shear strength, the flexural strength and compressive strength of CFRP laminates with embedded PZTs and a layer of woven E-glass fabric (G-specimens) were determined by performing short-beam and long-beam three-point bending tests, and compression tests. The same tests were performed using plain CFRP laminates (P-specimens) as well as CFRP composites in which the embedded PZTs were covered by a 500HN Kapton film layer (K-specimens). In addition, all specimens were subject to post-

test fractographic inspection with optical microscope to study the failure mode in each case study. Finally, the functionality of the proposed smart composite and its sensitivity in detecting material damage were examined by conducting Nonlinear Elastic Wave Spectroscopy (NEWS) experiments on CFRP plates with artificial in-plane delaminations.

2 Nonlinear Elastic Wave Spectroscopy Methods

Over the years, a number of ultrasonic algorithms have been developed to detect material damage in CFRP laminates [15-17]. NEWS techniques have been widely used in composites due to their higher sensitivity over linear ultrasonic methods to detect damage at early stages of formation (e.g. micro-cracks, delamination and voids) [19-23]. In particular, elastic waves propagating through the material can force micro-crack interfaces to either oscillate ("clapping" motion) or move relative to each other ("rubbing" motion), thus resulting in the generation of nonlinear elastic effects such as higher harmonics (even and odd multiples) and sub-harmonics (sub-multiples) of ultrasonic excitation signals [24]. According to Landau and Lifshitz [25], in the "classical" nonlinear material response, second harmonic generation can be considered as the principal signature for damage identification. As reported by many authors (e.g. Landau and Lifshitz [25] and, more recently, Zagrai et al. [26]), the one-dimensional elastodynamic wave equation in the second order approximation shows that the displacement u of propagating elastic waves is not only dependent on the linear properties of the medium such as the speed of sound c_0, but also on the nonlinear parameter β

$$\frac{\partial^2 u}{\partial t^2} - {c_0}^2 \cdot \frac{\partial^2 u}{\partial x^2} = -2\beta \cdot {c_0}^2 \cdot \frac{\partial u}{\partial x} \cdot \frac{\partial^2 u}{\partial x^2} . \quad (1)$$

This β parameter describes the second order nonlinear effect exhibited by the damaged material [26]. By measuring the signal amplitude at the fundamental and second harmonic frequencies (A_1 and A_2), the parameter β can be determined based on the following equation

$$|\beta| = \frac{A_2}{{A_1}^2} \cdot \frac{4{c_0}^2}{x\omega^2} , \quad (2)$$

where x and ω are the propagation distance inside the material and the angular frequency of the input waveform, respectively. Since c_0, x and ω are constants, the parameter β can be easily considered as [26]

$$|\beta| \propto \frac{A_2}{{A_1}^2}. \tag{3}$$

It has been proved that the parameter β increases proportionally with material degradation [27] and its estimation, originally introduced by Buck et al. [28] and Antonets et al. [29], allows NEWS techniques to detect damage in composites. Polimeno et al. [20] monitored the nonlinear response of a CFRP laminate with micro-cracks and delamination using a piezoelectric exciter and a microphone mounted onto the surface of the laminate. By exciting the laminate at one of its resonance frequencies and by monitoring the amplitude of harmonics in the spectrum of the received signal, second harmonic generation was proved to be highly accurate in the detection of damage and the estimation of damage size. More recently, Ciampa et al. [22] demonstrated that high order bispectral analysis of waveforms obtained using a pair of PZTs bonded onto the surface of a CFRP laminate with artificial delamination (i.e. Teflon insert) allowed the evaluation of second order nonlinearity. The "non-classical" nonlinear material response [30] including the effect of nonlinear local damage resonance (LDR) was also studied to enhance the identification of nonlinear elastic features in damaged materials [31]. In particular, if the driving frequency matches the damage resonance frequency, the vibrational amplitude of nonlinear elastic effects can be dramatically increased (up to ~20-40 dB). This LDR effect leads to a very efficient energy pumping at the damage area and ensures that even a low input acoustic power of few mW is sufficient to generate nonlinear elastic effects at the crack location. As a result, superharmonics of the LDR frequency in addition to higher harmonics of the input frequency can be generated [23]. This effect was analytically demonstrated by Solodov et al. [32] using a 1D model of a linear damped oscillator. Ciampa et al. [23] not only validated the results from the study of Solodov, but also introduced a 2D mathematical model and proved theoretically and experimentally the existence of intermodulation effects of the LDR frequency. However, the vast majority of NEWS testing has been performed using surface-bonded PZTs [18-23]. Sensor embedment would offer, instead, the opportunity to achieve better coupling with the material, thus resulting in higher signal amplitude and enhanced sensitivity for damage detection [33].

3 Assessment of Mechanical Properties

This section outlines the numerical and experimental work performed to analyse the combined effect of the embedded PZT and its insulating layer on the mechanical properties of CFRP laminates.

3.1 Numerical Finite Element Models

Prior to the specimen manufacture, static short-beam tests were simulated with FE models using ANSYS Workbench software (in accordance with the BS-EN-ISO-14130:1997 standard [34]). The aim of the numerical simulations was to determine the optimal position of the PZT and glass fibre along the thickness of the CFRP composite subject to three point bending, which minimised the interlaminar shear effects in the laminate. A standard cross-ply stacking sequence of the CFRP composite, which is widely used in aerospace applications (Figure 2), was here selected and employed in the numerical models and in the experimental Section 3.3. The CFRP and glass fibre layers, the PZT, the loading head and the supports were simulated using 3D 20-noded SOLID186 elements. This element type offers mixed formulation capability for simulating deformations of nearly incompressible elastoplastic materials. The loading head and supports were modelled as rigid hollow cylinders. The total number of elements was 67,860. Similarly to Moulin et al. [35], the epoxy resin-rich regions (Figure 3b) formed at the periphery of the PZT and the glass fibre layer were modelled as pure resin. Whilst the CFRP composite lamina and the glass fibre layer were assumed to be homogenous and transversely isotropic, the resin and PZT sensor were considered homogenous and isotropic. The elastic properties of all materials including the Young's modulus (E) the shear modulus (G) and the Poisson's ratio (ν) along with tensile, compressive and shear strengths (X, Y and S) are provided in Table 1 and Table 2. The subscripts 1 and 2 in each elastic constant denote the longitudinal and the transverse direction in the plane of the lamina, whilst 3 is the thickness direction. A cohesive zone model (CZM) represented by 3D 16-noded INTER204 elements was introduced at layer-layer and layer-PZT interfaces. Generally, INTER204 elements can simulate an interface between two surfaces and the subsequent delamination process, when used with SOLID186 elements. In addition, the frictionless Hertzian contact model represented by element types CONTA174 and TARGE170 was used to simulate the contact between the loading head

and the laminate and between the laminate and supports. Typically, CONTA174 elements are located on SOLID186 surfaces, and TARGE170 overlay the SOLID186 elements.

Table 1: Properties of CFRP layer and woven E-glass fibre fabric layer.

Orthotropic Property	**CFRP Layer [36, 37]**	**Woven E-glass Fibre Fabric Layer [38, 39]**
E_1, E_2, E_3 (GPa)	172, 8.9, 8.9	12.5, 11.8, 11.8
G_{12}, G_{13}, G_{23} (GPa)	4.2, 4.2, 0.0225	3.5, 3.5, 3.5
ν_{12}, ν_{13}, ν_{23}	0.35, 0.35, 0.01	0.17, 0.17, 0.07
X_1, X_2 (MPa)	2200, 61	322, 290
Y_1, Y_2 (MPa)	2200, 130	204, 200
S_1, S_2 (MPa)	85, 40	39, 39

Table 2: Properties of PZT and resin.

Isotropic Property	**PZT [40]**	**Resin [41]**
E (MPa)	1.1E+05	3780
G (MPa)	4.1E+04	1400
ν	0.34	0.35
X (MPa)	290	54.6

Three FE models of the CFRP laminate with embedded PZT and glass fibre located at different depths along the thickness were created. In the first FE simulation, the PZT and glass fibre were inserted at the middle plane, i.e. between layers 6 and 7 from the bottom (see Figure 2). In the second and third FE models, the PZT and glass fibre were inserted towards the laminate region under compression (between layers 8 and 9) and tension (between layers 4 and 5), respectively. As illustrated in Figure 3a, the PZT was not placed midway along the specimen length to avoid compressing it directly with the loading head. In this numerical analysis, it was assumed that boundary conditions remained constant during loading and that the CFRP material was deformed within their elastic region. Simulations were performed by applying a static nodal displacement of 0.4 mm to the loading head with a direction perpendicular to the laminate surface. Moreover, perfect bonding between the PZT, the glass fibre layer and CFRP layers was assumed.

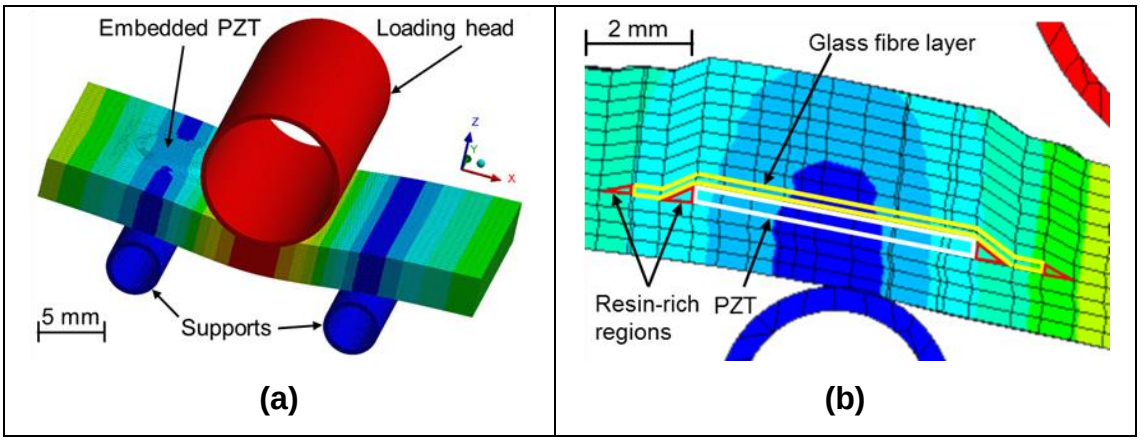

Figure 3: Illustration of the geometry used for the numerical FE short beam three point bending test (a) and a zoom of the section view of the numerical model with the PZT inserted between layers 4 & 5 (b).

The ANSYS's built-in Hashin's model for damage initiation and evolution was here used to identify the regions within the sample at which tensile or compressive damage in the fibre and matrix was initiated. This is described by the following four failure criteria modes for damage initiation [42]

Fibre Tension ($\hat{\sigma}_{11} \geq 0$): $$F_f^t = \left(\frac{\hat{\sigma}_{11}}{X_1}\right)^2 + \left(\frac{\hat{\tau}_{12}}{S_1}\right)^2; \quad (4)$$

Fibre Compression ($\hat{\sigma}_{11} < 0$): $$F_f^c = \left(\frac{\hat{\sigma}_{11}}{Y_1}\right)^2; \quad (5)$$

Matrix Tension ($\hat{\sigma}_{22} \geq 0$): $$F_m^t = \left(\frac{\hat{\sigma}_{22}}{X_2}\right)^2 + \left(\frac{\hat{\tau}_{12}}{S_1}\right)^2; \quad (6)$$

Matrix Compression ($\hat{\sigma}_{22} < 0$): $$F_m^c = \left(\frac{\hat{\sigma}_{22}}{2S_2}\right)^2 + \left[\left(\frac{Y_2}{2S_2}\right)^2 - 1\right]\frac{\hat{\sigma}_{22}}{Y_2} + \left(\frac{\hat{\tau}_{12}}{S_1}\right)^2; \quad (7)$$

where $\hat{\sigma}_{ij}$ and $\hat{\tau}_{ij}$ are the normal and shear components of the effective stress tensor, respectively. The constitutive law is provided by the following equation [36]

$$\sigma = C_d \varepsilon, \quad (8)$$

where σ is the true stress converted into the effective stress $\hat{\sigma}$ through a tensor operation [36], ε is the true strain and C_d is the damage elasticity matrix which describes material damage and has the following form

$$C_d = \frac{1}{D}\begin{bmatrix} (1-d_f)E_1 & (1-d_f)(1-d_m)\nu_{21}E_1 & 0 \\ (1-d_f)(1-d_m)\nu_{12}E_2 & (1-d_m)E_2 & 0 \\ 0 & 0 & D(1-d_s)G_{12} \end{bmatrix}, \quad (9)$$

where d_f, d_m and d_s are damage variables for tension, compression and shear [36], and

$$D = 1 - (1 - d_f)(1 - d_m)\nu_{12}\nu_{21} > 0. \quad (10)$$

Once the four failure criteria modes for damage initiation (4 - 7) are satisfied, further loading will cause a variation of the coefficients of the damage elasticity matrix (9) as function of damage variables d_i [36]. Indeed, the effective stress is equal to the true stress only if damage is not initiated, since damage variables are initially set equal to zero. An in-built damage evolution law for the damage variable in ANSYS is used to simulate the in-ply damage in each lamina. The damage evolution law is known as Continuum Damage Mechanics method that models gradually increasing damage. This is defined in terms of the fracture energy dissipated during the damage process, which is a generalisation of the CZM using cohesive elements [42, 43]. The input parameter is the energy dissipated per unit area G^C that accounts for fibre tension G_{ft}^C, fibre compression G_{fc}^C, matrix tension G_{mt}^C and matrix compression G_{mc}^C. The values used in this model of the energy dissipated for the CFRP material have been taken from literature and are equal to $G_{ft}^C = G_{fc}^C = 70\ \text{mJ/mm}^2$ and $G_{ft}^C = G_{fc}^C = 0.25\ \text{mJ/mm}^2$ [36]. As a result of the damage evolution law, an equivalent damage index variable d is obtained, which ranges from zero (undamaged material) to one (fully damaged material) and accounts for all four different modes mentioned above.

As illustrated in Figure 4 and Figure 5, damage was analysed at two specific layers in each FE simulation. For clarity, Figure 5 is an enlargement of Figure 4. The first layer examined was the CFRP ply under the PZT and glass fibre (Figure 4). The numerical results suggested that the centre of this layer (under the loading head) was more prone to fibre failure whereas, near the PZT periphery, delamination was more likely to occur. The second layer under examination was the glass fibre layer on top of the PZT (Figure 5). Also here, failure results revealed that damage was more likely to occur at the PZT periphery in the form of delamination. Although these observations were common between the three FE simulations, the lowest damage variable values (from 0 to 1) were obtained with the PZT and glass fibre layer placed above the middle plane. Conversely, the highest values were obtained with the PZT and glass fibre layer placed exactly at the middle plane. Failure results of FE simulations are summarised in Table 3. Based on this analysis, the PZT position with the minimum effect on the structural integrity of the laminate was achieved towards the surface under compression (i.e. between layers 8 and

9). Therefore, this final lay-up and PZT position (see Figure 2) were chosen for all specimens used in the experimental mechanical tests.

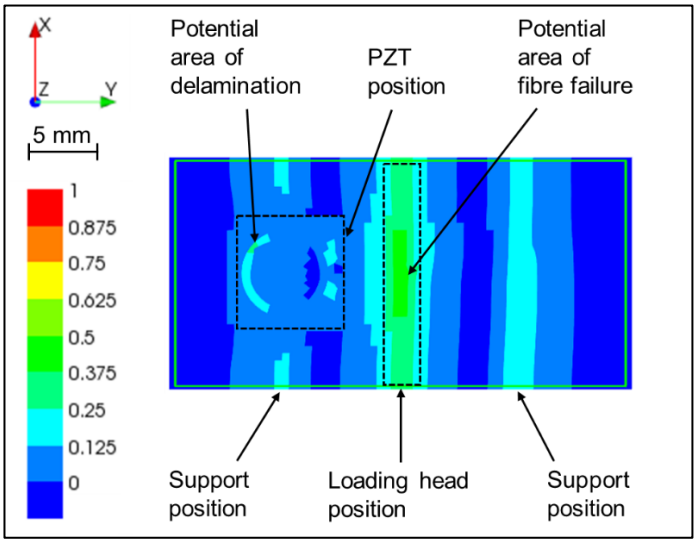

Figure 4: Contour plot of Hashin's damage index values on the CFRP Layer under the PZT (top view). The PZT and glass fibre layer were inserted between layers 8 & 9.

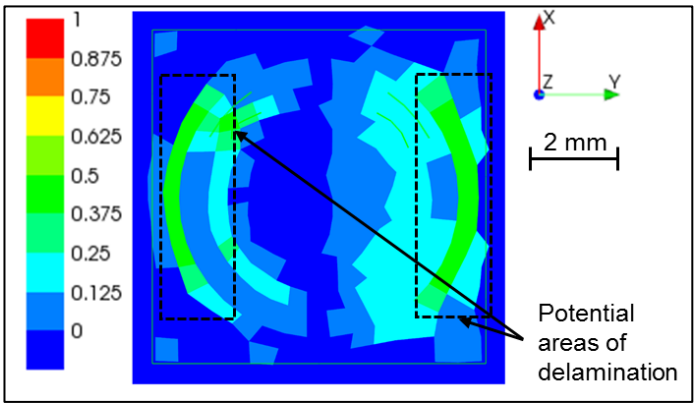

Figure 5: Contour plot of Hashin's damage index values on the glass fibre layer above the PZT (top view). The PZT and glass fibre layer were inserted between layers 8 & 9.

Table 3: Summary of Hashin's Failure Values.

PZT Position	**Maximum Damage Index Value**		
	CFRP Layer (at middle)	CFRP Layer (at PZT periphery)	Glass Fibre Layer (at PZT periphery)
Between layers 4 & 5	0.776	< 0.750	0.956
Between layers 6 & 7	0.663	< 0.500	0.774
Between layers 8 & 9	0.546	< 0.375	0.607

3.2 Specimen Manufacture

Three groups of six CFRP specimens (six P-, six G- and six K-specimens) were manufactured for each test (bending and compression). One specimen from each group was kept in pristine condition (control specimens) and used in post-test fractographic comparisons with damaged specimens. All samples were cut from larger plates (using a water-cooled diamond saw) made from unidirectional carbon/epoxy prepregs (Hexcel T800/M21) in [90°/0°/90°/0°/90°/0°]s stacking sequence, with a total thickness of around 3 mm (Figure 2). The composite plates were originally laid up by hand and cured inside an autoclave for 120 minutes at a pressure of 0.7 MPa and a temperature of 180ºC with a ramp rate of 3ºC/min. The diameter of the PZT was 6 mm and its thickness 0.3 mm. In G- and K-specimens, the size of glass fibre/Kapton layer over the PZT was approximately 10 × 10 mm.

3.2.1 Specimens used in Short-Beam and Long-Beam Bending Tests

The specimens used in the short-beam and the long-beam bending tests were manufactured in accordance with Section 3.1 and the BS EN ISO 14130:1997 and ASTM D7264/D7264M-07 standards, respectively [34, 44]. The dimensions of both specimen types are shown in Figure 6.

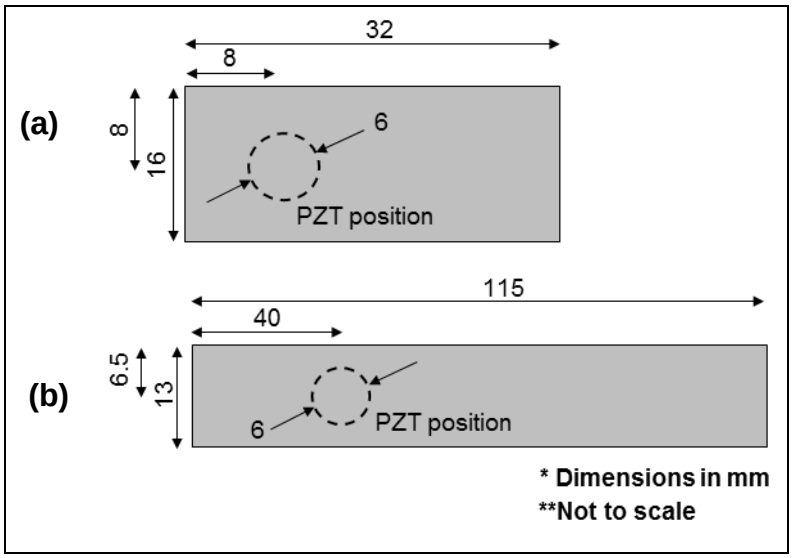

Figure 6: Dimensions of short-beam specimens (a) and long-beam specimens (b) used in bending tests.

3.2.2 Specimens used in Compression Test

The specimens used in the compression test were manufactured in accordance with Section 3.1 and BS-EN-ISO-14126:1999 standard [45]. As shown in Figure 7, the ends of the specimens were reinforced using tabs on either side to avoid damaging of the specimen during testing. For this reason, the PZTs were placed midway along the un-tabbed length of the specimens. The tabs were cut from larger plates made from unidirectional glass/epoxy prepregs (Hexcel UD192/8552). These were laid up by hand in [90°/0°/90°/0°/90°/0°]s stacking sequence and cured under the same conditions as the CFRP plates (ref. 3.2) but for 60 minutes longer. The tab plates were adhered to the CFRP plates before cutting of individual specimens using a two-part epoxy adhesive (Araldite 420 A/B) and the assembly was cured in accordance with the test standard.

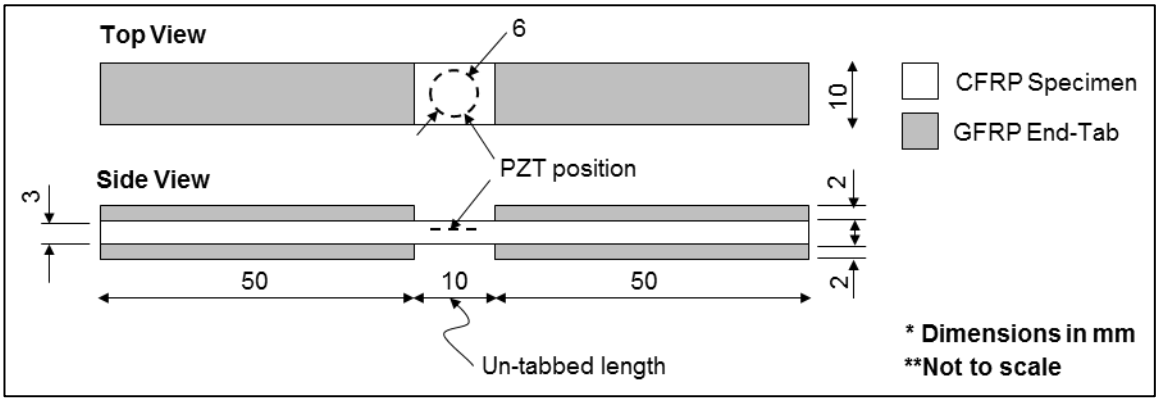

Figure 7: Dimensions of specimens used in compression tests.

3.3 Experimental Mechanical Tests

3.3.1 Short-Beam and Long-Beam Three-Point Bending Tests

The two mechanical tests were performed using a three-point bending configuration (Figure 8). According to the BS EN ISO 14130:1997 standard, the short-beam test was performed by maintaining a span-to thickness ratio of 5:1 and using a loading roller and supporting rollers of 5mm and 2mm radii respectively. In the long-beam test, the span-to-thickness ratio was 32:1 and all three rollers had a radius of 3mm in agreement with the ASTM D7264/D7264M-07 standard. All CFRP samples in both tests were loaded to failure on an Instron machine (Tabletop Model 3369) after setting the velocity of the loading head to 1 mm/min.

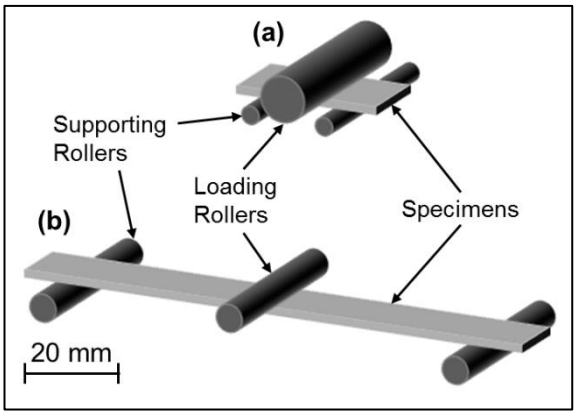

Figure 8: Schematic of short-beam (a) and long-beam (b) three-point-bending configurations.

3.3.2 Compression Test

According to method 1 of BS-EN-ISO-14126:1999 standard, the compressive load was applied to the specimens by shear through the surfaces of the end-tabs. A schematic of the compression fixture used is depicted in Figure 9. Briefly, each specimen was symmetrically clamped inside the fixture with its end-tabs being held between two rectangular steel blocks using eight bolts. A 10 mm gap was maintained between the top and bottom blocks; equal to the un-tabbed length of the specimen. The CFRP samples were compressed to failure on an Instron machine (Floor Model 5585) using a loading head velocity of 1 mm/min. The load was applied perpendicularly the top set of blocks that could move relative to the bottom blocks through the alignment rods.

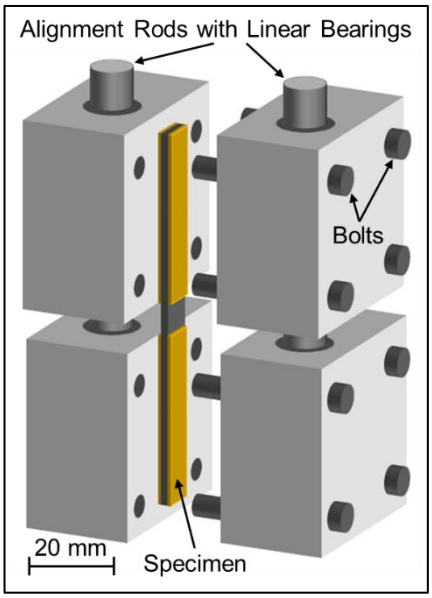

Figure 9: Schematic of compression test fixture.

3.4 Post-Test Fractographic Inspection of CFRP Specimens

After completing the tests, all short-beam and the long-beam specimens were encapsulated into epoxy resin to maintain their state of failure. Samples were then sectioned along their long axis to expose their internal structure (Figure 10). The failure mode and damage size in G- and K-specimens were studied and compared with those in P-specimens using a high-quality scanner (Epson Expression 1680 Professional) and an optical microscope (Leica DFC425). The control (pristine) specimens were also encapsulated into epoxy resin and used for comparisons with damaged specimens. The failure mode in compression samples was directly examined with the optical microscope. Encapsulation into epoxy resin was not possible because, as expected, the failure was not uniform along samples' width.

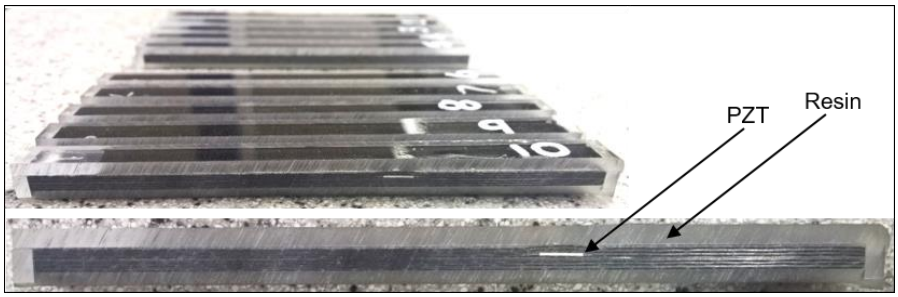

Figure 10: Long-beam specimen - section view.

3.5 Results and Discussion

A standard one-way analysis of variance (ANOVA) was conducted using Matlab to statistically determine if there was a significant difference, initially between the group means of P- and G-specimens, and then between P- and K-specimens. The null hypothesis (H_0) was that the group means were equal and the alternative hypothesis (H_A) that the means were not equal, with a significance level (α) of 0.1 (i.e. 90% confidence level). Briefly, in one-way ANOVA the F-value (or F-statistic) is the following ratio [46]

$$F = \frac{Variation\ Between\ Groups}{Variation\ Within\ Groups}\ . \tag{11}$$

For a true null hypothesis, F-value should be approximately equal to 1 with the sampling fluctuations following an F distribution. The F distribution was characterised by the numerator degrees of freedom (df_N) and the denominator degrees of freedom (df_D), where df_N was equal to the number of groups minus 1 (i.e. 2-1=1) and the df_D was equal

to the total group data minus the number of groups (i.e. 10-2=8) [47]. The probability (p-value) that F-value would exceed the computed test-statistic was derived by ANOVA from the cumulative distribution function of F distribution [48]. For p-values smaller than α (p < 0.1) the null hypothesis was rejected meaning that the group means were significantly different. Inversely, for p > 0.1 the null hypothesis was accepted.

3.5.1 Mechanical Testing Results

3.5.1.1 Short-Beam and Long-Beam Three-Point Bending Tests

The results from the two bending tests along with the F- and p-values form ANOVA are presented in Table 4. In the short-beam bending test, P- and G-specimens failed on average at a maximum interlaminar shear stress of around 51 MPa and a maximum deflection of 0.81 mm. The ANOVA results verified that the means of interlaminar shear strength and maximum deflection between these two groups were equal; p=0.45 and p=0.41 respectively. On the other hand, K-specimens failed on average at a maximum interlaminar shear stress of 45.6 MPa and a maximum deflection of 0.76 mm which were found to be significantly lower (p=0.0001 and p=0.0014) than the values of P-specimens. With regards to the long-beam bending test, the mean values of maximum flexural stress and maximum deflection of the P- and G-specimens were around 735 MPa and 8.56 mm, without any significant difference (p=0.47 and p=0.53). The corresponding values for the K-specimens were 685.7 MPa and 8.07 mm which were confirmed to be significantly different from those of P-specimens (p=0.01 and p=0.05).

3.5.1.2 Compression Test

Similarly, the compression test results (Table 4) indicated that the average compressive strength and maximum compressive extension of P- and G-specimens were almost the same (p=0.46 and p=0.58) and around 495 MPa and 1.035 mm. Again, for p-values of 0.0023 and 0.032, the mean compressive strength (438.9 MPa) and extension (0.95 mm) of K-specimens were evidently low compared with P-specimens.

Table 4: Summary of mechanical testing results.

Test	Property	P-specimens	G-specimens	K-specimens
Short-Beam Bending	**Int. Sh. Strength (MPa)** [a]	**51.0** (1.2)	**50.5** (1.0)	**45.6** (1.2)
	F-value	-	0.68	50.94
	p-value	-	0.4327	0.0001
	Max. Deflection (mm) [a]	**0.82** (0.02)	**0.80** (0.02)	**0.76** (0.02)
	F-value	-	0.78	22.6
	p-value	-	0.4106	0.0014
Long-Beam Bending	**Flex. Strength (MPa)** [a]	**741.3** (24.3)	**729.7** (24.6)	**685.7** (28.4)
	F-value	-	0.57	11.1
	p-value	-	0.4722	0.0104
	Max. Deflection (mm) [a]	**8.66** (0.42)	**8.46** (0.53)	**8.07** (0.41)
	F-value	-	0.44	5.08
	p-value	-	0.528	0.0542
Compression	**Comp. Strength (MPa)** [a]	**499.8** (21.1)	**488.8** (23.4)	**438.7** (22.9)
	F-value	-	0.61	19.18
	p-value	-	0.4579	0.0023
	Max. Comp. Ext. (mm) [a]	**1.05** (0.06)	**1.02** (0.08)	**0.95** (0.06)
	F-value	-	0.34	6.72
	p-value	-	0.5777	0.032

[a] Standard deviation in brackets

3.5.2 Fractography Results

3.5.2.1 Short-Beam Specimens

As depicted in Figure 11 and Figure 12, by observing the failure mode of short-beam specimens, interlaminar shear occurred at the interface between the two middle layers (6 and 7) and close to the specimen ends in all three types of specimen (P, G and K). In G-specimens the glass fibre layer over the PZT could not be easily visualised as it was covered by the matrix during the curing process. The propagation length (L) and opening (H) of shear damage were both measured in all specimens (Figure 12b) and the average values for each specimen group were calculated. The damage opening in each specimen was measured as the average of three measurements along the damage length (please see the experimental results in Table 5). The results from ANOVA suggested that the mean value of L in P-specimens was not different from that in G- and K-specimens (p=0.71 and p=0.37), but L was much more similar between P- and G-specimens rather than P- and K-specimens. On the other hand, the average value of H in P-specimens was found to be the same only with that in G-specimens (p=0.45), and significantly lower than in K-specimens (p=0.03). In addition, by examining the distribution of CFRP layers around the PZT, no difference was observed between the damaged and the control specimens

within each specimen group. It must be noted that the splitting of CFRP layers up to few hundred microns away from the PZT periphery (Figure 12c) was due to the direct insertion of the PZT and not because of the damage.

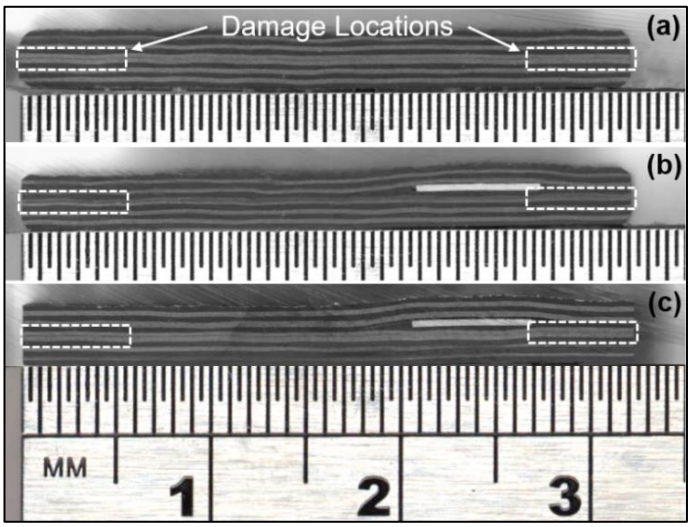

Figure 11: Short-beam specimens - cross-sectional view of damaged P-specimen (a), G-specimen (b) and K-specimen (c).

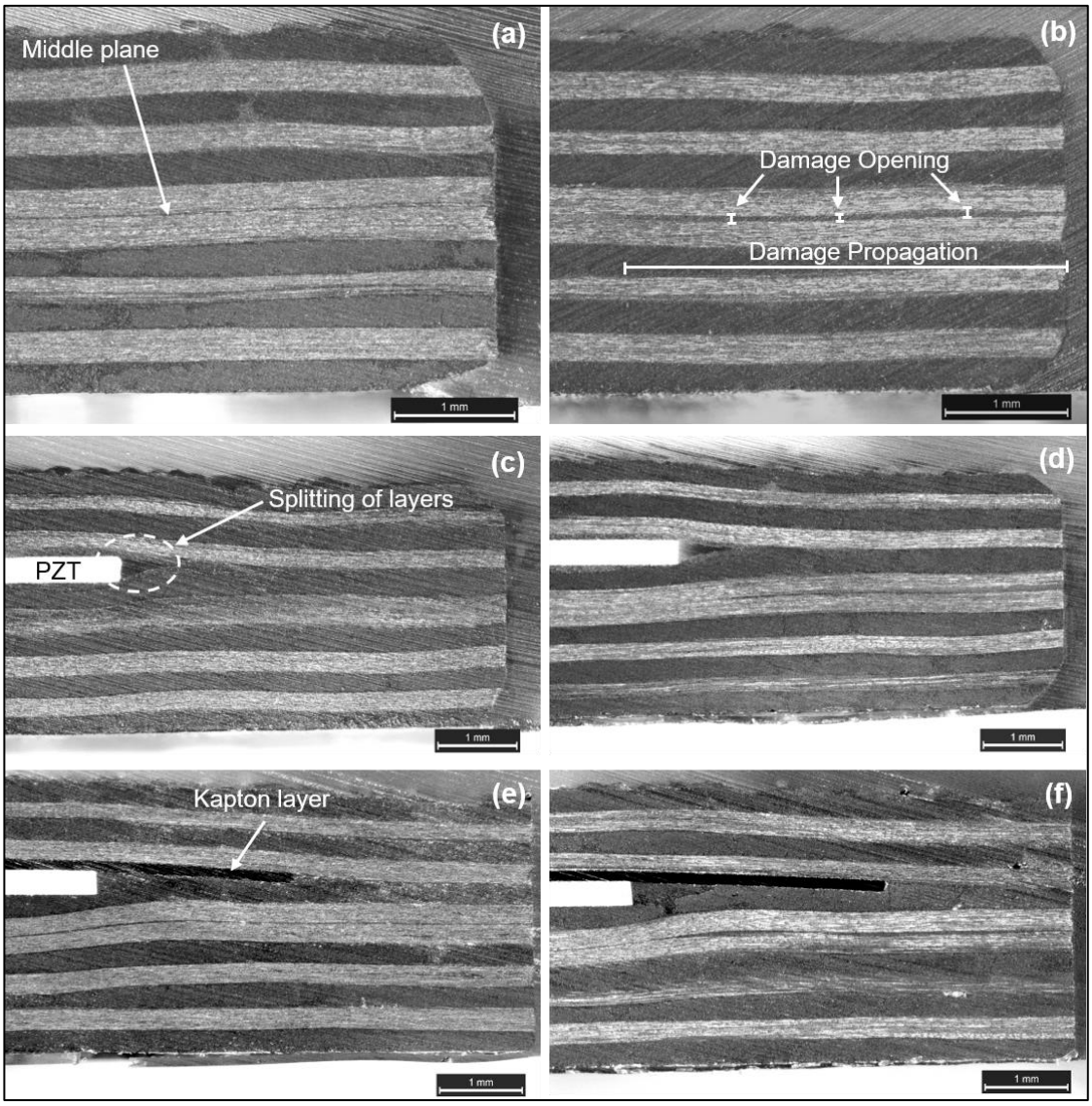

Figure 12: Short-beam specimens - closer view of specimen ends in the control P-specimen (a), damaged P-specimen (b), control G-specimen (c), damaged G-specimen (d), control K-specimen (e) and damaged K-specimen (f).

Table 5: Summary of damage measurements in short-beam specimens.

Damage Size	P-specimens	G-specimens	K-specimens
L (mm) [a]	**3.484** (0.477)	**3.599** (0.449)	**3.751** (0.413)
F-value	-	0.15	0.9
p-value	-	0.7050	0.3711
H (mm) [a]	**0.058** (0.022)	**0.061** (0.026)	**0.063** (0.024)
F-value	-	0.62	7.53
p-value	-	0.4541	0.0253

[a] Standard deviation in brackets

3.5.2.2 Long-Beam Specimens

With regards to the long-beam specimens used in the flexural test, the failure mode was also the same for all three specimen types. Damage occurred on the compression surface (top) midway along the specimen length as depicted in Figure 13. Closer inspection of the areas next to the damage and the PZT (Figure 14) revealed that fibre breakage occurred at the top three to five plies followed by in-plane delamination of the same plies up to few hundred microns away from the crack. By comparing the damaged specimens with the control specimens, no difference was noticed in the distribution of CFRP layers around the PZT. Similarly to the short-beam test, both L and H of delamination were here measured in all specimens (Figure 14), and the results are summarised in Table 6. The average values of L and H in both G- and K-specimens were considered equal to the values in P-specimens based on the ANOVA results ($p > 0.1$ in all cases). However, H and L values were again more similar between P- and G-specimens (p=0.87 and p=0.74) than between P- and K-specimens (p=0.79 and p=0.68).

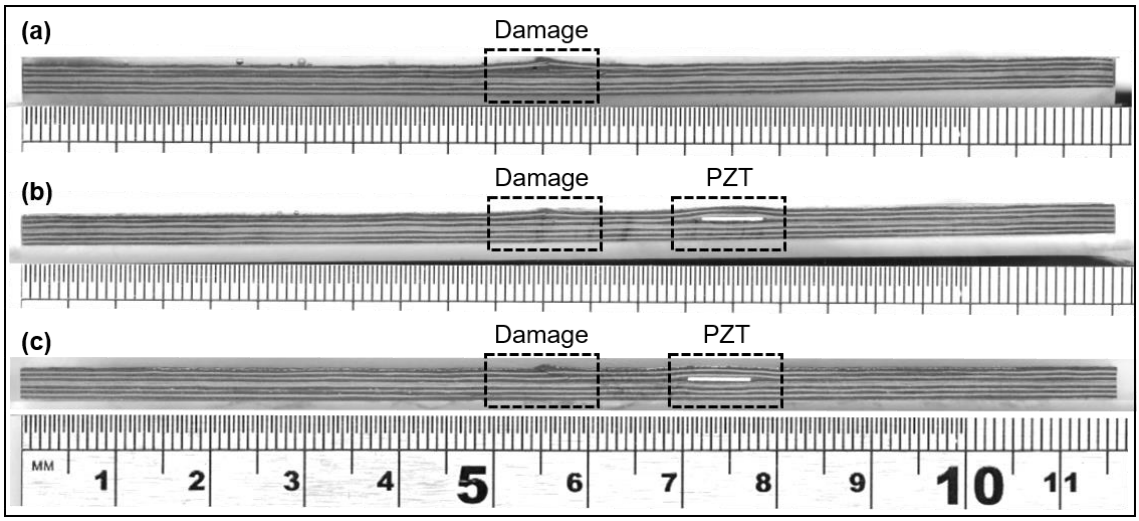

Figure 13: Long-beam specimens - cross-sectional view of P-specimen (a), G-specimen (b) and K-specimen (c).

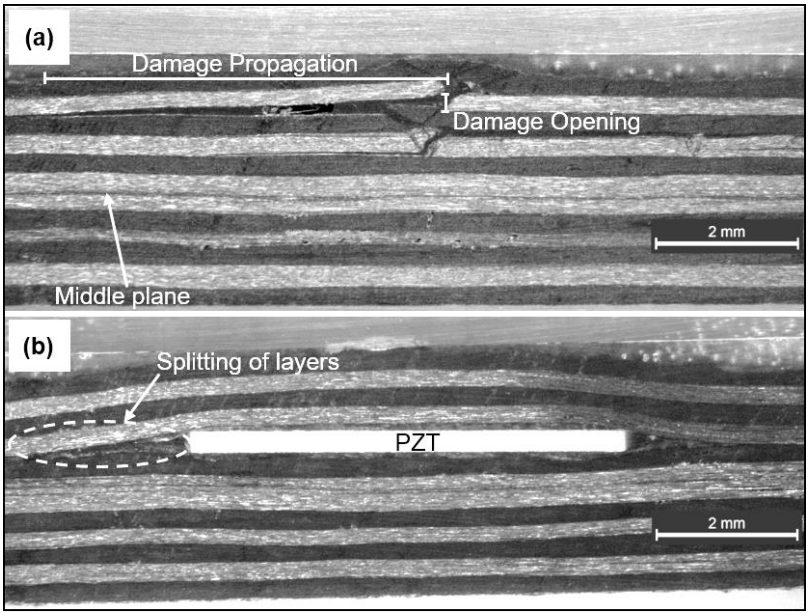

Figure 14: Long-beam specimens - closer view of damage area (a) and PZT area (b).

Table 6: Summary of damage measurements in long-beam specimens.

Damage Size	P-specimens	G-specimens	K-specimens
L (mm) [a]	**5.595** (1.556)	**5.742** (1.274)	**5.863** (1.462)
F-value	-	0.03	0.08
p-value	-	0.8745	0.7867
H (mm) [a]	**0.199** (0.030)	**0.206** (0.034)	**0.207** (0.027)
F-value	-	0.12	0.19
p-value	-	0.7398	0.6761

[a] Standard deviation in brackets

3.5.2.3 Compression Specimens

In the case of compression tests, damage in all P-, G- and K-specimens occurred within the un-tabbed section as expected. According to Figure 15, failure in K-samples was a combination of central through-thickness shear up to the plane of PZT/Kapton layer followed by complete delamination along that plane and finally through-thickness shear at both ends of un-tabbed section. G-samples also included a noticeable delamination at the plane of PZT/glass fibre layer. However, the brooming failure in both G- and P-specimens appeared to be almost identical.

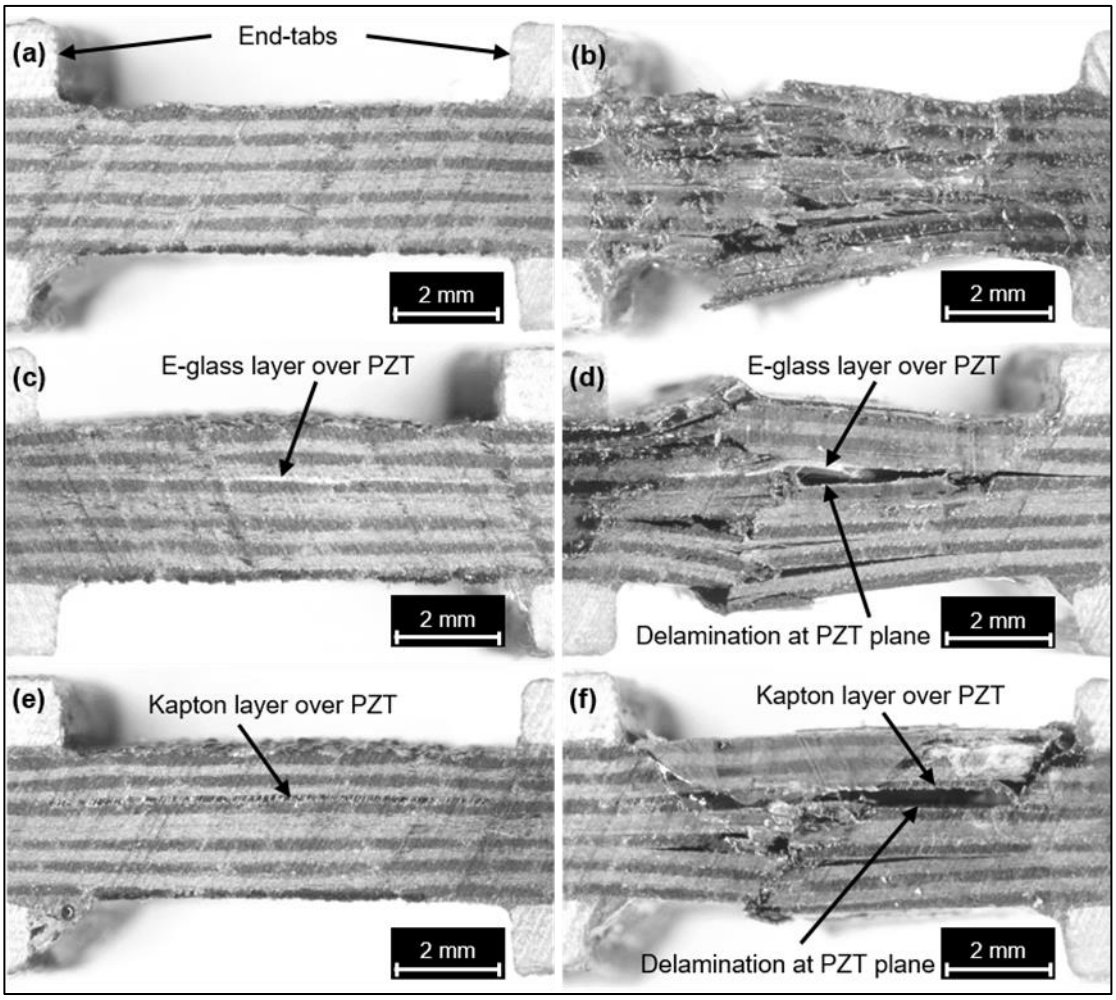

Figure 15: Compression specimens - closer view of un-tabbed section in the control P-specimen (a) damaged P-specimen (b), control G-specimen (c), damaged G-specimen (d), control K-specimen (e) and damaged K-specimen (f).

4 Functionality and Sensitivity of Embedded Transducers

Embedded PZTs with glass fibre layers were tested for the transmission and reception of elastic waves through the CFRP laminate in order to detect internal damage. The aim of this section was (i) to prove the effectiveness of glass fibre layers in protecting PZTs from being short-circuited and (ii) to demonstrate the ability of detecting internal damage using embedded PZTs and nonlinear ultrasound. The sensitivity of embedded PZTs to material damage was also compared with the sensitivity of surface-bonded PZTs. A double patch made from Fluorinated Ethylene Propylene (FEP) release film (12μm thick) was inserted in CFRP laminates to generate controlled “artificial” in-plane delamination [12].

4.1 Specimen Manufacture

Three 120 × 30 mm CFRP specimens with [90°/0°/90°/0°/90°/0°]s lay-up were manufactured using the same process described in Section 3.2. Each specimen included a 10 × 10 mm double FEP patch at its centre, between layers 8 and 9 (from the bottom). As depicted in Figure 16, all specimens included a pair of PZTs. In specimen 1, the transmitter PZT was placed between the same layers as the patch whereas the receiver PZT between layers 4 and 5. In specimen 2, both PZTs were placed at the same level as the patch. Both specimens included a glass fibre layer over the sensor for the electrical insulation of each PZT. Finally, in specimen 3 both transducers were bonded to the material surface using a conventional super glue (Loctite GO2 gel). The propagation of elastic waves through the material was expected to excite and vibrate the debonded layers (under clapping and rubbing motion) associated with the LDR effect, thus leading to the generation of new waves that could be detected as higher harmonics of excitation signal. As previously mentioned, the second harmonic was here used as the elastic signature for damage detection [23, 25].

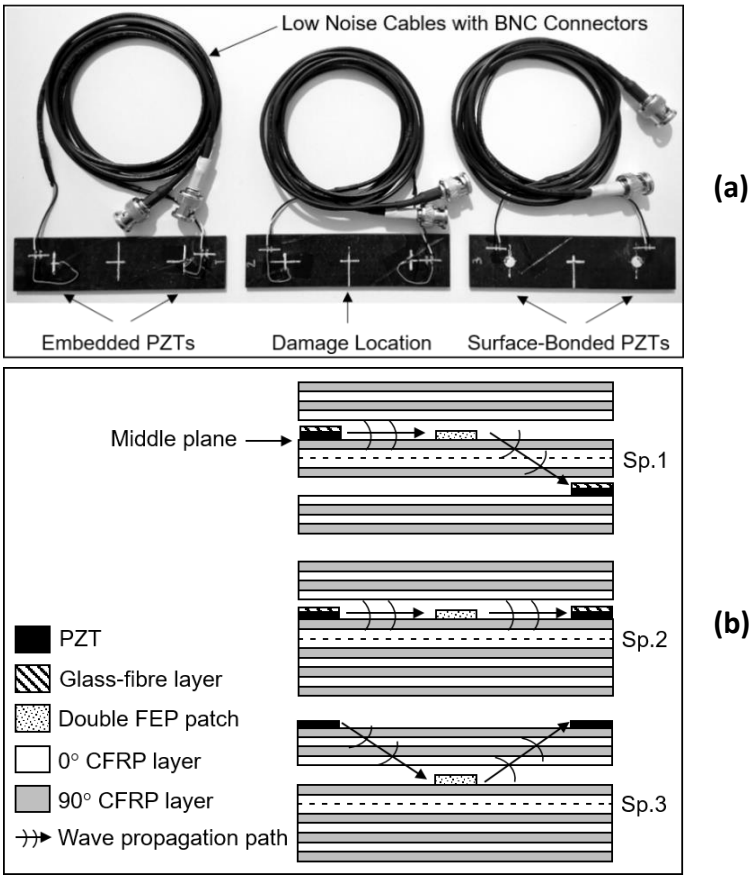

Figure 16: Composite specimens used in NEWS experiment with embedded PZTs (a) and their lay-up (b).

4.2 Experimental Procedure

A continuous periodic signal generated from an arbitrary waveform generator (TTi TGA12104) was sent to the transmitter PZT through a voltage amplifier (Falco Systems WMA-300) with a 50× amplification factor. The receiver PZT was connected to an oscilloscope (PicoScope 4423) and both the time domain and the frequency domain of the received signals were monitored at a sampling frequency of 350 kHz with an acquisition time of 2 ms (Figure 17). Initially, a frequency sweep was performed to identify the input frequency associated with the crack. The LDR frequency was found to be at 15 kHz. Hence, to achieve higher excitation of the debonded layers (at the patch location), a continuous signal at the input frequency of 15 kHz was transmitted. Different input voltages at 75 V, 87.5 V, 100 V, 112.5 V and 125 V were here tested. The material response was scanned using a Laser Doppler Vibrometer in order to verify that the frequency of 15 kHz was indeed associated with the damage location (i.e. with location of the FEP patch). For an input PZT signal of 100 V at 15 kHz, the out-of-plane vibrational velocity at 30kHz (second harmonic of input frequency) was measured on the surface of specimen 1. A three-dimensional plot of the results around the patch area is presented in Figure 18a and Figure 18b, which reveal that the area at which the vibrational velocity was higher matched the position of the FEP patch. From Figure 18a and Figure 18b, it can also be seen that the higher harmonic second response (i.e. the red zone) was also similar to the size of the patch (around 10 × 10 mm). These measurements proved that second harmonic generation caused by the LDR effect of the debonded layers occurred uniquely at the damage location and not elsewhere.

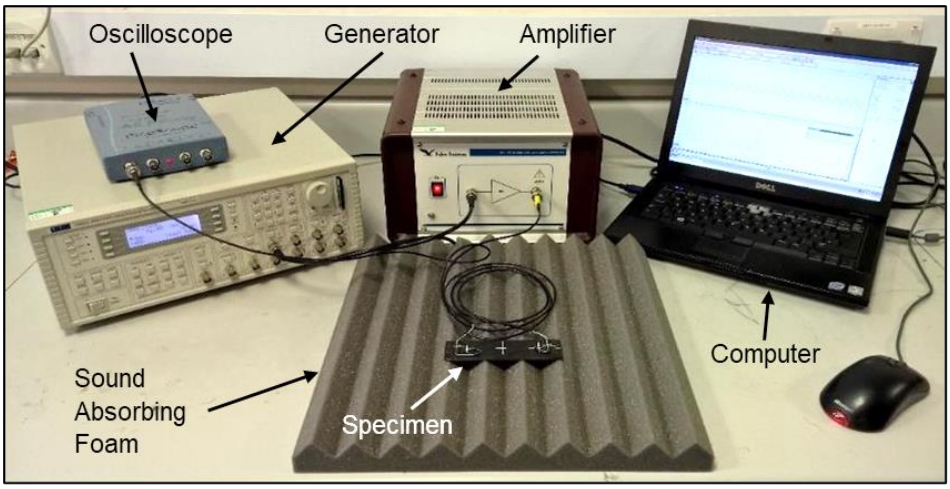

Figure 17: Illustration of set-up used in NEWS experiment.

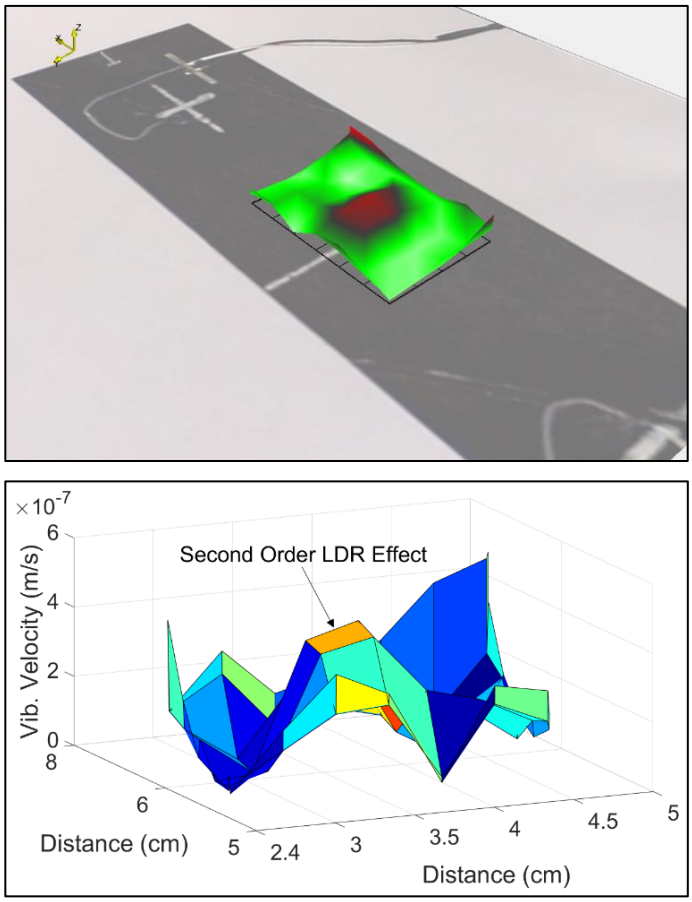

Figure 18: Illustration of the damaged area scanned by the laser Doppler vibrometer (a) and 3D representation of the out-of-plane vibrational velocity on the specimen 1 surface at the second harmonic frequency of 30 kHz.

4.3 Results and Discussion

The proposed technique for electrical insulation of the embedded PZTs with glass fibre layers was proved to be successful because the transmission and reception of signals was achieved in both specimens 1 and 2 without the formation of short-circuits. For the case of input signal of 100 V, the amplitude of the received signals in the time domain and the frequency domain are shown in Figure 19. The presence of A_2 harmonic verified that in-plane delamination in CFRP laminates could be detected using the proposed configuration of embedded PZTs. The amplitude at A_2 harmonic corresponding to the embedded PZTs (specimens 1 and 2) was an order of magnitude higher relative to that of surface bonded PZTs (specimen 3) indicating higher sensitivity to internal damage detection. This could be explained by considering the attenuation (energy loss) of the waves propagating through each specimen. The propagation distance from the transmitter to the receiver PZT as well as the distance from the damage location to the receiver PZT was shorter in specimens 1 and 2 relative to specimen 3 Consequently, the attenuation of waves was lower in both specimens with embedded PZTs resulting in a higher A_2 amplitude.

For a more accurate comparison between the two specimens with embedded PZTs, the $\beta = A_2/{A_1}^2$ ratio was calculated using the results from the case of input signal of 100V (Table 7). As explained in Section 2, the parameter β is proportional to the material degradation. By assuming that the damage size was very similar in all specimens, any variation in parameter β between the specimens would indicate a variation in damage sensitivity. The configuration of PZTs in specimen 2 was found to be more sensitive to damage detection (β = 0.00065) relative to that in specimen 1 (β = 0.00042). This was reasonable based on the attenuation of waves explained above. The same ratio was also calculated for specimen 3. As expected, that was significantly lower (β = 0.00023) than the other two indicating that the surface-bonded PZTs were less sensitive to damage detection than the embedded PZTs. The observations described above were also valid for the remaining four cases of input voltage. In fact, by increasing the voltage from 75 V to 125 V, the signal amplitude of both the A_1 and the A_2 terms increased. In all cases, β was approximately two to three times higher for the embedded PZTs. Between specimens 1 and 2, the sensitivity was always higher in specimen 2. The results are summarised in Table 7.

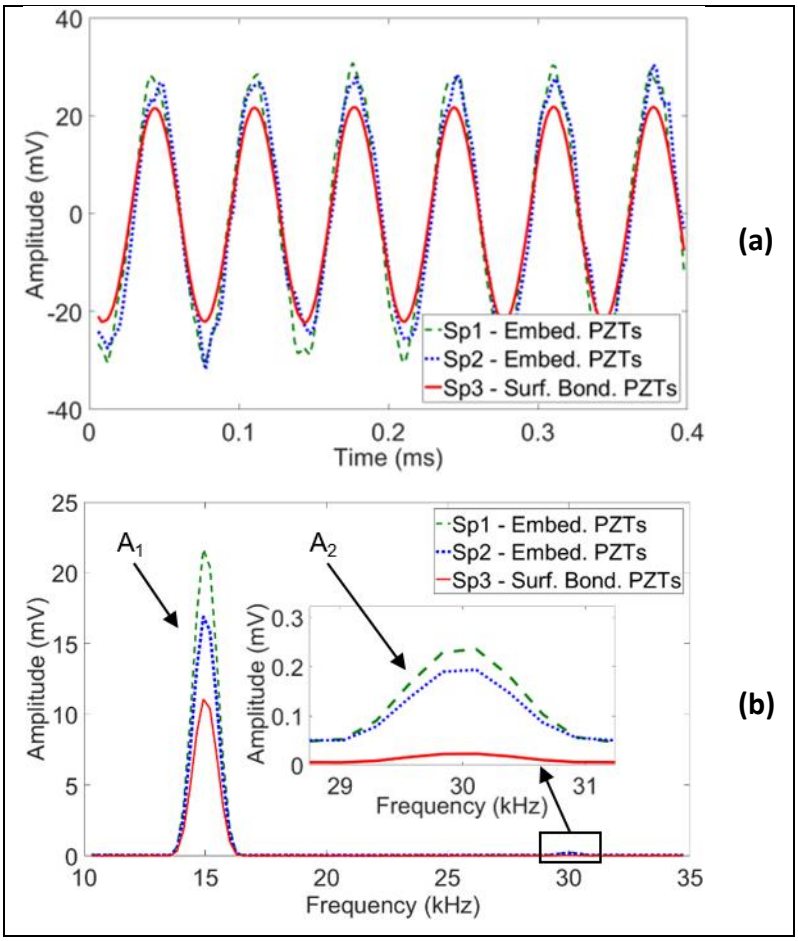

Figure 19: Amplitude of the received signal in time domain (a) and its associated spectrum (b) - case of 100V input signal at 15 kHz.

Table 7: Summary of results from NEWS experiment.

Input Signal	Specimen ID	A1 Amp. (mV)	A2 Amp. (mV)	Parameter $\lvert\beta\rvert$
75Vpp	1	15.733	0.209	0.00084
at	2	11.358	0.185	0.00143
15kHz	3	6.719	0.019	0.00042
87.5Vpp	1	18.485	0.226	0.00066
at	2	14.087	0.196	0.00099
15kHz	3	8.041	0.024	0.00038
100Vpp	1	23.786	0.235	0.00042
at	2	17.899	0.207	0.00065
15kHz	3	10.637	0.026	0.00023
112.5Vpp	1	27.626	0.243	0.00032
at	2	20.456	0.218	0.00052
15kHz	3	13.974	0.032	0.00016
125Vpp	1	30.961	0.259	0.00027
at	2	23.058	0.230	0.00043
15kHz	3	17.132	0.041	0.00014

5 Conclusions

In this paper a novel material processing technique for the electrical insulation of circular PZTs inserted between the plies of CFRP laminates was proposed. The top (conductive) surface of the embedded PZT was covered with a layer of E-glass fibre fabric. The effect of this embedding technique on the interlaminar properties of CFRP laminates was studied both numerically and experimentally, and it was compared with the effect of the conventional embedding technique using Kapton layers.

Specifically, short-beam and long-beam three-point bending tests, and compression tests were performed to determine the interlaminar shear strength, flexural strength and compressive strength of CFRP laminates with embedded PZTs and a layer of woven E-Glass fabric (G-specimens). Similarly, plain CFRP laminates (P-specimens) as well as CFRP laminates with embedded PZTs and a Kapton layer (K-specimens) were subject to the same tests. By analysing the results with a one-way ANOVA it was found that the mean values of compressive, flexural and interlaminar shear strength of G-specimens were all equal to those of P-specimens ($0.41 < p < 0.58$), suggesting that the proposed insulation technique had no impact on the mechanical properties of the CFRP laminates. The corresponding strength values in the case of K-specimens were all confirmed to be significantly lower ($0.0001 < p < 0.05$) than those of P-specimens.

In addition, a comparative post-test fractographic analysis showed that in the bending tests, the mean damage size in G- and K-specimens was similar to the damage size in P-specimens ($0.37 < p < 0.87$). Only the damage opening in short-beam K-specimens was significantly bigger from that in P-specimens ($p = 0.03$). However, the remaining damage length and opening values were more similar between P-and G-specimens ($0.45 < p < 0.87$) than between P-and K-specimens ($0.37 < p < 0.79$). In compression tests, the brooming failure in P- and G-specimens was very similar suggesting that their behaviour under compressive loading was almost identical, whereas K-specimens failed by through-thickness shear followed by significant delamination at PZT plane.

Finally, NEWS experiments on CFRP laminates with artificial in-plane delamination proved the effectiveness of glass fibre layers in protecting the PZTs from being short-circuited, and also demonstrated the ability of detecting internal damage using embedded PZTs and nonlinear ultrasound. The sensitivity of embedded PZTs to damage detection based on the effect of second harmonic generation was around two times higher than that

of conventionally surface-bonded PZTs. In conclusion, this study can be considered as a contribution towards the development of composite materials with integrated sensing capabilities for ultrasonic SHM of aerospace structures. However, there are additional aspects to be studied in the future such as the effect of the proposed embedding technique on the fatigue endurance of composites and the ability of embedded arrays of PZTs with glass fibre layers to estimate the size and location of damage.

References

1. Masmoudi, S., El Mahi, A., Turki, S., & El Guerjouma, R. (2014). Mechanical behavior and health monitoring by Acoustic Emission of unidirectional and cross-ply laminates integrated by piezoelectric implant. *Applied Acoustics*, 86(1), 118-125.
2. Konka, H. P. (2010). *Characterization of composite piezoelectric materials for smart joint applications*. Thesis (Master's). Louisiana State University.
3. Birman, V. (1996). Thermal effects on measurements of dynamic processes in composite structures using piezoelectric sensors. *Smart Materials and Structures*, 5(4), 379.
4. Mall S., & Coleman, J. M. (1998). Monotonic and fatigue loading behavior of quasi-isotropic graphite/epoxy laminate embedded with piezoelectric sensor. *Smart Materials and Structures*, 7(6), 822.
5. Paget, C. A., & Levin, K. (1999). Structural integrity of composites with embedded piezoelectric ceramic transducers. In *Smart Structures and Materials 1999: Smart Structures and Integrated Systems* (Vol. 3668, pp. 306-313). International Society for Optics and Photonics.
6. Mall, S. (2002). Integrity of graphite/epoxy laminate embedded with piezoelectric sensor/actuator under monotonic and fatigue loads. *Smart Materials and Structures*, 11(4), 527-533.
7. Lin, M., & Chang, F. K. (2002). The manufacture of composite structures with a built-in network of piezoceramics. *Composites Science and Technology*, 62(7-8), 919-939.
8. Su, Z., Wang, X., Chen, Z., Ye, L., & Wang, D. (2006). A built-in active sensor network for health monitoring of composite structures. *Smart Materials and Structures*, 15(6), 1939-1949.
9. Arellano, M. T., Crouzeix, L., Collombet, F., Douchin, B., & Grunevald, Y. H. (2012). Mechanical characterization of an alternative technique to embed sensors in composite structures: the monitoring patch. *Applied Composite Materials*, 19(3-4), 379-391.
10. Tang, H. Y., Winkelmann, C., Lestari, W., & La Saponara, V. (2011). Composite structural health monitoring through use of embedded PZT sensors. *Journal of Intelligent Material Systems and Structures*, 22(8), 739-755.
11. Masmoudi, S., El Mahi, A., & Turki, S. (2015). Use of piezoelectric as acoustic emission sensor for in situ monitoring of composite structures. *Composites Part B: Engineering*, 80(1), 307-320.
12. Wooh, S. C., & Wei, C. (1999). A high-fidelity ultrasonic pulse-echo scheme for detecting delaminations in composite laminates. *Composites Part B: Engineering*, 30(5), 433-441.
13. Huang, Y., & Nemat-Nasser, S. (2007). Structural integrity of composite laminates with embedded micro-sensors. In *Sensor Systems and Networks: Phenomena, Technology, and Applications for NDE and Health Monitoring 2007* (Vol. 6530, p. 65300W). International Society for Optics and Photonics.
14. Clausen, J., Specht, U., Busse, M., Lang, A., & Sanders, J. (2013). Integration of glass fibre structures in aluminium cast parts for CFRP aluminium transition structures. *Procedia Materials Science*, 2(1), 197-203.

15. Boccardi, S., Calla, D. B., Ciampa, F., & Meo, M. (2018). Nonlinear elastic multi-path reciprocal method for damage localisation in composite materials. *Ultrasonics*, 82(1), 239-245.

16. Ciampa, F., Mankar, A., & Marini, A. (2017). Phononic crystal waveguide transducers for nonlinear elastic wave sensing. *Scientific Reports*, 7(1), 1-8.

17. Scarselli, G., Ciampa, F., Nicassio, F., & Meo, M. (2017). Non-linear methods based on ultrasonic waves to analyse disbonds in single lap joints. *Proceedings of the Institution of Mechanical Engineers, Part C: Journal of Mechanical Engineering Science*, 231(16), 3066-3076.

18. Van Den Abeele, K. E., Sutin, A., Carmeliet, J., & Johnson, P. A. (2001). Micro-damage diagnostics using nonlinear elastic wave spectroscopy (NEWS). *NDT & E International*, 34(4), 239-248.

19. Sohn, H., Park, G., Wait, J. R., Limback, N. P., & Farrar, C. R. (2003). Wavelet-based active sensing for delamination detection in composite structures. *Smart Materials and Structures*, 13(1), 153.

20. Polimeno, U., Meo, M., Almond, D. P., & Angioni, S. L. (2010). Detecting low velocity impact damage in composite plate using nonlinear acoustic/ultrasound methods. *Applied Composite Materials*, 17(5), 481-488.

21. Ricci, F., Mal, A. K., Monaco, E., Maio, L., Boffa, N. D., Di Palma, M., & Lecce, L. (2014). Guided waves in layered plate with delaminations. In *EWSHM - 7th European Workshop on Structural Health Monitoring* (hal-01020322). IFSTTAR.

22. Ciampa, F., Pickering, S., Scarselli, G., & Meo, M. (2014). Nonlinear damage detection in composite structures using bispectral analysis. In *Health Monitoring of Structural and Biological Systems 2014* (Vol. 9064, p. 906402). International Society for Optics and Photonics.

23. Ciampa, F., Scarselli, G., & Meo, M. (2017). On the generation of nonlinear damage resonance intermodulation for elastic wave spectroscopy. *The Journal of the Acoustical Society of America*, 141(4), 2364-2374.

24. Meo, M., & Zumpano, G. (2005). Nonlinear elastic wave spectroscopy identification of impact damage on a sandwich plate. *Composite Structures*, 71(3-4), 469-474.

25. Landau, L. D. & Lifshitz, E. M. (1986). *Theory of Elasticity* (Vol. 7, p. 476). 3rd ed. Oxford: Pergamon.

26. Zagrai, A., Donskoy, D., Chudnovsky, A., & Golovin, E. (2008). Micro-and macroscale damage detection using the nonlinear acoustic vibro-modulation technique. *Research in Nondestructive Evaluation*, 19(2), 104-128.

27. Zaitsev, V., & Sas, P. (2000). Nonlinear response of a weakly damaged metal sample: a dissipative modulation mechanism of vibro-acoustic interaction. *Journal of Vibration and Control*, 6(6), 803-822.

28. Buck, O., Morris, W. L., & Richardson, J. M. (1978). Acoustic harmonic generation at unbonded interfaces and fatigue cracks. *Applied Physics Letters*, 33(5), 371-373.

29. Antonets, V. A., Donskoy, D. M., & Sutin, A. M. (1986). Nonlinear vibro-diagnostics of flaws in multilayered structures. *Mechanics of Composite Materials*, 15(1), 934-937.

30. Hirsekorn, S., & Delsanto, P. P. (2004). On the universality of nonclassical nonlinear phenomena and their classification. *Applied Physics Letters*, 84(8), 1413-1415.

31. Solodov, I., Bai, J., Bekgulyan, S., & Busse, G. (2011). A local defect resonance to enhance acoustic wave-defect interaction in ultrasonic nondestructive evaluation. *Applied Physics Letters*, 99(21), 211911.

32. Solodov, I. (2014). Resonant acoustic nonlinearity of defects for highly-efficient nonlinear NDE. *Journal of Nondestructive Evaluation*, 33(2), 252-262.

33. Dragan, K., Dziendzikowski, M., Kurnyta, A., Leski, A., & Bienias, J. (2014). Structural health monitoring of composite structures with use of embedded PZT piezoelectric sensors. In *ECCM-16th European Conference on Composite Materials.*

34. British Standards Institute. (1997). *EN ISO 14130:1997 Fibre-reinforced plastic composites - Determination of apparent interlaminar shear strength by short-beam method*. London: BSI.

35. Moulin, E., Assaad, J., Delebarre, C., Kaczmarek, H., & Balageas, D. (1997). Piezoelectric transducer embedded in a composite plate: application to Lamb wave generation. *Journal of Applied Physics*, 82(5), 2049-2055.

36. Shin, D. K., Kim, H. C., & Lee, J. J. (2014). Numerical analysis of the damage behavior of an aluminum/CFRP hybrid beam under three point bending. *Composites Part B: Engineering*, 56, 397-407.

37. Giddings, P. F., Bowen, C. R., Salo, A. I., Kim, H. A., & Ive, A. (2010). Bistable composite laminates: effects of laminate composition on cured shape and response to thermal load. *Composite Structures*, 92(9), 2220-2225.

38. Phadnis, V. A., Pandya, K. S., Naik, N. K., Roy, A., & Silberschmidt, V. V. (2013). Ballistic impact behaviour of woven fabric composite: Finite element analysis and experiments. In *Journal of Physics: Conference Series* (Vol. 451, p. 012019). IOP Publishing.

39. Zako, M., Uetsuji, Y., & Kurashiki, T. (2003). Finite element analysis of damaged woven fabric composite materials. *Composites Science and Technology*, 63(3-4), 507-516.

40. Physik Instrumente (PI) GmbH & Co. (2012). Piezoelectric Actuators. Datasheet (Online) available from http://fisica.cab.cnea.gov.ar/bt/images/d/d3/PICat.pdf.

41. Hyer, M. W. (1998) *Stress analysis of fiber-reinforced composite materials* (Vol. 1, p. 26). Boston: WBC McGraw-Hill.

42. Willis, B. M. (2013). *Applying finite element analysis with a focus on tensile damage modeling of carbon fiber reinforced polymer laminates*. Thesis (Master's). The Ohio State University.

43. Shi, Y., Swait, T., & Soutis, C. (2012). Modelling damage evolution in composite laminates subjected to low velocity impact. *Composite Structures*, 94(9), 2902-2913.

44. American Society for Testing and Materials. (2007). *ASTM D7264/D7264-07 Standard test method for flexural properties of polymer matrix composite materials*. West Conshohocken: ASTM International.

45. British Standards Institute. (1999). *BS EN ISO 14126:1999 Fibre-reinforced plastic composites - Determination of compressive properties in the in-plane direction*. London: BSI.

46. Daniel, W. W. (1999). *Biostatistics: a foundation for analysis in the health sciences* (Chapter 8). 7th ed. Hoboken: John Wiley and Sons.

47. Pezzullo, J. (2013). *Biostatistics for dummies* (Vol. 1, p. 164). Hoboken: John Wiley & Sons.

48. Hogg, R. V., & Ledolter, J. (1987). *Engineering statistics*. New York: Macmillan Pub Co.

Chapter 4

Nonlinear Ultrasonic Detection of Damage in Smart CFRP Composites

The inspection process of spacecraft structures can benefit from the use of smart CFRP laminates, not only for the ultrasonic detection of manufacturing flaws, but mainly for the identification of impact damage from orbital debris particles which usually need to be examined by the astronauts during lengthy and difficult extravehicular inspections. Also, as previously mentioned, the use of internal networks of sensors offers an additional level of protection to the SHM systems from the extreme conditions of space.

The publication (Paper II) presented in this chapter explored the suitability of the embedded PZT transducers introduced in Chapter 3 for nonlinear ultrasonic detection of two types of damage with different size in CFRP plates. In fact, pairs of embedded sensors were used for the transmission and reception of ultrasonic waves in damaged CFRP plates. One plate was “artificially” damaged (AD-laminate) at two locations using embedded polymeric patches of different size. This created delamination at a single interface between the composite layers, similar to the defects caused by manufacturing errors (e.g. inclusions, dust spots or grease). A separate plate was originally damaged with an impact of certain energy (ID-laminate), and the damage size was later increased with a second impact of higher energy. This type of damage is characterised by delamination, broken fibres and cracked matrix at multiple interfaces through the thickness of the material, as in the case of real impact events.

Damage identification was successfully demonstrated with ultrasonic NEWS experiments. Initially, this was achieved using the method of second harmonic generation under the propagation of single-frequency waves. Then, the existence of damage was confirmed based on the effect of nonlinear modulation of waves transmitted at two different frequencies. In both cases of NEWS experiments, the acoustic response acquired from the AD- and ID-plates plates was studied against the response recorded on an undamaged plate (UD-laminate). This verified the generation of nonlinear phenomena when defects are presented.

In addition, the excitation of the damaged layers inside the material due to their interaction with the propagating ultrasonic waves was confirmed with a separate set of tests. Specifically, the out-of-plane vibrational velocity of the material at the top surface of the laminates was measured with the use of a laser Doppler vibrometer. These measurements revealed that the vibrational velocity at the location of damage was higher relative to the surrounding area, and it was found to increase with increasing voltage of the transmitted signals.

The “Statement of Authorship” form and Paper II are provided on the following pages.

This declaration concerns the article entitled:			
Nonlinear ultrasonic inspection of smart carbon fibre reinforced plastic composites with embedded piezoelectric lead zirconate titanate transducers for space applications			
Publication status			
Draft manuscript ☐ Submitted ☐ Accepted ☐ Published ☒			
Publication details (reference)			
Andreades, C., Malfense Fierro, G. P., Meo, M., & Ciampa, F. (2019). Nonlinear ultrasonic inspection of smart carbon fibre reinforced plastic composites with embedded piezoelectric lead zirconate titanate transducers for space applications. *Journal of Intelligent Material Systems and Structures*, 30(20), 2995-3007.			
Candidate's contribution to the paper (detailed, and also given as a percentage)			
Formulation of ideas: 75% I proposed the idea of performing nonlinear ultrasonic detection of two areas of delamination with different size in one composite plate, using the layout of embedded PZT transducers developed in my previous study. My previous supervisor Dr Francesco Ciampa suggested the detection of real damage caused by impact at two different levels of energy.			
Design of methodology: 80% I chose the design, lay-up and material for the fabrication of the composite samples along with the positions of the PZT transducers and the damage. Dr Francesco Ciampa suggested improvements to the above.			
Experimental work: 90% I manufactured the composite plates, performed the ultrasonic tests and collected the data. My co-author Dr Gian Piero Malfense Fierro helped in the set-up of the experimental equipment.			
Presentation of data in journal format: 95% I analysed the collected data, prepared the figures, chose the layout of the paper and wrote the manuscript. My co-author Dr Gian Piero Malfense Fierro and my supervisors provided feedback on the above and supported the process of submission and review.			
Statement from Candidate			
This paper reports on original research I conducted during the period of my Higher Degree by Research candidature.			
Signed		**Date**	02/10/2020

Nonlinear Ultrasonic Inspection of Smart CFRP Composites with Embedded PZT Transducers for Space Applications

Christos Andreades[1], Gian Piero Malfense Fierro[1], Michele Meo[1], Francesco Ciampa[2]

[1]Department of Mechanical Engineering, University of Bath, Bath BA2 7AY, UK

[2]Department of Mechanical Engineering Sciences, University of Surrey, Guildford GU2 7XH, UK

Abstract

Carbon fibre reinforced plastic (CFRP) composites used in spacecraft structures are susceptible to delamination, debonding and fibre-cracking that may arise during manufacturing, assembly or in-service operations (e.g. caused by debris impacts in near-Earth orbital spaceflights). Therefore, in-situ and real-time health monitoring is necessary to avoid time-consuming and unsafe visual inspections performed either on-ground or during extra vehicular activities. In this paper, a recently created "smart" CFRP composite structure with embedded piezoelectric (PZT) transducers was used to detect multiple areas of artificial delamination and real impact damage of different size using nonlinear ultrasound. The electrical insulation of embedded PZTs was achieved by interlaying a dry layer of woven glass fibre fabric between the sensor and the CFRP plies before curing. Damage detection was successfully demonstrated using both second harmonic generation and nonlinear modulation (sidebands) of the measured ultrasonic spectrum. The material nonlinear response at the second harmonic and sidebands frequencies was also measured with a laser Doppler vibrometer to validate the nonlinear ultrasonic tests and provide damage localisation. Experimental results revealed that the proposed configuration of embedded PZTs can be utilised for on-board ultrasonic inspection of spacecraft composite parts.

1 Introduction

Modern spacecraft structures are made of carbon fibre reinforced plastic (CFRP) composites because of their advantages over metals including high strength-to-weight ratio, fatigue performance, design flexibility and corrosion resistance [1]. CFRP material, for example, offers increased ballistic protection over aluminium when used as the inner wall in dual-wall spacecraft shields [2, 3]. Nevertheless, one of the major problems of CFRP is the susceptibility to damage such as micro-cracks and delamination, which may arise during manufacturing, assembly or in-service operations. In-service defects, in particular, are caused by hypervelocity impacts from micrometeoroids and orbital debris (MMOD) in the near-Earth environment [4, 5]. Because of the high orbital speed of debris objects (~10 km/s), even sub-millimetre particles can cause severe damage to the spacecraft [6]. Hence, there is a need to provide real-time and in-situ monitoring of material defects at any stage of satellite's component life cycle, especially for the International Space Station and future manned space missions.

Visual inspection is currently the most common technique for inspecting spacecraft components. It relies on the skills and experience of specialised technicians on-ground or astronauts during in-service extravehicular activities [7]. In the last few decades, material defect identification has also been achieved using a number of different non-destructive evaluation (NDE) methods such as those related to linear ultrasonic wave propagation [8, 9], acoustic emission [10-12], thermography [13, 14] and X-ray scanning [15, 16]. Among NDE methods, ultrasonic technology has the advantage to be simply converted into structural health monitoring (SHM) systems by integrating acoustic/ultrasonic piezoelectric transducers on the monitored component [17]. Therefore, ultrasonic SHM technology can be used for in-service monitoring of spacecraft structures and it is the focus of this research work. Nonlinear ultrasound, commonly known in the ultrasonic scientific community as nonlinear elastic wave spectroscopy (NEWS) techniques, is a family of ultrasonic inspection methods that have shown higher sensitivity to the detection and localisation of damage (material flaws and micro-cracks) at the early stages of formation than linear ultrasound [18-20]. NEWS methods can rely on higher harmonic generation [21-26], time reversal [27-29], wave modulation [30-35], phase modulation [36], local defect resonance [37-39], imaging of nonlinear scatters [40-41] and shift in resonance frequency characteristics [42-45].

Previous researchers [17, 46-48], reported damage detection in composite materials by applying NEWS techniques using externally mounted piezoelectric lead zirconate titanate (PZT) transducers. For spacecraft applications though, there is a strong demand for composite structures with integrated PZTs in order to (i) provide information about micro-cracks during on-ground and in-service ultrasonic monitoring, and (ii) protect the sensors from being directly exposed to the harsh space environment. According to the literature [49-52], both CFRP and glass fibre reinforced plastic (GFRP) composites can include PZTs between the material layers, thus creating "smart" composite structures. However, the integration of PZTs in CFRP composites requires electrical insulation of the transducers from the conductive carbon fibres to avoid short circuits. In previous studies [50-52], insulation was achieved by covering the embedded PZTs with layers of polyimide (Kapton) films. However, the embodiment of polymeric films such as Kapton and Teflon between the composite plies is a typical method for constraining ply adhesion and causing artificial delamination [53]. Consequently, the structural integrity of the composite can be significantly affected by the use of polymeric films.

An innovative material processing technique for the electrical insulation of embedded PZTs in CFRP plates was proposed by the authors in a recent study [54]. In particular, a dry layer of woven E-glass fibre fabric was inserted between the conductive surface of the PZTs and the CFRP plies before curing process. This "smart" CFRP composite was subject to mechanical tests including compression, long-beam and short-beam three-point bending tests. An analysis of variance (ANOVA) was conducted on the experimental results and proved that the mean values of compressive, flexural and interlaminar shear strength were equal to the means of plain CFRP specimens. In addition, preliminary NEWS experiments were carried out on the "smart" CFRP composite containing "artificial" delamination simulated by double Teflon patches. The experimental results revealed that the sensitivity to damage based on the amplitude (A_2) of second harmonic generation was nearly twice as high as the sensitivity of surface-bonded PZTs.

The aim of this paper is to further examine the capability of the "smart" CFRP composite with embedded PZTs to detect multiple areas of damage with various dimensions and defect nature. For this scope, NEWS experiments were conducted on two damaged CFRP laminates; one plate with two "artificial" delamination defects (i.e. polymeric film patches) and one plate with real impact flaws. Artificial damage is

generally characterised by debonding at a single interface (in-plane delamination) similarly to delamination caused by manufacturing errors [55]. Impacts, on the other hand, usually generate debonding, fibre breakage and matrix cracking at multiple interfaces in the form of through-thickness damage within the laminate [56]. In the first part of this paper, defect detection was accomplished based on the second harmonic generation method, whereas in the second part damage identification was achieved using the nonlinear wave modulation technique (see Section 2). In both experimental parts, damage detection at the chosen wave propagation frequency was investigated by scanning the plate surface with a laser Doppler vibrometer (LV) and recording the out-of-plane vibrational velocity surrounding the damage location.

The layout of the paper is as follows. In Section 2, the second harmonic generation and the nonlinear wave modulation methods are explained. In Section 3, the manufacture and the damage assessment of CFRP plates along with the NEWS and the LV experiments are outlined. In Section 4, the results from the NEWS and the LV tests are presented. In Section 5, the conclusions of this paper are discussed.

2 Theory

2.1 Second Harmonic Generation

As it is explained by Melchor et al. [57], the propagation of elastic waves at specific frequencies (single-frequency excitation) through composite materials with cracked matrix, debonded fibres or delaminated plies forces the damaged layers to either oscillate ("clapping" motion) or move relative to each other ("rubbing" motion). This leads to the generation of nonlinear wave effects that can be detected in the form of higher harmonics (even and odd multiples) of the input signal frequency [58]. In particular, second harmonic generation has been reported as the most efficient NEWS feature for damage identification [59, 60]. This can be explained by considering the second order nonlinear stress-strain relationship (from Hooke's law)

$$\sigma = E\varepsilon + \frac{E\beta}{2}\varepsilon^2 \tag{1}$$

and the one-dimensional (1D) elastodynamic wave equation

$$\rho \frac{\partial^2 u(x,t)}{\partial t^2} = \frac{\partial \sigma}{\partial x}\,, \tag{2}$$

where E is the Young's modulus, $\varepsilon = \frac{\partial u(x,t)}{\partial x}$ is the strain, β is the second order nonlinear coefficient (parameter), ρ is the material density, $u(x,t)$ is the displacement [61]. By substituting equation (1) into equation (2), yields

$$\frac{\partial^2 u(x,t)}{\partial t^2} - c^2 \frac{\partial^2 u(x,t)}{\partial x^2} = \beta c^2 \left(\frac{\partial u(x,t)}{\partial x}\right)\left(\frac{\partial^2 u(x,t)}{\partial x^2}\right), \quad (3)$$

where $c = \sqrt{E/\rho}$ is the longitudinal wave speed. Equation (3) can be then solved using a first-order perturbation method, which has the general solution

$$u(x,t) = u^{(1)}(x,t) + u^{(2)}(x,t), \quad (4)$$

with $u^{(1)} \gg u^{(2)}$. Both linear, $u^{(1)}(x,t)$, and nonlinear, $u^{(2)}(x,t)$, terms can be rewritten as

$$u(x,t) = A_1 \sin(kx - 2\pi ft) - \frac{\beta k^2 A_1^2}{8} x \cos[2(kx - 2\pi ft)], \quad (5)$$

where A_1 is the amplitude of the fundamental frequency harmonic, $A_2 = \frac{\beta k^2 A_1^2}{8} x$ is the amplitude of the second harmonic wave associated with the nonlinear material behaviour, x is the wave propagation distance within the material and k is the wave number [61].

2.2 Nonlinear Wave Modulation

In the case of multiple-frequency excitation of damaged composite materials, further nonlinear wave effects are generated due to the interaction of the propagating waves with the damage. When a damaged material is excited using two continuous periodic waves, one with a low frequency (f_1) and one with a high frequency (f_2), the damage behaves as a multiplier and mixer of the two excitation frequencies. The amplitude of the high frequency wave is modulated by the low frequency one and, in addition to higher harmonics, intermodulation products (sidebands) can be generated in the frequency spectrum of the received signal at frequencies equal to $f_2 \pm nf_1$, where n is a positive integer [62]. Undamaged (intact) materials are, instead, characterised by a linear response as the elastic waves are not interacting with any damage. Therefore, only the fundamental frequencies (f_1 and f_2) are detectable in the frequency domain of the received signal [63]. Nonlinear wave modulation method has also been proved to be effective for defect detection [31-34]. Similarly to the second harmonic generation, equation (3) can be solved with dual periodic excitation using the first-order perturbation method, and the

amplitudes A_+ and A_- associated to each sideband $f_+ = f_2 + f_1$ and $f_- = f_2 - f_1$ can be expressed as

$$A_+ = \frac{\beta_+ k_{f_1} k_{f_2} A_{f_1} A_{f_2}}{4} x \quad (6)$$

and

$$A_- = \frac{\beta_- k_{f_1} k_{f_2} A_{f_1} A_{f_2}}{4} x \quad (7)$$

where A_{f_1} and A_{f_2} are the amplitudes and k_{f_1} and k_{f_2} are the wave numbers of the input signals at f_1 and f_2 frequencies, respectively, and β_+ and β_- are the nonlinear parameters [64].

3 Experimentation

3.1 Manufacture of CFRP Plates

A total of three carbon/epoxy (T800/M21) laminates with dimensions of 180 × 140 × 3.5 mm were used in the experiments of this study. The laminates were made from unidirectional prepreg layers with a [90°/0°/90°/0°/90°/0°]s lay-up, and they were cured in an autoclave for 180 minutes at a pressure of 0.7 MPa and a temperature of 150°C with a ramp rate of 3°C/min. As illustrated in Figure 1, all three plates included two embedded PZTs (ferroelectric soft piezo material PIC 255) of 6 mm diameter and 0.3mm thickness, for the propagation of ultrasonic elastic waves. A 10 × 10 mm layer of woven E-glass fibre fabric was also interlaid between the top surface of the PZTs and the CFRP plies, for electrical insulation. The PZTs were directly placed between the 8th and the 9th layers from the bottom. The thin wires from to the positive and negative electrodes of the PZTs were connected to 50 Ω straight Bayonet Neill-Concelman (BNC) plugs through low noise cables (RG174/U). The wires were directed outside the top surface of the plate through small slits in the fibre direction of every CFRP ply (i.e. without cutting any fibres).

3.2 Damage Assessment and Sensor Functionality

The first laminate (Figure 1) was kept intact and used as the reference plate. The second laminate (Figure 2a) included two double-layered patches of different size to cause controlled artificial in-plane delamination. Each patch consisted of two square layers of 12 μm thick Fluorinated Ethylene Propylene (FEP) film stacked one on top of the other.

The FEP patches were inserted at the same plane of the PZTs (between layers 8 and 9 from the bottom). The third plate (Figure 2b) was impacted at its centre with a hemispherical indentor of 20 mm diameter. The damage was initially created with an impact energy of 10 J and, once the experimental detection was completed, the damage size was increased with another impact of higher energy (15 J). In the following paragraphs, the first plate is referred to as the undamaged (UD) laminate, and the second and third plates as the artificially damaged (AD) and the impact damaged (ID) laminates respectively.

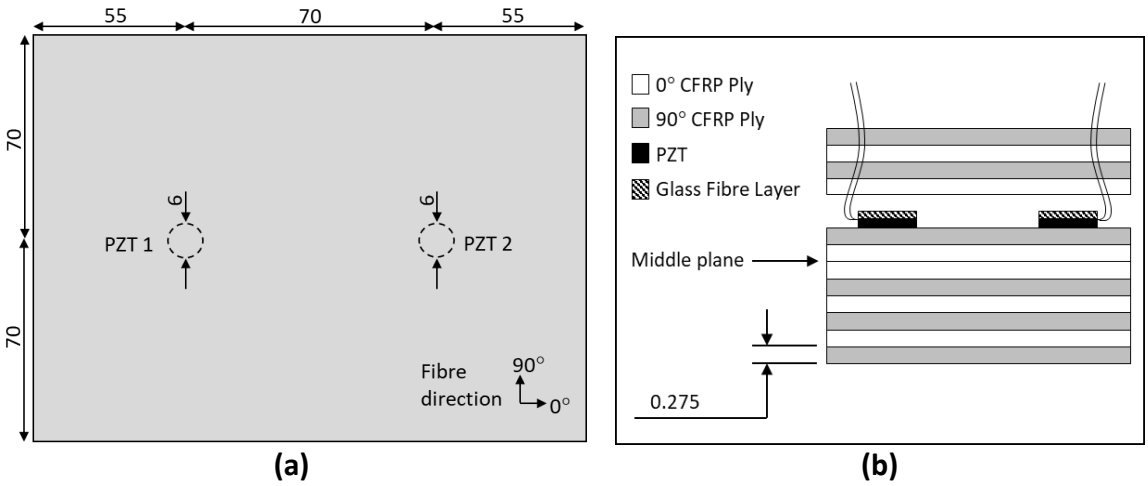

Figure 1: Design of undamaged CFRP plate - top view (a) and stacking sequence (b). Dimensions in mm. Not to scale.

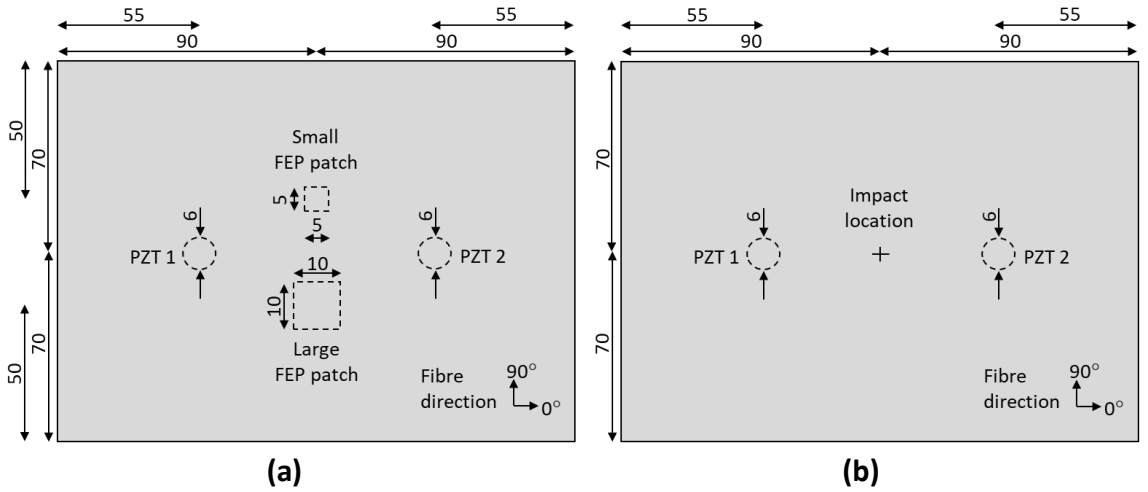

Figure 2: Design of artificially damaged plate (a) and impact damaged plate (b). Dimensions in mm. Not to scale.

It must be noted that the capacitance of the PZTs was measured with the use of a Keithley 2110 5 1/2 multimeter before their embedment in the composite plates, after the curing process of the plates, and after impacting the ID-laminate. In all cases, the capacitance was the same (1.54±0.02 nF) suggesting that the PZTs were functional. This is a typical sensor inspection method in literature [65, 66]. In fact, any noticeable drop in capacitance would indicate cracking or depoling of the transducer from either the high curing pressure and temperature or the applied impact load.

Prior to performing any experiment, the size of the damage in AD- and ID- plates was evaluated by conducting stepped linear C-scans using a phased array system (Diagnostic Sonar Ltd) equipped with a 5 MHz probe containing 128 elements. More specifically, the C-scans were carried out in steps of 12 elements (single cycle pulse, element pitch of 0.52 mm) and the damage was assessed based on the signal amplitude. The front face of the probe included a 30 mm acrylic (Perspex) delay line and coupling was achieved using ultrasonic gel. As shown in Figure 3 and Figure 4, the areas at which delamination was detected matched the positions of the double FEP patches and the impact damage. In the AD-plate, the two defects had a similar size to that of the double FEP patches. In the ID-plate, the initial damage diameter (10 J impact) was approximately 18 mm, and the final diameter (15 J impact) was around 32 mm.

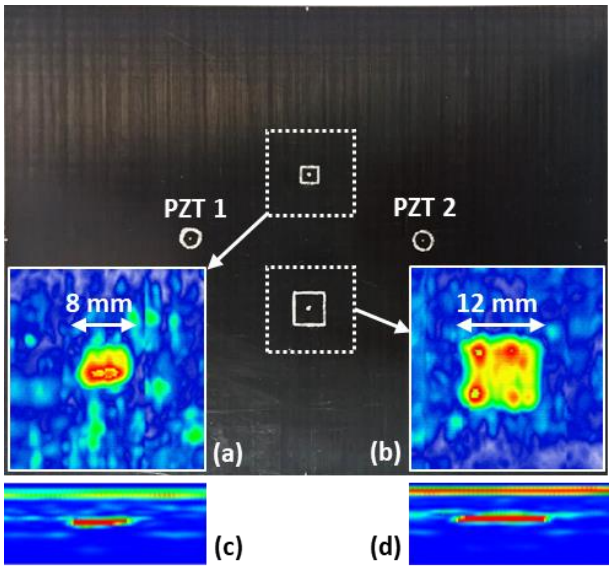

Figure 3: Ultrasonic C-scan of the small (a) and the big (b) artificial damage in AD-laminate and the associated B-scans (c), (d) - Images not to scale.

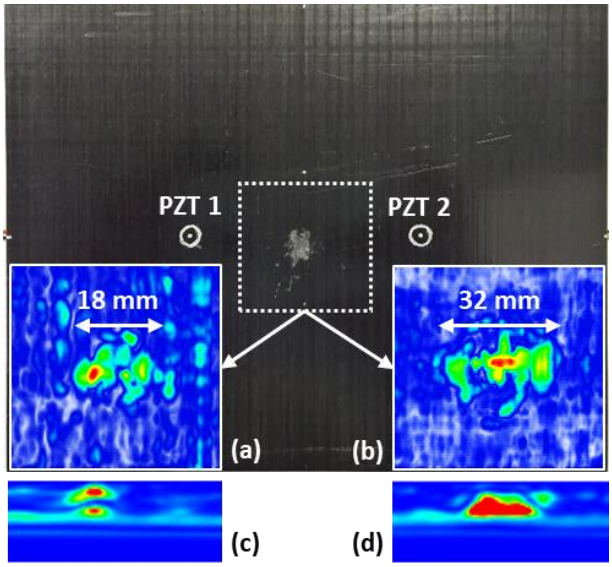

Figure 4: Ultrasonic C-scan of the 10 J (a) and the 15 J (b) impact damage in ID-laminate and the associated B-scans (c), (d) - Images not to scale.

3.3 Experimental Set-up and Method

3.3.1 NEWS Experiments

Starting from the NEWS experiments based on the second harmonic generation method, in each CFRP plate PZT1 was used for the transmission and PZT2 for the reception of continuous periodic ultrasonic signals (i.e. single-frequency excitation). As illustrated in Figure 5 below, the input signal was generated from an arbitrary waveform generator (TTi TGA12104) and its amplitude was increased using a voltage amplifier (Falco Systems WMA-300). The received signal was monitored in the time and frequency domains at a sampling frequency of 2 MHz and a total acquisition time of 50 ms using an oscilloscope (PicoScope 4424).

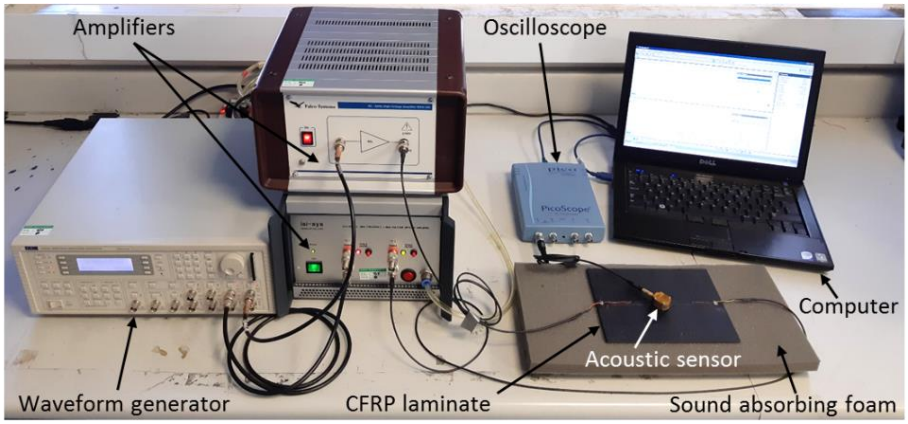

Figure 5: Illustration of the set-up used in NEWS experiments.

Initially, in the AD- and ID-laminates the input signal frequency of PZT1 was swept between 20 and 500 kHz to determine the two frequencies corresponding to the highest A_2 amplitudes of the received signal. In the case of the AD-plate, the two chosen frequencies were very likely to be associated with the excitation of the two FEP patches, whereas for the ID-plate, the chosen frequencies were related to the excitation of the damage caused initially with 10 J, and then with 15 J of impact energy. At these four frequencies, the amplitude of the fundamental (A_1) and A_2 harmonics was recorded for input signal voltages of 60, 70, 80, 90 and 100 V. It must be noted that the chosen input signal frequencies would not necessarily correspond to the highest A_1 amplitude as this is highly dependent on the excitation of the PZT1 and the tested material. For clarification, Table 1 summaries the input frequencies and voltages used with the PZT1. The UD-plate was also excited at the same four frequencies and its ultrasonic response was compared to the damaged samples.

Table 1: Input signal frequencies and voltages used in NEWS experiments for second harmonic generation.

CFRP Plate	**Sweep analysis freq. band - PZT1 (kHz)**	**Input volt. to PZT1 (V)**	**Chosen damage excitation freq. (kHz)**
AD	20-500	60, 70, 80, 90, 100	f_1=104.5, 184.7
ID	20-500	60, 70, 80, 90, 100	f_1=128, 310

For the NEWS experiments associated with the nonlinear wave modulation technique, both embedded PZTs were used to excite the ID- and UD-laminates (i.e. multiple-frequency excitation). In each plate, PZT1 was used to send ultrasonic waves at low frequency (f_1) whereas PZT2 enabled high frequency (f_2) transmission. According to Figure 5, PZT1 was connected to a channel of the waveform generator through the Falco Systems WMA-300 amplifier and PZT2 was powered by a separate channel through an ISI-SYS HVA-B100-2 amplifier. The propagating waves were received using an external acoustic transducer (McWade 300 kHz NS3303) connected to the oscilloscope. In the ID-plate, PZT1 was swept between 10-50 kHz and the f_1 values associated with the five highest peaks of the received signal amplitude were recorded. For every f_1 value, PZT2 was swept between 100-300 kHz and the frequency spectrum of the received signal was examined in order to determine the combination of f_1 and f_2 which results in the strongest wave modulation, based on the amplitude of the sidebands. By keeping the input voltage

to PZT2 constant at 50 V and increasing the input voltage to PZT1 from 60 to 100 V in steps of 10 V, the received signal amplitude was recorded at f_1, f_2 and $f_2 \pm f_1$ frequencies. A summary of the input signal frequencies and voltages to the PZT1 and PZT2 in the ID-plate is provided in Table 2, together with the frequencies found to cause damage excitation. The UD-plate was also subject to multiple-frequency excitation using the chosen f_1 and f_2 frequencies.

Table 2: Input signal frequencies and voltages used in NEWS experiments for nonlinear wave modulation.

CFRP Plate	Sweep analysis freq. band - PZT1 (kHz)	Input volt. to PZT1 (V)	Sweep analysis freq. band - PZT2 (kHz)	Input volt. to PZT2 (V)	Chosen damage excitation freq. (kHz)
ID	10-50	60, 70, 80, 90, 100	100-300	50	f_1=18 f_2=192

3.3.2 LV Experiments

In both NEWS experiments with second harmonic and sidebands generation, a series of LV experiments were performed to examine whether the generation of second harmonics and the presence of sidebands at the chosen input signal frequencies was actually attributed to the damage excitation. As shown in Figure 6, ultrasonic waves were transmitted from the same PZTs as described in Section 3.3.1, using the same configuration of arbitrary waveform channels and amplifiers. Second harmonic generation in the AD- and ID-plate was studied by measuring the out-of-plane vibrational velocity of the plate surface at A_1 and A_2 frequencies, using the LV scanning head (Polytec PSV-400). The input signal voltage applied to PZT1 was fixed at 300 V. Similarly, nonlinear wave modulation in the ID-plate was investigated by applying input voltages of 100 V and 300 V to the PZT1 and PZT2 respectively, and recording the vibrational velocity of the plate surface at f_1, f_2 and $f_2 \pm f_1$ frequencies.

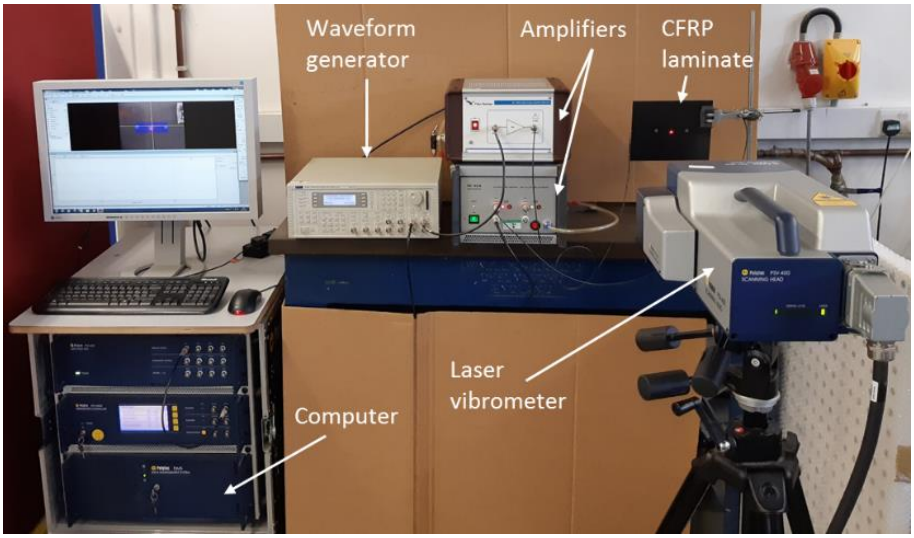

Figure 6: Illustration of the set-up used in LV experiments.

4 Results and Discussion

4.1 Second Harmonic Generation Experiments

As explained in Section 3.3.1, by sweeping the frequency of PZT1 in the AD-plate from 20 to 500 kHz, the two highest A_2 amplitudes were observed at 104.5 kHz and 184.7 kHz frequencies. Hence, these two were considered as the frequencies causing the strongest excitation of the two FEP patches. Similarly, in the ID-plate, the two input signal frequencies related to the excitation of the 10 J and the 15 J impact damage were chosen at 310 kHz and 128 kHz, respectively, based on the A_2 amplitude. After exciting the UD-laminate at these four frequencies, A_2 harmonics were not found in the frequency spectrum, thus verifying that the plate was intact. An example is presented in Figure 7.

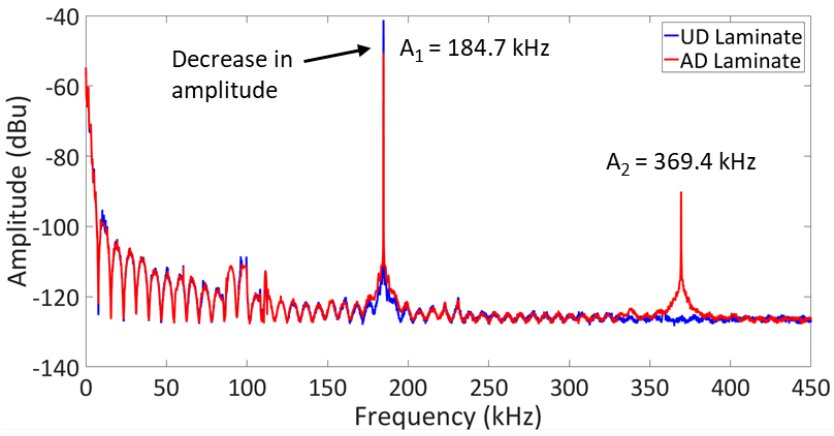

Figure 7: Frequency spectrum of the received signal in the UD-laminate and in the AD-laminate - Input signal of 60 V at 184.7 kHz.

Additionally, the A_1 amplitude in the case of the UD-plate was always greater than in the damaged laminates. That was expected as in the damaged laminates part of the transmitted wave energy was transferred from the fundamental input wave to the nonlinear harmonic one. Moreover, as can be seen in Figure 8 and Figure 9, the results obtained from the AD- and ID-plates indicated that by increasing the input voltage to PZT1 from 60 to 100 V, the received signal amplitude at A_1 and A_2 frequencies was also rising. The A_2 amplitude was around two orders of magnitude smaller than the A_1 amplitude, in both plates.

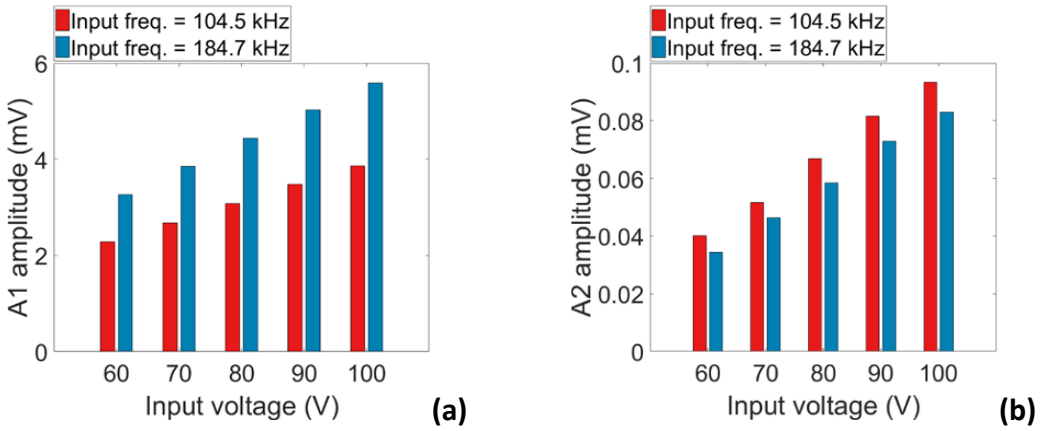

Figure 8: Amplitude of the received signal in AD-laminate at the fundamental (a) and second (b) harmonic frequencies - Input signals of 60, 70, 80, 90, and 100 V at 104.5 and 184.7 kHz.

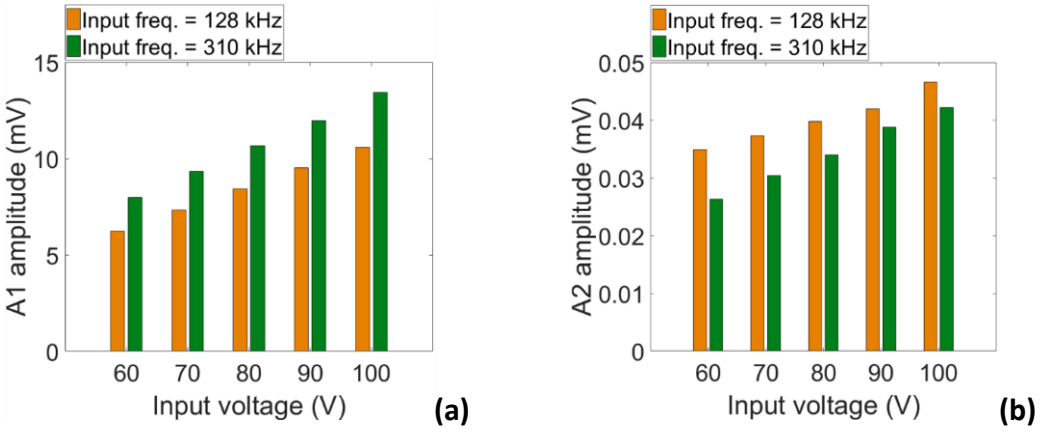

Figure 9: Amplitude of the received signal in ID-laminate at the fundamental (a) and second (b) harmonic frequencies - Input signals of 60, 70, 80, 90, and 100 V at 128 and 310 kHz.

Furthermore, three-dimensional plots of the results obtained from the LV experiments on AD- and ID-laminates (Figure 10 and Figure 11) confirmed that the out-of-plane vibrational velocity was always higher at the location of the impact. The A_2 amplitude was about an order of magnitude smaller than the A_1 amplitude. The LV experiments on the AD-laminate showed that the input signal at 104.5 kHz caused excitation only to the big FEP patch and, at 184.7 kHz, only to the small FEP patch. Similarly, the 10 J impact damage in the ID-laminate was only excited at 310 kHz, and after the second impact of 15 J only at 128 kHz. This verified the correct selection of damage excitation frequencies.

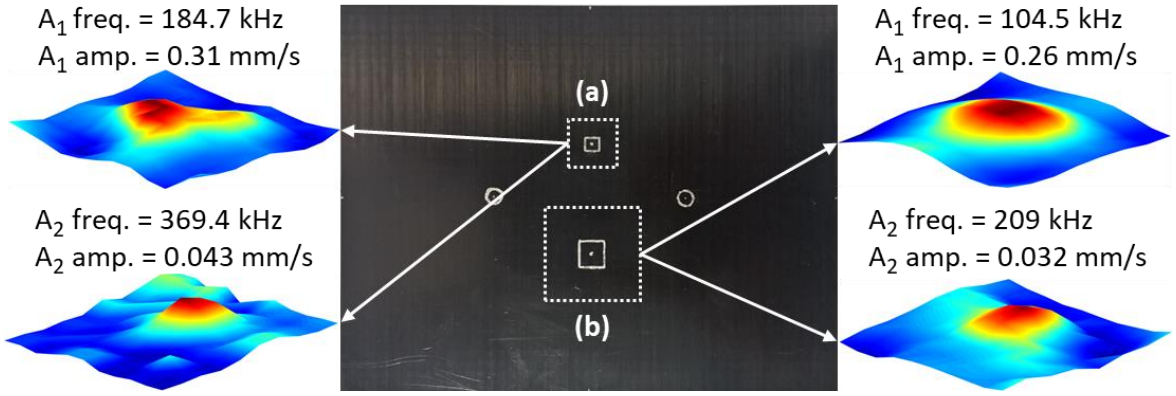

Figure 10: 3D representation of the out-of-plane vibrational velocity around the location of the small (a) and the big (b) artificial damage at the fundamental and second harmonic frequencies.

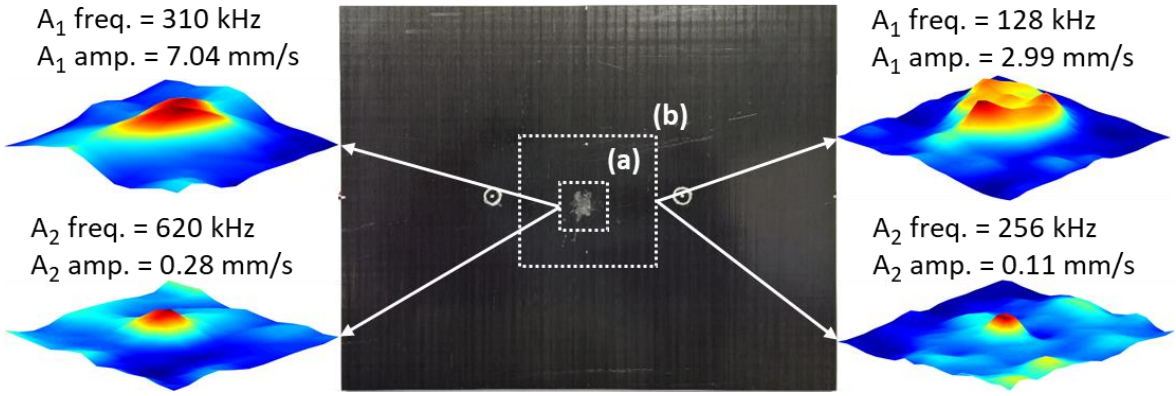

Figure 11: 3D representation of the out-of-plane vibrational velocity around the location of the 10 J (a) and the 15 J (b) impact damage at the fundamental and second harmonic frequencies.

4.2 Nonlinear Wave Modulation Experiment

According to the process described in Section 3.3.1 and based on the amplitude of the sidebands in the ultrasonic response of the ID-plate, the effect of nonlinear wave modulation was evaluated by transmitting periodic waves from PZT1 at f_1=18 kHz and from PZT2 at f_2=192 kHz. The UD-laminate was also subject to multiple-frequency using the same f_1 and f_2 frequencies. For an input voltage of 60 V applied to PZT1 and 50 V applied to PZT2, the received signal amplitude at 18 kHz and 192 kHz was lower in the case of the ID-plate (Figure 12). As previously explained, that was reasonable because an amount of the input wave energy was transferred from the f_1 and f_2 signals to the sidebands. In addition, first-order sidebands were only presented in the spectrum of the ID-laminate at 174 kHz ($f_- = f_2 - f_1$) and 210 kHz ($f_+ = f_2 + f_1$), and this confirmed its nonlinear response under wave modulation. Also, in the ID-plate, by increasing the input voltage to PZT1 from 60 to 100 V and keeping the input voltage to PZT2 constant at 50 V, the amplitude of the f_1 harmonic and the two sidebands increased proportionally by around 70%, whereas the amplitude of f_2 harmonic remained almost constant (Figure 13). This verified that the existence of sidebands was attributed to the wave modulation by the f_1 signal. For all five values of the input voltage, the amplitude of sidebands was three orders of magnitude smaller than the amplitude of f_2 harmonic and one order of magnitude smaller than the amplitude of f_1 harmonic. The amplitude of the right sideband f_+ was on average 27% greater than the left one f_-.

Regarding to the LV experiments, the three-dimensional plots of the results illustrated in Figure 14 proved that the out-of-plane vibrational velocity at f_1, f_2, f_+ and f_- was always higher at the impact location. These results were in agreement with the results from the NEWS experiments with respect to the amplitude difference between the sidebands and the f_1, f_2 harmonics. Particularly, the amplitude of the right sideband, f_+, was around 30% greater than the amplitude of the left one, f_-. Moreover, the amplitude of both sidebands was two orders of magnitude smaller than the amplitude of the f_2 harmonic and one order of magnitude smaller than the amplitude of the f_1 harmonic. Hence, the LV experiments confirmed that the detection of intermodulation products was associated with the nonlinear elastic behaviour of the damaged plate.

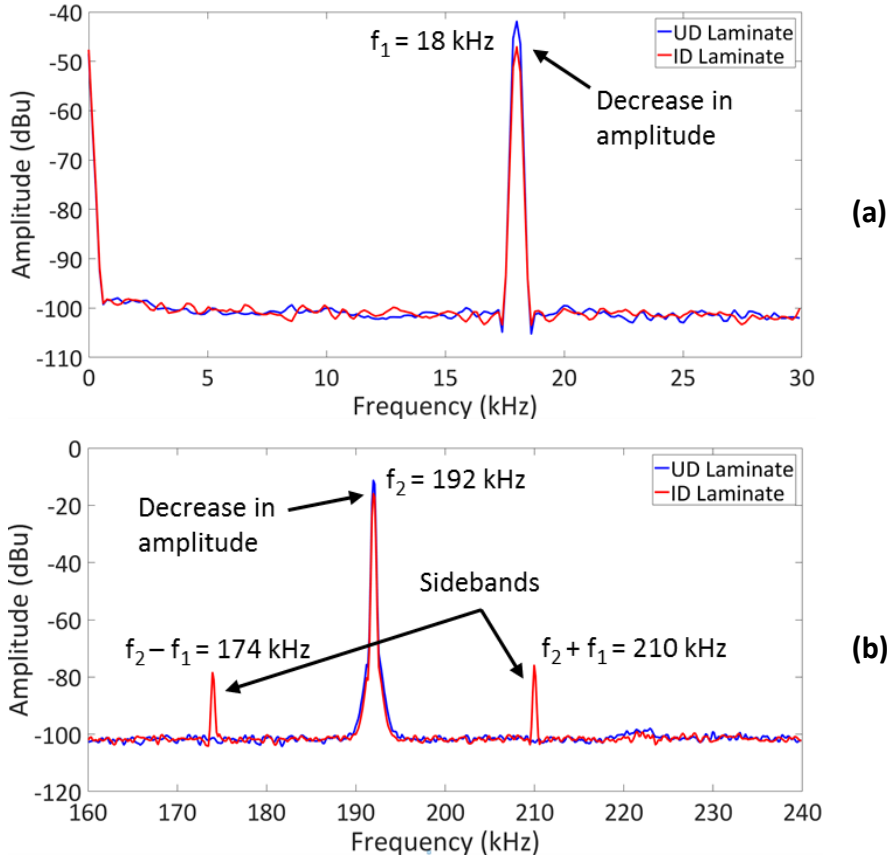

Figure 12: Amplitude of the received signal in the UD-laminate and the ID-laminate at f_1 (a) and at f_2 and $f_2 \pm f_1$ (b) - Input signal voltage to PZT2 = 50 V and to PZT1 = 60 V.

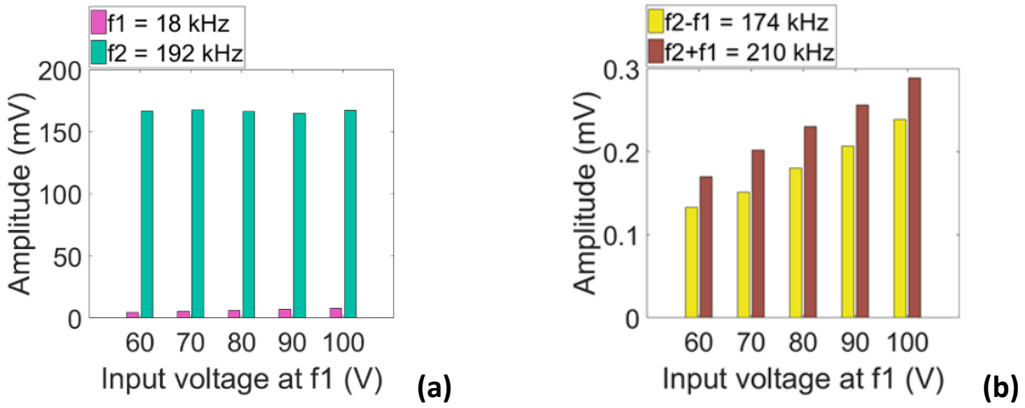

Figure 13: Amplitude of the received signal in the ID-laminate at f_1 & f_2 (a) and at $f_2 \pm f_1$ (b) - Input signal voltage to PZT2 = 50 V and to PZT1 = 60, 70, 80, 90 and 100 V.

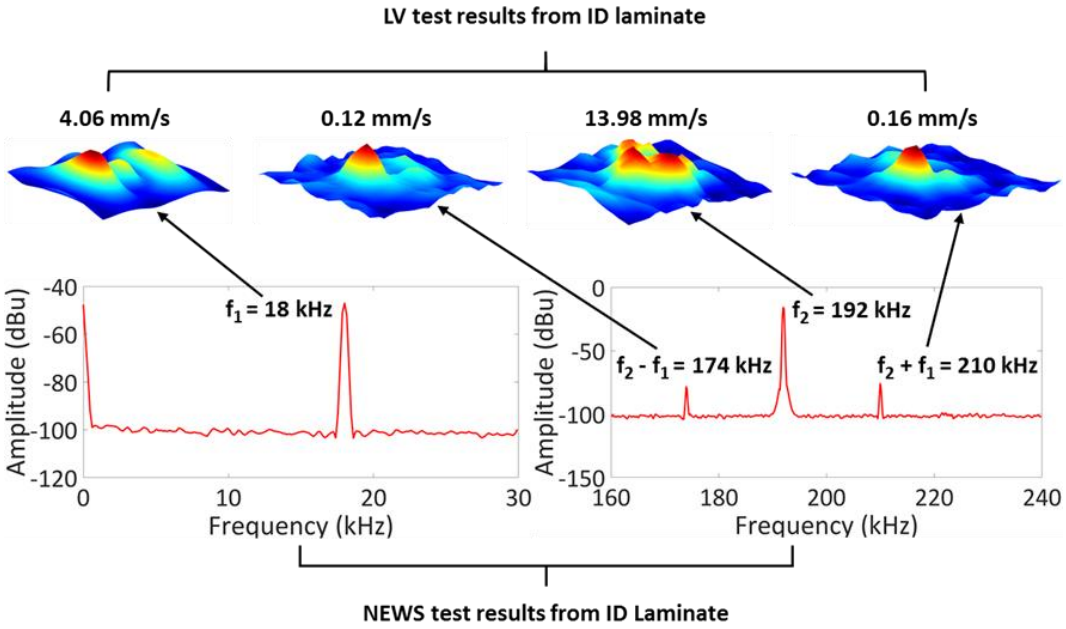

Figure 14: 3D representation of the out-of-plane vibrational velocity at the location of the impact damage at f_1, f_2 and $f_2 \pm f_1$.

5 Conclusions

The aim of this study was to demonstrate the damage detection capabilities of directly embedded PZTs in CFRP composites with nonlinear ultrasound. PZTs were electrically insulated using a novel embedding technique in which the conductive surface of each transducer was covered by a single layer of woven E-glass fibre fabric. The ultrasonic response of CFRP plates with areas of artificial (polymeric film patches) and real (impact) damage of different size was compared with the response of an intact plate, using pairs of embedded PZTs.

In the first part of experiments, one PZT was used as the transmitter and the other as the receiver of ultrasonic elastic waves. Excitation of each damage type (artificial and impact) was achieved at a different input signal frequency. This was detected based on the generation of A_2 harmonics in the frequency spectrum of the received signal, and the amplitude of these harmonics was found to increase with increasing input signal voltage.

Furthermore, by using an LV, the out-of-plane vibration velocity of the laminate surface was also recorded at A_1 and A_2 frequencies and found to be greater at the damage location. In the second experimental part, nonlinear wave modulation was employed for defect detection. The undamaged and impacted plates were excited by ultrasonic waves

transmitted from both PZTs at different frequencies (f_1 and f_2). An external transducer was used as the receiver. The nonlinear response of the impacted laminate was verified by the presence of first-order sidebands ($f_+ = f_2 + f_1$ and $f_- = f_2 - f_1$) in the frequency spectrum of the received signal, and the amplitude of sidebands was increasing with rising input voltage at f_1. Again, by scanning the material response at f_1, f_2, f_+ and f_- frequencies with the LV, the out-of-plane vibrational velocity of the laminate surface was confirmed higher at the impact location.

The experimental results revealed that multiple damage locations of different size in composite laminates were successfully detected. Moreover, it was demonstrated that these embedded PZTs were capable of detecting in-plane delamination which is usually related to manufacturing errors, but also through-thickness damage (multi-layer fibre and matrix cracking) that commonly occur after impacts. Therefore, it is concluded that the proposed configuration of embedded PZTs has the potential to be used for the development of "smart" composite structures to enable in-situ and real-time ultrasonic inspection of satellite components. Future challenges are to implement optimal signal transmission/reception and data storage strategies for real satellite operations in order to make the proposed NEWS technology with embedded PZT transducers compliant with other spacecraft sub-systems.

References

1. Francesconi, A., Giacomuzzo, C., Kibe, S., Nagao, Y., & Higashide, M. (2012). Effects of high-speed impacts on CFRP plates for space applications. *Advances in Space Research*, 50(5), 539-548.
2. Schonberg, W. P., & Walker, E. J. (1994). Hypervelocity impact of dual-wall space structures with graphite/epoxy inner walls. *Composites Engineering*, 4(10), 1045-1054.
3. Schonberg, W. P. (2017). Studies of hypervelocity impact phenomena as applied to the protection of spacecraft operating in the MMOD environment. *Procedia Engineering*, 204(1), 4-42.
4. Schonberg, W. P. (2010). Protecting Earth-orbiting spacecraft against micro-meteoroid/orbital debris impact damage using composite structural systems and materials: An overview. *Advances in Space Research*, 45(6), 709-720.
5. Yashiro, S., Ogi, K., Nakamura, T., & Yoshimura, A. (2013). Characterization of high-velocity impact damage in CFRP laminates: Part I–Experiment. *Composites Part A: Applied Science and Manufacturing*, 48(1), 93-100.
6. Christiansen, E. L., Arnold, J., Corsaro, B., et al. (2009). *Handbook for designing MMOD protection* (TM-2009-214785, p. 13). Houston: NASA Johnson Space Center.
7. Christiansen, E. L. (2003). *Meteoroid/debris shielding* (TP−2003-210788, p. 75). Houston: NASA Johnson Space Center.

8. Briks, A. S., & Green, R. E. (1991). *Nondestructive Testing Handbook: Ultrasonic Testing*. Ohio: American Society for Nondestructive Testing.
9. Amerini, F., & Meo, M. (2011). Structural health monitoring of bolted joints using linear and nonlinear acoustic/ultrasound methods. *Structural Health Monitoring*, 10(6), 659-672.
10. Cesari, F., Dal Re, V., Minak, G., & Zucchelli, A. (2007). Damage and residual strength of laminated carbon–epoxy composite circular plates loaded at the centre. *Composites Part A: Applied Science and Manufacturing*, 38(4), 1163-1173.
11. R'Mili, M., Moevus, M., & Godin, N. (2008). Statistical fracture of E-glass fibres using a bundle tensile test and acoustic emission monitoring. *Composites Science and Technology*, 68(7-8), 1800-1808.
12. Oskouei, A. R., & Ahmadi, M. (2010). Acoustic emission characteristics of mode I delamination in glass/polyester composites. *Journal of Composite Materials*, 44(7), 793-807.
13. Holland, S. D., & Reusser, R. S. (2016). Material evaluation by infrared thermography. *Annual Review of Materials Research*, 46(1), 287-303.
14. Almond, D. P., Angioni, S. L., & Pickering, S. G. (2017). Long pulse excitation thermographic non-destructive evaluation. *NDT & E International*, 87(1), 7-14.
15. De Moura, M. F., & Marques, A. T. (2002). Prediction of low velocity impact damage in carbon–epoxy laminates. *Composites Part A: Applied Science and Manufacturing*, 33(3), 361-368.
16. Wright, P., Fu, X., Sinclair, I., & Spearing, S. M. (2008). Ultra high resolution computed tomography of damage in notched carbon fiber-epoxy composites. *Journal of Composite Materials*, 42(19), 1993-2002.
17. Aymerich, F., & Staszewski, W. J. (2010). Impact damage detection in composite laminates using nonlinear acoustics. *Composites Part A: Applied Science and Manufacturing*, 41(9), 1084-1092.
18. Su, Z., Ye, L., & Lu, Y. (2006). Guided Lamb waves for identification of damage in composite structures: A review. *Journal of Sound and Vibration*, 295(3-5), 753-780.
19. Zagrai, A., Donskoy, D., Chudnovsky, A., & Golovin, E. (2008). Micro-and macroscale damage detection using the nonlinear acoustic vibro-modulation technique. *Research in Nondestructive Evaluation*, 19(2), 104-128.
20. Boccardi, S., Calla, D. B., Ciampa, F., & Meo, M. (2018). Nonlinear elastic multi-path reciprocal method for damage localisation in composite materials. *Ultrasonics*, 82, 239-245.
21. Buck, O., Morris, W. L., & Richardson, J. M. (1978). Acoustic harmonic generation at unbonded interfaces and fatigue cracks. *Applied Physics Letters*, 33(5), 371-373.
22. Polimeno, U., Meo, M., Almond, D. P., & Angioni, S. L. (2010). Detecting low velocity impact damage in composite plate using nonlinear acoustic/ultrasound methods. *Applied Composite Materials*, 17(5), 481-488.
23. Solodov, I. (2014). Resonant acoustic nonlinearity of defects for highly-efficient nonlinear NDE. *Journal of Nondestructive Evaluation*, 33(2), 252-262.
24. Ciampa, F., Pickering, S. G., Scarselli, G., & Meo, M. (2017). Nonlinear imaging of damage in composite structures using sparse ultrasonic sensor arrays. *Structural Control and Health Monitoring*, 24(5), 1911.
25. Scarselli, G., Ciampa, F., Nicassio, F., & Meo, M. (2017). Non-linear methods based on ultrasonic waves to analyse disbonds in single lap joints. *Proceedings of the Institution of Mechanical Engineers, Part C: Journal of Mechanical Engineering Science*, 231(16), 3066-3076.
26. Fierro, G. P. M., & Meo, M. (2019). A combined linear and nonlinear ultrasound time-domain approach for impact damage detection in composite structures using a constructive nonlinear array technique. *Ultrasonics*, 93(1), 43-62.
27. Ciampa, F., & Meo, M. (2012). Nonlinear elastic imaging using reciprocal time reversal and third order symmetry analysis. *The Journal of the Acoustical Society of America*, 131(6), 4316-4323.

28. Liu, Z., Yu, H., Fan, J., Hu, Y., He, C., & Wu, B. (2015). Baseline-free delamination inspection in composite plates by synthesizing non-contact air-coupled Lamb wave scan method and virtual time reversal algorithm. *Smart Materials and Structures*, 24(4), 045014.

29. Lints, M., Dos Santos, S., & Salupere, A. (2017). Solitary waves for non-destructive testing applications: Delayed nonlinear time reversal signal processing optimization. *Wave Motion*, 71(1), 101-112.

30. Van Den Abeele, K. A., Johnson, P. A., & Sutin, A. (2000). Nonlinear elastic wave spectroscopy (NEWS) techniques to discern material damage, part I: nonlinear wave modulation spectroscopy (NWMS). *Journal of Research in Nondestructive Evaluation*, 12(1), 17-30.

31. Chrysochoidis, N. A., Barouni, A. K., & Saravanos, D. A. (2011). Delamination detection in composites using wave modulation spectroscopy with a novel active nonlinear acousto-ultrasonic piezoelectric sensor. *Journal of Intelligent Material Systems and Structures*, 22(18), 2193-2206.

32. Klepka, A., Pieczonka, L., Staszewski, W. J., & Aymerich, F. (2014). Impact damage detection in laminated composites by non-linear vibro-acoustic wave modulations. *Composites Part B: Engineering*, 65(1), 99-108.

33. Pieczonka, L., Klepka, A., Martowicz, A., & Staszewski, W. J. (2015). Nonlinear vibroacoustic wave modulations for structural damage detection: an overview. *Optical Engineering*, 55(1), 011005.

34. Dionysopoulos, D., Fierro, G. P. M., Meo, M., & Ciampa, F. (2018). Imaging of barely visible impact damage on a composite panel using nonlinear wave modulation thermography. *NDT & E International*, 95(1), 9-16.

35. Fierro, G. P. M., & Meo, M. (2018). IWSHM 2017: Structural health monitoring of the loosening in a multi-bolt structure using linear and modulated nonlinear ultrasound acoustic moments approach. *Structural Health Monitoring*, 17(6), 1349-1364.

36. Vila, M., Vander Meulen, F., Dos Santos, S., Haumesser, L., & Matar, O. B. (2004). Contact phase modulation method for acoustic nonlinear parameter measurement in solid. *Ultrasonics*, 42(1-9), 1061-1065.

37. Solodov, I., Rahammer, M., Derusova, D., & Busse, G. (2015). Highly-efficient and noncontact vibro-thermography via local defect resonance. *Quantitative InfraRed Thermography Journal*, 12(1), 98-111.

38. Post, W., Kersemans, M., Solodov, I., Van Den Abeele, K., García, S. J., & Van Der Zwaag, S. (2017). Non-destructive monitoring of delamination healing of a CFRP composite with a thermoplastic ionomer interlayer. *Composites Part A: Applied Science and Manufacturing*, 101(1), 243-253.

39. Segers, J., Kersemans, M., Hedayatrasa, S., Calderon, J., & Van Paepegem, W. (2018). Towards in-plane local defect resonance for non-destructive testing of polymers and composites. *NDT & E International*, 98(1), 130-133.

40. Haupert, S., Renaud, G., & Schumm, A. (2017). Ultrasonic imaging of nonlinear scatterers buried in a medium. *NDT & E International*, 87(1), 1-6.

41. Solodov, I., & Busse, G. (2012). Multi-frequency defect selective imaging via nonlinear ultrasound. In *Acoustical imaging: Conference Series* (Vol. 31, p. 385-398). Springer.

42. Van Den Abeele, K. A., Carmeliet, J., Ten Cate, J. A., & Johnson, P. A. (2000). Nonlinear elastic wave spectroscopy (NEWS) techniques to discern material damage, Part II: Single-mode nonlinear resonance acoustic spectroscopy. *Journal of Research in Nondestructive Evaluation*, 12(1), 31-42.

43. Polimeno, U., & Meo, M. (2009). Detecting barely visible impact damage detection on aircraft composites structures. *Composite Structures*, 91(4), 398-402.

44. Chakrapani, S. K., Barnard, D. J., & Dayal, V. (2015). Influence of fiber orientation on the inherent acoustic nonlinearity in carbon fiber reinforced composites. *The Journal of the Acoustical Society of America*, 137(2), 617-624.

45. Solodov, I. (2018). Nonlinear frequency shift and decay of local damage resonance: CAN Version. In *Proceedings of Meetings on Acoustics* (Vol. 34, p. 065001). Acoustical Society of America.

46. Tang, H. Y., Winkelmann, C., Lestari, W., & La Saponara, V. (2011). Composite structural health monitoring through use of embedded PZT sensors. *Journal of Intelligent Material Systems and Structures*, 22(8), 739-755.

47. Klepka, A., Strączkiewicz, M., Pieczonka, L., Staszewski, W. J., Gelman, L., Aymerich, F., & Uhl, T. (2015). Triple correlation for detection of damage-related nonlinearities in composite structures. *Nonlinear Dynamics*, 81(1-2), 453-468.

48. Liu, X., Bo, L., Yang, K., et al. (2018). Locating and imaging contact delamination based on chaotic detection of nonlinear Lamb waves. *Mechanical Systems and Signal Processing*, 109(1), 58-73.

49. Masmoudi, S., El Mahi, A., & Turki, S. (2015). Use of piezoelectric as acoustic emission sensor for in situ monitoring of composite structures. *Composites Part B: Engineering*, 80(1), 307-320.

50. Mall, S. (2002). Integrity of graphite/epoxy laminate embedded with piezoelectric sensor/actuator under monotonic and fatigue loads. *Smart Materials and Structures*, 11(4), 527-533.

51. Paget, C. A., Levin, K., & Delebarre, C. (2002). Actuation performance of embedded piezoceramic transducer in mechanically loaded composites. *Smart Materials and Structures*, 11(6), 886-891.

52. Su, Z., Wang, X., Chen, Z., Ye, L., & Wang, D. (2006). A built-in active sensor network for health monitoring of composite structures. *Smart Materials and Structures*, 15(6), 1939-1949.

53. Wooh, S. C., & Wei, C. (1999). A high-fidelity ultrasonic pulse-echo scheme for detecting delaminations in composite laminates. *Composites Part B: Engineering*, 30(5), 433-441.

54. Andreades, C., Mahmoodi, P., & Ciampa, F. (2018). Characterisation of smart CFRP composites with embedded PZT transducers for nonlinear ultrasonic applications. *Composite Structures*, 206(1), 456-466.

55. Smith, R. A. (2009). Composite defects and their detection. *Materials Science and Engineering*, 3(1), 103-143.

56. Soutis, C., & Curtis, P. T. (1996). Prediction of the post-impact compressive strength of CFRP laminated composites. *Composites Science and Technology*, 56(6), 677-684.

57. Melchor, J., Parnell, W. J., Bochud, N., Peralta, L., & Rus, G. (2019). Damage prediction via nonlinear ultrasound: A micro-mechanical approach. *Ultrasonics*, 93(1), 145-155.

58. Ciampa, F., Scarselli, G., & Meo, M. (2017). On the generation of nonlinear damage resonance intermodulation for elastic wave spectroscopy. *The Journal of the Acoustical Society of America*, 141(4), 2364-2374.

59. Landau, L. D. & Lifshitz, E. M. (1986). *Theory of Elasticity* (Vol. 7, p. 476). 3rd ed. Oxford: Pergamon.

60. Munoz, R., Bochud, N., Rus, G., et al. (2015). Model-based damage evaluation of layered CFRP structures. In *AIP Conference Proceedings* (Vol. 1650, p. 1170-1177). AIP Publishing.

61. Amura, M., Meo, M., & Amerini, F. (2011). Baseline-free estimation of residual fatigue life using a third order acoustic nonlinear parameter. *The Journal of the Acoustical Society of America*, 130(4), 1829-1837.

62. Fierro, G. P. M. (2014). *Development of nonlinear ultrasound techniques for multidisciplinary engineering applications*. Thesis (Doctoral), University of Bath.

63. Meo, M., Polimeno, U., & Zumpano, G. (2008). Detecting damage in composite material using nonlinear elastic wave spectroscopy methods. *Applied composite materials*, 15(3), 115-126.

64. Fierro, G. P. M., & Meo, M. (2015). Residual fatigue life estimation using a nonlinear ultrasound modulation method. *Smart Materials and Structures*, 24(2), 025040.

65. Konka, H. P., Wahab, M. A., & Lian, K. (2012). On mechanical properties of composite sandwich structures with embedded piezoelectric fiber composite sensors. *Journal of Engineering Materials and Technology*, 134(1).: 011010.

66. Yoo, S., Khatibi, A. A., & Kandare, E. (2014). Durability of embedded PZTs in structural health monitoring systems under cyclic loading. In *Advanced Materials Research* (Vol. 891, p. 1255-1260). Trans Tech Publications Ltd.

Chapter 5

Tensile-Mode Fatigue of Smart CFRP Composites and Nonlinear Ultrasonic Monitoring of Damage

In the research article (Paper III) of this chapter, the "smart" CFRP laminates proposed in Chapter 3 and Chapter 4 were subject to static and cyclic tensile tests to investigate the effect of the embedded PZT transducers on the mechanical performance of the laminates. In addition, this study investigated the durability of the transducers under repeated loading, and their capability to monitor the evolution of damage in the material.

In particular, tensile and fatigue tests were performed using both pristine and impact damaged CFRP specimens containing a pair of glass fibre insulated sensors (G-specimens). These tests were also completed using undamaged and impacted plain samples (P-specimens), which experienced the same type of failure as G-specimens. A statistical comparison of the results suggested that the G-specimens and P-specimens failed on average at the same tensile stress and extension, as well as the same number of fatigue cycles. This was valid for both cases of undamaged and damaged samples. The transducers in some of the impacted G-specimens were used to conduct nonlinear ultrasonic experiments at regular steps of fatigue cycles, and at every step the functionality of the sensors was inspected by measuring their electrical capacitance. The level of material nonlinearities was quantified based on the value of $A_2/{A_1}^2$ ratio (i.e. relative parameter β) from the ultrasonic response recorded by the sensors. The results verified that the transducers remained functional for the biggest part of the fatigue life of the samples, and the value of β was found to increase with increasing number of fatigue cycles proving that the growth of impact damage could be monitored with these internal sensors.

The "Statement of Authorship" form and Paper III are provided on the following pages. The publication presented in this chapter was the last part of the thesis related to the development of "smart" CFRP laminates. However, it should be mentioned that another research contribution has been the use of the proposed configuration of embedded

PZT disks in two collaboration studies which confirmed the suitability of this solution for different SHM applications [198, 199]. In fact, these two studies showed for the first time that the so-called time reversal (TR) method could be applied with embedded transducers. The studies also verified that the design of "smart" CFRP composites could be used in SHM systems requiring the localisation of low or high energy impacts, or even the determination of the velocity and direction of the impacting particle. A brief explanation of each study is provided below, before moving to Paper III.

In the first study, De Simone et al. created a system named Smart Composite Orbital Debris Detector (SCODD), as a proof-of-concept for the characterisation of impact events on spacecraft components from orbital debris particles [198]. According to Figure 1a, the design consisted of two thin parallel CFRP laminates fastened securely one on top of the other. Each laminate included three such internal sensors surrounding the monitored area inside which calibration impacts (baseline data) were originally recorded at the nodes of a square grid (Figure 1b). The SCODD was proved capable of estimating the locations at which the particle penetrated the two plates by processing the acoustic signals captured by the sensors during the impact, using the TR method. In addition, the direction of the propagating particle was determined from the estimated impact positions. Moreover, the particle velocity was calculated using the previously measured speed of waves in the plates and the time delay in signal capturing between the sensors sharing the same coordinates on the two plates.

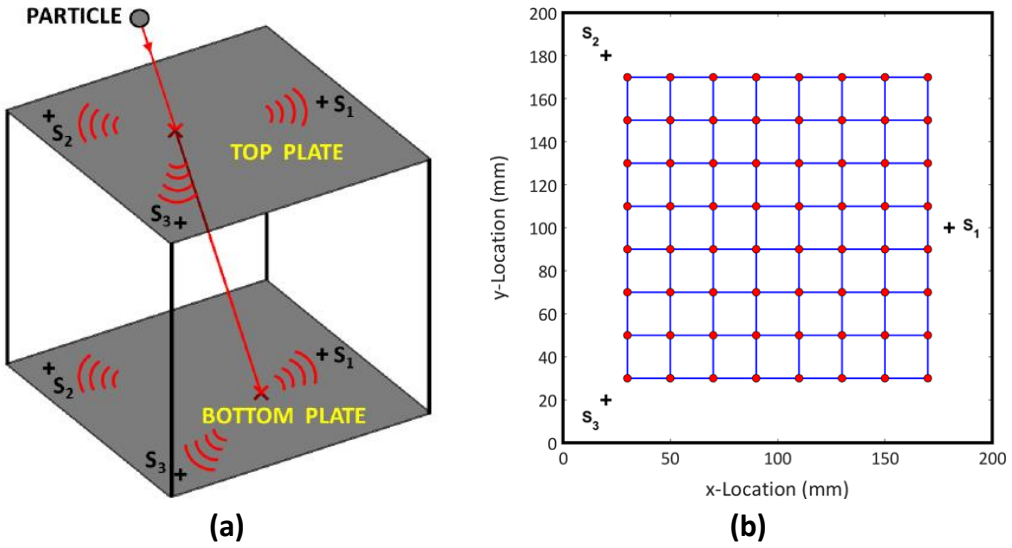

Figure 1: Illustration of the SCODD system (a) and the arrangement of sensors around the impact monitoring grid (b) [198].

In the second study, Coles et al. developed a new topological algorithm named Minimum Average (MA) to enable more reliable and precise localisation of impacts on composite plates when using the TR method [199]. Application of the MA method was demonstrated on CFRP plates instrumented with four embedded PTZ disks (Figure 2a) using the suggested layout with glass fibre insulation. The MA algorithm aimed at detecting with enhanced accuracy the position of impact within the chosen cell on the monitoring grid (Figure 2b), especially for impacts occurring at points other than the centre of the cell. This would also help in minimising the localisation error in cases where the cell determined by the TR method is next to the actual cell of impact, because the MA method would shift the estimated impact point inside the chosen cell towards the actual cell. The effectiveness of MA method was experimentally tested on intact CFRP plates and plates with permanent damage, and the results showed accurate localisation of both single and double bouncing impacts.

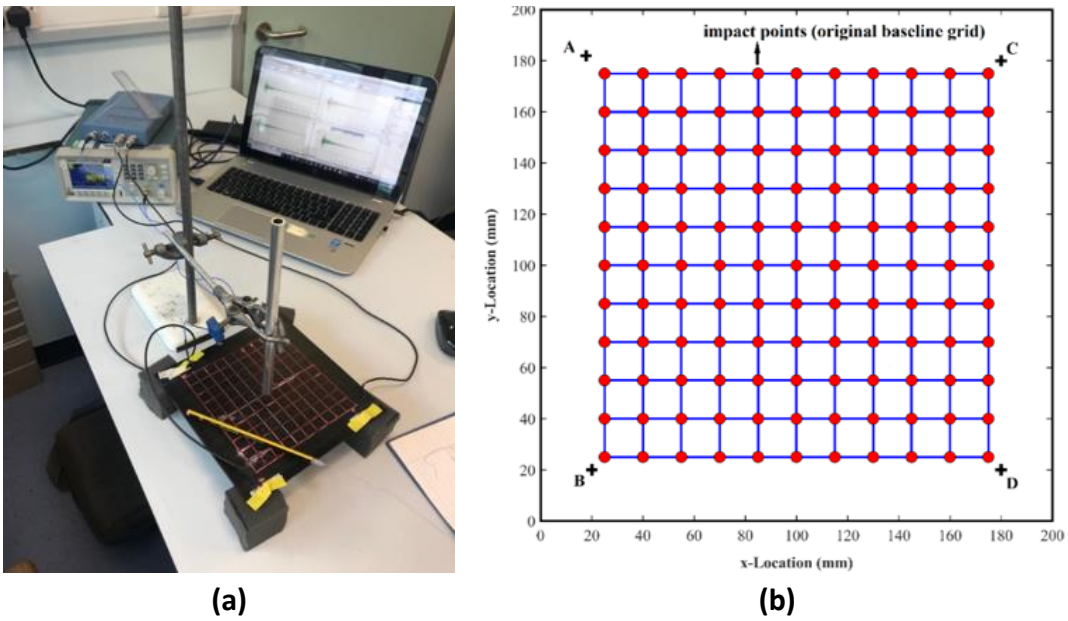

Figure 2: Illustration of the set-up used to test the MA method (a) and the arrangement of sensors around the impact monitoring grid (b) [199].

This declaration concerns the article entitled:			
Tensile and fatigue testing of impacted smart CFRP composites with embedded PZT transducers for nonlinear ultrasonic monitoring of damage evolution			
Publication status			
Draft manuscript ☐ Submitted ☐ Accepted ☐ Published ☒			
Publication details (reference)			
Andreades, C., Meo, M., & Ciampa, F. (2020). Tensile and fatigue testing of impacted smart CFRP composites with embedded PZT transducers for nonlinear ultrasonic monitoring of damage evolution. *Smart Materials and Structures,* 29(5), 055034.			
Candidate's contribution to the paper (detailed, and also given as a percentage)			
Formulation of ideas: 80% The idea to investigate how the fatigue performance of CFRP laminates is affected by the presence of the specific type of embedded PZT transducers used in my previous studies, was suggested by my former supervisor Dr Francesco Ciampa. I proposed the idea of performing fatigue tests on specimens with impact damage between an active (wired) pair of sensors, in order to assess the functionality of sensors under dynamic stress conditions, as well as to check if such embedded transducers were capable of monitoring the growth of impact damage under repeated loading.			
Design of methodology: 100% I chose the design, lay-up and material of the composite samples along with the positions of the PZT transducers and the impact damage.			
Experimental work: 100% I manufactured the composite specimens, introduced the impact damage to the samples, performed the mechanical and ultrasonic tests, recorded the capacitance measurements and collected the data.			
Presentation of data in journal format: 95% I processed the obtained data, created the figures, chose the structure of the paper and wrote the manuscript. My supervisors provided feedback on the above and supported the process of submission and review.			
Statement from Candidate			
This paper reports on original research I conducted during the period of my Higher Degree by Research candidature.			
Signed		**Date**	02/10/2020

Tensile and fatigue testing of impacted smart CFRP composites with embedded PZT transducers for nonlinear ultrasonic monitoring of damage evolution

Christos Andreades[1], Michele Meo[1], Francesco Ciampa[2]

[1]Department of Mechanical Engineering, University of Bath, Bath, BA2 7AY, UK

[2]Department of Mechanical Engineering Sciences, University of Surrey, Guildford, GU2 7XH, UK

Abstract

Ultrasonic systems based on "smart" composite structures with embedded sensor networks can reduce both inspection time and costs of aircraft components during maintenance or in-service. This paper assessed the tensile strength and fatigue endurance of carbon fibre reinforced plastic (CFRP) laminates with embedded piezoelectric (PZT) transducers, which were covered with glass fibre patches for electrical insulation. This sensor layout was proposed and tested by the authors in recent studies, proving its suitability for nonlinear ultrasonic detection of material damage without compromising the compressive, flexural or interlaminar shear strength of the "smart" CFRP composite. In this work, CFRP samples including PZTs (G-specimens) were tested against plain samples (P-specimens), and their mean values of tensile strength and fatigue cycles to failure were found to be statistically the same (910MPa and 713,000 cycles) using the one-way analysis of variance method. The same tests on P- and G-specimens with barely visible impact damage (BVID) showed that the corresponding group means were also the same (865MPa and 675,000 cycles). Nonlinear ultrasonic experiments on impacted G-samples demonstrated that embedded PZTs could monitor the growth of BVID during fatigue testing, for a minimum of 480,000 cycles. This was achieved by calculating an increase of nearly two orders of magnitude in the ratio of second-to-fundamental harmonic amplitude. Finally, PZT transducers were confirmed functional under cyclic loading up to ~70% of sample's life, since their capacitance remained constant during ultrasonic testing.

1 Introduction

A large percentage (~50%) of metal components that were traditionally used in aerospace structures has been replaced with fibre reinforced plastic (FRP) composite materials [1, 2]. The reason is the high strength and stiffness, low weight, corrosion resistance and fatigue performance that FRP materials exhibit, enabling the development of structures with advanced durability and safety [3]. Carbon fibre reinforced plastic (CFRP) is the most commonly used composite material as it offers the best balance of the above properties. However, the biggest drawback of CFRP parts is that, unlike metallic components, they can sustain internal damage due to impact events with nearly invisible marks on their surface, known as barely visible impact damage (BVID) [4]. Normally, BVID from bird strikes, hailstorms and tool drops is characterised by delamination, matrix micro-cracking and fibre failure [5]. These material flaws tend to evolve with high rates under operating dynamic stresses and, thus, safety regulations in aviation require frequent inspections of composite structures [6]. These inspections can result in time delays and high costs, especially when the aircrafts must be set out of service for visual examination or scanning using various non-destructive evaluation (NDE) techniques.

Examples of NDE inspection include methods relying on ultrasonic wave propagation [7, 8], acoustic emission [9, 10], electromagnetic radiation [11, 12], thermal imaging [13, 14] and shearography [15, 16]. Although NDE methods are effective in detecting material damage, they are not ideal for in-service inspection due to size and weight limitations [17]. As an alternative, the fabrication of “smart” composites with incorporated networks of piezoelectric lead zirconate titanate (PZT) sensors has gained considerable attention because it enables the conversion of ultrasonic NDE techniques into structural health monitoring (SHM) systems for in-flight inspection of aerospace structures [18]. Ultrasonic methods relying on the examination of the nonlinear features exhibited in the material response have been proved more sensitive and effective in the detection of micro-cracks than linear ultrasonic techniques [19-22]. Nonlinear effects such as (a) higher harmonic and sub-harmonic generation [23-28], (b) wave modulation [29-33] and (c) nonlinear resonance [34-37] can be generated in the material spectrum due to clapping and/or frictional movement of the crack surfaces caused by their interaction with propagating waves. Among these phenomena, higher harmonic generation and, particularly, second harmonic generation, is widely considered an

indication of damage existence. With this method, the level of material nonlinearity can be quantified based on the second-order elastic coefficient known as the parameter β, which is proportional to the ratio of second-to-fundamental harmonic amplitude [38]. This ratio has already been found to increase with growing damage size [39-41].

In regard to the fabrication of "smart" CFRP composites for ultrasonic SMH monitoring, many studies focused on the use of internally rather than externally bonded PZT transducers, in order to eliminate the need for expensive and heavy sensor shielding, and to minimise sensor wear from exposure to harsh environmental conditions [42-46]. On the other hand, PZTs inside CFRP composites must have insulated electrodes to prevent direct contact with carbon fibres. The usual practice in literature involves separation of the sensor from the composite plies using polymeric layers such as Kapton film, but this can lead to inappropriate ply adhesion and eventually delamination with serious effects on the structural integrity of the material [19, 47, 48].

In a previous study from the authors [49], a novel material processing method was proposed for the electrical insulation of PZT disks that were directly inserted between the layers of CFRP plates. This method relied on covering the top conductive side of the PZTs with single-layer patches of dry E-glass fibre fabric to avoid contact with carbon fibres. The "smart" CFRP composite was subject to monotonic (static) mechanical testing including short-beam and long-beam three-point bending tests, and compression tests. The mean values of interlaminar shear, flexural and compressive strength were found to be equal to the means of plain CFRP composites. Although these results were promising, one of the main requirements for "smart" SHM composites is their durability under dynamic loading conditions, which can progressively damage the sensors and their interconnections. Available studies on CFRP composites with internal PZTs examined the functionality of sensors during fatigue testing by recording the change in output voltage or signal amplitude [50-53]. However, the monitoring of damage evolution with increasing number of fatigue cycles was not accomplished, and this is one of the main areas of interest of this paper.

In particular, this study focused on the assessment of (i) the mechanical performance of the "smart" CFRP composite under cyclic loading, and (ii) the capability of the embedded PZTs to monitor the increase in damage size with repeated loading based on nonlinear ultrasonic testing. To achieve these two objectives, impact damaged CFRP samples containing pairs of glass fibre insulated PZTs (G-specimens) were subject to

tension-tension fatigue testing, and their endurance was compared with that of plain samples (P-specimens). The design of the test samples is shown in Figure 3. Static tensile testing was also required as part of the fatigue testing procedure, for the determination of the material strength. That was an opportunity to study the tensile strength of the G-specimens against that of P-specimens. In relation to the nonlinear ultrasonic experiments, the PZTs inside the G-specimens were used for the propagation of elastic waves through the material, and the calculation of the nonlinear parameter β at different stages of fatigue testing.

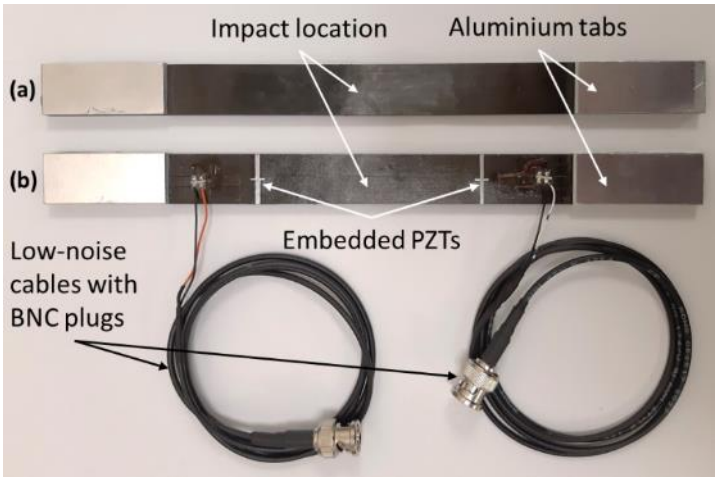

Figure 3: Illustration of P-specimen (a) and G-specimen (b) used in this study.

2 Second-Order Acoustic Nonlinearity Parameter

Tight cracks with contact surfaces inside composite plates can interact with propagating ultrasonic waves. The compressive part of the waves tends to close the crack interface whereas the tensile part to open it. Hence, cracks behave as half-wave rectifiers allowing only the compressive part of the wave field to propagate through. This means that the material stiffness at the damage location is higher in compression and lower in tension, and this asymmetry changes the local stress-strain relationship into nonlinear [54]. The contact ("clapping") between the crack surfaces can generate new waves of twice the frequency of the incident waves, which are detectable in the form of even higher harmonics. Conversely, the friction between the crack surfaces due to slipping ("rubbing") motion changes the local stiffness symmetrically, leading to the generation of odd higher harmonics [54]. Nevertheless, in literature, the detection of second-order frequency harmonics has been broadly associated with the presence of defects [55, 56],

as it allows direct calculation of the material nonlinearity. Briefly, the elastodynamic wave equation describing the propagation of one-dimensional longitudinal waves in the x-direction of the material has a second order approximation of

$$\frac{\partial^2 u(x,t)}{\partial t^2} - c^2 \frac{\partial^2 u(x,t)}{\partial x^2} = \beta c^2 \left(\frac{\partial u(x,t)}{\partial x}\right)\left(\frac{\partial^2 u(x,t)}{\partial x^2}\right), \quad (1)$$

where $u(x,t)$ and c are the displacement and speed of waves respectively, and parameter β is an elastic coefficient describing the second-order material nonlinearities. By solving equation (1) using a first-order perturbation method, β can be expressed as [57]

$$\beta = \frac{8A_2}{{A_1}^2 x\, k^2}\,. \quad (2)$$

In equation (2), A_1 and A_2 are equal to the wave amplitude at the fundamental and second harmonic frequencies, x is the wave propagation distance inside the material and k is the wave number. Considering that x and k are constants, the nonlinear parameter β becomes proportional to the following ratio [57]

$$\beta \propto \frac{A_2}{{A_1}^2}\,. \quad (3)$$

In general, as material damage grows with repeated loading, a drop in A_1 amplitude and a rise in A_2 amplitude is expected due to acoustic energy transfer from A_1 to A_2. Therefore, for impact damaged composite plates subject to fatigue testing, the value of β is expected to increase with increasing number of cycles. In fact, it has already been shown experimentally that there is a strong correlation between fatigue damage and β [58-62].

3 Experimentation

3.1 Fabrication of Test Samples

Likewise previous studies from the authors [49, 63], the composite specimens were manufactured using twelve unidirectional prepreg layers (Hexcel T800/M21) that were laid by hand in [0°/90°/0°/90°/0°/90°]s orientation. The in-plane size of samples was 260 × 20 mm with a nominal thickness of 3 mm. Aluminium end-tabs (50 × 20 × 1.5 mm) were bonded to these samples using a two-part epoxy adhesive (Araldite 420 A/B), as shown in Figure 4. The specimens were divided into two groups. The first group was that of plain CFRP samples, here called P-specimens. The second one included CFRP samples with pairs of embedded PIC 255 piezoelectric disks (6 mm diameter × 0.3 mm thick)

each of which was covered with a dry fabric layer of E-glass fibres (10 × 10 mm × 0.1 mm) for electrical insulation. These samples are referred to as the G-specimens in this paper. The PZTs with the glass fibre layers were symmetrically placed 85 mm away from the specimen ends (Figure 4), at the interface between the 4th and the 5th plies (above the middle plane). Each of the four CFRP plies above the sensor interface included short and narrow openings in the fibre direction (i.e. no fibre cutting) through which the positive and negative wires of the PZTs were directed outside the top surface of the plates. The wire ends were attached to low-noise cables (RG174/U) with BNC plugs (50 Ω).

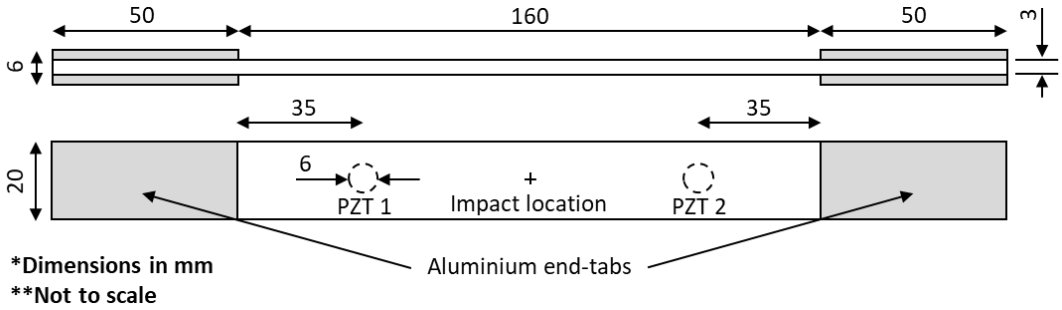

Figure 4: Design of test specimens.

3.2 Impact Damaging of Test Samples

Composite specimens were initially impacted at their centre using a testing machine configuring a 2.66 kg drop mass with a hemispherical tip of 20 mm diameter. Multiple impacts of different energy were performed on spare samples for the determination of the energy level required to cause BVID to the material. The energy was controlled by adjusting the drop height accordingly, and the material damage was examined through stepped linear C-scanning using an ultrasonic imaging system (from Diagnostic Sonar Ltd) equipped with a phased array transducer (5 MHZ, 128 elements). As can be seen in Figure 5, an impact energy of 3 J was high enough to introduce delamination and matrix cracking into the CFRP samples without any visible breakage of fibres. Hence, for consistency, all of the test samples with BVID used in the tensile and fatigue tests of this work were impacted with 3 J using the same testing facility and clamping layout.

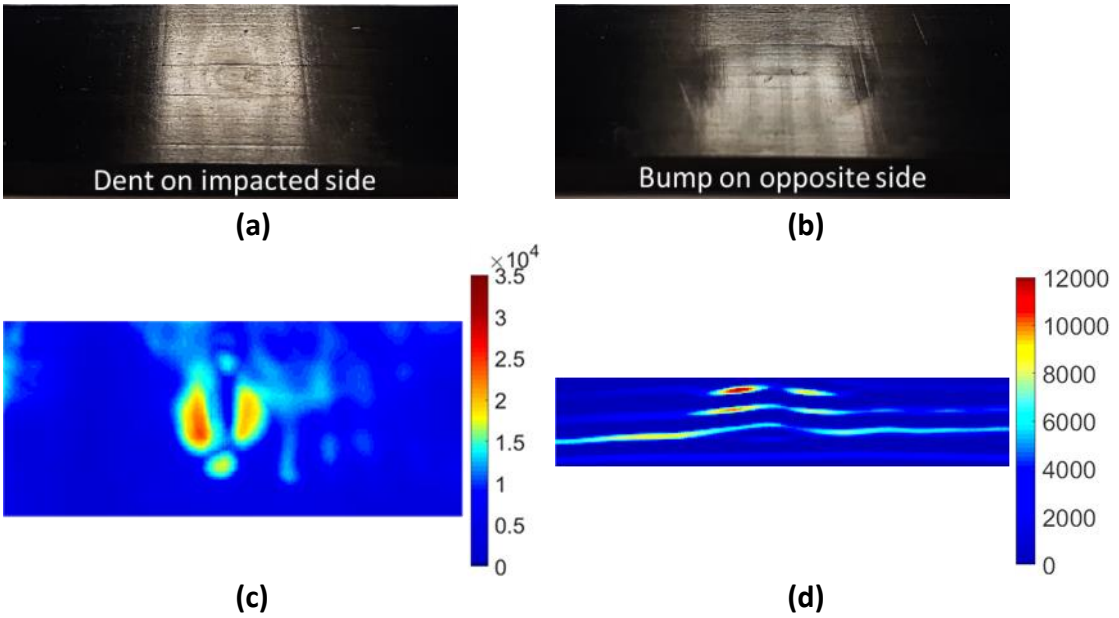

Figure 5: BVID on top (b) and bottom (c) specimen surfaces from 3 J impact, and the associated C-scan (c) and B-scan (d).

3.3 Tensile and Fatigue Tests

Prior to performing fatigue tests, the ultimate tensile strength (UTS) of the P-specimens was calculated and compared with that of the G-specimens. In accordance with ASTM D 3039/D 3039M standard [64], five undamaged samples of each group were tensile loaded on a 100 kN servo-hydraulic Instron 1342 testing frame, at a displacement rate of 1 mm/min. Since all samples failed at a very similar maximum load of around 60kN, the UTS of P- and G-samples with BVID was then determined by tensile testing three samples of each type.

After completing the tensile tests, five P- and five G-specimens with BVID were used to perform tension-tension fatigue tests based on the ASTM D3479/D 3479M standard [65], using the same 100kN servo-hydraulic testing machine. In these tests, the samples were subject to sinusoidal waveform loading of constant amplitude (4.5 to 45 kN) with a cyclic frequency of 5 Hz. The lower and upper load limits corresponded to the 7.5% and 75% of the maximum tensile load of undamaged samples (~60 kN) as mentioned in the previous paragraph. Finally, three P-samples and three G-samples without damage were also fatigue tested within the same stress limits, to compare their endurance when starting from the pristine condition.

3.4 Functionality of Embedded Transducers

It is important to note that damaging of the embedded PZTs (e.g. cracking) due to cycling loading, or sensor depoling due to curing conditions (e.g. high pressure and temperature) would affect the performance of transducers during the ultrasonic tests for damage monitoring. In such case, part of the change in parameter β would be related to sensor malfunction. Therefore, the capacitance of the PZTs inside the G-specimens was measured using a digital multimeter (Keithley 2110 5 1/2) before starting the fatigue tests, and after completing each interval of 120 thousand cycles. This is a common practice in literature for confirming the functionality of PZTs before using them for data acquisition [53, 66, 67]. In fact, any noticeable decrease in capacitance would indicate possible sensor damaging.

3.5 Nonlinear Ultrasonic Monitoring of Damage Evolution

Nonlinear ultrasonic tests were conducted on three impact-damaged G-specimens subject to fatigue testing. The aim was to demonstrate that the growth of BVID with increasing number of loading cycles could be monitored using the embedded PZTs. This was achieved by removing all three G-specimens from the Instron testing machine every 120 thousand cycles, and by recording their acoustic response using the set-up presented in Figure 6. In particular, the transmitter PZT was excited with a continuous sinusoidal signal of constant amplitude (100 V) using a waveform generator (TTi TGA12104) in series with an amplifier (Falco Systems WMA-300). The second PZT was connected to an oscilloscope (PicoScope 4424) for acquisition of the propagating waves at a sampling rate of 10 MHz and a time window of 2 ms. At first, the frequency of the driving waveform was swept in the range of 80-600 kHz in steps of 20-50 kHz. Then, for every input frequency, the amplitude of A_1 and A_2 harmonics was obtained from the average frequency spectrum of the received signal, without using any band-pass filters. This allowed the calculation of the nonlinear parameter β ($\propto A_2/{A_1}^2$) across the range of 80-600 kHz, during fatigue testing. An example of the acoustic response of one G-specimen after completing the first 120,000 loading cycles is illustrated in Figure 7.

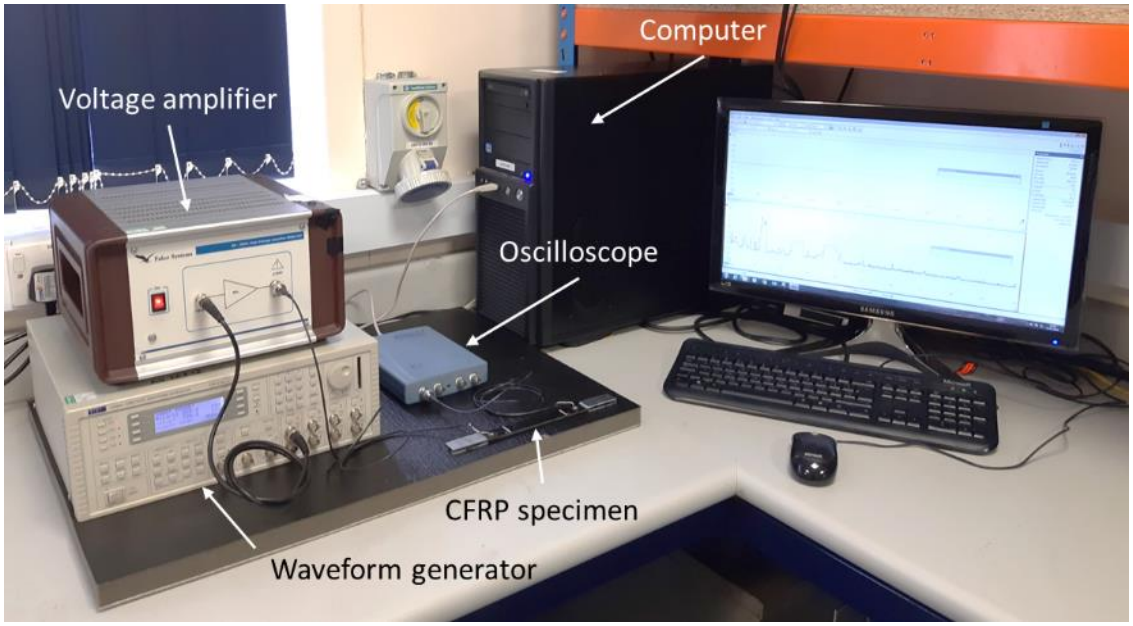

Figure 6: Illustration of the set-up used in the nonlinear ultrasonic experiments.

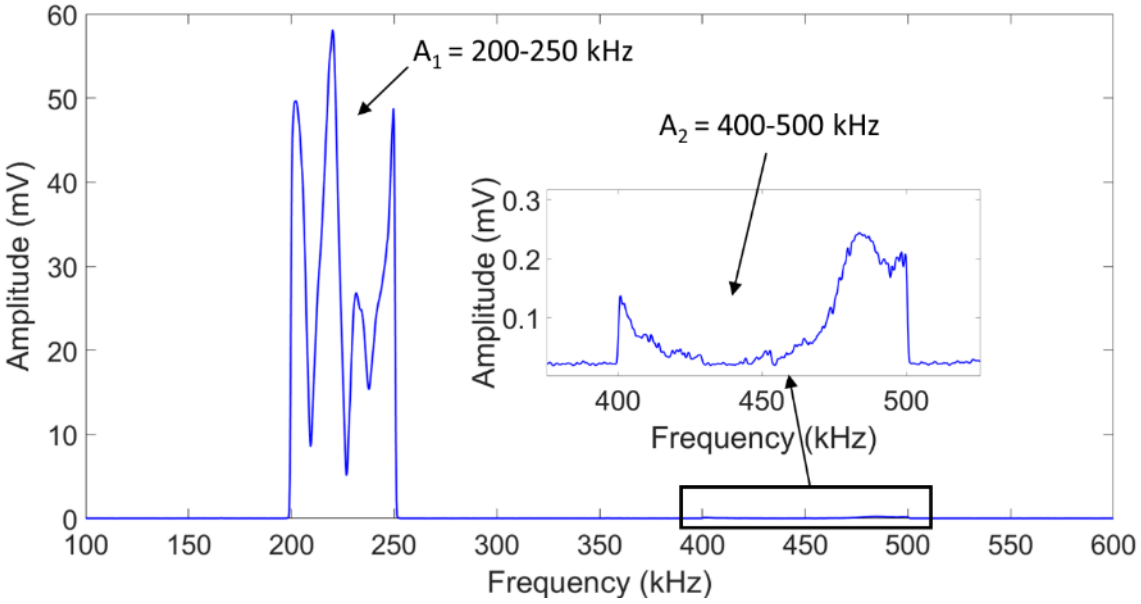

Figure 7: Received signal amplitude in frequency spectrum of G-specimen after 120k fatigue cycles - case of 100 V input signal between 200-250 kHz.

4 Results and Discussion

4.1 Tensile and Fatigue Testing Results

In tensile tests, the P- and G-specimens (both intact and impacted) failed by lateral through-thickness shear at the centre of their un-tabbed length (impact location), as shown in Figure 8 and Figure 9. Considering that the tabbed sections of the samples were free of

damage, this type of failure was acceptable according to the ASTM D 3039/D 3039M standard. This indicated that in each case of initial sample state (undamaged or impacted), the failure behaviour under static tensile loading was the same between the P-specimens the G-specimens, using the proposed layout of embedded sensors.

The composite samples used in tension-tension fatigue tests experienced explosive failure at the impact location without any damage in the end-tabs of the specimen. With reference to the ASTM D3479/D 3479M standard, this failure mode was valid. As it is shown in Figure 10 and Figure 11, there was not any noticeable difference between the two specimen groups (P- and G-specimens). This proved that the evolution of material damage in the G-samples was not affected by the presence of the internal transducers, and it was true for both cases of initial sample condition: pristine and impacted.

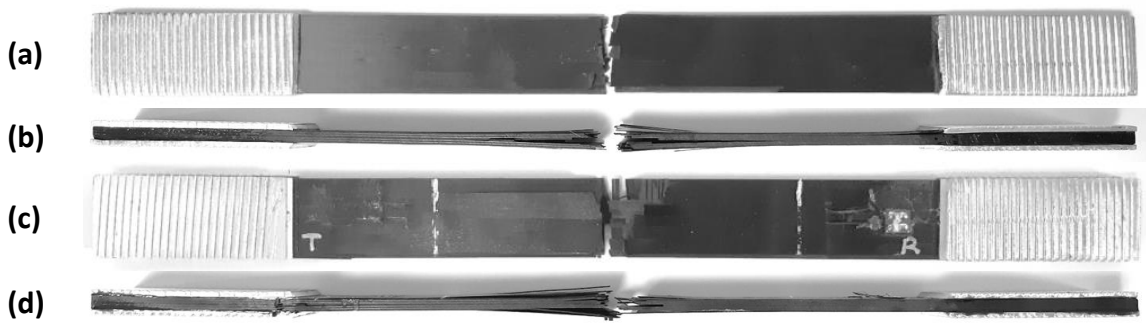

Figure 8: Tensile failure of specimens without BVID. Top view (a) and side view (b) of P-specimen, and top view (c) and side view (d) of G-specimen.

Figure 9: Tensile failure of specimens with BVID. Top view (a) and side view (b) of P-specimen, and top view (c) and side view (d) of G-specimen.

Figure 10: Tension-tension fatigue failure of specimens without BVID. Top view (a) and side view (b) of P-specimen, and top view (c) and side view (d) of G-specimen.

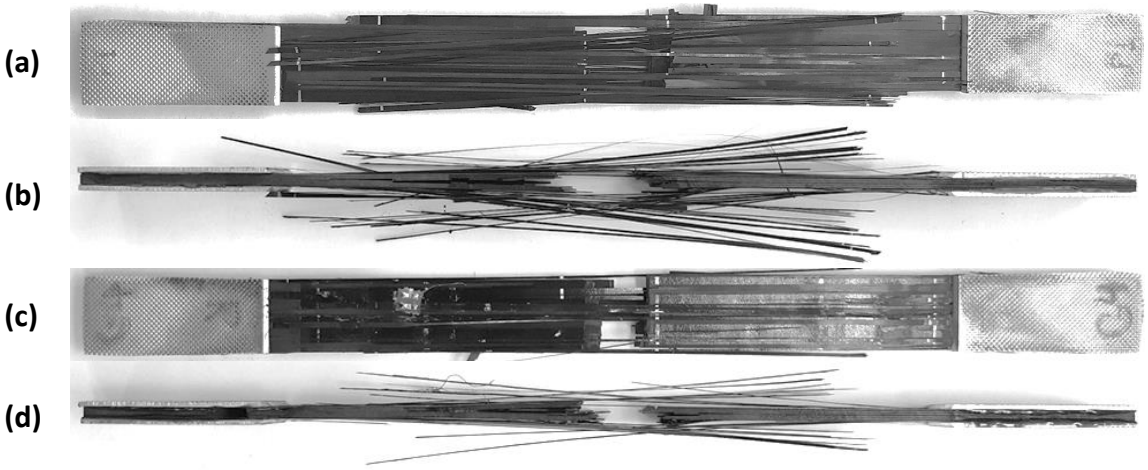

Figure 11: Tension-tension fatigue failure of specimens with BVID. Top view (a) and side view (b) of P-specimen, and top view (c) and side view (d) of G-specimen.

The results from the tensile and fatigue tests were subject to a standard one-way analysis of variance (ANOVA) method using Matlab. This technique enabled to determine statistically whether the mean values of the specimen groups were significantly different between the undamaged P- and G-samples and between the impacted P- and G-samples. In addition, ANOVA was chosen for consistency purposes, as it has already been used in a previous study of the authors to analyse the results from compressive, flexural and interlaminar shear tests on the same "smart" composite samples [49]. In this analysis, the null hypothesis (H_0) was that the group means were the same whereas the alternative hypothesis (H_A) was that the means were different, with a significance level (α) of 0.1

(i.e. 90% confidence level). In general, the F-value (or F-statistic) in one-way ANOVA describes the following ratio

$$F = \frac{Between-group\ variance}{Within-group\ variance},$$

which is expected to be equal or close to 1 if H_0 is valid. Also, F-value is characterised by an F distribution with k-1 numerator degrees of freedom and n-k denominator degrees of freedom, where k is the number of groups and n is the total number of values from all k groups. From the cumulative distribution function of the F distribution, ANOVA calculates the probability (p-value) that the F-value can exceed the computed test-statistic. The null hypothesis is rejected for p-values less than α ($p < 0.1$) indicating that the group means are significantly different. Inversely, for $p > 0.1$ the null hypothesis is accepted. Based on the above, the mechanical testing results along with the F- and p-values are summarised in Table 1.

Starting from the tensile tests, the pristine P- and G-specimens failed on average at a maximum stress of 910 MPa and a maximum extension of 1.81 mm. The ANOVA confirmed that the two specimen groups had the same means of ultimate tensile strength (p=0.57) and maximum extension (p=0.83). In the case of impact-damaged P- and G-samples, failure occurred at an average stress of 865 MPa and an average extension of 1.72 mm. Again, the ANOVA outcome suggested that the samples with and without PZTs had equal values of tensile strength and extension, i.e. p=0.41 and p=0.70, respectively. It must be mentioned that the extension results referred to the total extension of the system and not the elongation of the sample, because the Instron readings included the stretching of the machine grips and the aluminium end-tabs. Nevertheless, the extension results were reported as an additional parameter for comparison, and they certainly showed high consistency between the two specimen groups.

About the tension-tension fatigue tests, the number of cycles to failure for the P- and G-specimens without impact damage was about 713,000, and the group means were considered the same based on the p-value of 0.55. Similarly, the maximum number of loading cycles for the impacted P- and G-samples was nearly 675,000, without any significant difference between the group means (p=0.64). The results from these mechanical tests revealed that the presented configuration of embedded PZTs had no effect on the strength or the endurance of the “smart” CFRP composite when subject to static or dynamic tensile loading conditions.

Table 1: Summary of tensile and fatigue testing results.

Test	Property	Pristine P-specimens	Pristine G-specimens	Impacted P-specimens	Impacted G-specimens
Tensile	**Ult. Strength (MPa)** [a]	**916.8** (36.2)	**903.4** (31.1)	**871.2** (34.4)	**859.5** (38.9)
	F-value	0.35		0.86	
	p-value	0.57		0.41	
	Max. Extension (mm) [a]	**1.82** (0.11)	**1.79** (0.15)	**1.73** (0.14)	**1.71** (0.10)
	F-value	0.05		0.16	
	p-value	0.83		0.70	
Fatigue	**Cycles to failure ($\times 10^3$)** [a]	**720** (30.4)	**705** (25.4)	**683** (58)	**667** (46)
	F-value	0.43		0.23	
	p-value	0.55		0.64	

[a] Standard deviation in brackets

4.2 Functionality of Embedded Transducers

As previously mentioned in paragraph 3.4, the capacitance of the embedded transducers in three G-specimens was measured at the pristine and impacted state of the samples, and then at 120, 240, 360 and 480 thousand cycles of fatigue testing. Capacitance measurements and nonlinear ultrasonic experiments were not conducted beyond 480,000 cycles as the test specimens were severely damaged. The results for both the transmitting and the receiving PZTs were summarised in Figure 12a and Figure 12b respectively, indicating that the capacitance was 1.54 ± 0.02 nF at all different states of composite samples. This suggested that PZT transducers remained functional at least up to 480,000 cycles, which is nearly 70% of the fatigue life of undamaged composite samples used in this study. In addition, these capacitance measurements verified that the data from the ultrasonic experiments described in Section 3.5, were acquired using undamaged sensors.

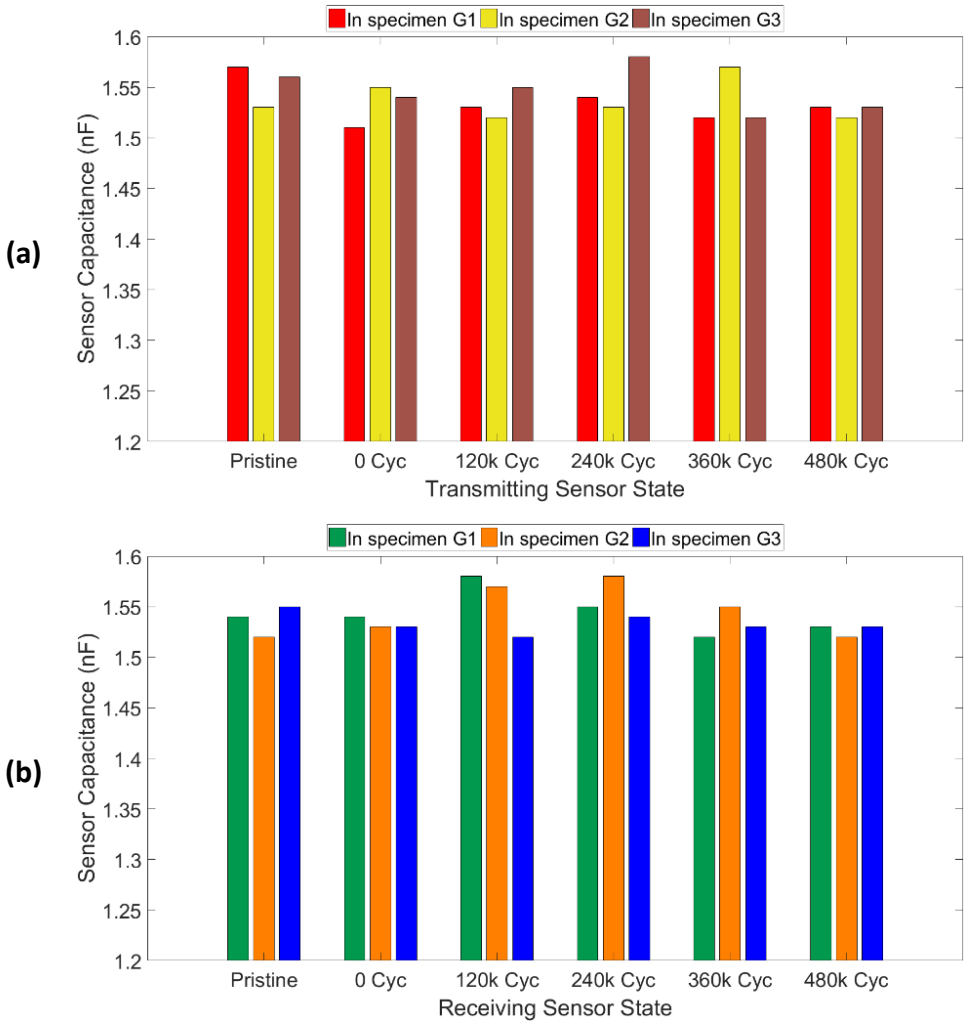

Figure 12: Capacitance of transmitting (a) and receiving (b) sensors in G-specimens.

4.3 Nonlinear Ultrasonic Testing Results

The above G-specimens were used in nonlinear ultrasonic experiments following the procedure explained in Section 3.5. After examining the received signal spectrum in each test sample, the highest amplitude of A_2 harmonics corresponded to an input frequency range of 200-220 kHz. That was reasonable since the 200-220 kHz range was close to the radial resonance frequency of the PZT transducers (~300 kHz), meaning that the energy of propagating waves should be relatively high. By plotting the value of parameter β ($\propto A_2/{A_1}^2$) across that range, it showed that the material damage was excited strongly at the driving frequency of around 210 kHz. According to Figure 13 below, the value of β in all three cases was found to increase from the pristine to the impacted state of samples and, then, every 120,000 loading cycles. This behaviour of β was expected because the material damage was also increasing.

For clarification, the peak value of β was plotted at each state of the G-specimens (Figure 14), showing a consistent increase from about 0.07×10^{-3} to 3×10^{-3}. It is worth noting that β was not equal to zero at the pristine state of the samples, because low-amplitude A_2 harmonics were present in the received signal spectrum. This could possibly be attributed to instrumentation noise, since the initial value of β was almost identical in all three G-specimens. Moreover, it must be noted that high repeatability was observed in the increase of β ($\sim 0.2 \times 10^{-3}$) between the pristine and the impacted state, and that was reasonable considering that the test specimens were initially damaged using the same impact energy of 3 J. From the impacted state and up to 480,000 cycles, the rising trend of β contained small fluctuations, but that was also expected because the shape and size of damage in composite laminates could not change linearly and uniformly as in isotropic materials (e.g. metals).

The above results proved that except for BVID detection, this novel arrangement of internal PZT disks was capable of monitoring the growth of material damage for more than two-thirds of the mean sample life (~713,000 cycles).

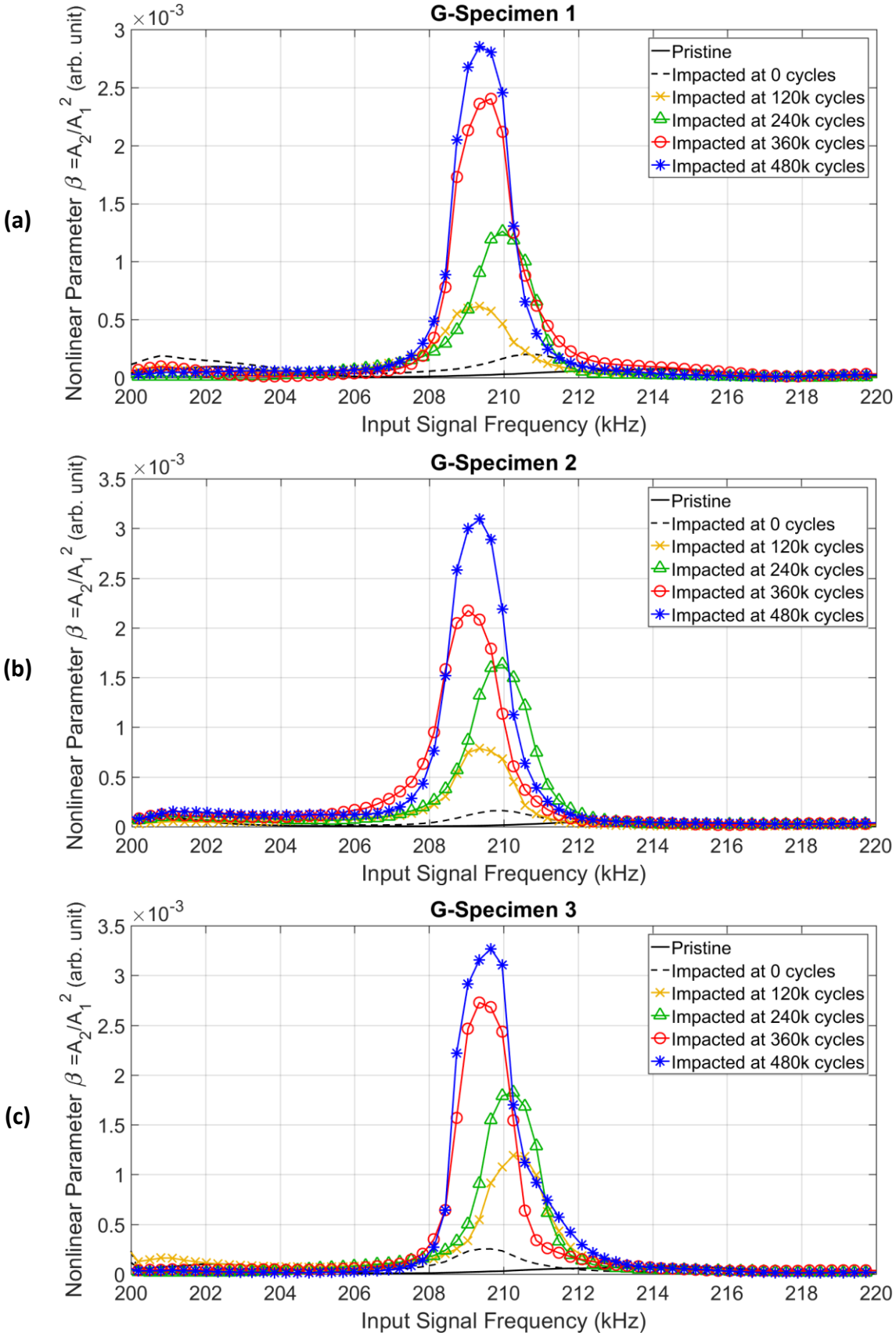

Figure 13: Change in nonlinear parameter β with increasing number of fatigue cycles for G-specimen 1 (a), G-specimen 2 (b) and G-specimen 3 (c) - Input signal of 100V at 200-220 kHz.

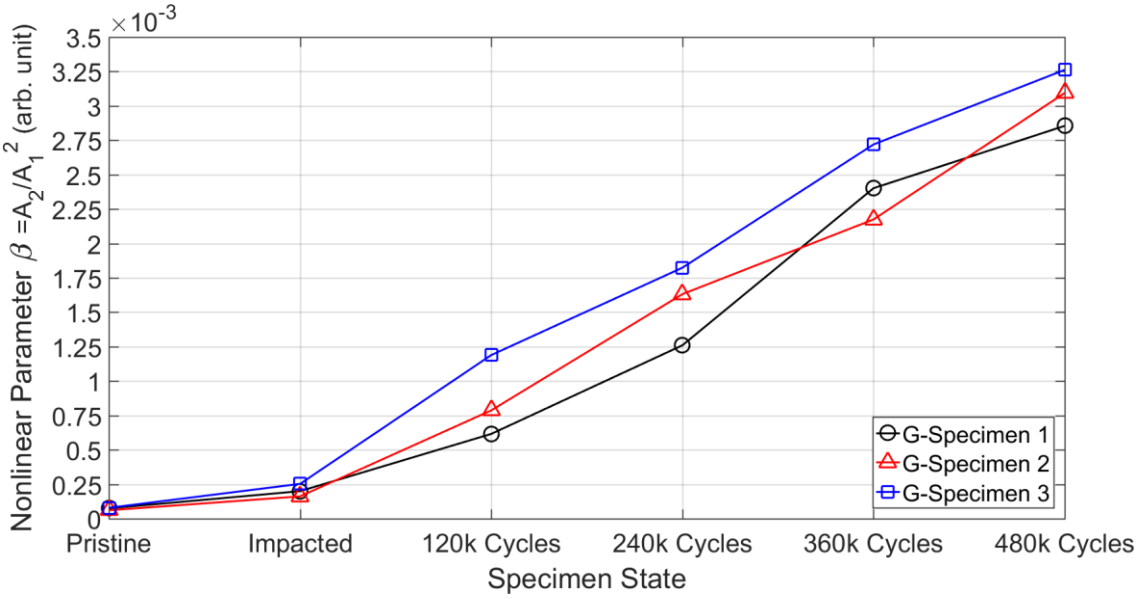

Figure 14: Peak value of nonlinear parameter β at each state of G-specimens 1, 2 and 3 during fatigue testing - Input signal of 100V at ~210 kHz.

5 Conclusions

This study assessed the tensile strength and the fatigue endurance of a recently developed design of "smart" CFRP composite plates containing internal PZT transducers that were covered with glass fibre patches for electrical insulation. Specifically, CFRP samples with two embedded sensors (G-specimens) were tested against plain samples (P-specimens). The tests were performed using undamaged specimens of each group, as well as specimens with BVID caused from low energy (3 J) impacts. The ultimate tensile strength of the P- and G-specimens was similar in both tests; ~910 MPa for undamaged samples and ~865 MPa for impact damaged samples. Based on these values, the specimens of each group with and without damage were subject to tension-tension fatigue testing at a stress level ranging from about 8 to 80% of the associated material strength. Again, the P- and G-samples failed on average at the same number of cycles, which was around 713,000 for the pristine samples and 675,000 for the damaged samples. The test data obtained from P-specimens were statistically compared to those of G-specimens using a standard one-way ANOVA. This analysis indicated that the pristine P- and G-samples had equal mean values of maximum tensile strength (p=0.57), maximum extension (p=0.83) and fatigue cycles to failure (p=0.55). The same outcome applied to the case of impact damaged samples and the corresponding p-values were 0.41, 0.70, and 0.64. These

results suggested that the proposed configuration of internal PZT disks had not reduced the tensile strength or the fatigue endurance of the "smart" CFRP composite. In addition, the failure mode of the tensile test samples was central through-thickness shear, whereas in the fatigue test samples experienced central explosive failure. It must be noted that the failure type in both tests was the same between the undamaged P- and G-specimens and between the impacted P-and G-specimens. This revealed that the damage propagation in G-samples had not changed by the existence of internal sensors.

Moreover, during fatigue testing, nonlinear ultrasonic experiments were conducted on three impacted G-samples, to examine the ability of the internal sensors to monitor the evolution of BVID with increasing number of loading cycles. These experiments were performed before and after impacting the G-samples, and then every 120,000 cycles. In each specimen, one PZT was used for the transmission of elastic waves ranging from 80 kHz to 600 kHz, and the nonlinear parameter β was calculated from the A_1 and A_2 amplitudes received by the second PZT. The data acquired at a driving frequency of 210 kHz showed that between the pristine and the impacted state of the samples, β raised by approximately 0.2×10^{-3}, and then continued to increase (up to $\sim 3 \times 10^{-3}$) until the samples completed a total of 480 thousand fatigue cycles. After that point, nonlinear ultrasonic testing stopped because the composites were severely damaged. The change in parameter β was very similar between the tested G-specimens proving that the specific arrangement of embedded PZT disks could not only be used for the detection of BVID in CFRP composites, but it was also capable of monitoring the increase in damage size. Finally, at all stages of ultrasonic data acquisition up to 480,000 cycles, the capacitance of the sensors was about 1.54 nF verifying that the PZT transducers remained functional for at least 70% of the specimen's life.

The above results suggest that future solutions for on-board ultrasonic inspections of aerospace structures could possibly rely on SHM systems consisting of composite panels with embedded PZT transducers, similar to the "smart" CFRP composite design presented in this work.

References

1. Panin, S., Burkov, M., Lyubutin, P., & Altukhov, Y. (2014). Application of aluminum foil for "strain sensing" at fatigue damage evaluation of carbon fiber composite. *Science China Physics, Mechanics and Astronomy*, 57(1), 59-64.
2. El-Hofy, M. H., Soo, S. L., Aspinwall, D. K., Sim, W. M., Pearson, D., M'Saoubi, R., & Harden, P. (2017). Tool temperature in slotting of CFRP composites. *Procedia Manufacturing*, 10(1), 371-381.
3. Francesconi, A., Giacomuzzo, C., Kibe, S., Nagao, Y., & Higashide, M. (2012). Effects of high-speed impacts on CFRP plates for space applications. *Advances in Space Research*, 50(5), 539-548.
4. Garnier, C., Pastor, M. L., Lorrain, B., & Pantale, O. (2013). Fatigue behavior of impacted composite structures. *Composite Structures*, 100(1), 443-450.
5. Tian, Z., Leckey, C., & Yu, L. (2017). Multi-site delamination detection and quantification in composites through guided wave based global-local sensing. In *AIP Conference Proceedings* (Vol. 1806, p. 020007). AIP Publishing.
6. Sudevan, D., Prakash, R. V., & Kamaraj, M. (2015). Post-impact fatigue response of CFRP laminates under constant amplitude and programmed FALSTAFF spectrum loading. *Procedia Engineering*, 101(1), 395-403.
7. Briks, A. S., & Green, R. E. (1991). *Nondestructive Testing Handbook: Ultrasonic Testing*. Ohio: American Society for Nondestructive Testing.
8. Amerini, F., & Meo, M. (2011). Structural health monitoring of bolted joints using linear and nonlinear acoustic/ultrasound methods. *Structural Health Monitoring*, 10(6), 659-672.
9. Cesari, F., Dal Re, V., Minak, G., & Zucchelli, A. (2007). Damage and residual strength of laminated carbon–epoxy composite circular plates loaded at the centre. *Composites Part A: Applied Science and Manufacturing*, 38(4), 1163-1173.
10. Oskouei, A. R., & Ahmadi, M. (2010). Acoustic emission characteristics of mode I delamination in glass/polyester composites. *Journal of Composite Materials*, 44(7), 793-807.
11. De Moura, M. F., & Marques, A. T. (2002). Prediction of low velocity impact damage in carbon–epoxy laminates. *Composites Part A: Applied Science and Manufacturing*, 33(3), 361-368.
12. Wright, P., Fu, X., Sinclair, I., & Spearing, S. M. (2008). Ultra high resolution computed tomography of damage in notched carbon fiber-epoxy composites. *Journal of Composite Materials*, 42(19), 1993-2002.
13. Holland, S. D., & Reusser, R. S. (2016). Material evaluation by infrared thermography. *Annual Review of Materials Research*, 46(1), 287-303.
14. Almond, D. P., Angioni, S. L., & Pickering, S. G. (2017). Long pulse excitation thermographic non-destructive evaluation. *NDT & E International*, 87(1), 7-14.
15. Ruzek, R., Lohonka, R., & Jironc, J. (2006). Ultrasonic C-Scan and shearography NDI techniques evaluation of impact defects identification. *NDT & E International*, 39(2), 132-142.
16. De Angelis, G., Meo, M., Almond, D. P., Pickering, S. G., & Angioni, S. L. (2012). A new technique to detect defect size and depth in composite structures using digital shearography and unconstrained optimization. *NDT & E International*, 45(1), 91-96.
17. Hettler, J., Tabatabaeipour, M., Delrue, S., & Van Den Abeele, K. (2016). Linear and nonlinear guided wave imaging of impact damage in CFRP using a probabilistic approach. *Materials*, 9(11), 901.
18. Aymerich, F., & Staszewski, W. J. (2010). Impact damage detection in composite laminates using nonlinear acoustics. *Composites Part A: Applied Science and Manufacturing*, 41(9), 1084-1092.
19. Su, Z., Wang, X., Chen, Z., Ye, L., & Wang, D. (2006). A built-in active sensor network for health monitoring of composite structures. *Smart Materials and Structures*, 15(6), 1939-1949.
20. Zagrai, A., Donskoy, D., Chudnovsky, A., & Golovin, E. (2008). Micro-and macroscale damage detection using the nonlinear acoustic vibro-modulation technique. *Research in Nondestructive Evaluation*, 19(2), 104-128.

21. Boccardi, S., Calla, D. B., Ciampa, F., & Meo, M. (2018). Nonlinear elastic multi-path reciprocal method for damage localisation in composite materials. *Ultrasonics*, 82(1), 239-245.

22. Kundu, T. (2019). *Nonlinear ultrasonic and vibro-acoustical techniques for nondestructive evaluation* (Vol. 1, p. 2). Cham: Springer.

23. Buck, O., Morris, W. L., & Richardson, J. M. (1978). Acoustic harmonic generation at unbonded interfaces and fatigue cracks. *Applied Physics Letters*, 33(5), 371-373.

24. Polimeno, U., Meo, M., Almond, D. P., & Angioni, S. L. (2010). Detecting low velocity impact damage in composite plate using nonlinear acoustic/ultrasound methods. *Applied Composite Materials*, 17(5), 481-488.

25. Solodov, I. (2014). Resonant acoustic nonlinearity of defects for highly-efficient nonlinear NDE. *Journal of Nondestructive Evaluation*, 33(2), 252-262.

26. Scarselli, G., Ciampa, F., Nicassio, F., & Meo, M. (2017). Non-linear methods based on ultrasonic waves to analyse disbonds in single lap joints. *Proceedings of the Institution of Mechanical Engineers, Part C: Journal of Mechanical Engineering Science*, 231(16), 3066-3076.

27. Ciampa, F., Scarselli, G., & Meo, M. (2017). On the generation of nonlinear damage resonance intermodulation for elastic wave spectroscopy. *The Journal of the Acoustical Society of America*, 141(4), 2364-2374.

28. Fierro, G. P. M., & Meo, M. (2018). IWSHM 2017: Structural health monitoring of the loosening in a multi-bolt structure using linear and modulated nonlinear ultrasound acoustic moments approach. *Structural Health Monitoring*, 17(6), 1349-1364.

29. Van Den Abeele, K. A., Johnson, P. A., & Sutin, A. (2000). Nonlinear elastic wave spectroscopy (NEWS) techniques to discern material damage, part I: nonlinear wave modulation spectroscopy (NWMS). *Journal of Research in Nondestructive Evaluation*, 12(1), 17-30.

30. Meo, M., Polimeno, U., & Zumpano, G. (2008). Detecting damage in composite material using nonlinear elastic wave spectroscopy methods. *Applied Composite Materials*, 15(3), 115-126.

31. Pieczonka, L., Klepka, A., Martowicz, A., & Staszewski, W. J. (2015). Nonlinear vibroacoustic wave modulations for structural damage detection: an overview. *Optical Engineering*, 55(1), 011005.

32. Li, N., Sun, J., Jiao, J., Wu, B., & He, C. (2016). Quantitative evaluation of micro-cracks using nonlinear ultrasonic modulation method. *NDT & E International*, 79, 63-72.

33. Chen, B. Y., Soh, S. K., Lee, H. P., Tay, T. E., & Tan, V. B. (2016). A vibro-acoustic modulation method for the detection of delamination and kissing bond in composites. *Journal of Composite Materials*, 50(22), 3089-3104.

34. Van Den Abeele, K. A., Carmeliet, J., Ten Cate, J. A., & Johnson, P. A. (2000). Nonlinear elastic wave spectroscopy (NEWS) techniques to discern material damage, Part II: Single-mode nonlinear resonance acoustic spectroscopy. *Journal of Research in Nondestructive Evaluation*, 12(1), 31-42.

35. Solodov, I., Rahammer, M., Derusova, D., & Busse, G. (2015). Highly-efficient and noncontact vibro-thermography via local defect resonance. *Quantitative InfraRed Thermography Journal*, 12(1), 98-111.

36. Post, W., Kersemans, M., Solodov, I., Van Den Abeele, K., García, S. J., & Van Der Zwaag, S. (2017). Non-destructive monitoring of delamination healing of a CFRP composite with a thermoplastic ionomer interlayer. *Composites Part A: Applied Science and Manufacturing*, 101(1), 243-253.

37. Segers, J., Kersemans, M., Hedayatrasa, S., Calderon, J., & Van Paepegem, W. (2018). Towards in-plane local defect resonance for non-destructive testing of polymers and composites. *NDT & E International*, 98(1), 130-133.

38. Espinoza, C., Feliu, D., Aguilar, C., Espinoza-Gonzalez, R., Lund, F., Salinas, V., & Mujica, N. (2018). Linear versus nonlinear acoustic probing of plasticity in metals: A quantitative assessment. *Materials*, 11(11), 2217.

39. Cantrell, J. H. (2006). Quantitative assessment of fatigue damage accumulation in wavy slip metals from acoustic harmonic generation. *Philosophical Magazine*, 86(11), 1539-1554.

40. Apple, T. M., Cantrell, J. H., Amaro, C. M., Mayer, C. R., Yost, W. T., Agnew, S. R., & Howe, J. M. (2013). Acoustic harmonic generation from fatigue-generated dislocation substructures in copper single crystals. *Philosophical Magazine*, 93(21), 2802-2825.

41. Matlack, K. H., Kim, J. Y., Jacobs, L. J., & Qu, J. (2015). Review of second harmonic generation measurement techniques for material state determination in metals. *Journal of Nondestructive Evaluation*, 34(1), 273.

42. Mook, G., Pohl, J., & Michel, F. (2003). Non-destructive characterization of smart CFRP structures. *Smart Materials and Structures*, 12(6), 997.

43. Arellano, M. T., Crouzeix, L., Collombet, F., Douchin, B., & Grunevald, Y. H. (2012). Mechanical characterization of an alternative technique to embed sensors in composite structures: the monitoring patch. *Applied Composite Materials*, 19(3-4), 379-391.

44. Chilles, J. S., Croxford, A., & Bond, I. P. (2015). Design of an embedded sensor, for improved structural performance. *Smart Materials and Structures*, 24(11), 115014.

45. Masmoudi, S., El Mahi, A., & Turki, S. (2015). Use of piezoelectric as acoustic emission sensor for in situ monitoring of composite structures. *Composites Part B: Engineering*, 80(1), 307-320.

46. Lampani, L., Sarasini, F., Tirillo, J., & Gaudenzi, P. (2018). Analysis of damage in composite laminates with embedded piezoelectric patches subjected to bending action. *Composite Structures*, 202(1), 935-942.

47. Lin, M., & Chang, F. K. (2002). The manufacture of composite structures with a built-in network of piezoceramics. *Composites Science and Technology*, 62(7-8), 919-939.

48. Butler, S., Gurvich, M., Ghoshal, A., et al. (2011). Effect of embedded sensors on interlaminar damage in composite structures. *Journal of Intelligent Material Systems and Structures*, 22(16), 1857-1868.

49. Andreades, C., Mahmoodi, P., & Ciampa, F. (2018). Characterisation of smart CFRP composites with embedded PZT transducers for nonlinear ultrasonic applications. *Composite Structures*, 206(1), 456-466.

50. Mall, S. (2002). Integrity of graphite/epoxy laminate embedded with piezoelectric sensor/actuator under monotonic and fatigue loads. *Smart Materials and Structures*, 11(4), 527-533.

51. Paget, C. A., Levin, K., & Delebarre, C. (2002). Actuation performance of embedded piezoceramic transducer in mechanically loaded composites. *Smart Materials and Structures*, 11(6), 886-891.

52. Yocum, M., Abramovich, H., Grunwald, A., & Mall, S. (2003). Fully reversed electromechanical fatigue behavior of composite laminate with embedded piezoelectric actuator/sensor. *Smart Materials and Structures*, 12(4), 556-564.

53. Yoo, S., Khatibi, A. A., & Kandare, E. (2014). Durability of embedded PZTs in structural health monitoring systems under cyclic loading. In *Advanced Materials Research* (Vol. 891, p. 1255-1260). Trans Tech Publications Ltd.

54. Soleimanpour, R., Ng, C. T., & Wang, C. H. (2017). Higher harmonic generation of guided waves at delaminations in laminated composite beams. *Structural Health Monitoring*, 16(4), 400-417.

55. Landau, L. D. & Lifshitz, E. M. (1986). *Theory of Elasticity* (Vol. 7, p. 476). 3rd ed. Oxford: Pergamon.

56. Munoz, R., Bochud, N., Rus, G., et al. (2015). Model-based damage evaluation of layered CFRP structures. In *AIP Conference Proceedings* (Vol. 1650, p. 1170-1177). AIP Publishing.

57. Amura, M., Meo, M., & Amerini, F. (2011). Baseline-free estimation of residual fatigue life using a third order acoustic nonlinear parameter. *The Journal of the Acoustical Society of America*, 130(4), 1829-1837.

58. Suzuki, T., Hikata, A., & Elbaum, C. (1964). Anharmonicity due to glide motion of dislocations. *Journal of Applied Physics*, 35(9), 2761-2766.

59. Hikata, A., Chick, B. B., & Elbaum, C. (1965). Dislocation contribution to the second harmonic generation of ultrasonic waves. *Journal of Applied Physics*, 36(1), 229-236.

60. Morris, W. L., Buck, O., & Inman, R. V. (1979). Acoustic harmonic generation due to fatigue damage in high-strength aluminum. *Journal of Applied Physics*, 50(11), 6737-6741.

61. Kim, J. Y., Qu, J., Jacobs, L. J., Littles, J. W., & Savage, M. F. (2006). Acoustic nonlinearity parameter due to microplasticity. *Journal of Nondestructive Evaluation*, 25(1), 28-36.

62. Cai, Z., Liu, S., & Zhang, C. (2017). Measurement of ultrasonic nonlinear parameter by using electromagnetic acoustic transducer. In *AIP Conference Proceedings* (Vol. 1806, p. 050015). AIP Publishing.

63. Andreades, C., Malfense Fierro, G. P., Meo, M., & Ciampa, F. (2019). Nonlinear ultrasonic inspection of smart carbon fibre reinforced plastic composites with embedded piezoelectric lead zirconate titanate transducers for space applications. *Journal of Intelligent Material Systems and Structures*, 30(20), 2995-3007.

64. American Society for Testing and Materials Standard. (2002). *D3039/D3039M-00 Standard test method for tensile properties of polymer matrix composite materials*. West Conshohocken: ASTM International.

65. American Society for Testing and Materials Standard. (2002). *D3479/D3479M-96 Standard test method for tension-tension fatigue of polymer matrix composite materials*. West Conshohocken: ASTM International.

66. Konka, H. P., Wahab, M. A., & Lian, K. (2012). On mechanical properties of composite sandwich structures with embedded piezoelectric fiber composite sensors. *Journal of Engineering Materials and Technology*, 134(1), 011010.

67. Dragan, K., Dziendzikowski, M., Kurnyta, A., Leski, A., & Bienias, J. (2014). Structural health monitoring of composite structures with use of embedded PZT piezoelectric sensors. In *ECCM-16th European Conference on Composite Materials*.

Chapter 6

A Nonlinear Ultrasonic Method for In-Plane Localisation of Impact Damage

The publication (Paper IV) outlined in the following pages of this chapter refers to the second research area of this PhD, about the development of an efficient SHM algorithm for nonlinear ultrasonic inspection of composite laminates using a surface-mounted network of sensors. The aim for this algorithm was to enable detection of the location of impact damage without any previous knowledge of the material properties such as the wave velocity in different directions, and without the need for calculations involving the use of baseline data.

In this study, the proposed SHM method was applied through eight piezoelectric transducers arranged in a circle, and the recording of ultrasonic data was completed by transmitting and receiving waves in the forward and backward directions of the paths connecting the transducers. Initially, the transmission-reception process was performed using ultrasonic signals of sweeping frequency, and the algorithm verified the functionality of the transducers with comparisons between the ultrasonic signals acquired only in the paths around the periphery of the array. This ensured reliable inspection of the sensors because the level of similarity between the signals captured in the outer paths should not be seriously affected by the existence of BVID within the monitored region.

After confirming the functionality of the sensors, the average frequency spectrum of all captured signals was plotted, and the frequency (f_S) corresponding to the maximum amplitude was identified. The energy of waves propagating through the material was expected to be higher at f_S, resulting in stronger excitation of the damaged layers. Hence, the recording of ultrasonic data in all paths was repeated by transmitting ultrasonic waves only at the chosen f_S. Next, the frequency domain of the signal recorded in each path was used for the evaluation of the relative acoustic nonlinearity parameter β (i.e. ratio of $A_2/{A_1}^2$). In general, the magnitude of β should be considerably higher in the paths crossing the damaged zone than in other paths further away from the damage. Therefore,

a map displaying the amplitude of acoustic nonlinearity within the inspected area was plotted by adding up the obtained values of β, and the location of maximum amplitude was expected to match the position of the damage. In fact, this SHM method offered accurate localisation of BVID on three random CFRP panels with different dimensions and unspecified layer orientation. The capability of identifying a faulty sensor was also shown on one of the composite panels.

The “Statement of Authorship” form and Paper IV are provided on the following pages.

This declaration concerns the article entitled:			
A Nonlinear ultrasonic SHM method for impact damage localisation in composite panels using a sparse array of piezoelectric PZT transducers			
Publication status			
Draft manuscript ☐ Submitted ☐ Accepted ☒ Published ☐			
Publication details (reference)			
Andreades, C., Fierro, G. P. M., & Meo, M. (2020). A Nonlinear ultrasonic SHM method for impact damage localisation in composite panels using a sparse array of piezoelectric PZT transducers. *Ultrasonics*, 106181.			
Candidate's contribution to the paper (detailed, and also given as a percentage)			
Formulation of ideas: 70% The idea of developing a nonlinear ultrasonic method for the localisation of impact damage was proposed by my supervisor Professor Michele Meo. I suggested to focus on the introduction of a practical method that would not rely on the recording of baseline data or the measurement of the arrival time of signals, but only on the calculation of the acoustic nonlinearity parameter across the material. I also proposed the idea of including the initial step of sensor functionality check before attempting the detection of damage.			
Design of methodology: 60% I decided on the layout of the sensor array and I proposed the inspection of sensor functionality using the data recorded only in the outer (peripheral) paths of the array. I also suggested the creation of the damage localisation map by summing the values of the acoustic nonlinearity parameter measured in all paths. My co-author Dr Gian Piero Malfense Fierro proposed the drawing of the paths using ellipses instead of lines, and the strategy for the transmission and reception of ultrasonic signals within the sensor array.			
Experimental work: 80% I chose the different experimental composite panels, manufactured the ultrasonic transducers that constituted the array, conducted the ultrasonic tests and collected the data. Dr Gian Piero Malfense Fierro designed (in LabVIEW) the computer system used to control the transmission-reception of ultrasonic signals and assisted in the development of the data processing code in Matlab.			
Presentation of data in journal format: 95% I analysed the collected data, prepared the figures, chose the layout of the paper and wrote the manuscript. Dr Gian Piero Malfense Fierro and my supervisor provided feedback on the above and supported the process of submission and review.			
Statement from Candidate			
This paper reports on original research I conducted during the period of my Higher Degree by Research candidature.			
Signed		Date	02/10/2020

A Nonlinear ultrasonic SHM method for impact damage localisation in composite panels using a sparse array of piezoelectric PZT transducers

Christos Andreades, Gian Piero Malfense Fierro, Michele Meo

Department of Mechanical Engineering, University of Bath, Bath BA2 7AY, UK

Abstract

Structural health monitoring techniques (SHM) for material damage identification have demonstrated higher sensitivity and accuracy when relying on the assessment of nonlinear features exhibited in the material response under ultrasonic wave propagation. In this paper, a novel nonlinear ultrasonic SHM method is introduced for the localisation of impact damage in composite laminates using an array of surface-bonded sensors. Unlike existing algorithms, this method enables quick selection of a suitable signal transmission frequency based on the combined sensor-material response, it does not rely on baseline data or complex measurements of signal arrival time, and it allows identification of malfunctioning sensors to minimise damage localisation errors. The proposed technique is based on the transmission and reception of ultrasonic waves through the inspected panel. Initially, the functionality of the transducers is inspected by comparing the signal amplitude in both directions of sensor-to-sensor paths. Then a planar map of material nonlinearity parameter β is created, and the damage position is defined as the point of highest β amplitude. Experimental tests on three CFRP panels confirmed successful positioning of barely visible impact damage (BVID) within a range of 4-22 mm. Sensor functionality check was demonstrated on one of the composite laminates, and a malfunctioning transducer was detected. The results suggested that the presented method could be considered an improved alternative to existing SHM techniques for localisation of BVID in composite panels.

1 Introduction

Structural health monitoring (SHM) is a general term for the processes aiming at the detection of material defects or damage using various types of sensing systems, in order to assess the condition and performance of engineering structures [1]. Examples of SHM methods include those based on the evaluation of thermal gradients [2-5], Eddy currents [6-8], vibrations [9-11] and acousto-ultrasonic wave propagation [12-16]. Except for civil, automotive and marine applications, SHM is widely used in aerospace industry mainly because of the high percentage of composite materials incorporated into aircraft structures [17]. Layered composite parts, particularly those made from carbon fibre reinforced plastic (CFRP) layers, have a number of advantages over traditional metal parts. They are strong, stiff and lightweight with great fatigue performance and corrosion resistance [17]. On the other hand, composite laminates may exhibit reduction of their mechanical properties at localised areas where damage is present beneath the surface, in the form of delamination or debonding [18]. This type of damage is not always attributed to manufacturing errors such as fibre misalignment, matrix voids or trapped moisture [18]. In fact, it can also occur from in-service impacts with low-velocity objects, leaving shallow surface dents that are hardly detectable under visual inspection [18]. Barely visible impact damage (BVID) can have serious effects on the integrity of the structure, especially if the damage size grows due to operating stresses, vibrations and temperature differentials [19]. Therefore, reliable SHM methods for on-board identification of damage in composite structures such as aircraft wing skins and fuselage panels is of utmost importance. Ultrasonic techniques (linear and nonlinear) are suitable due to the high damage sensitivity and long wave propagation distances they offer, but also because they can be implemented using lightweight piezoelectric transducers permanently attached or embedded into the structure [20].

Over the last years, many research studies focused on the development of ultrasonic SHM methods and algorithms. Some of them were based on phased array techniques [21-27], which utilised compact sensor arrays to guide wave-beams in all directions within the material (similar to a radar), for interaction with possible defects that would result in wave reflection back to the source. This enabled the creation of two-dimensional cross-sectional images of the inspected material. Another category of SHM methods is that of delay-and-sum beamforming [28-34], where the energy of scattered waves was delayed

and summed to form images of scatter locations, based on a delay law defined by the geometry of the specific application, as well as the propagation mode and group velocity of the waves. Moreover, other methods applied the concept of time-reversal [35-41]. Briefly, the signals generated from a source were captured in different paths within a sensor network, and the acquired waveforms are then focused on the source by reversing them in time and re-transmitting them backwards through the material. Any change between the two signals of the same path could be attributed to the presence of damage. Furthermore, probabilistic techniques such as the correlation-based algorithms [42, 43], the maximum-likelihood estimation methods [44, 45] and the reconstruction algorithm for probabilistic inspection of damage (RAPID) [46-52], relied on the comparison between the time-of-arrival or energy-of-arrival of signals in the forward and backward directions of each sensor path. Assuming a change to these signal characterises was due to defect presence, then the probability of damage existence at a certain point was based on the magnitude of signal difference coefficient (SDC).

Although the methods mentioned above were proved capable of identifying and localising damage in composite materials, the majority of them was dependent on the evaluation of linear ultrasonic features [21-42, 44-48, 50, 52]. This may not be suitable for defect detection in the micro-scale, since impedance mismatch is not high enough to cause wave reflection or scattering. On the other hand, ultrasonic techniques relying on the measurement of nonlinear effects exhibited in the material response (e.g. higher harmonics and sub-harmonics) due to interaction of propagating waves with damaged interfaces offer higher sensitivity to micro-flaws [49, 51, 53, 54]. However, most of the aforementioned linear or nonlinear techniques [22-45, 51, 53], required estimation of wave velocity and arrival time, which can be very complex in composite structures. Also, in many of the above studies [23, 28, 30, 33-38, 40, 43-45, 48, 49, 52], there was lack of explanation about the choice of signal transmission frequency, which could be challenging for successful identification of damage. In addition, the effectiveness of most existing algorithms relied on (i) the changes in the acquired signals compared to baseline signals originally recorded at the undamaged state of the structure [22, 28-32, 34, 41, 43-45, 47, 50], and (ii) the assumption that the transducers included in the array were all functional [20-54]. It is very unlikely though for a structure to be subject to future SHM under the same environmental and boundary conditions as the baseline, and also, sensor

networks are susceptible to damage (partial or total) due to corrosion, degradation or impacts. These two issues can introduce significant defect positioning errors.

This paper focuses on the development of a novel nonlinear ultrasonic method for impact damage localisation, with the aim of addressing the above challenges. The proposed method is applied through an algorithm, and it is based on the transmission and reception of ultrasonic waves using a circular array of sensors coupled to the surface of the inspected panel. It enables quick determination of an appropriate signal transmission frequency based on the acoustic response of the material and the transducers. In addition, estimation of damage location does not involve complex calculations related to the time-of-flight, velocity or time-reversal of propagating waves, and the accuracy of defect positioning does not rely on the acquisition of baseline signals (i.e. data obtained at the pristine state of the material). Moreover, this technique is capable of detecting faulty sensors, based on the correlation coefficient between the signals in the forward and backward directions of the paths located around the periphery of the senor network (ref. Section 3.1). Defect location is defined as the point (within the inspected area) corresponding to the maximum amplitude of material nonlinearity parameter β (ref. Section 3.2).

2 Nonlinear Parameter Beta

Parameter β is directly related to the effect of the second harmonic generation in the acoustic response of materials. In general, the waves propagating inside a material can interact and excite cracked interfaces and debonded layers [55]. The frictional (rubbing) or out-of-plane (clapping) excitation at the region of damage can give rise to waves of higher frequency. In particular, these waves have frequencies that are odd and even multiples of the original signal frequency, and thus they can be identified as higher harmonics in the frequency domain of the captured signal [56]. One-dimensional plane waves moving in a single direction (x-direction) inside the material can be expressed by the following second order elastodynamic wave equation

$$\frac{\partial^2 u(x,t)}{\partial t^2} - c^2 \frac{\partial^2 u(x,t)}{\partial x^2} = \beta c^2 \left(\frac{\partial u(x,t)}{\partial x}\right)\left(\frac{\partial^2 u(x,t)}{\partial x^2}\right), \quad (1)$$

where $u(x,t)$ denotes the wave displacement, c represents the wave velocity and β is a pressure-volumetric nonlinear factor in the second order [57]. The second order perturbation solution of equation (1) is

$$u(x,t) = A_1 \sin(kx - \omega t) - A_2 \cos[2(kx - \omega t)] \,, \tag{2}$$

with

$$A_2 = \frac{\beta k^2 A_1^2}{8} x \,, \tag{3}$$

where A_1 is the amplitude of the waves received at the fundamental harmonic frequency, A_2 is the amplitude of waves received at the second harmonic frequency related to the nonlinear material behaviour, x is the distance of wave propagation, ω is the angular frequency and k is the wave number [58]. Since k is constant, parameter β can be considered

$$\beta \propto \frac{A_2}{{A_1}^2 x} \,. \tag{4}$$

Assuming A_2 amplitude is higher when the receiving transducer is closer to the damage location, due to lower attenuation of ultrasonic waves, then β is also expected to be higher in the sensor-to-sensor paths near the damage. Hence, a map of β magnitude across the inspected area can be created by calculating the β values in all paths.

3 Damage Localisation Method

As illustrated in Figure 1, damage localisation was performed using a circular array of eight ultrasonic transducers containing piezoelectric lead zirconate titanate (PZT) disks with central frequency of 310 kHz (PI Ceramic PIC255-00004137). The sensors were coupled to the CFRP panels using water-based gel.

3.1 Sensor Functionality Check

In the initial part of the method, sensor functionality is checked to avoid taking into consideration additional ultrasonic nonlinearities arising from malfunctioning transducers instead of the acoustic response of the CFRP material. As shown in Figure 1, the transducers are inspected by assessing the propagation of ultrasonic waves in both directions of each path on the periphery of the inspected region (d_{12}, d_{21}, d_{23}, d_{32}, etc.). The forward and backward directions between two sensors (e.g. sensors S1 and S2) have the same length and fibre orientation. Hence, signals in directions d_{12} and d_{21} must be almost identical if both sensors are operating normally and no damage exists in the path. This can be confirmed by calculating the Pearson product-moment correlation coefficient (r) for the two time signals. This is a numerical measure of the strength (i.e. signal

amplitude) and direction of the linear relationship between two variables. The value of r ranges from −1 to +1, where ±1 indicates the strongest possible agreement and 0 the strongest possible disagreement [59].

At this point it must be noticed that the comparison between the forward and backward signals is a common technique for sensor inspection in literature. However, the way the sensor functionality check was carried out in this SHM method offers some advantages. Firstly, the waves propagating in the short outer paths are expected to have less interaction with possible material defects compared to the paths crossing through the inspected area. Hence, a change in the signal is more likely to indicate a malfunctioning sensor. In addition, each transducer is checked using the signals acquired only in the two paths connecting it to its adjacent sensors (on either side of it), making the process simpler and quicker. In fact, as illustrated in Figure 1, one value of r is obtained for every pair of sensors (r_{12}, r_{23}, etc.). A transducer is considered faulty, only if the two values of r associated with it are both evidently lower than 1. For example, if r_{12}= 0.323, r_{23}= 0.445 and r_{34} to r_{81}= 0.998, then there is probably an issue with S2. However, if r_{12}= 0.997, r_{23}= 0.445 and r_{34} to r_{81}= 0.998, then sensor S2 cannot be regarded faulty since r_{12} is almost equal to 1. This suggests that the effectiveness of sensor functionality check is not affected by the presence of damage in the peripheral paths, and this is another advantage. For composite plates with different material properties and lay-up, the magnitude of r can vary. Therefore, the following calculation is used to determine what magnitude of r is relatively low. At first, the mean and standard deviation (SD) of all r values is calculated. Then the SD is subtracted from the mean, and the obtained value is set as a limit. Next, the mean of r values being greater than the limit is re-calculated, and used as the final limit. Any r values smaller than 95% of the final limit are assumed “low” and a value of 0.5 is assigned to them. The remaining ones are assumed “high” and become equal to 1. By plotting the paths with values of either 0.5 or 1 helps to decide whether a transducer is malfunctioning.

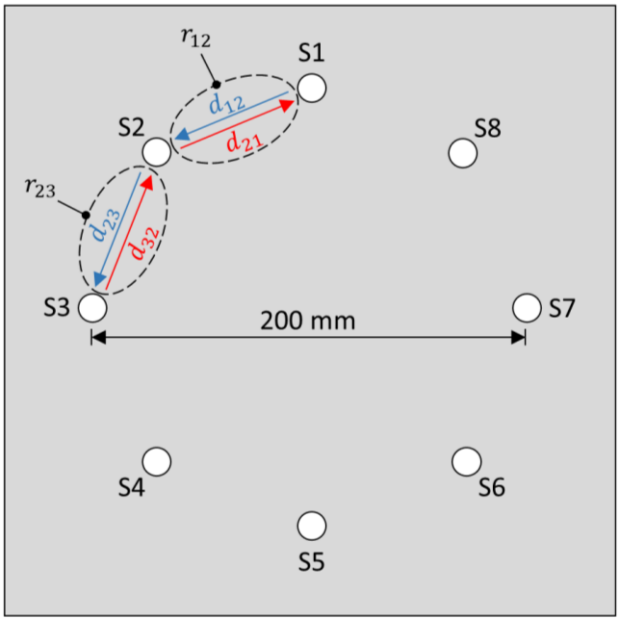

Figure 1: Example of functionality check of sensor S2 based on the correlation coefficients r_{12} and r_{23} of the time signals in directions d_{12}, d_{21} and d_{23}, d_{32} respectively.

3.2 Damage Localisation

The second part of the method enables damage localisation in composite panels by examining the nonlinear ultrasonic response of the material. Every transducer on the array transmits an ultrasonic signal in turn, and the waves propagating inside the material are received by the remaining sensors. The input signal is initially swept from a low frequency (f_L) to a high frequency (f_H), where f_L and f_H are around 200 kHz above and below the central frequency of the transducers. Next, the average of all signals recorded in both directions of the sensor-to-sensor paths is plotted in the frequency spectrum. This allows the identification of the single frequency (f_S) associated with the highest received signal amplitude. At f_S, stronger damage excitation is expected due to higher wave propagation energy. Hence, to achieve damage localisation, the transmission-reception process is performed using driving signals of f_S. The ultrasonic spectrum acquired from each pair of sensors is used to obtain the received signal amplitude (measured as voltage) at f_S and $2f_S$ (i.e. A_{f_s} and A_{2f_s}). According to the theory provided in Section 2, the nonlinear parameter β can be calculated using the following expression

$$\beta_{ij} \propto \frac{A_{2f_s}}{\left(A_{fs}{}^2\right)L_{ij}}, \tag{5}$$

where the subscripts i and j indicate the transmitting and receiving sensors, and L_{ij} is the distance between sensors i and j (i.e. path length).

The path connecting each pair of transducers is then drawn as a flat in-plane ellipse (in x- and y-axes) with an out-of-plane amplitude (z-axis) equal to the corresponding value of β (Figure 2). By adding up the ellipses, a map is created showing the in-plane variation of β magnitude on the composite plate, and the location of maximum β is expected to indicate the position of damage. It must be mentioned that the use of ellipses instead of lines for path representation is common in literature [43, 50, 51, 60]. The main benefit is that depending on the number of sensors used, the minor axis (width) of the ellipses can be adjusted to avoid leaving gaps within the inspected region. This adjustment is required only once for an array of specific size and number of sensors, and it is achieved by trial and error during the drawing of ellipses.

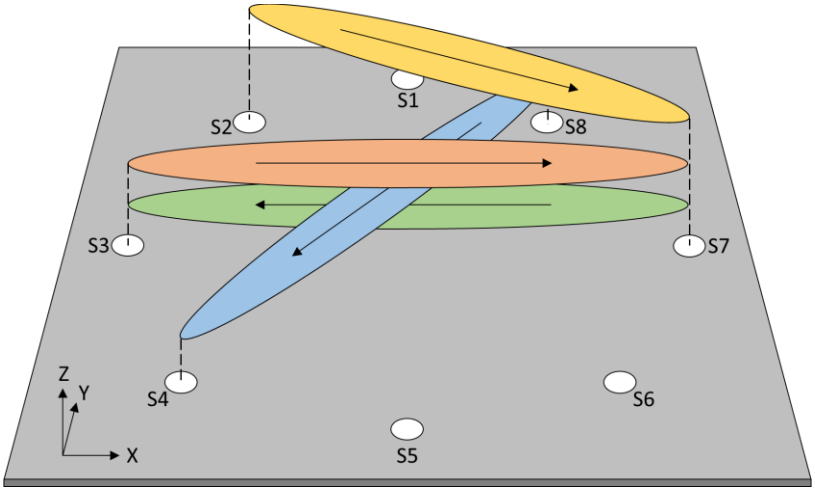

Figure 2: Illustration of nonlinear parameter β amplitude assigned to four sensor-to-sensor paths in the form of ellipses.

4 Experimentation

4.1 CFRP Test Panels

The method explained in the previous section, was experimentally tested on three different CFRP panels of unknown lay-up and prepreg type, with BVID from unknown impact object and energy level. As shown in Figure 3, panels 1 and 2 were flat and rectangular (~13 mm thick), whereas panel 3 was trapezoid (~6 mm thick) and slightly curved in the direction of its long axis. In all composite laminates, the area around the impact location was examined through C-scanning, to reveal the shape and size of internal delamination. The inspection was performed with a 5 MHz ultrasonic probe made of 128 elements, connected to an imaging system from Diagnostic Sonar Ltd. The results are presented in Figure 4.

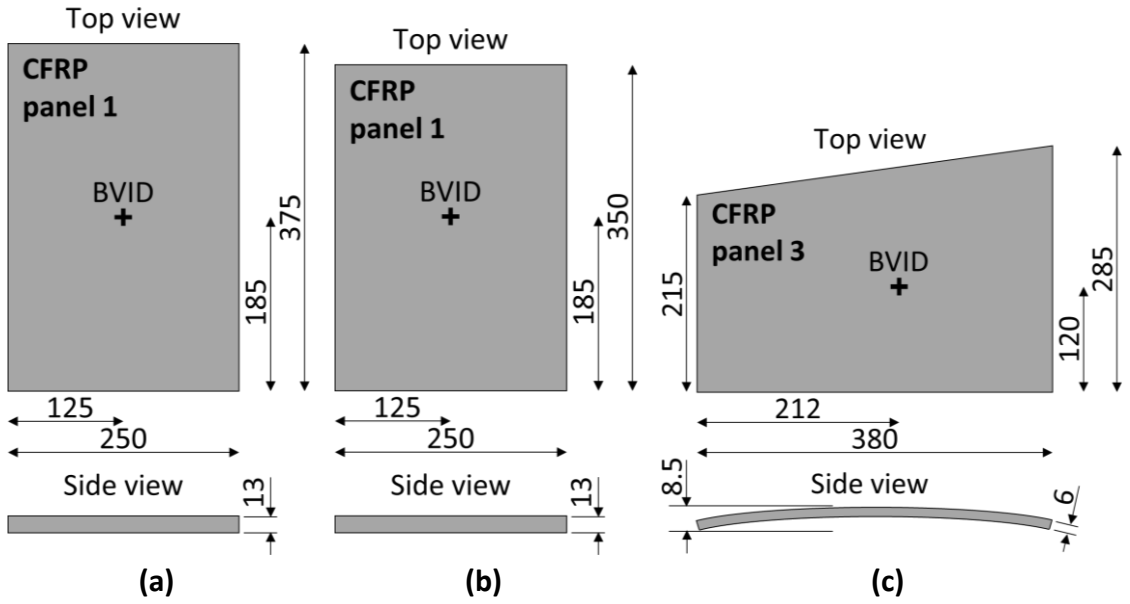

Figure 3: Illustration of CFRP panel 1 (a), 2 (b) and 3 (c) - Dimensions in mm. Not to scale.

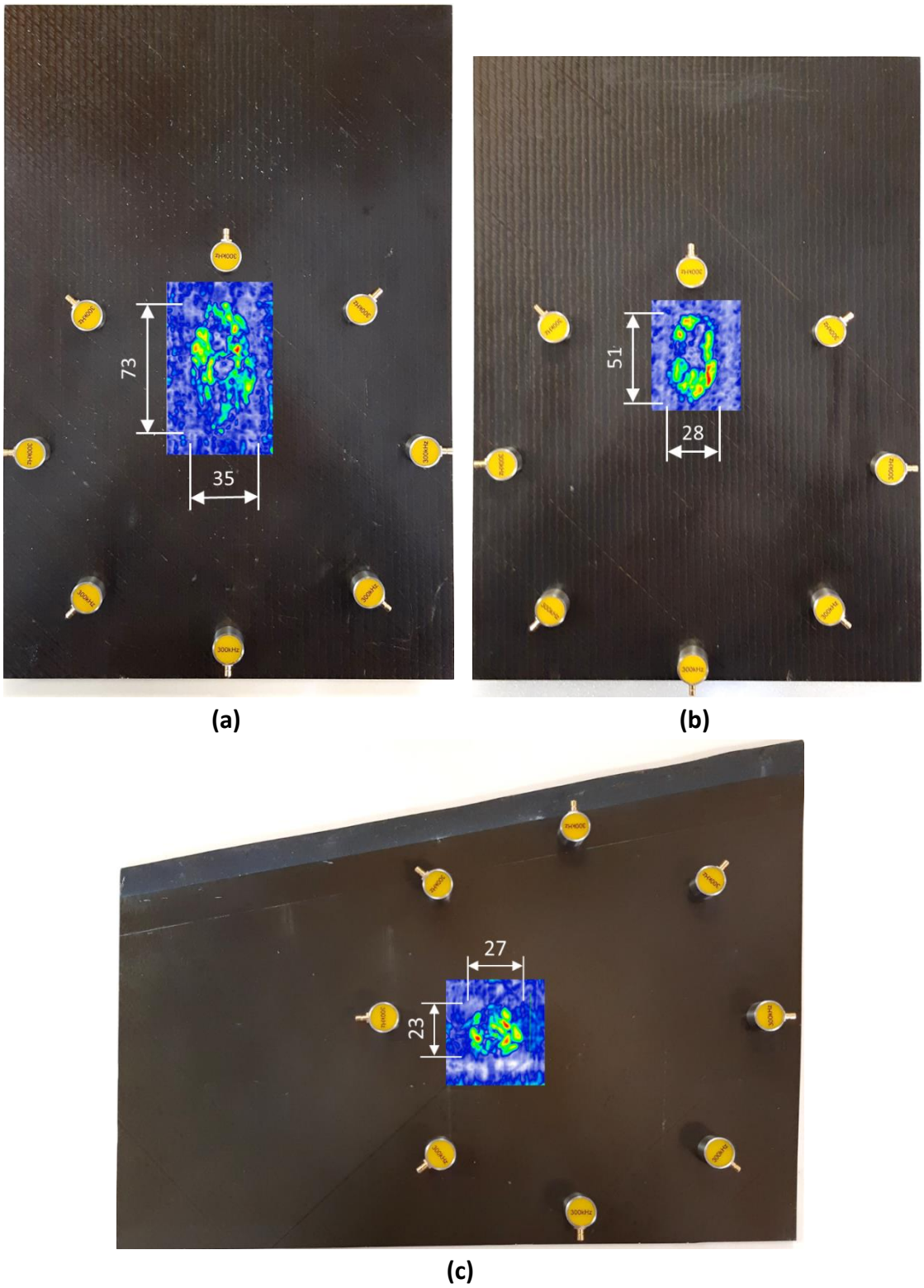

Figure 4: C-scan around the location of BVID on CFRP panels 1 (a), 2 (b) and 3 (c).

4.2 Ultrasonic Data Acquisition

The set-up illustrated in Figure 5 was used for the acquisition of ultrasonic data in all three CFRP laminates through eight circular piezoelectric PZT transducers (PIC 255 elements) with 310 kHz central frequency. An NI PXI-1033 chassis equipped with a single-channel arbitrary waveform generator module (NI PXI-5421) and an eight-channel signal digitiser module (NI PXI-5105) was controlled by a computer system designed in LabVIEW platform. The input signal voltage was set to 250 V with the use of an amplifier (Falco Systems WMA-300). The process of ultrasonic wave transmission-reception was performed sequentially. At every step, one of the transducers was excited for 10 ms and the propagating waves were captured by the remaining seven sensors over a period of 11 ms at a sampling rate of 6 MHz. This resulted in a total of 56 signals obtained from 28 sensor-to-sensor paths with two directions each.

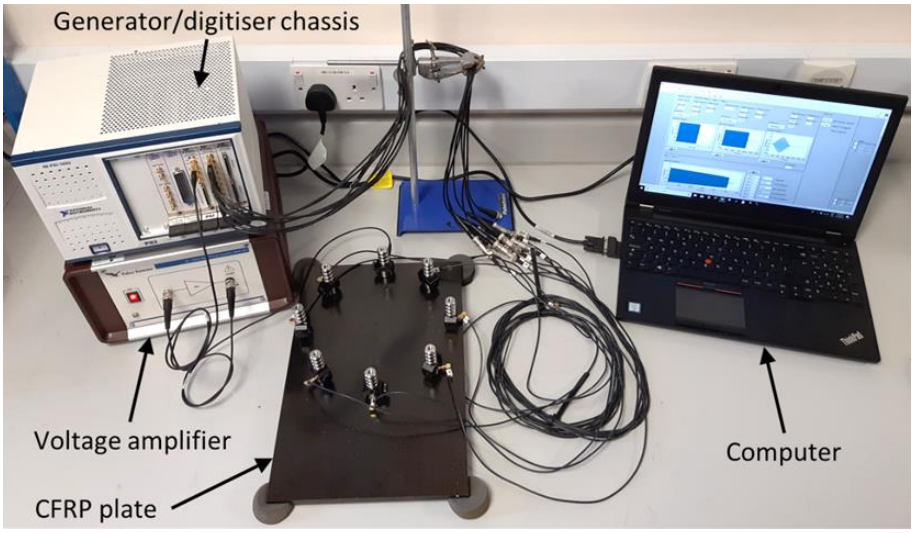

Figure 5: Illustration of the set-up used in the nonlinear ultrasonic experiments.

Prior to performing damage localisation, the ability of the proposed method to inspect the functionality of sensors was demonstrated on CFRP panel 1 following the procedure described in Section 3.1. The input signal frequency was swept from 100 kHz (f_L) to 500 kHz (f_H). Initially, ultrasonic data were recorded using eight fully functional transducers. Then, sensor S6 was replaced with an identical transducer that was partially damaged due to accidental application of high voltage for a long period, and data acquisition was repeated. In the latter case, correlation coefficients r_{56} and r_{67} were expected to be

evidently lower than the remaining r values, thus they were expected to be assigned with a value of 0.5.

Moving to the damage localisation process, the eight-sensor array was positioned on each CFRP panel as shown in Figure 6. The exact coordinates of the sensors and the damage were listed in Table 1, with the origin taken as the bottom left corner of the panels. Starting from panel 1, the sensor array was placed at two different positions around the BVID (Figure 6a) to confirm that the detected damage location would change relative to the array. Next, the experiment was carried out on laminate 2 to localise BVID of different size on a CFRP plate with similar thickness. Finally, the method was tested on sample 3, for the detection of BVID position on a thinner CFRP laminate of more complex shape (i.e. curved with unparallel sides).

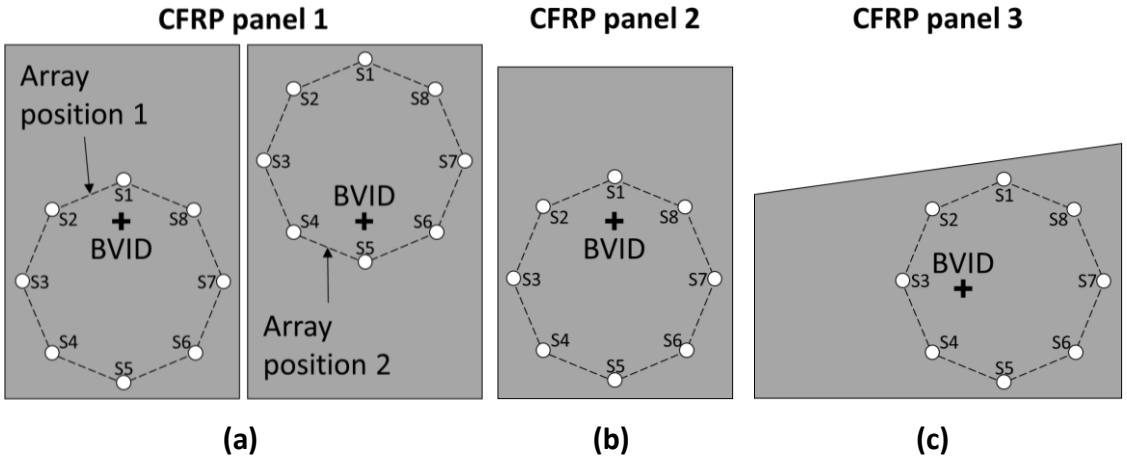

Figure 6: Positioning of sensor array around the location of BVID on CFRP panel 1 (a), 2 (b) and 3 (c).

Table 1: Coordinates of sensors and damage on CFRP panels 1, 2 and 3.

Sensor/Damage ID	**Panel 1 - Array 1 x, y (mm)**	**Panel 1 - Array 2 x, y (mm)**	**Panel 2 x, y (mm)**	**Panel 3 x, y (mm)**
S1	125, 226	125, 344	125, 222	260, 225
S2	55, 196	55, 314	55, 192	190, 195
S3	25, 126	25, 244	25, 122	160, 125
S4	55, 56	55, 174	55, 52	190, 55
S5	125, 26	125, 144	125, 22	260, 25
S6	195, 56	195, 174	195, 52	330, 55
S7	225, 126	225, 244	225, 122	360, 125
S8	195, 196	195, 314	195, 192	330, 195
Damage	125, 185	125, 185	125, 185	212, 120

The signals of 100-500 kHz sweeps (f_L to f_H) that were previously recorded in all paths during the sensor functionality check, were averaged to obtain the combined frequency response of each CFRP panel. As an example, the average frequency spectrum of CFRP plate 2 was plotted in Figure 7. From this plot, the single frequency f_S corresponding to the highest received signal amplitude (in mV) was identified as 357.9 kHz. According to Section 3.2, the ultrasonic transmission-reception process was performed using input signals of single frequency f_S, and the nonlinear parameter β in each of the 56 paths was calculated from the recorded signal amplitude at f_S and $2f_S$ (ref. equation 5). For example, in the case of panel 2, the spectrum of the signals captured by S1 and S5 under excitation of S3 was plotted in Figure 8. Paths S3-S1 and S3-S5 had the same length and fibre orientation in the material, but only S3-S1 was directly crossing through the damage. As can be seen in Figure 8a, the signal received by S1 had lower amplitude at f_S and higher at $2f_S$, relative to the signal captured by S5 (Figure 8b). Therefore, the β value of path S3-S1 was twice as big as that of S3-S5. In the same way, the signals captured in all 56 paths of each CFRP panel were used to create the map of β (as explained in Section 3.2) highlighting the location of impact damage.

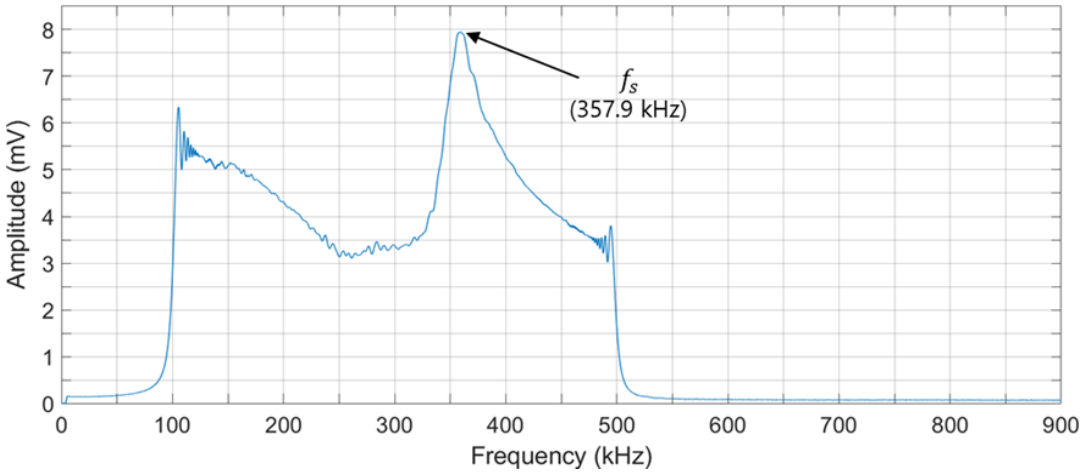

Figure 7: Average plot of the received signals spectrum captured in all paths of CFRP panel 2 under ultrasonic excitation from 100 kHz to 500 kHz.

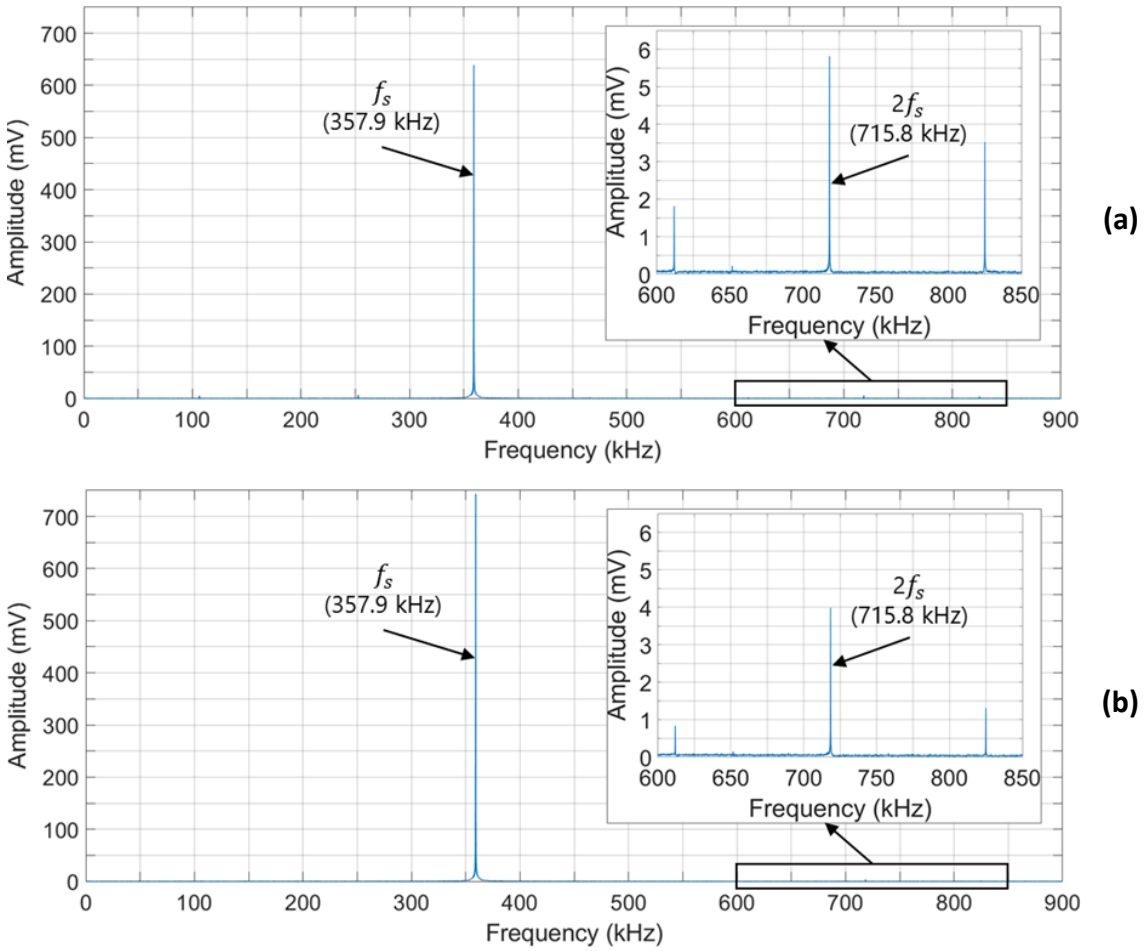

Figure 8: Frequency spectrum of the signal received by (a) sensor S1 and (b) sensor S5 on CFRP panel 2 under ultrasonic excitation of sensor S3 at f_s = 357.9 kHz.

5 Results and Discussion

Starting from the sensor functionality check conducted on CFRP panel 1, when all eight transducers were operating normally, the correlation coefficients between the signals in both directions of each sensor-to-sensor path (ie. r_{12} to r_{81}) were all assigned with a value of 1 (see Figure 9a) based on the procedure explained in Section 3.1. However, when a partially damaged transducers was included in the array at position S6, both r_{56} and r_{67} were marked with a value of 0.5 while the remaining r values remained equal to 1 (Figure 9b). This confirmed the capability of the proposed algorithm to detect a malfunctioning sensor.

About the damage localisation results, in CFRP laminate 1 the determined value of f_S related to the highest signal amplitude was found to be 280 kHz for sensor array position 1, and 237.1 kHz for position 2. In panels 2 and 3, f_S was 357.9 kHz and 341.9 kHz respectively. After performing ultrasonic wave transmission at f_S (ref. Section 3.2), the normalised map of nonlinear parameter β on CFRP panel 1 was plotted for each sensor array position (1 and 2), as illustrated in Figure 10a and Figure 10b. The analogous maps of β for panels 2 and 3 were presented in Figure 10c and Figure 10d. In Figure 11, the same maps were plotted after applying a threshold from 0.99 to 1, for better illustration of the peak values of β. According to these maps, the BVID was successfully located in all different cases within an error range of 4 to 22 mm (average of ~12 mm). It must be noted that the localisation error was measured from the estimated damage location to the boundary of BVID. If the error was measured from the centre of impact, the corresponding range would be 23 to 43 mm. However, this would not be sensible because stronger acoustic nonlinearities may arise from specific areas (e.g. bigger delamination areas) within the damaged region, and not necessarily from the centre of impact. In fact, the C-scans provided in Figure 4 indicated that the areas of bigger delamination were off-centred, and in most cases, they were close to the estimated damage position.

Finally, it is important to be noticed that in the experiments of this paper the transducers were not placed symmetrically away from the laminate edges, and panel 3 was slightly curved with unparallel sides. This suggested that multi-directional wave reflections of different amplitude had not a significant effect on the accuracy of the presented method.

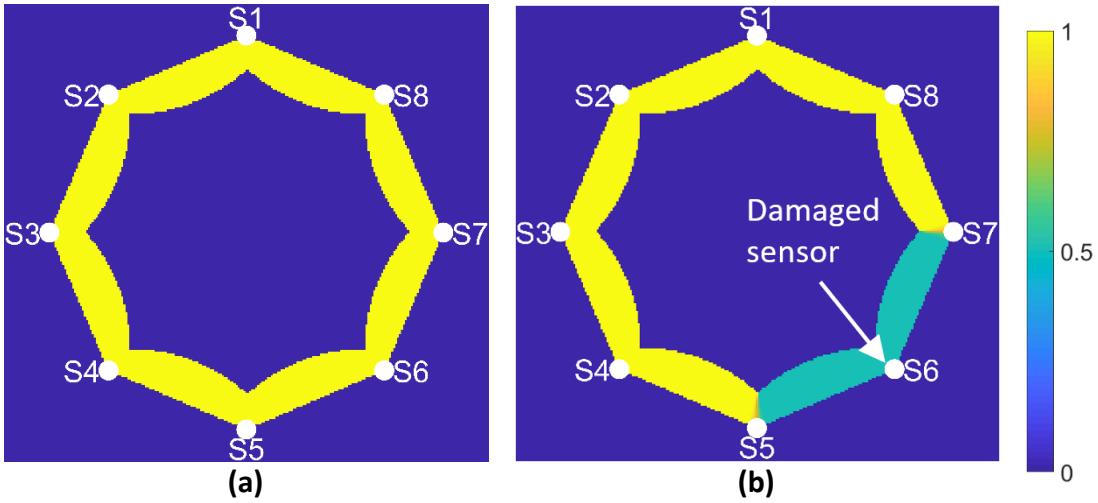

Figure 9: Plot of correlation coefficients between the forward and backward signals in outer sensor-to-sensor paths using eight functional sensors (a) and after replacing S6 with a partially damaged sensor (b).

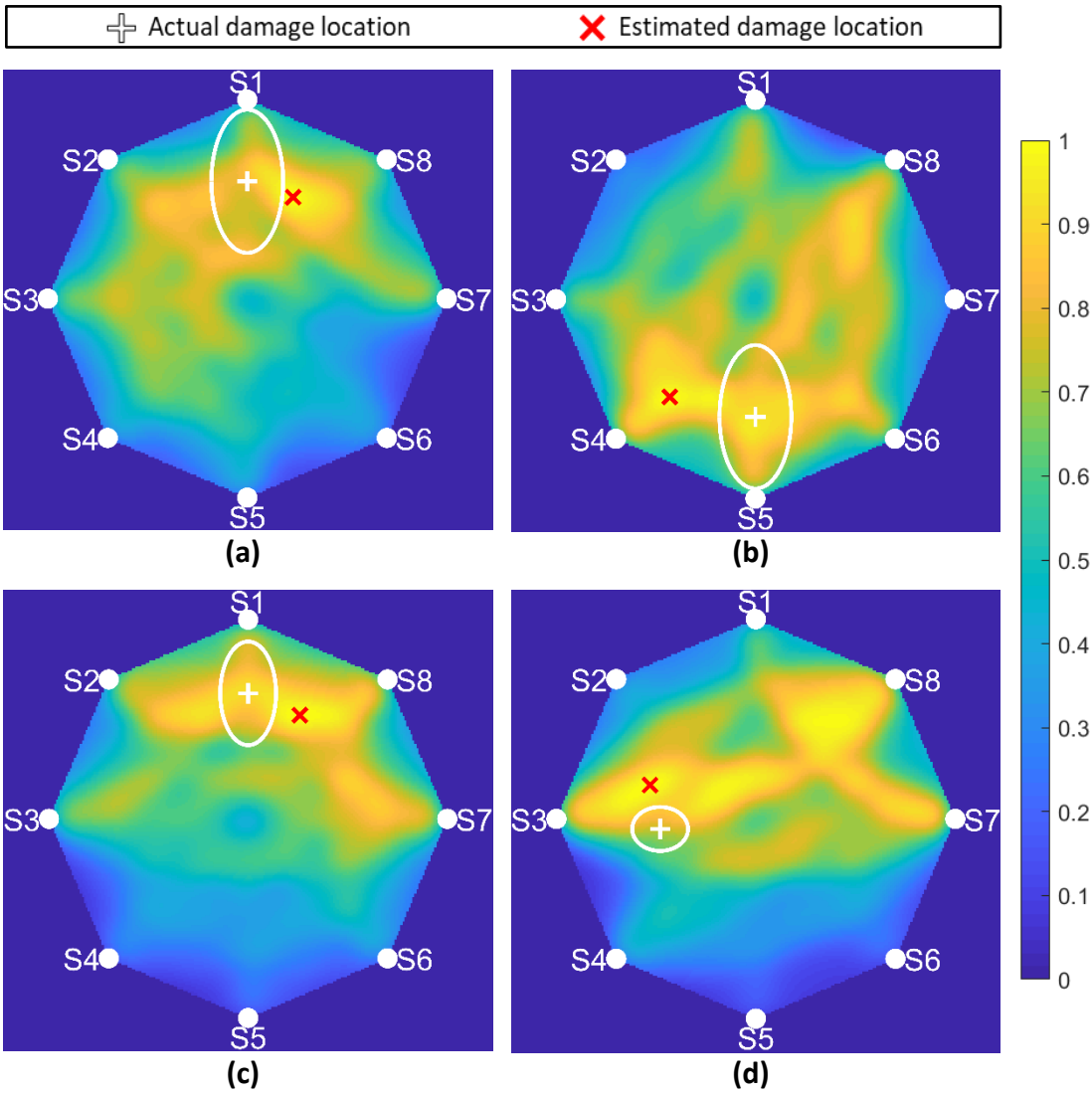

Figure 10: Normalised map of nonlinear parameter β in CFRP panel 1 - array position 1 (a), panel 1 - array position 2 (b), panel 2 (c) and panel 3 (d). The ellipses represent the actual size of internal delamination.

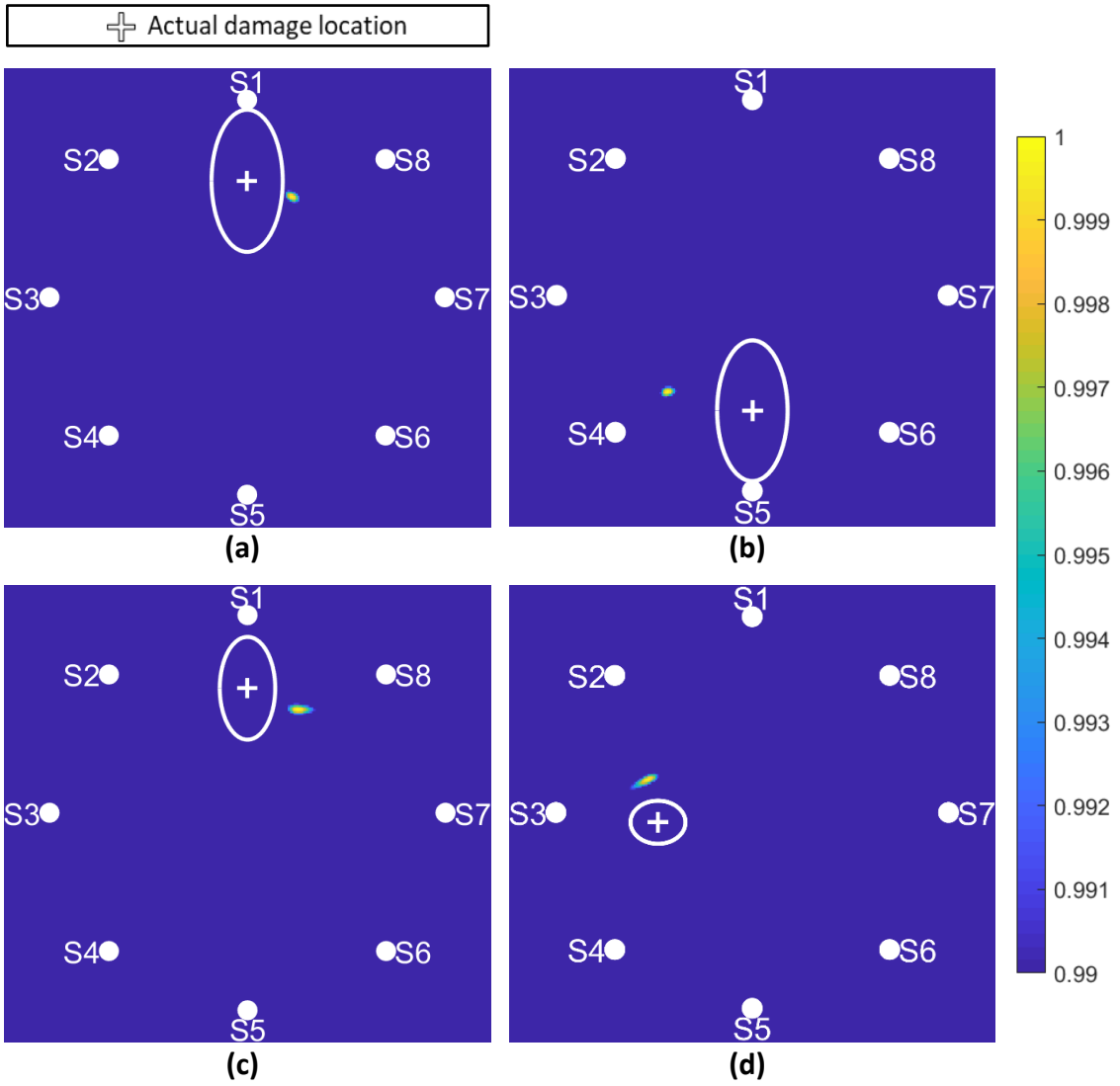

Figure 11: Normalised map with threshold of nonlinear parameter β in CFRP panel 1 - array position 1 (a), panel 1 - array position 2 (b), panel 2 (c) and panel 3 (d). The ellipses represent the actual size of internal delamination.

6 Conclusions

A new method for nonlinear ultrasonic localisation of BVID in composite materials was introduced in this paper. This method involves simple determination of the required signal transmission frequency, there is no need for complex measurements related to the time-of-flight of propagating waves, and the accuracy of damage positioning does not rely on the acquisition of baseline signals (i.e. data obtained at the pristine state of the material). The proposed technique is based on the transmission and reception of ultrasonic waves through the material using a circular array of transducers coupled to the surface of the

inspected laminate. As explained in Section 3, this method is capable of checking the functionality of sensors, based on the correlation coefficient between the signals in the forward and backward directions of the paths around the periphery of the senor network. Regarding the detection of damage location, this can be achieved by acquiring ultrasonic signals in sensor-to-sensor paths over a wide range of frequencies (frequency sweep). Once the average of all received signals in the frequency domain is calculated, the frequency associated with the highest received signal amplitude can be determined. Ultrasonic signals of the chosen frequency are then re-transmitted from every transducer in turn, and the value of nonlinear parameter β in the individual paths is calculated from the signal received by the remaining sensors. By summing up the β values, a map of the material nonlinearity amplitude across the composite panel can be created.

The effectiveness of the presented method was experimentally tested on three CFRP panels of unknown lay-up and prepreg type with different dimensions, shape and size of BVID. In all cases, the position of damage was estimated with an accuracy of 4 to 22 mm, and the detection of a malfunctioning transducer was successfully demonstrated on CFRP laminate 1. Based on the above, it is concluded that the proposed method can be considered an improved alternative to existing techniques for localisation of damage in fibre reinforced composite laminates.

References

1. Yeum, C. M., Sohn, H., Ihn, J. B., & Lim, H. J. (2012). Instantaneous delamination detection in a composite plate using a dual piezoelectric transducer network. *Composite Structures*, 94(12), 3490-3499.
2. Vavilov, V. P., & Burleigh, D. D. (2015). Review of pulsed thermal NDT: Physical principles, theory and data processing. *NDT & E International*, 73(1), 28-52.
3. Chrysafi, A. P., Athanasopoulos, N., & Siakavellas, N. J. (2017). Damage detection on composite materials with active thermography and digital image processing. *International Journal of Thermal Sciences*, 116(1), 242-253.
4. Wang, Z., Tian, G., Meo, M., & Ciampa, F. (2018). Image processing based quantitative damage evaluation in composites with long pulse thermography. *NDT & E International*, 99(1), 93-104.
5. Deane, S., Avdelidis, N. P., Ibarra-Castanedo, et al. (2019). Application of NDT thermographic imaging of aerospace structures. *Infrared Physics & Technology*, 97(1), 456-466.
6. Cheng, J., Qiu, J., Xu, X., Ji, H., Takagi, T., & Uchimoto, T. (2016). Research advances in eddy current testing for maintenance of carbon fiber reinforced plastic composites. *International Journal of Applied Electromagnetics and Mechanics*, 51(3), 261-284.
7. Hamill, L., Emerson, J., McGushion, K., & Nutt, S. (2018). Low frequency eddy current testing of insulators and composites. *Journal of Nondestructive Evaluation*, 37(3), 58.

8. Mizukami, K., bin Ibrahim, A. S., Ogi, K., Matvieieva, N., Kharabet, I., Schulze, M., & Heuer, H. (2019). Enhancement of sensitivity to delamination in eddy current testing of carbon fiber composites by varying probe geometry. *Composite Structures*, 226(1), 111227.

9. Dos Santos, F. L. M., Peeters, B., Van der Auweraer, H., Góes, L. C. S., & Desmet, W. (2016). Vibration-based damage detection for a composite helicopter main rotor blade. *Case Studies in Mechanical Systems and Signal Processing*, 3(1), 22-27.

10. Segers, J., Kersemans, M., Hedayatrasa, S., Calderon, J., & Van Paepegem, W. (2018). Towards in-plane local defect resonance for non-destructive testing of polymers and composites. *NDT & E International*, 98(1), 130-133.

11. Samir, K., Brahim, B., Capozucca, R., & Wahab, M. A. (2018). Damage detection in CFRP composite beams based on vibration analysis using proper orthogonal decomposition method with radial basis functions and cuckoo search algorithm. *Composite Structures*, 187(1), 344-353.

12. Staszewski, W. J. (2004). Structural health monitoring using guided ultrasonic waves. In *Advances in Smart Technologies in Structural Engineering* (Vol. 1, p. 117-162). Springer.

13. Jhang, K. Y. (2009). Nonlinear ultrasonic techniques for nondestructive assessment of micro damage in material: a review. *International journal of precision engineering and manufacturing*, 10(1), 123-135.

14. Romhany, G., Czigany, T., & Karger-Kocsis, J. (2017). Failure assessment and evaluation of damage development and crack growth in polymer composites via localization of acoustic emission events: a review. *Polymer Reviews*, 57(3), 397-439.

15. Mitra, M., & Gopalakrishnan, S. (2016). Guided wave based structural health monitoring: A review. *Smart Materials and Structures*, 25(5), 053001.

16. Ono, K. (2018). Review on structural health evaluation with acoustic emission. *Applied Sciences*, 8(6), 958.

17. Ghori, S. W., Siakeng, R., Rasheed, M., Saba, N., & Jawaid, M. (2018). The role of advanced polymer materials in aerospace. In *Sustainable Composites for Aerospace Applications* (Vol.1, p. 19-34). Woodhead Publishing.

18. Abbas, S., Li, F., & Qiu, J. (2018). A review on SHM techniques and current challenges for characteristic investigation of damage in composite material components of aviation industry. *Materials Performance and Characterization*, 7(1), 224-258.

19. Sudevan, D., Prakash, R. V., & Kamaraj, M. (2015). Post-impact fatigue response of CFRP laminates under constant amplitude and programmed FALSTAFF spectrum loading. *Procedia Engineering*, 101(1), 395-403.

20. Wu, Z., Liu, K., Wang, Y., & Zheng, Y. (2015). Validation and evaluation of damage identification using probability-based diagnostic imaging on a stiffened composite panel. *Journal of Intelligent Material Systems and Structures*, 26(16), 2181-2195.

21. Wilcox, P. D. (2003). Omni-directional guided wave transducer arrays for the rapid inspection of large areas of plate structures. *IEEE Transactions on Ultrasonics, Ferroelectrics, and Frequency Control*, 50(6), 699-709.

22. Giurgiutiu, V., & Bao, J. (2004). Embedded-ultrasonics structural radar for in situ structural health monitoring of thin-wall structures. *Structural Health Monitoring*, 3(2), 121-140.

23. Malinowski, P., Wandowski, T., Trendafilova, I., & Ostachowicz, W. (2009). A phased array-based method for damage detection and localization in thin plates. *Structural Health Monitoring*, 8(1), 5-15.

24. Leleux, A., Micheau, P., & Castaings, M. (2013). Long range detection of defects in composite plates using Lamb waves generated and detected by ultrasonic phased array probes. *Journal of Nondestructive Evaluation*, 32(2), 200-214.

25. Liu, Z., Sun, K., Song, G., He, C., & Wu, B. (2016). Damage localization in aluminum plate with compact rectangular phased piezoelectric transducer array. *Mechanical Systems and Signal Processing*, 70(1), 625-636.

26. Kudela, P., Radzienski, M., Ostachowicz, W., & Yang, Z. (2018). Structural Health Monitoring system based on a concept of Lamb wave focusing by the piezoelectric array. *Mechanical Systems and Signal Processing*, 108(1), 21-32.

27. Senyurek, V. Y., Baghalian, A., Tashakori, S., McDaniel, D., & Tansel, I. N. (2018). Localization of multiple defects using the compact phased array (CPA) method. *Journal of Sound and Vibration*, 413(1), 383-394.

28. Michaels, J. E. (2008). Detection, localization and characterization of damage in plates with an in situ array of spatially distributed ultrasonic sensors. *Smart Materials and Structures*, 17(3), 035035.

29. Ihn, J. B., & Chang, F. K. (2008). Pitch-catch active sensing methods in structural health monitoring for aircraft structures. *Structural Health Monitoring*, 7(1), 5-19.

30. Cai, J., Shi, L., Yuan, S., & Shao, Z. (2011). High spatial resolution imaging for structural health monitoring based on virtual time reversal. *Smart Materials and Structures*, 20(5), 055018.

31. Qiu, L., Liu, M., Qing, X., & Yuan, S. (2013). A quantitative multidamage monitoring method for large-scale complex composite. *Structural Health Monitoring*, 12(3), 183-196.

32. Sharif-Khodaei, Z., & Aliabadi, M. H. (2014). Assessment of delay-and-sum algorithms for damage detection in aluminium and composite plates. *Smart Materials and Structures*, 23(7), 075007.

33. Yu, L., & Tian, Z. (2016). Guided wave phased array beamforming and imaging in composite plates. *Ultrasonics*, 68(1), 43-53.

34. Nokhbatolfoghahai, A., Navazi, H. M., & Groves, R. M. (2019). Use of delay and sum for sparse reconstruction improvement for structural health monitoring. *Journal of Intelligent Material Systems and Structures*, 30(18-19), 2919-2931.

35. Fink, M. (1992). Time reversal of ultrasonic fields. I. Basic principles. *IEEE Transactions on Ultrasonics, Ferroelectrics, and Frequency Control*, 39(5), 555-566.

36. Wang, C. H., Rose, J. T., & Chang, F. K. (2004). A synthetic time-reversal imaging method for structural health monitoring. *Smart Materials and Structures*, 13(2), 415-423.

37. Ciampa, F., & Meo, M. (2012). Impact detection in anisotropic materials using a time reversal approach. *Structural Health Monitoring*, 11(1), 43-49.

38. Mustapha, S., Ye, L., Dong, X., & Alamdari, M. M. (2016). Evaluation of barely visible indentation damage (BVID) in CF/EP sandwich composites using guided wave signals. *Mechanical Systems and Signal Processing*, 76(1), 497-517.

39. De Simone, M. E., Andreades, C., Hilmi, A. M., Meo, M., & Ciampa, F. (2019). Proof of concept for a smart composite orbital debris detector. *Acta Astronautica*, 160(1), 499-508.

40. Huang, L., Du, J., Chen, F., & Zeng, L. (2019). An Efficient Time Reversal Method for Lamb Wave-Based Baseline-Free Damage Detection in Composite Laminates. *Applied Sciences*, 9(1), 11.

41. Eremin, A., Glushkov, E., Glushkova, N., & Lammering, R. (2019). Guided wave time-reversal imaging of macroscopic localized inhomogeneities in anisotropic composites. *Structural Health Monitoring*, 18(5-6), 1803-1819.

42. Quaegebeur, N., & Masson, P. (2012). Correlation-based imaging technique using ultrasonic transmit-receive array for non-destructive evaluation. *Ultrasonics*, 52(8), 1056-1064.

43. Memmolo, V., Ricci, F., Boffa, N. D., Maio, L., & Monaco, E. (2016). Structural health monitoring in composites based on probabilistic reconstruction techniques. *Procedia Engineering*, 167(1), 48-55.

44. Flynn, E. B., Todd, M. D., Wilcox, P. D., Drinkwater, B. W., & Croxford, A. J. (2011). Maximum-likelihood estimation of damage location in guided-wave structural health monitoring. *Proceedings of the Royal Society A: Mathematical, Physical and Engineering Sciences*, 467(2133), 2575-2596.

45. Haynes, C., & Todd, M. (2015). Enhanced damage localization for complex structures through statistical modeling and sensor fusion. *Mechanical Systems and Signal Processing*, 54(1), 195-209.

46. Gao, H., Shi, Y., & Rose, J. L. (2005). Guided wave tomography on an aircraft wing with leave in place sensors. In *AIP Conference Proceedings* (Vol. 760, p. 1788-1794). AIP Publishing.

47. Zhao, X., Gao, H., Zhang, G., Ayhan, B., Yan, F., Kwan, C., & Rose, J. L. (2007). Active health monitoring of an aircraft wing with embedded piezoelectric sensor/actuator network: I. Defect detection, localization and growth monitoring. *Smart Materials and Structures*, 16(4), 1208-1217.

48. Yan, F., Royer Jr, R. L., & Rose, J. L. (2010). Ultrasonic guided wave imaging techniques in structural health monitoring. *Journal of intelligent material Systems and Structures*, 21(3), 377-384.

49. Tabatabaeipour, M., Hettler, J., Delrue, S., & Van Den Abeele, K. (2014). Reconstruction algorithm for probabilistic inspection of damage (RAPID) in composites. In *11th European conference on non-destructive testing (ECNDT 2014)*.

50. Keulen, C. J., Yildiz, M., & Suleman, A. (2014). Damage detection of composite plates by Lamb wave ultrasonic tomography with a sparse hexagonal network using damage progression trends. *Shock and Vibration*, 949671.

51. Hettler, J., Tabatabaeipour, M., Delrue, S., & Van Den Abeele, K. (2016). Linear and nonlinear guided wave imaging of impact damage in CFRP using a probabilistic approach. *Materials*, 9(11), 901.

52. Lambinet, F., Sharif Khodaei, Z., & Aliabadi, F. M. (2018). Effectiveness of RAPID and SSM Algorithms on Composite Scarf Repair. In *Key Engineering Materials* (Vol. 774, p. 535-540). Trans Tech Publications Ltd.

53. Boccardi, S., Calla, D. B., Fierro, G. P. M., Ciampa, F., & Meo, M. (2016). Nonlinear damage detection and localization using a time domain approach. In *Nondestructive Characterization and Monitoring of Advanced Materials, Aerospace, and Civil Infrastructure 2016* (Vol. 9804, p. 98040T). International Society for Optics and Photonics.

54. Boccardi, S., Calla, D. B., Ciampa, F., & Meo, M. (2018). Nonlinear elastic multi-path reciprocal method for damage localisation in composite materials. *Ultrasonics*, 82(1), 239-245.

55. Soleimanpour, R., Ng, C. T., & Wang, C. H. (2017). Higher harmonic generation of guided waves at delaminations in laminated composite beams. *Structural Health Monitoring*, 16(4), 400-417.

56. Ciampa, F., Pickering, S. G., Scarselli, G., & Meo, M. (2017). Nonlinear imaging of damage in composite structures using sparse ultrasonic sensor arrays. *Structural Control and Health Monitoring*, 24(5), 1911.

57. Zagrai, A., Donskoy, D., Chudnovsky, A., & Golovin, E. (2008). Micro-and macroscale damage detection using the nonlinear acoustic vibro-modulation technique. *Research in Nondestructive Evaluation*, 19(2), 104-128.

58. Amura, M., Meo, M., & Amerini, F. (2011). Baseline-free estimation of residual fatigue life using a third order acoustic nonlinear parameter. *The Journal of the Acoustical Society of America*, 130(4), 1829-1837.

59. Taylor, J. R. (1997). *An Introduction to Error Analysis: The Study of Uncertainties in Physical Measurements* (Vol. 1, p. 217). 2nd ed. Sausalito: University Science Books.

60. Zhao Zhao, X., Royer, R. L., Owens, S. E., & Rose, J. L. (2011). Ultrasonic Lamb wave tomography in structural health monitoring. *Smart Materials and Structures*, 20(10), 105002.

Chapter 7

A Nonlinear Ultrasonic Approach for Through-Thickness Localisation of Contact Defects

The work reported in the journal paper (Paper V) of this chapter, was the last part of this research study, and focused on the localisation of several contact defects at different depths inside the inspected materials using an alternative phased array method for pulse-echo inspection. In particular, this work focused on the improvement of the signal-to-noise ratio in the acoustic response of the material for more effective identification of defect-related peaks. This was approached by optimising a nonlinear ultrasonic phased array technique which was based on the concept of frequency and amplitude modulation of longitudinal waves propagating at two different frequencies.

The presented method involved the recording of the material response at four individual steps of ultrasonic excitation. At each step, the elements of the phased array probe were excited in a programmed order for the transmission of waves through the inspected material at either a single frequency (f_1 or f_2), or at two frequencies (f_1 and f_2). The signals recorded at these four steps were then processed (added and/or subtracted) following a unique expression enabling the filtering of both the fundamental and the second-order harmonic features. More specifically, the ultrasonic response obtained from the processing expression was equal to the sum of the acoustic nonlinearity parameters ($\beta_s + \beta_d$) corresponding to the modulation sidebands at $f_s = f_2 + f_1$ and $f_d = f_2 - f_1$. In the present paper, this response was referred to as the nonlinear modulated response ($R_{\beta_s+\beta_d}$), and it was plotted in the time domain for the detection of peaks indicating the positions of contact flaws through the thickness of metallic and composite samples.

In fact, this alternative phased array method was tested on four multi-layered samples, two of which were made from aluminium disks and two from rectangular CFRP plates. The defect-related peaks in $R_{\beta_s+\beta_d}$ were compared to the peaks exhibited in the linear ultrasonic response (R_{f_1}) from wave transmission at f_1. The results obtained from all four test samples, revealed that the peaks in $R_{\beta_s+\beta_d}$ offered significantly higher values

of SNR, appeared to be substantially narrower (width at half-height) and indicated the expected positions of the interfaces with considerably smaller error.

The "Statement of Authorship" form and Paper V are following.

This declaration concerns the article entitled:			
A Nonlinear Ultrasonic Modulation Approach for the Detection and Localisation of Contact Defects			
Publication status			
Draft manuscript ☐ Submitted ☒ Accepted ☐ Published ☐			
Publication details (reference)			
Not Applicable			
Candidate's contribution to the paper (detailed, and also given as a percentage)			
Formulation of ideas: 50% My supervisor Professor Michele Meo proposed the idea of performing through-transmission modulation of waves for the detection of a contact defect laying perpendicularly to the direction of wave propagation. I suggested the localisation of multiple contact interfaces using a phased array probe in pulse-echo configuration. This required high sensitivity to ultrasonic nonlinearities which lead to the need for optimisation of the frequency and amplitude modulation evaluation (FAME) technique, which was previously developed by my co-author Dr Gian Piero Malfense Fierro.			
Design of methodology: 70% I decided on testing this method on both metallic and composite samples. Also, I designed and ordered the aluminium disks, and I chose the composite laminates used in the experiments. Dr Gian Piero Malfense Fierro helped in the programming of the ultrasonic signal firing from the phased array probe.			
Experimental work: 100% I designed the experimental set-up, chose the stacking sequence of the aluminium and composite samples, performed the ultrasonic experiments and collected the data.			
Presentation of data in journal format: 95% I processed the obtained data, created the figures, chose the structure of the paper and wrote the manuscript. Dr Gian Piero Malfense Fierro and my supervisor provided feedback on the above and supported the submission and review process.			
Statement from Candidate			
This paper reports on original research I conducted during the period of my Higher Degree by Research candidature.			
Signed		**Date**	02/10/2020

A Nonlinear Ultrasonic Modulation Approach for the Detection and Localisation of Contact Defects

Christos Andreades, Gian Piero Malfense Fierro, Michele Meo

Department of Mechanical Engineering, University of Bath, Bath BA2 7AY, UK

Abstract

Critical metallic and composite structures are periodically inspected for contact defects such as kissing bonds and delamination, using phased array techniques based on linear ultrasound. The detection of contact flaws at multiple depths in the material can be challenging due to high signal attenuation and noise level. In this study a new ultrasonic phased array approach relying on the nonlinear modulation of dual-frequency excitation was developed to improve the sensitivity and accuracy in the detection of contact defects. A phased array probe was used for the generation of single-frequency and dual-frequency waves, and the capturing of echoes. The flaws were detected using a new nonlinear modulated parameter characterising the response of the material arising only from the modulation sidebands at the sum and difference frequencies f_2+f_1 and f_2-f_1. Ultrasonic tests were conducted on materials with multiple contact interfaces. The novel parameter was plotted against the linear response, and the peaks indicating the contact interfaces were compared based on their signal-to-noise ratio (*SNR*), their width at half-height (6 dB drop) and their positioning error. The peaks of the novel modulated parameter offered up to 10^3 times higher *SNR*, up to 10 times smaller width at half-height and around 45% smaller localisation error than classical linear ultrasonic response. The results showed that the proposed approach could lead to more effective detection and more accurate localisation of contact defects in structural materials such as kissing bonds and closed delamination.

1 Introduction

Contact type defects can be found in metallic and composite structures in the form of kissing bond, closed crack, delamination and debonding [1]. This defect type can be described as an interface of plastic contact between the surfaces of two elastic solid layers with similar material properties. The layers are typically separated by a gap due to surface imperfections/roughness, meaning that a contact interface has no strength [2]. For this reason, the early identification of such flaws has been a significant requirement in non-destructive evaluation (NDE) of materials.

Contact defects of certain size are detectable using various linear ultrasonic methods relying on the interaction of propagating waves with the contact interface [3-6]. This interaction causes reflections, scattering and attenuation of waves that can be recorded by the same ultrasonic source or other transducers. Among these, linear pulse-echo techniques using phased arrays of piezoelectric elements are widely preferred for the inspection of internal defects in many aerospace, automotive and civil structures [7-9]. They enable quick acquisition of multiple one-dimensional amplitude waveforms (A-scans) that can be added to provide a cross-sectional amplitude image (B-scan) of the inspected medium. In addition, the array elements can be excited in a specific order and according to pre-set delay laws to achieve steering or focusing of ultrasonic wave beams for improved localisation and sizing of damage [10, 11]. Various studies on linear phased array methods demonstrated effective identification of contact flaws at a single interface in metallic or composite parts [12-16], but only few of them detected multiple defect interfaces through the material thickness [17, 18]. This can be very challenging, depending on the mechanical contact between the surfaces at each damaged plane. In the case of multiple contact defects with almost perfectly mated surfaces, the propagating waves are transmitted through the interfaces, meaning that the amplitude of reflected waves will be relatively low [19]. For a given noise level in the signal, such reflections may not be detectable. Equally, in a poor-contact scenario most of the incident wave energy will be reflected to the source from the first interface, thus only low-amplitude waves will be reflected from any interfaces existing deeper in the material [20]. Hence, new ultrasonic methods of higher sensitivity to defect identification are required.

Over the last years, different research studies proposed nonlinear ultrasonic phased array techniques. In general, ultrasonic methods focusing on the assessment of acoustic

nonlinearities in the material response have shown higher accuracy to the detection of micro-defects than linear ultrasonic methods, especially at the early stages of damage formation [21]. Briefly, under single-frequency (f_1) excitation, nonlinearities are detectable in the received signal spectrum in the form of higher harmonics ($2f_1, 3f_1$ etc.) and sub-harmonics ($f_1/2$, $f_1/3$ etc.) [22-24]. Based on that, some studies demonstrated accurate monitoring of fatigue crack growth in metallic samples using nonlinear phased array methods relying on the measurement of the second harmonic [25], the sub-harmonics [26-29] and the diffuse field energy [30, 31]. However, higher harmonic and sub-harmonic generation can be partially or totally related to system/instrumentation nonlinearities, and the acquisition of the diffused field of all array elements is time consuming and requires advanced signal processing [31, 32].

Alternatively, recent studies focused on the development of nonlinear phased array methods based on ultrasonic wave modulation of signals with two frequencies. In fact, under dual-frequency (f_1 and f_2) excitation, modulation sidebands can be generated in the received spectrum at the sum and difference frequencies ($f_s = f_2 + f_1$ and $f_d = f_2 - f_1$) [33, 34]. The main advantage of wave modulation technique is that the amplitude of generated sidebands is less affected by equipment nonlinearities, compared with the amplitude of generated harmonics [1, 35-38]. Thus, the detection of spectral sidebands is more likely to be attributed to the presence of defects. In addition, it is relatively easier to satisfy the conditions necessary for defect excitation by using input waves of two different frequencies instead of a single frequency [38]. For example, Haupert et al. introduced an amplitude modulation method relying on image acquisition from phased arrays, where the linear material response is subtracted from the modulated signal revealing the image of nonlinear scattering in steel specimens with thermal fatigue cracks [39, 40]. Alston et al. focused on the detection of a kissing bond between two aluminium blocks based on non-collinear mixing of shear waves from two sources producing nonlinear longitudinal waves at sum-frequency that were captured by a phased array of sensors [41]. Finally, in a previous study of Fierro and Meo, a nonlinear frequency and amplitude modulation evaluation (FAME) technique was developed for more accurate detection of fatigue crack tips in aluminium specimens through phased array testing. This method focused on the assessment of acoustic nonlinearities based on the combined response of modulation sidebands and higher harmonics, after filtering out the linear ultrasonic effects [42].

Although the above nonlinear techniques offered improved sensitivity to micro-flaws compared to conventional linear ultrasonic methods, these were demonstrated on experimental samples containing a single interface of damage, and in most cases, the defects were oriented vertically relative to the plane of phased array elements. The identification of contact defects at multiple interfaces through the material remains challenging because the generation of detectable nonlinearities requires high amplitudes and signals of long duration, which is usually an equipment limitation for ordinary phased array systems [42].

This study introduces an optimised version of the phased array technique developed by Fierro and Meo [42], capable of identifying multiple contact interfaces in metallic and composite materials. In fact, this method focuses on the improvement of signal-to-noise ratio (SNR) relative to the case of linear ultrasonic testing, to enable more sensitive and accurate detection of peaks in the time domain of the received signal. The proposed version is also relying on the nonlinear modulation of ultrasonic waves from dual-frequency excitation. However, the acoustic nonlinearities generated by the damage were assessed using a parameter describing the nonlinear modulated response of the material arising only from the sidebands at f_s and f_d. This is achieved by employing the pulse inversion technique in some of the signal processing steps, to filter out both the fundamental and the second-order frequency harmonics from the captured signals [43, 44]. The performance of the presented method was compared with that of conventional linear ultrasonic inspection, by performing phased array (pulse-echo) experiments on aluminium and CFRP samples containing multiple horizontal interfaces of contact defects.

2 Elastic Wave Propagation Through Contact Interfaces

As illustrated in Figure 1, a contact defect can be considered the interface between the surfaces of two similar elastic solid layers, that are separated by a gap of height h due to material imperfections/roughness. According to Richardson [45] and Biwa et al. [46], the value of h is a function of the contact pressure p. In the absence of ultrasonic excitation,

the layers are assumed to be in equilibrium under static pressure p_0 and the gap height is $h_0 = X_+ - X_-$ (i.e. $p(h_0) = p_0$).

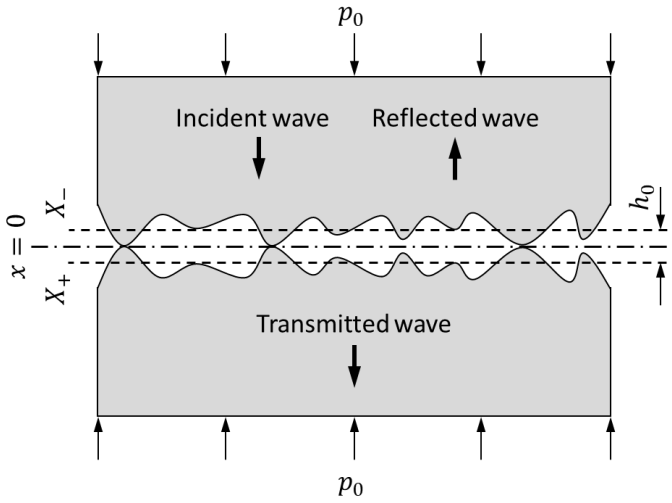

Figure 1: Longitudinal wave propagation through contact interface between two material layers held under pressure.

When longitudinal elastic waves are propagating perpendicularly to the plane of the interface, the equation of wave motion is

$$\rho \frac{\partial^2 u}{\partial t^2} = \frac{\partial \sigma}{\partial x} \tag{1}$$

where ρ is the material density, $u(x,t)$ is the wave displacement, t is the time, $\sigma(x,t) = E\varepsilon - p_0$ is the stress, E is the material elasticity (Young's modulus) and $\varepsilon = \frac{\partial u}{\partial x}$ is the strain. As the waves interact with contact surfaces, part of the incident wave energy is reflected to the source and part of it is transmitted through the interface (Figure 1). Based on this, the solution to equation (1) can be expressed as

$$u(x,t) = u_I(x - ct) + u_R(x + ct) \quad \text{for} \quad x < 0 \tag{2a}$$

and

$$u(x,t) = u_T(x - ct) \quad \text{for} \quad x > 0\,, \tag{2b}$$

where $c = \sqrt{E/\rho}$ is the longitudinal wave speed and u_I, u_R and u_T represent the displacement fields of the incident, reflected and transmitted waves [45, 46]. In addition, an amount of p is applied on the mated surfaces by the incident waves. This results in the variation of h with time (opening-closing motion), in a nonlinear manner described by the following expression

$$h(t) = h_0 + u(X_+, t) - u(X_-, t). \tag{3}$$

Hence, the contact interface is subject to a continuous stress that relies on the relationship between p and h.

By considering the case of dual-frequency excitation of the contact surfaces using two monochromatic sinusoidal waves with frequencies f_1 and f_2 and amplitudes A_1 and A_2, the incident wave can be written as

$$u_I(x-ct) = A_1 cos\left[\frac{2\pi f_1}{c}(x-ct)\right] + A_2 cos\left[\frac{2\pi f_2}{c}(x-ct)\right]. \quad (4)$$

The explicit analysis provided in the study of Guo et al. [47], which followed the works of Richardson [45] and Biwa et al. [46], showed that both the reflected and the transmitted signals would exhibit linear harmonics at f_1 and f_2 frequencies with A_{f_1} and A_{f_2} amplitudes, second-order nonlinear harmonics at $2f_1$ and $2f_2$ frequencies with A_{2f_1} and A_{2f_2} amplitudes, and first-order nonlinear intermodulation peaks (sidebands) at the sum-frequency ($f_s = f_2 + f_1$) and the difference-frequency ($f_d = f_2 - f_1$) with A_s and A_d amplitudes. The A_{2f_1} and A_{2f_2} were found to be proportional to the square of A_{f_1} and A_{f_2}, respectively, whereas A_s and A_d were linear functions of the product of A_{f_1} and A_{f_2}. Hence, the dependency of the interface nonlinearity on the contact pressure was successfully monitored by calculating the magnitude of the relative acoustic nonlinearity parameters β_s and β_d from the corresponding sidebands

$$\beta_s \approx \frac{A_s}{A_{f_1} A_{f_2}} \quad (5a)$$

and

$$\beta_d \approx \frac{A_d}{A_{f_1} A_{f_2}}. \quad (5b)$$

The technique used in this study relied on the detection of the acoustic nonlinearities using the nonlinear modulated response ($R_{\beta_s+\beta_d}$) of the material, which is calculated as the sum of β_s and β_d parameters

$$R_{\beta_s+\beta_d} = \beta_s + \beta_d \approx \frac{A_s + A_d}{A_{f_1} A_{f_2}}. \quad (6)$$

Before moving to the explanation of the technique and how $R_{\beta_s+\beta_d}$ can be practically obtained, it must be noticed that when the contact interface is excited using ultrasonic waves of single-frequency (e.g. f_1), the reflected and the transmitted signals contain the second-order nonlinear harmonic at $2f_1$ (and higher-order harmonics) without any intermodulation products. The studies of Biwa et al. [46] and Kim and Lee [48] showed that, in such case, the level of interface nonlinearity could be monitored using the following relative acoustic nonlinearity parameter

$$\beta \approx \frac{A_{2f_1}}{{A_{f_1}}^2} \quad (7)$$

However, as mentioned and referenced in the Introduction section, the main benefit of dual-frequency over single-frequency transmission is that the amplitude of modulation sidebands (A_s and A_d) is less influenced by the nonlinearities induced by the power instruments of the setup relative to the second harmonic amplitude (A_{2f_1}).

3 Phased Array Method based on Nonlinear Ultrasound Modulation

The nonlinear phased array method used in this study is an optimised version of the FAME method introduced by Fierro and Meo [42]. To obtain the $R_{\beta_s+\beta_d}$ response of the material under ultrasonic phased array inspection, the four signals illustrated in Figure 2 are required. The difference between those signals is the order in which the elements of the phased array probe are generating waves at f_1 and f_2 frequencies. For the first signal, waves are transmitted from all the elements at f_1 (i.e. signal u_{f_1}), whereas for the second one at f_2 (i.e. signal u_{f_2}). This allows the recording of the linear ultrasonic response of the samples at these two frequencies. For the third signal, waves are fired at f_1 from the odd-numbered elements and at f_2 from the even-numbered elements (i.e. signal $u_{f_{12}}$), to achieve nonlinear modulation of the propagating waves. The last signal has the inverse element order of the third one (i.e. signal $u_{f_{21}}$).

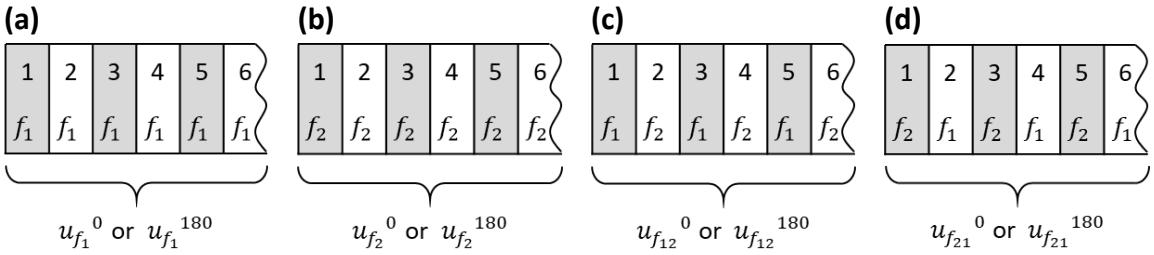

Figure 2: Frequency order of phased array elements in signal u_{f1} (a), signal u_{f2} (b), signal u_{f12} (b) and signal u_{f21} (d). The numerical superscripts indicate the 0º and 180º phase angles respectively.

It is worth noting that the sum of $u_{f_{12}}$ and $u_{f_{21}}$ results in the same amount of transmitted energy at f_1 and f_2 as with the individual u_{f_1} or u_{f_2}, because for $u_{f_{12}}$ and $u_{f_{21}}$ only half of the array elements are generating f_1 and f_2 waves. In addition, the inputs signals are focused on the back surface of the samples because in a real case of inspection the depth

of possible contact defects will be unknown. Moreover, for f_{12} and f_{21} signals, a delay is applied between the firing of waves at f_1 and f_2 frequencies. Specifically, f_2 transmission starts immediately after f_1 transmission has stopped (i.e. delayed by one wavelength of f_1 signal). In this way, the f_1 waves can reach and excite the contact surfaces first, and then the f_2 waves will arrive and modulate that excitation.

The transmission of the above four signals is initially performed with a phase angle of 0º ($u_{f_1}{}^{0}$, $u_{f_2}{}^{0}$, $u_{f_{12}}{}^{0}$ and $u_{f_{21}}{}^{0}$), and then with a phase angle of 180º ($u_{f_1}{}^{180}$, $u_{f_2}{}^{180}$, $u_{f_{12}}{}^{180}$ and $u_{f_{21}}{}^{180}$). This is also known as pulse inversion, and it is a common method in literature for the extraction of the second harmonics at $2f_1$ and $2f_2$ [49-51]. The frequency spectrum resulting from the summation of the signals captured under single- or dual-frequency excitation with 0º and 180º phase angles is presented in Figure 3. Ideally, by adding the 0º and 180º signals, the fundamental harmonic amplitudes (A_{f_1} and A_{f_2}) will be minimised because the signals are identical in amplitude and wavelength, but opposite in phase. In the case of single-frequency excitation (Figure 3c and Figure 3d), the amplitude of second harmonics ($A_{2f_1}$and A_{2f_2}) after adding the 0º and 180º signals will be doubled since the nonlinear waves generated at the contact interfaces are propagating in phase. For dual-frequency signals (Figure 3e and Figure 3f), $A_{2f_1}$and A_{2f_2} will not be doubled because, as explained in the previous paragraph, the sum of harmonic amplitudes is equal to the individual harmonic amplitudes in u_{f_1} or u_{f_2} signals (i.e. same number of firing elements in total).

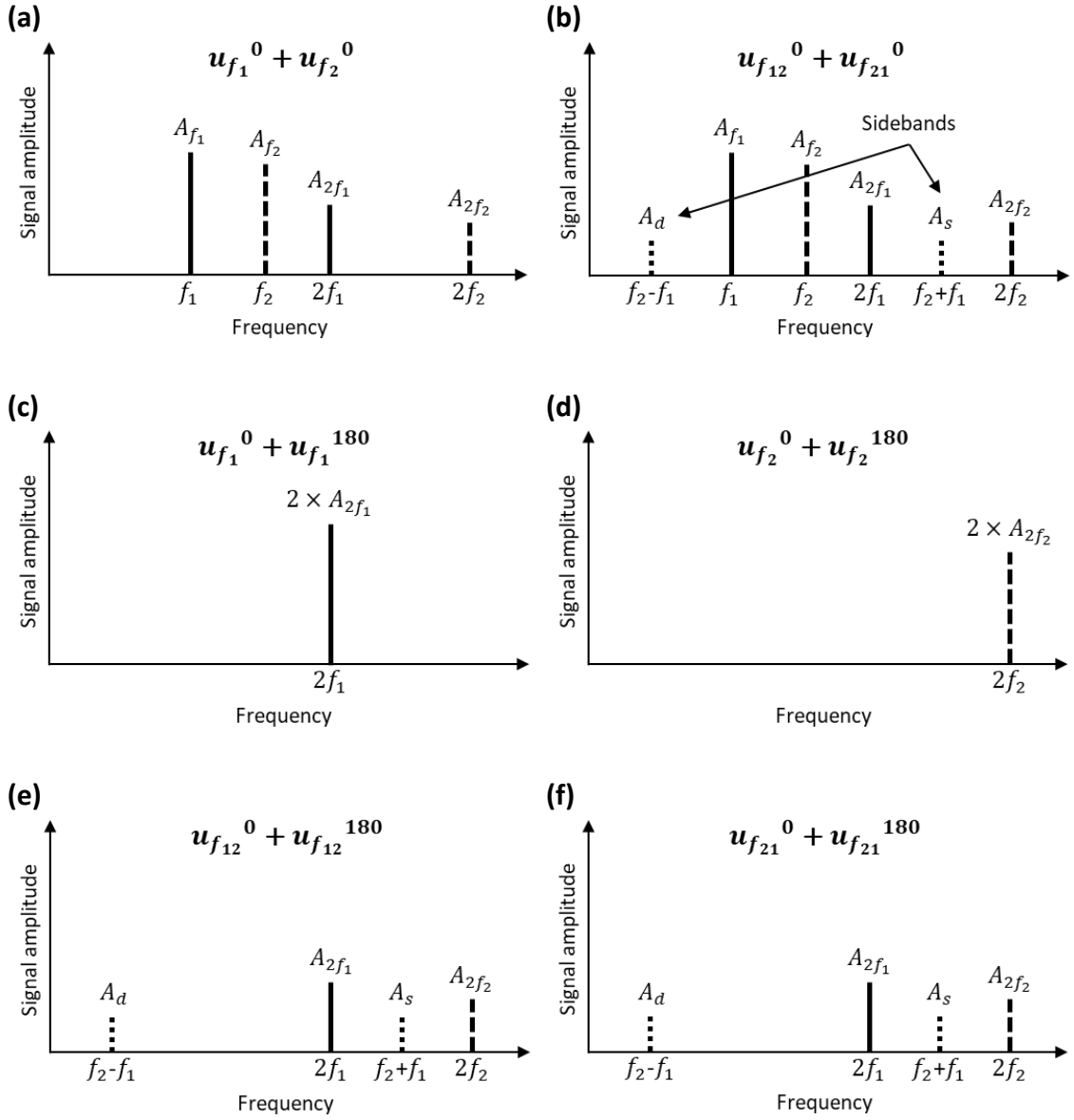

Figure 3: Illustration of the frequency spectrum resulting from signal summation $u_{f1}{}^0 + u_{f2}{}^0$ (a), $u_{f12}{}^0 + u_{f21}{}^0$ (b), $u_{f1}{}^0 + u_{f1}{}^{180}$ (c), $u_{f2}{}^0 + u_{f2}{}^{180}$ (d), $u_{f12}{}^0 + u_{f12}{}^{180}$ (e) and $u_{f21}{}^0 + u_{f21}{}^{180}$ (f).

Based on the above, the response corresponding to the sum of sideband components ($R_{sideband}$), and the response corresponding to the product of fundamental harmonics ($R_{fund.\ harm.}$) can be obtained by inserting the captured time signals in the following expressions

$$R_{sideband} = \left[\left(u_{f_1}{}^0 + u_{f_2}{}^0\right) - \left(u_{f_1}{}^0 + u_{f_1}{}^{180}\right) - \left(u_{f_2}{}^0 + u_{f_2}{}^{180}\right)\right] - \left[\left(u_{f_{12}}{}^0 + u_{f_{21}}{}^0\right) - \left(u_{f_{12}}{}^0 + u_{f_{12}}{}^{180}\right) - \left(u_{f_{21}}{}^0 + u_{f_{21}}{}^{180}\right)\right] \quad (8)$$

and

$$R_{fund.\ harm.} = \left[{u_{f_1}}^0 - \frac{1}{2}\left({u_{f_1}}^0 + {u_{f_1}}^{180}\right)\right] \times \left[{u_{f_2}}^0 - \frac{1}{2}\left({u_{f_2}}^0 + {u_{f_2}}^{180}\right)\right]. \quad (9)$$

By considering the frequency spectrum of the signals in equations (8) and (9), and according to Figure 3, $R_{sideband}$ and $R_{fund.\ harm.}$ can be expressed based on the received amplitudes of harmonics and sidebands

$$\begin{aligned} R_{sideband} &= \left[\left(A_{f_1} + A_{2f_1} + A_{f_2} + A_{2f_2}\right) - 2A_{2f_1} - 2A_{2f_2}\right] \\ &\quad -\left[\left(A_{f_1} + A_{2f_1} + A_{f_2} + A_{2f_2} + A_s + A_d\right) - 2A_{2f_1} - 2A_{2f_2} - 2A_s - 2A_d\right] \\ &= \left(A_{f_1} + A_{f_2} - A_{2f_1} - A_{2f_2}\right) - \left(A_{f_1} + A_{f_2} - A_{2f_1} - A_{2f_2} - A_s - A_d\right) \\ &= A_s + A_d\ . \end{aligned} \quad (10)$$

and

$$\begin{aligned} R_{fund.\ harm.} &= \left[\left(A_{f_1} + A_{2f_1}\right) - A_{2f_1}\right] \times \left[\left(A_{f_2} + A_{2f_2}\right) - A_{2f_2}\right] \\ &= A_{f_1}A_{f_2}\ . \end{aligned} \quad (11)$$

Equation (10) can be then divided by (11), and the resulting ratio is equal to that of equation (6) in Section 2 (i.e. equal to $R_{\beta_s+\beta_d}$)

$$R_{\beta_s+\beta_d} = \frac{R_{sideband}}{R_{fund.\ harm.}} = \frac{A_s + A_d}{A_{f_1}A_{f_2}}\ . \quad (12)$$

4 Experimental Process

4.1 Aluminium and CFRP Test Samples

To assess the proposed approach, various samples made by two different materials, aluminium and CFRP, with multiples interfaces were manufactured. In the first case, aluminium disks with four holes (Figure 4a) were machined from a 6082-T6 aluminium round bar to different thicknesses (23, 19, 15, 11 and 7 mm). The maximum deviation in flatness was 0.03 mm and the surface finish equal to 0.1 μm. As illustrated in Figure 4, the disks were stacked in two separate orders and held under constant pressure using M4 bolts through the holes, that were all tightened to a maximum torque of 2.5 Nm. These two assemblies were used to simulate aluminium rods with contact interfaces at multiple depths. In this paper, the assemblies shown in Figure 4b and Figure 4c are referred as the aluminium test samples AL1 and AL2 respectively.

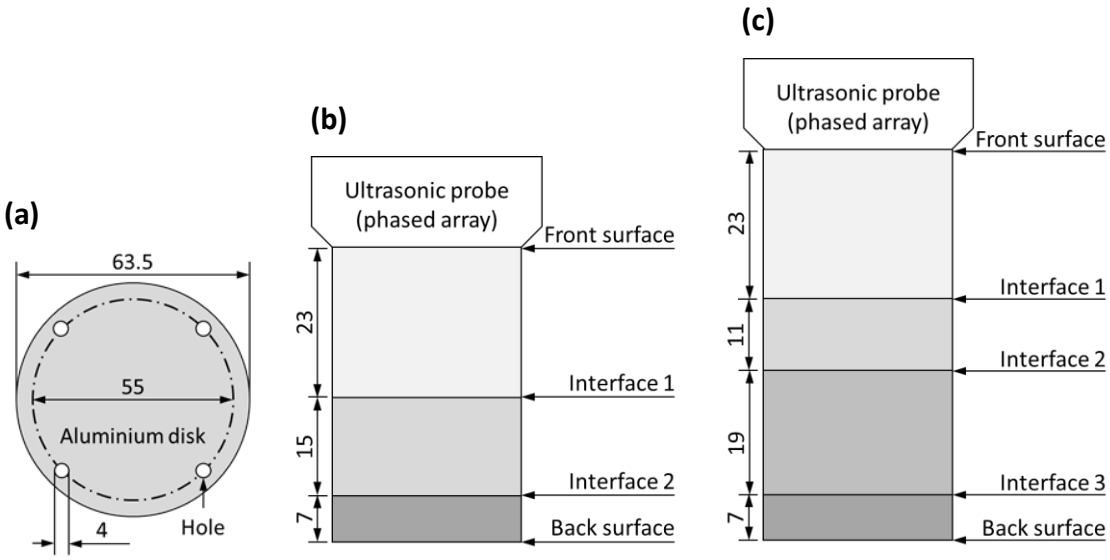

Figure 4: Size of aluminium disks (a) and their stacking sequence in test sample AL1 (b) and AL2 (c). Dimensions in mm. Not to scale.

Similarly, rectangular CFRP laminates (Figure 5a) of various thicknesses (13.5, 8.5 and 4.1 mm) were used for the assembly of two composite test samples. The laminates were made from unidirectional carbon-epoxy (Hexcel T800-M21) layers in quasi-isotropic orientation, but the exact number of layers and lay-up in each laminate was unknown. The flatness across the length and width of the laminates had a maximum deviation of 0.2 mm and 0.07 mm respectively, and the surface finish was measured as 0.15 μm. The stacking orders of the laminates in samples CFRP1 and CFRP2 are presented in Figure 5b and Figure 5c. The laminates forming each composite sample were also subject to fixed pressure, using one vice clamp on either end.

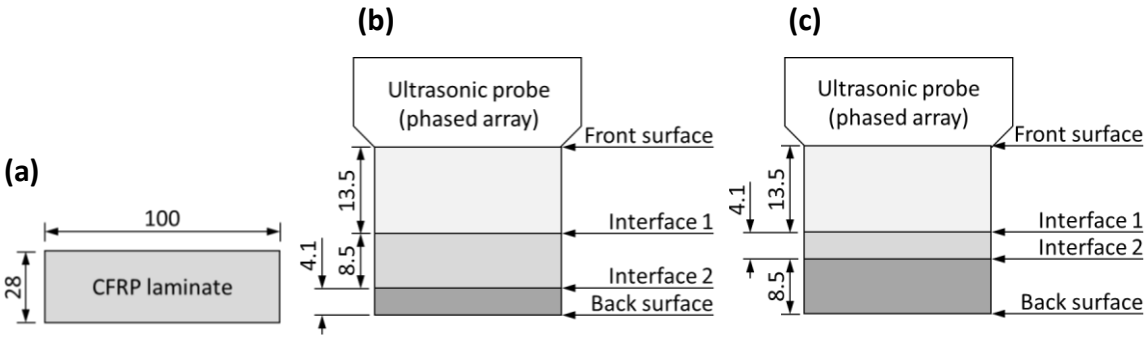

Figure 5: Size of composite laminates (a) and their stacking sequence in test sample CFRP1 (b) and CFRP2 (c). Dimensions in mm. Not to scale.

4.2 Phased Array Ultrasonic (Pulse-Echo) Tests

The following experimental activities were completed using a phased array system (from Diagnostic Sonar Ltd) equipped with a 5 MHz ultrasonic probe of 128 piezoelectric elements (pitch of 0.5 mm). In all cases, the probe was directly coupled to the top surface of the material using water-based gel. In addition, ultrasonic excitation was performed only at two frequencies, f_1 = 4.8 MHz and f_2 = 5.3 MHz, and the transmitted signals were sinusoidal waves of one cycle. These were close to the central frequency of the probe, meaning that the energy of the propagating waves was expected to be high. For the tests on the aluminium samples the input signal voltage was set to 20 V whereas for the CFRP specimens to 60 V.

4.2.1 Speed of Sound Measurement

Prior to conducting acoustic inspection experiments, the average speed of ultrasound in the aluminium and CFRP samples was calculated through pulse-echo testing in accordance with the ASTM E494-15 standard. Specifically, the speed was measured on a single aluminium disk (23 mm thick), initially at 4.8 MHz and then at 5.3 MHz, suggesting an average value of 6420 m/s. In the same way, the mean velocity of ultrasound in the 13.5 mm thick CFRP laminate was estimated as 3040 m/s. These velocity values were used for the calculation of the expected positions of the contact interfaces in the time domain, as well as for the focusing of the transmitted signals.

4.2.2 Detection of Contact Interfaces in Test Samples

The aluminium and CFRP test specimens were then subject to ultrasonic pulse-echo tests for the detection of the contact interfaces in the form of amplitude peaks in the captured time domain. The phased array system was programmed to perform signal transmission in beams of 32 elements and in steps of one element (i.e. 97 beams in total). The waves reflected from the contact interfaces and the back surface of the samples were recorded by the probe in the time domain and stored in the form of an image (B-scan). At this point it must be mentioned that around 10-15 beams on either end of the probe were located outside the top surface of the specimens, and hence, those beams were excluded from the

analysis of data. The time signals associated with the remaining beams were summed up to obtain the combined ultrasonic signal of the material.

According to the method described in Section 3, four input signals were initially transmitted with a phase angle of 0º ($u_{f_1}{}^0$, $u_{f_2}{}^0$, $u_{f_{12}}{}^0$ and $u_{f_{21}}{}^0$) and then with a phase angle of 180º ($u_{f_1}{}^{180}$, $u_{f_2}{}^{180}$, $u_{f_{12}}{}^{180}$ and $u_{f_{21}}{}^{180}$), allowing the calculation of the nonlinear modulated response $R_{\beta_s+\beta_d}$ arising from the sum of β_s and β_d parameters (ref. equations (8)-(12)). For comparison, the linear ultrasonic response of the material was represented by the signal recorded under $f_1{}^0$ transmission (i.e. $R_{f_1} = u_{f_1}{}^0$).

5 Results and Discussion

The results obtained from the linear ultrasonic and nonlinear modulation experiments on each aluminium and CFRP sample were plotted and analysed for comparison. More specifically, the Hilbert transform of R_{f_1} was plotted against the absolute value of $R_{\beta_s+\beta_d}$. As an example, the normalised plots corresponding to the AL1 and CFRP1 samples are shown in Figure 6a and Figure 7a respectively. The initial part of the signal was truncated to remove the near-field effect. In addition, the expected positions of the contact interfaces and the back surface were marked on the plot with vertical dashed lines. These positions were calculated based on the speed of sound in the material, as explained in Section 4.2.1.

According to Figure 6a and Figure 7a, both the R_{f_1} and $R_{\beta_s+\beta_d}$ responses included peaks close to the expected positions of the interfaces. By considering the attenuation of waves transmitted to deeper interfaces with almost the same size, shape and surface contact, then the amplitude of the peaks in the linear R_{f_1} response would be expected to have a decreasing trend as shown in Figure 6a. However, for a better surface contact at an interface, most of the incident wave could be transmitted through instead of being reflected to the source. As a result, the linear peaks corresponding to deeper interfaces (e.g. back wall) could have higher amplitudes as illustrated in Figure 7a. In the case of $R_{\beta_s+\beta_d}$, the amplitude of the peaks was expected to depend primarily on the level of nonlinearity at each contact interface (i.e. based on the characteristics of the interface). As can be seen in Figure 6a and Figure 7a, the peaks with the highest amplitude were those indicating the back surface. This could possibly be attributed to strong nonlinearities induced by the contact between the material and the bolts or clamps used to hold under pressure the aluminium and composite samples (ref. section 4.1).

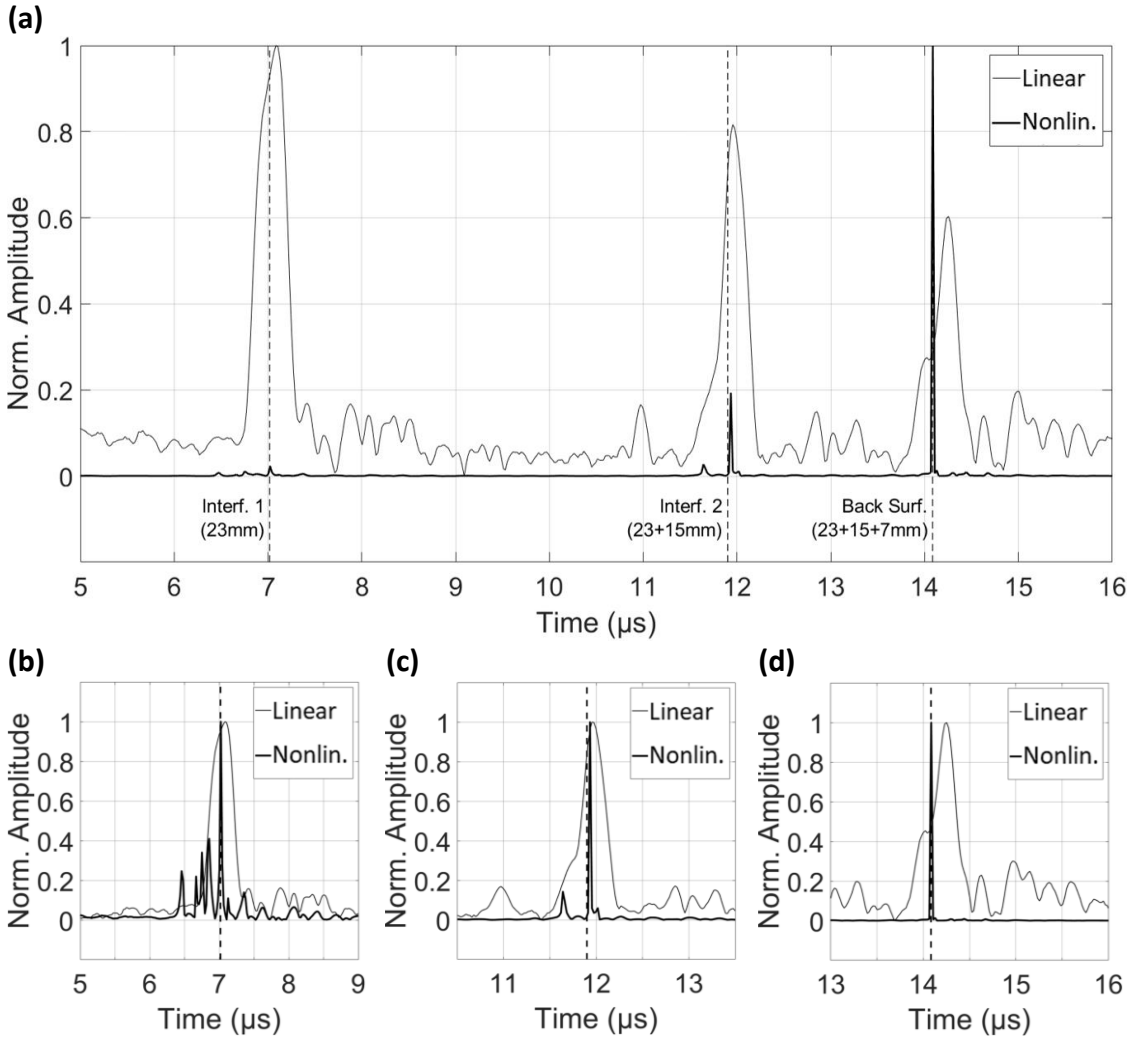

Figure 6: Hilbert transform of linear response against absolute nonlinear modulated response of sample AL1. Normalised plot showing the contact interfaces and back surface (a), and normalised plot around interface 1 (b), interface 2 (c) and back surface (d).

(a)

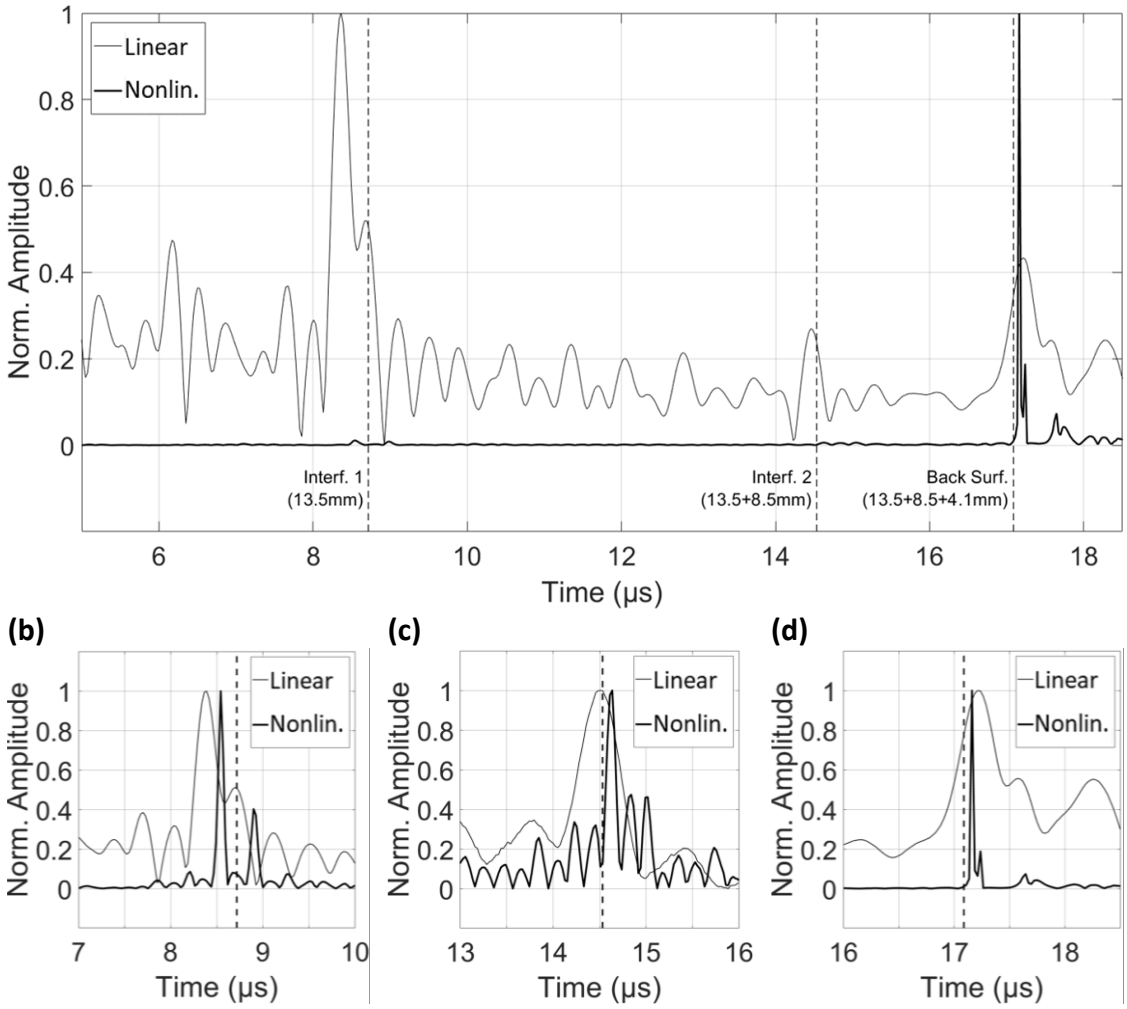

Figure 7: Hilbert transform of linear response against absolute nonlinear modulated response of sample CFRP1. Normalised plot showing the contact interfaces and back surface (a), and normalised plot around interface 1 (b), interface 2 (c) and back surface (d).

The linear and nonlinear modulated peaks at each interface could not be directly compared because the R_{f_1} and $R_{\beta_s+\beta_d}$ plots were individually normalised with respect to their maximum amplitude. Instead, the parts of the time domain around the locations of the interfaces were normalised separately, and plotted as illustrated in Figure 6b to Figure 6d for AL1, and Figure 7b to Figure 7d for CFRP1. The peaks in R_{f_1} and $R_{\beta_s+\beta_d}$ indicating the contact defects were compared based on three parameters. The first one was the magnitude of SNR which was calculated as

$$SNR = \frac{A_{peak}}{A_{noise}}, \tag{10}$$

where A_{peak} was the amplitude of every peak and A_{noise} was the amplitude of noise along the entire time domain. The value of A_{noise} was estimated as the mean amplitude of all values below 3 standard deviations.

The second parameter of comparison was the peak width at a 50% drop (i.e. 6 dB drop) from its maximum point. This is a common measure in literature, also known as the peak width at half-height (w_h), which can be used to indicate how localised (narrow) the peaks are. The last comparison was made based on the positioning error (ε_p) of the peaks in R_{f_1} and $R_{\beta_s+\beta_d}$ relative to the expected positions of the interfaces and back surface in the time domain (i.e. relative to the dashed lines in Figure 6 and Figure 7). Similar plots of linear ultrasonic and nonlinear modulated signal responses were obtained from the phased array experiments on the AL2 and CFRP2 samples. The results of SNR and w_h from all four tests specimens were summarised in Table 1.

Table 1: *SNR*, w_h and ε_p of the peaks in R_{f1} and $R_{\beta s+\beta d}$ responses of aluminium and CFRP samples.

Sample	Response	Interface 1			Interface 2			Interface 3			Back Surface		
		SNR (−)	w_h (μs)	ε_p (μs)	SNR (−)	w_h (μs)	ε_p (μs)	SNR (−)	w_h (μs)	ε_p (μs)	SNR (−)	w_h (μs)	ε_p (μs)
AL1	R_{f_1}	14.31	0.37	0.07	11.68	0.29	0.07	–	–	–	8.63	0.27	0.02
	$R_{\beta_s+\beta_d}$	23.89	0.03	0.00	199.69	0.03	0.02	–	–	–	1030.93	0.02	0.00
AL2	R_{f_1}	12.67	0.29	0.01	6.18	0.29	0.05	9.96	0.26	0.23	4.04	0.40	0.31
	$R_{\beta_s+\beta_d}$	247.86	0.03	0.05	51.41	0.03	0.02	1020.41	0.03	0.05	188.88	0.09	0.02
CFRP1	R_{f_1}	5.56	0.51	0.32	1.48	0.48	0.02	–	–	–	2.41	0.5	0.13
	$R_{\beta_s+\beta_d}$	6.90	0.10	0.16	3.73	0.12	0.08	–	–	–	909.09	0.03	0.07
CFRP2	R_{f_1}	5.26	0.28	0.17	3.30	0.37	0.25	–	–	–	2.67	0.41	0.24
	$R_{\beta_s+\beta_d}$	7.60	0.09	0.14	8.47	0.09	0.05	–	–	–	1612.90	0.03	0.27

As can be seen, in all cases, the SNR values of the peaks in $R_{\beta_s+\beta_d}$ were significantly higher than those corresponding to the peaks in R_{f_1}. Regarding the aluminium samples, the difference in SNR was varying from a minimum of ~70% (interface 1 in AL1) up to a maximum of more than two orders of magnitude (back surface in AL1). The equivalent SNR variation in CFRP specimens was from ~25% (interface 2 in CFRP1) to nearly three orders of magnitude (back surface in CFRP2). The w_h measurements showed that in all

samples the width of the peaks in the nonlinear modulated signal was much smaller than the peaks in the linear response. For the aluminium specimens, the difference in peak width was almost constant at around one order of magnitude. In the case of CFRP samples, the width of the nonlinear peaks at some interfaces (e.g. interfaces 1 and 2 in CFRP1) was smaller than that of the linear peaks by at least three times, whereas at other interfaces (e.g. back surface in CFRP1) by more than one order of magnitude. Regarding the positioning accuracy of the peaks, the nonlinear peaks offered smaller ε_p values than the linear peaks for the majority of the interfaces and back surfaces (10 out of 13 cases). Also, in two cases the ε_p of nonlinear peaks was equal to zero. Most importantly though, the mean ε_p of the peaks in $R_{\beta_s+\beta_d}$ (0.07 μs) was around 45% smaller than the average ε_p of the peaks in R_{f_1} (0.16 μs). Finally, as a general observation, the majority of the peaks in both R_{f_1} and $R_{\beta_s+\beta_d}$ of the aluminium samples indicated higher SNR, smaller w_h and smaller ε_p values compared with those of CFRP specimens, which could be translated to lower accuracy in the detection of contact defects in CFRP samples. This could be true to some extent, considering that the CFRP laminates were not fully isotropic and their cut edges included broken fibres and cracked matrix. Hence, the propagation of nonlinear waves from the interfaces should not be as uniform as in the isotropic aluminium specimens. However, it must be noted that the SNR and w_h results from the aluminium samples should not be directly studied against those from the CFRP specimens, because of their differences in geometry, thickness and speed of sound.

6 Conclusions

This work introduced an alternative phased array (pulse-echo) method relying on the nonlinear ultrasonic modulation of elastic waves from dual-frequency excitation. The aim was to localise contact type defects at multiple interfaces in metallic and composite materials with higher sensitivity and accuracy, compared to the traditional linear phased array technique. The proposed method assessed the material nonlinearities based on the sum of β_s and β_d modulation parameters, that were obtained from effective signal processing involving the use of pulse inversion technique in some steps.

Phased array experiments were conducted on two circular aluminium samples and two rectangular CFRP specimens containing contact interfaces at different depths through the thickness. The received linear ultrasonic and nonlinear modulated responses (R_{f_1} and

$R_{\beta_s+\beta_d}$) were plotted in the time domain, and as explained in the previous section, their peaks indicating the positions of the contact interfaces and the back surfaces were compared based on the values of SNR, w_h and ε_p. The results revealed that for all four test samples, the SNR associated with the peaks in $R_{\beta_s+\beta_d}$ signal was higher than the SNR of the peaks in R_{f_1} response, with a maximum difference of around three orders of magnitude. Similarly, the results of w_h measurements suggested that, in all cases, the nonlinear peaks were narrower compared with the linear peaks, and the largest difference in width was more than one order of magnitude. Lastly, the mean value of ε_p corresponding to the peaks in $R_{\beta_s+\beta_d}$ was on around 45% smaller than that of the peaks in R_{f_1}.

In conclusion, this work proved that the presented nonlinear phased array method enabled the identification of multiple contact flaws in the test specimens with significantly higher sensitivity and localisation accuracy relative to the conventional linear phased array method. This technique could potentially be implemented in the design of future phased array systems for enhanced performance in pulse-echo inspection of metallic and composite structures.

References

1. Donskoy, D., Sutin, A., & Ekimov, A. (2001). Nonlinear acoustic interaction on contact interfaces and its use for nondestructive testing. *NDT & E International*, 34(4), 231-238.
2. Kim, J. Y., & Lee, J. S. (2007). A micromechanical model for nonlinear acoustic properties of interfaces between solids. *Journal of Applied Physics*, 101(4), 043501.
3. Bastianini, F., Di Tommaso, A., & Pascale, G. (2001). Ultrasonic non-destructive assessment of bonding defects in composite structural strengthenings. *Composite Structures*, 53(4), 463-467.
4. Benammar, A., Drai, R., & Guessoum, A. (2008). Detection of delamination defects in CFRP materials using ultrasonic signal processing. *Ultrasonics*, 48(8), 731-738.
5. Kato, Y., Tanaka, H., & Sugiura, T. (2015). Detection of low-frequency components in ultrasonic waves transmitted through contact solids. In *2015 IEEE International Ultrasonics Symposium* (Vol. 1, p. 1-4). IEEE.
6. Yeh, F. W. T., Lukomski, T., Haag, J., Clarke, T., Stepinski, T., & Strohaecker, T. R. (2018). An alternative ultrasonic Time-of-Flight Diffraction (TOFD) method. *NDT & E International*, 100(1), 74-83.
7. Drinkwater, B. W., & Wilcox, P. D. (2006). Ultrasonic arrays for non-destructive evaluation: A review. *NDT & E International*, 39(7), 525-541.
8. Bai, Z., Chen, S., Xiao, Q., Jia, L., Zhao, Y., & Zeng, Z. (2018). Compressive sensing of phased array ultrasonic signal in defect detection: Simulation study and experimental verification. *Structural Health Monitoring*, 17(3), 434-449.

9. Caminero, M. A., Garcia-Moreno, I., Rodriguez, G. P., & Chacon, J. M. (2019). Internal damage evaluation of composite structures using phased array ultrasonic technique: Impact damage assessment in CFRP and 3D printed reinforced composites. *Composites Part B: Engineering*, 165(1), 131-142.
10. Safari, A., Zhang, J., Velichko, A., & Drinkwater, B. W. (2018). Assessment methodology for defect characterisation using ultrasonic arrays. *NDT & E International*, 94(1), 126-136.
11. Taheri, H., & Hassen, A. A. (2019). Nondestructive ultrasonic inspection of composite materials: a comparative advantage of phased array ultrasonic. *Applied Sciences*, 9(8), 1628.
12. Zhang, J., Drinkwater, B. W., & Wilcox, P. D. (2010). The use of ultrasonic arrays to characterize crack-like defects. *Journal of Nondestructive Evaluation*, 29(4), 222-232.
13. Tant, K. M., Mulholland, A. J., & Gachagan, A. (2015). A model-based approach to crack sizing with ultrasonic arrays. *IEEE transactions on ultrasonics, ferroelectrics, and frequency control*, 62(5), 915-926.
14. Van Pamel, A., Huthwaite, P., Brett, C. R., & Lowe, M. J. (2016). Numerical simulations of ultrasonic array imaging of highly scattering materials. *NDT & E International*, 81(1), 9-19.
15. Jiao, J., Ma, T., Hou, S., Wu, B., & He, C. (2018). A Pulse Compression Technique for Improving the Temporal Resolution of Ultrasonic Testing. *Journal of Testing and Evaluation*, 46(3), 1238-1249.
16. Mohammadkhani, R., Zanotti Fragonara, L., Padiyar M, J., Petrunin, I., Raposo, J., Tsourdos, A., & Gray, I. (2020). Improving Depth Resolution of Ultrasonic Phased Array Imaging to Inspect Aerospace Composite Structures. *Sensors*, 20(2), 559.
17. Zhang, J., Drinkwater, B. W., Wilcox, P. D., & Hunter, A. J. (2010). Defect detection using ultrasonic arrays: The multi-mode total focusing method. *NDT & E International*, 43(2), 123-133.
18. Abdessalem, B., Ahmed, K., & Redouane, D. (2017). Signal Quality Improvement Using a New TMSSE Algorithm: Application in Delamination Detection in Composite Materials. *Journal of Nondestructive Evaluation*, 36(1), 16.
19. Ohara, Y., Shintaku, Y., Horinouchi, S., Ikeuchi, M., & Yamanaka, K. (2012). Enhancement of selectivity in nonlinear ultrasonic imaging of closed cracks using amplitude difference phased array. *Japanese Journal of Applied Physics*, 51(7S), 07GB18.
20. Kawashima, K., Murase, M., Yamada, R., Matsushima, M., Uematsu, M., & Fujita, F. (2006). Nonlinear ultrasonic imaging of imperfectly bonded interfaces. *Ultrasonics*, 44(1), 1329-1333.
21. Kundu, T. (2019). *Nonlinear ultrasonic and vibro-acoustical techniques for nondestructive evaluation* (Vol. 1, p. 2). Cham: Springer.
22. Buck, O., Morris, W. L., & Richardson, J. M. (1978). Acoustic harmonic generation at unbonded interfaces and fatigue cracks. *Applied Physics Letters*, 33(5), 371-373.
23. Soleimanpour, R., Ng, C. T., & Wang, C. H. (2017). Higher harmonic generation of guided waves at delaminations in laminated composite beams. *Structural Health Monitoring*, 16(4), 400-417.
24. Sasaki, R., Ogata, T., Ohara, Y., Mihara, T., & Yamanaka, K. (2005). Simulation and analysis of subharmonics and tail effect for ultrasonic nondestructive evaluation of closed cracks. *Japanese Journal of Applied Physics*, 44(6S), 4389.
25. Seo, H., Pyun, D. K., & Jhang, K. Y. (2019). Synthetic aperture imaging of contact acoustic nonlinearity to visualize the closing interfaces using tone-burst ultrasonic waves. *Mechanical Systems and Signal Processing*, 125(1), 257-274.
26. Ohara, Y., Mihara, T., Sasaki, R., Ogata, T., Yamamoto, S., Kishimoto, Y., & Yamanaka, K. (2007). Imaging of closed cracks using nonlinear response of elastic waves at subharmonic frequency. *Applied Physics Letters*, 90(1), 011902.
27. Sugawara, A., Jinno, K., Ohara, Y., & Yamanaka, K. (2015). Closed-crack imaging and scattering behavior analysis using confocal subharmonic phased array. *Japanese Journal of Applied Physics*, 54(7S1), 07HC08.

28. Ohara, Y., Mihara, T., & Yamanaka, K. (2019). Subharmonic Phased Array for Crack Evaluation (SPACE). In *Nonlinear Ultrasonic and Vibro-Acoustical Techniques for Nondestructive Evaluation* (Vol. 1, p. 419-469). Cham: Springer.
29. Park, C. S., Kim, J. W., Cho, S., & Seo, D. C. (2016). A high resolution approach for nonlinear sub-harmonic imaging. *NDT & E International*, 79(1), 114-122.
30. Potter, J. N., Croxford, A. J., & Wilcox, P. D. (2014). Nonlinear ultrasonic phased array imaging. *Physical Review Letters*, 113(14), 144301.
31. Cheng, J., Potter, J. N., & Drinkwater, B. W. (2018). The parallel-sequential field subtraction technique for coherent nonlinear ultrasonic imaging. *Smart Materials and Structures*, 27(6), 065002.
32. Fierro, G. P. M., & Meo, M. (2018). IWSHM 2017: Structural health monitoring of the loosening in a multi-bolt structure using linear and modulated nonlinear ultrasound acoustic moments approach. *Structural Health Monitoring*, 17(6), 1349-1364.
33. Van Den Abeele, K. A., Johnson, P. A., & Sutin, A. (2000). Nonlinear elastic wave spectroscopy (NEWS) techniques to discern material damage, part I: nonlinear wave modulation spectroscopy (NWMS). *Journal of Research in Nondestructive Evaluation*, 12(1), 17-30.
34. Chen, B. Y., Soh, S. K., Lee, H. P., Tay, T. E., & Tan, V. B. (2016). A vibro-acoustic modulation method for the detection of delamination and kissing bond in composites. *Journal of Composite Materials*, 50(22), 3089-3104.
35. Zagrai, A., Donskoy, D., & Lottiaux, J. L. (2004). N-Scan: New Vibro-Modulation System for Crack Detection, Monitoring and Characterization. In *AIP Conference Proceedings* (Vol. 700, No. 1, p. 1414-1421). AIP Publishing.
36. Zhang, Z., Xu, H., Liao, Y., Su, Z., & Xiao, Y. (2017). Vibro-acoustic modulation (VAM)-inspired structural integrity monitoring and its applications to bolted composite joints. *Composite Structures*, 176(1), 505-515.
37. Dunn, M. (2018). *Nonlinear vibro-ultrasonics for detection of damage and weak bonds in composites*. Thesis (Doctoral), The University of Queensland.
38. Sohn, H., Liu, P., Lim, H. J., & Park, B. (2019). Noncontact Nonlinear Ultrasonic Wave Modulation for Fatigue Crack and Delamination Detection. In *Nonlinear Ultrasonic and Vibro-Acoustical Techniques for Nondestructive Evaluation* (Vol. 1, p. 661-697). Cham: Springer.
39. Haupert, S., Renaud, G., & Schumm, A. (2017). Ultrasonic imaging of nonlinear scatterers buried in a medium. *NDT & E International*, 87(1), 1-6.
40. Haupert, S., Ohara, Y., Carcreff, E., & Renaud, G. (2019). Fundamental wave amplitude difference imaging for detection and characterization of embedded cracks. *Ultrasonics*, 96(1), 132-139.
41. Alston, J., Croxford, A., Potter, J., & Blanloeuil, P. (2018). Nonlinear non-collinear ultrasonic detection and characterisation of kissing bonds. *NDT & E International*, 99(1), 105-116.
42. Fierro, G. P. M., & Meo, M. (2019). Nonlinear phased array imaging of flaws a modulation technique. In *Nondestructive Characterization and Monitoring of Advanced Materials, Aerospace, Civil Infrastructure, and Transportation XIII* (Vol. 10971, p. 1097116). International Society for Optics and Photonics.
43. Ohara, Y., Kawashima, K., Yamada, R., & Horio, H. (2004). Evaluation of amorphous diffusion bonding by nonlinear ultrasonic method. In *AIP Conference Proceedings* (Vol. 700, p. 944-951). AIP Publishing.
44. Xie, F., Guo, Z., & Zhang, J. (2014). Strategies for reliable second harmonic of nonlinear acoustic wave through cement-based materials. *Nondestructive Testing and Evaluation*, 29(3), 183-194.
45. Richardson, J. M. (1979). Harmonic generation at an unbonded interface - I. Planar interface between semi-infinite elastic media. *International Journal of Engineering Science*, 17(1), 73-85.
46. Biwa, S., Nakajima, S., & Ohno, N. (2004). On the acoustic nonlinearity of solid-solid contact with pressure-dependent interface stiffness. *Journal of Applied Mechanics*, 71(4), 508-515.

47. Guo, X., Zhang, D., & Wu, J. (2010). Quantitative evaluation of contact stiffness between pressed solid surfaces using dual-frequency ultrasound. Journal of Applied Physics, 108(3), 034902.

48. Kim, J. Y., & Lee, J. S. (2007). A micromechanical model for nonlinear acoustic properties of interfaces between solids. Journal of Applied Physics, 101(4), 043501.

49. Kim, J. Y., Jacobs, L. J., Qu, J., & Littles, J. W. (2006). Experimental characterization of fatigue damage in a nickel-base superalloy using nonlinear ultrasonic waves. *The Journal of the Acoustical Society of America*, 120(3), 1266-1273.

50. Blanloeuil, P., Meziane, A., & Bacon, C. (2014). Numerical study of nonlinear interaction between a crack and elastic waves under an oblique incidence. *Wave Motion*, 51(3), 425-437.

51. Malfense Fierro, G. P., Ciampa, F., & Meo, M. (2020). Phase symmetry analysis for nonlinear ultrasonic modulated signals. *Structural Control and Health Monitoring*, 27(5), 2516.

Chapter 8

Conclusions and Recommendations for Future Work

8.1 Concluding Remarks

This research project aimed at providing unique solutions and new techniques for the improvement of ultrasonic SHM systems and NDE procedures, in order to achieve more effective detection and localisation of defects in metallic and composite materials. This was approached by identifying some challenges in specific engineering applications concerning the ultrasonic inspection of structural parts, and those challenges were considered as opportunities for research and contribution. Specifically, the work presented in this thesis focused on three individual research topics.

8.1.1 First Research Topic

The first one was related to the development of "smart" composite materials where, according to the literature, the insertion of sensing networks in CFRP laminates was found to affect the structural integrity of the material. That was mainly attributed to the use of polymeric film or coating for the electrical insulation of the sensors, which was reported to inhibit the adhesion between the composite layers and cause delamination. This part of the work introduced a novel configuration of embedded sensors in CFRP plates, involving the use of thin PZT disks insulated with a single-layered patch of glass fibre fabric. The experimental activities associated with this research topic were divided and completed in the three journal articles (Paper I – Paper III) presented from Chapter 3 to Chapter 5.

In Chapter 3, initial numerical simulations suggested that the PZT disks should be embedded at a position above the middle plane of the laminate to minimise the interlaminar shear stress exerted on the sensors under bending of the laminate. Then, the results from mechanical tests indicated that CFRP specimens with the proposed layout of internal PZTs and ordinary specimens without sensors had statistically equal means of compressive strength (~495 MPa), flexural strength (~735 MPa) and interlaminar shear strength (~51 MPa). Also, post-test examinations of the fractured surfaces in the samples revealed that the failure mode and size of damage was the same between the "smart" and

the normal composite samples. Next, the insulation method was found to prevent the short-circuiting of the embedded transducers during ultrasonic excitation. Finally, the results from ultrasonic experiments on CFRP plates containing delamination at a single interface, suggested that the internal sensors detected the damage with nearly two times higher sensitivity than surface-bonded sensors, with reference to the nonlinear ultrasonic effect of second harmonic generation.

In the publication of Chapter 4 (Paper II), pairs of the proposed design of embedded PZT transducers were employed for the detection of different damage scenarios in composite laminates, including damage presented only at a single interface, and damage extending through multiple layers. In particular, ultrasonic experiments under single- and dual-frequency excitation were conducted on a CFRP plate containing two areas of in-plane delamination with different size, and on a plate including through-thickness damage caused by two impacts of different energy. The results obtained based on the method of second-order harmonic detection and the technique of wave modulation verified the capability of these embedded sensors to excite and identify each damage at a unique frequency. Indeed, measurements of the out-of-plane vibration velocity on the surface of the plates showed that each damage was excited at the determined ultrasonic frequency.

In the last research paper (Chapter 5) related to the embedding of transducers in composites, CFRP samples with two sensors and plain samples were subject to tensile and fatigue tests, and the results indicated that the two specimen groups had approximately the same values of tensile strength (~910 MPa) and fatigue life (~713,000 cycles). These tests were also performed using specimens with central impact damage, and the results were again similar between the two groups (~865 MPa and ~675,000 cycles). In both cases of undamaged and damaged samples, the failure type of the "smart" samples was the same as that of the normal samples under static and cyclic tensile loading. In addition, three of the impacted samples with embedded PZT disks were also subject to ultrasonic experiments every 120,000 cycles up to the limit of 480,000 cycles where the sensors were found to start failing, according to the measurements of their electrical capacitance. These experiments confirmed that the embedded transducers remained functional for more than 70% of the fatigue life of the specimens. Moreover, the results proved that these sensors were capable of monitoring the growth of impact damage under cyclic loading, by recording a total increase of more than one order of magnitude in the amplitude of the relative acoustic nonlinearity parameter β.

Before moving to the second topic of this research project, it should be mentioned that the unique design of CFRP laminates with glass fibre insulated PZT disks was also employed in the studies of De Simone at al. [198] and Coles et al. [199]. As explained at the beginning of Chapter 5, both studies demonstrated the capabilities of the "smart" CFRP plates in the localisation of impacts within a monitoring grid on the surface of the plates using the TR method. This was the first time that TR method was applied using embedded transducers for the positioning of impacts on composites. In the work of De Simone et al., a dual-plate system was developed for the characterisation of impacts on satellite structures from particles of space debris. This system achieved the detection of the impact position on the plates, and the calculation of the velocity and direction of the impacting particle. Coles et al. introduced a topological algorithm that could be used with the TR method for more precise detection of impacts within the cells of the monitoring grid. This algorithm was successfully applied to the inspection of undamaged and damaged plates using the embedded PZTs, and the results suggested better accuracy in the localisation of single and double bouncing impacts. According to the above, it is concluded that the specific design of "smart" CFRP laminates could be exploited in the manufacture of composite structures with built-in ultrasonic SHM capabilities.

8.1.2 Second Research Topic

The second research topic of this project looked at developing an innovative SHM method that could effectively highlight the position of impact damage on laminated composite structures using ultrasonic signals recorded by a surface-attached array of sensors. To overcome the limitations of existing techniques, the accuracy of the new algorithm should not rely on data that were collected when the structures was defect-free, or measurements of the wave velocity or even on the assumption that the sensors would be functional.

This was explored in the publication outlined in Chapter 6. The proposed SHM method involved the transmission and capturing of ultrasonic waves in the forward and backward directions of all paths existing in a circular network of transducers. The developed algorithm included an initial process for the detection of malfunctioning sensors. That was achieved based on the correlation coefficient between the signals recorded in the two directions of the peripheral paths, as these signals were expected to be less affected by the presence of damage within the array. Regarding the process for the localisation of impact damage, the algorithm began with the determination of the single

frequency corresponding to the highest received signal amplitude in the average spectrum of the signals acquired in all paths under wide-frequency excitation. By repeating the transmission-reception process at the chosen frequency, the value of the relative parameter β in each path was calculated from the amplitude of the captured signal at the fundamental and second harmonic frequencies. These values of β were assigned to the corresponding paths, and then, the paths were summed up to produce a surface plot of the amplitude of β inside the monitored region. The location of crossing paths with the highest values of β resulted in a maximum point on the surface plot that indicated the position of impact damage. Experimental application of this method on three CFRP panels with different design and size of impact damage suggested successful detection of the location of BVID within a range of 4-22 mm. Also, in a separate case, a partially damaged transducer in the array was identified correctly. Therefore, the developed algorithm could potentially be used as an alternative SHM method in applications requiring simple and reliable localisation of impact damage in composite laminates.

8.1.3 Third Research Topic

The third and last topic of this research study was related to the introduction of an ultrasonic phased array method capable of detecting accurately the positions of horizontal contact defects present simultaneously at various levels through the thickness of metallic and composite materials. Ideally, this type of inspection would require strong excitation of the contact surfaces using waveforms of long duration and high amplitude, but this would equally be a limitation for standard phased array systems. Alternatively, this work aimed at increasing the SNR in the recorded response of the material, for higher sensitivity in the detection of acoustic nonlinearities generated by the defects.

In particular, a nonlinear ultrasonic phased array technique was optimised with further processing of the single-frequency (f_1 or f_2) and dual-frequency (f_1 and f_2) signals recorded using four different firing orders of the piezoelectric elements. This processing of the signals combined with the use of the pulse inversion technique, allowed the filtering of the fundamental and second-order harmonics, and the isolation of the modulation sidebands at $f_s = f_2 + f_1$ and $f_d = f_2 - f_1$. From there, the nonlinear modulated response ($R_{\beta_s+\beta_d}$) equal to the sum of modulation parameters ($\beta_s + \beta_d$) was obtained and used for the inspection of the material. More specifically, the positions of the contact interfaces

and the back surface of the material could be recognised as distinctive peaks in the time domain of $R_{\beta_s+\beta_d}$. This was successfully demonstrated on two stacks of aluminium disks and two stacks of rectangular CFRP laminates representing parts with horizontal interfaces between the front and back surfaces. The detected peaks were studied against the corresponding peaks present in the linear ultrasonic response (R_{f_1}) of the material under f_1 excitation. The SNR for the nonlinear modulated peaks was up to three orders of magnitude higher. In addition, the peaks in $R_{\beta_s+\beta_d}$ appeared to be more localised (narrower) as their width at 50% drop (i.e. 6 dB drop) from the maximum point was up to one order of magnitude smaller than the width of peaks in R_{f_1}. Finally, the positioning error between the peaks and the expected positions of the contact flaws was about 45% smaller in the case of nonlinear modulated response. Therefore, the results of this comparative analysis proved that the presented technique could possibly be integrated into future phased array systems for more precise pulse-echo inspection of materials.

8.2 Summary of Contributions and Thesis Conclusion

The major contributions and the main conclusion of this thesis are summarised below.

The novel design of smart composites developed and tested in Chapters 3 to 5 proved for the first time that:

- Piezoelectric PZT sensors can be inserted directly at the interface between the layers of CFRP laminates without reducing the mechanical performance of the material.
- Short-circuiting of embedded PZTs can be successfully avoided using a thin dry layer of woven glass fibre fabric which provides stronger adhesion to the surrounding matrix relative to the conventionally used polyimide (Kapton) layer.
- Embedded PZT disks can be employed for the detection and monitoring of delamination and impact damage in composites based on nonlinear ultrasonic testing methods, which are widely-approved for their higher sensitivity to micro-defects compared with linear ultrasonic techniques.

The SHM algorithm introduced in Chapter 6 combined a balanced set of capabilities that together offered a more practical, reliable and effective solution for the detection of impact damage position on composite panels. In fact, the proposed method offers:

- Improved practicality in the acquisition and processing of ultrasonic data because, unlikely most of the existing methods, the algorithm is independent of baseline data and calculations involving the arrival time of signals.
- Enhanced reliability in the inspection of the panels due to the ability of the algorithm to identify malfunctioning sensors (i.e. avoidance of incorrect readings).
- Higher effectiveness in the localisation of impact damage, by determining a suitable signal transmission frequency that is expected to cause stronger excitation of the damaged layers (i.e. stronger ultrasonic nonlinearities).

The optimisation of the technique presented in Chapter 7 was based on a new expression for the post-processing of ultrasonic signals acquired with different firing combinations of the phased array elements at two frequencies, in order to extract the nonlinearities related only to the modulation of ultrasonic waves. Such a technique can be used to:

- Achieve significantly higher values of SNR and consequently better resolution of ultrasonic inspection.
- Identify flaws at deeper levels inside the material without the need for signals of higher voltage and longer duration, which is the main limitation of phased array systems.
- Detect multiple horizontal contact-type defects presented simultaneously at different interfaces through the thickness of the material, which is particularly challenging for both linear and nonlinear ultrasonic methods.

In conclusion, according to the current literature it is obvious that there is not (and may never be) a single system or method for ultrasonic inspection of materials, to perfectly meet the requirements of all the different engineering applications. Instead, there is a continuous effort by academic and industrial research centres for the creation of new tools and/or the advancement of techniques which aim at characterising the condition of specific structures with high sensitivity and accuracy. As explained at the beginning of the thesis, that was also the primary focus of this research project. The work presented in the previous chapters resulted in a set of ultrasonic SHM designs and NDE techniques that could potentially be utilised in aerospace and other engineering fields for enhanced detection, localisation and monitoring of defects in metallic and composite materials.

8.3 Future Work

The experimental activities completed in the individual research areas of this thesis showed promising results. However, there are still some aspects that can be studied in the future to gain a better understanding of the capabilities and limitations of the proposed SHM designs and NDE methods.

Starting from the layout of integrated PZT transducers in CFRP composites, besides the fatigue tests completed on impacted samples, the damage tolerance of these "smart" composites can be further examined by performing compression tests on impacted samples (compression-after-impact tests). Also, apart from the interlaminar shear tests carried out using short-beam bending method, it will be interesting to assess the mode I interlaminar fracture toughness of the laminates with double cantilever beam tests. About the ultrasonic performance of the embedded transducers, except for the identification of damage existence in composites, additional experiments can be performed using arrays of internal PZT sensors for the detection of damage position using techniques other than the TR method which has already been applied by De Simone and Coles [198, 199]. The nonlinear ultrasonic SHM method presented in Chapter 6 is an example. In addition, the possibility of estimating the size of damage (i.e. damage imaging) using networks of embedded transducers can be examined by either creating a new algorithm or using an existing technique from studies with surface-bonded sensors, such as the nonlinear elastic multi-path imaging (NEMI) method [200].

Moving to the SHM method introduced in Chapter 6 for damage positioning in composite materials, a possible topic for future study is the application of the developed algorithm using non-circular arrays of sensors. For instance, demonstration of damage localisation using square or hexagonal sensor networks will be interesting as these arrangements can provide more efficient coverage of the surface depending on the shape of the structure under inspection. Moreover, future investigations can be focused on the reduction of damage positioning error of the algorithm. Experiments can be carried out using arrays with greater number of transducers (i.e. additional sensor-to-sensor paths) to study the effect on the resolution of the map of material nonlinearity.

Regarding the nonlinear ultrasonic phased array method presented in Chapter 7, future work shall explore its suitability for the detection of contact flaws through the walls of parts with curved profile (e.g. aircraft wing skin) or round tubular symmetry (e.g. pipe) using flexible or curved phased array probes. Furthermore, it will be useful to test the

performance of this method on different damage layouts. Examples include the inspection of thinner parts where the distance between the contact interfaces is smaller, and parts with contact defects that are not necessarily located exactly one on top of the other or covering the entire plane of the material.

References

1. Irving, P. E., & Soutis, C. (2019). *Polymer composites in the aerospace industry* (Vol. 1, p. 195-252). 2nd ed. Cambridge: Woodhead Publishing.
2. Heslehurst, R. B. (2014). *Defects and damage in composite materials and structures*. Boca Raton: CRC press.
3. Marcantonio, V., Monarca, D., Colantoni, A., & Cecchini, M. (2019). Ultrasonic waves for materials evaluation in fatigue, thermal and corrosion damage: A review. *Mechanical Systems and Signal Processing*, 120(1), 32-42.
4. Wang, B., Zhong, S., Lee, T. L., Fancey, K. S., & Mi, J. (2020). Non-destructive testing and evaluation of composite materials/structures: A state-of-the-art review. *Advances in Mechanical Engineering*, *2*(4), 1687814020913761.
5. Munoz, R., Rus, G., Bochud, N., et al. (2020). Nonlinear ultrasonics for early damage detection. In *Virtual and Mobile Healthcare: Breakthroughs in Research and Practice* (Vol. 1, p. 697-732). Hershey: IGI Global
6. Mitra, M., & Gopalakrishnan, S. (2016). Guided wave based structural health monitoring: A review. *Smart Materials and Structures*, 25(5), 053001.
7. Tuloup, C., Harizi, W., Aboura, Z., Meyer, Y., Khellil, K., & Lachat, R. (2019). On the use of in-situ piezoelectric sensors for the manufacturing and structural health monitoring of polymer-matrix composites: A literature review. *Composite Structures*. 215(1), 127-149.
8. Daum, W. (2013). Embedded sensors. In *Handbook of Technical Diagnostics* (Vol. 1, p. 259-285). Heidelberg: Springer.
9. Wu, Z., Liu, K., Wang, Y., & Zheng, Y. (2015). Validation and evaluation of damage identification using probability-based diagnostic imaging on a stiffened composite panel. *Journal of Intelligent Material Systems and Structures*, 26(16), 2181-2195.
10. Hettler, J., Tabatabaeipour, M., Delrue, S., & Van Den Abeele, K. (2016). Linear and nonlinear guided wave imaging of impact damage in CFRP using a probabilistic approach. *Materials*, 9(11), 901.
11. Yeum, C. M., Sohn, H., Ihn, J. B., & Lim, H. J. (2012). Instantaneous delamination detection in a composite plate using a dual piezoelectric transducer network. *Composite Structures*, 94(12), 3490-3499.
12. Tabatabaeipour, M., Hettler, J., Delrue, S., & Van Den Abeele, K. (2014). Reconstruction algorithm for probabilistic inspection of damage (RAPID) in composites. In *11th European conference on non-destructive testing (ECNDT 2014)*.
13. Biwa, S., Nakajima, S., & Ohno, N. (2004). On the acoustic nonlinearity of solid-solid contact with pressure-dependent interface stiffness. *Journal of Applied Mechanics*, 71(4), 508-515.
14. Brizuela, J., Camacho, J., Cosarinsky, G., Iriarte, J. M., & Cruza, J. F. (2019). Improving elevation resolution in phased-array inspections for NDT. *NDT & E International*, 101(1), 1-16.
15. Sugawara, A., Jinno, K., Ohara, Y., & Yamanaka, K. (2015). Closed-crack imaging and scattering behavior analysis using confocal subharmonic phased array. *Japanese Journal of Applied Physics*, 54(7S1), 07HC08.
16. Cheng, J., Potter, J. N., & Drinkwater, B. W. (2018). The parallel-sequential field subtraction technique for coherent nonlinear ultrasonic imaging. *Smart Materials and Structures*, 27(6), 065002.
17. Ohara, Y., Nakajima, H., Tsuji, T., & Mihara, T. (2019). Nonlinear surface-acoustic-wave phased array with fixed-voltage fundamental wave amplitude difference for imaging closed cracks. *NDT & E International*, 108(1), 102170.
18. Briks, A. S., & Green, R. E. (1991). *Nondestructive Testing Handbook: Ultrasonic Testing*. Ohio: American Society for Nondestructive Testing.
19. Graff, K. F. (1981). A history of ultrasonics. In *Physical acoustics* (Vol. 15, pp. 1-97). Academic Press.

20. Stepinski, T. (2012). Ultrasonic nondestructive inspection of solid objects. In *AIP Conference Proceedings* (Vol. 1433, p. 11-20). AIP Publishing.
21. Kimura, M., Ando, A., Maurya, D., & Priya, S. (2017). Lead zirconate titanate-based piezoceramics. In *Advanced Piezoelectric Materials* (Vol.1, p. 95-126). Woodhead Publishing.
22. Krautkramer, J., & Krautkramer, H. (1990). *Ultrasonic Testing of Materials*. Berlin: Springer.
23. Rose, J. L. (2014). *Ultrasonic Waves in Solid Media.* Cambridge University Press.
24. Rose, J. L. (2002). A baseline and vision of ultrasonic guided wave inspection potential. *Journal of Pressure Vessel Technology*, 124(3), 273-282.
25. Cheeke, J. D. N. (2017). *Fundamentals and applications of ultrasonic waves* (Vol. 1 p. 125-138). 2nd ed. Boca Raton: CRC press.
26. Hong, M., & Su, Z. (2019). Characterizing Fatigue Cracks Using Active Sensor Networks. In *Nonlinear Ultrasonic and Vibro-Acoustical Techniques for Nondestructive Evaluation* (Vol. 1, p. 699-739). Cham: Springer.
27. Blitz, J. and Simpson, G. (1996). *Ultrasonic Methods of Non-destructive Testing.* London: Chapman and Hall.
28. Bond, L. J. (2018). Fundamentals of Ultrasonic Inspection. In *ASM Handbook, Volume 17, Nondestructive Evaluation of Materials* (p. 155-168). ASM International.
29. Felice, M. V., & Fan, Z. (2018). Sizing of flaws using ultrasonic bulk wave testing: A review. *Ultrasonics*, 88(1), 26-42.
30. Worlton, D. C. (1957). Ultrasonic Testing with Lamb Waves. *Non-Destructive Testing*, 15(4), 218-222.
31. Worlton, D. C. (1961). Experimental Confirmation of Lamb Waves at Megacycles Frequencies. *Journal of Applied Physics*, 32(6), 967-971.
32. Viktorov, I. A. (1967). *Rayleigh and Lamb Waves - Physical Theory and Applications*. New York: Plenum Press.
33. Achenbach, J. D. (1973). *Wave Propagation in Elastic Solids*. Amsterdam: Elsevier.
34. Graff, K. F. (1975), *Wave Motion in Solids*, New York: Dover.
35. Rose, J. L. (1995). Recent advances in guided wave NDE. In *1995 IEEE Ultrasonics Symposium. Proceedings. An International Symposium* (Vol. 1, p. 761-770). IEEE.
36. Su, Z., Ye, L., & Lu, Y. (2006). Guided Lamb waves for identification of damage in composite structures: A review. *Journal of Sound and Vibration*, 295(3-5), 753-780
37. Guan, R., Lu, Y., Duan, W., & Wang, X. (2017). Guided waves for damage identification in pipeline structures: A review. *Structural Control and Health Monitoring*, 24(11), e2007.
38. Worden, K. (2001). Rayleigh and Lamb Waves-Basic Principles. *Strain*, 37(4), 167-172.
39. Kundu, T. (2019). *Nonlinear ultrasonic and vibro-acoustical techniques for nondestructive evaluation* (Vol. 1, p. 2). Cham: Springer.
40. Cantrell, J. H. (2009). Nonlinear dislocation dynamics at ultrasonic frequencies. *Journal of Applied Physics*, 105(4), 043520.
41. Cantrell, J. H. (2004). Substructural organization, dislocation plasticity and harmonic generation in cyclically stressed wavy slip metals. *Proceedings of the Royal Society of London. Series A: Mathematical, Physical and Engineering Sciences*, 460(2043), 757-780.
42. Koehler, J. S. (1952). *Imperfections in Nearly Perfect Crystals*. New York: Wiley.
43. Suzuki, T., Hikata, A., & Elbaum, C. (1964). Anharmonicity due to glide motion of dislocations. *Journal of Applied Physics*, 35(9), 2761-2766.
44. Landau, L. D. & Lifshitz, E. M. (1986). *Theory of Elasticity* (Vol. 7, p. 476). 3rd ed. Oxford: Pergamon.

45. Hamilton, M.F. (1986). Fundamentals and applications of nonlinear acoustics. In *Nonlinear wave propagation in Mechanics - AMD-77*. New York: American Society of Mechanical Engineers.

46. Jhang, K. Y. (2009). Nonlinear ultrasonic techniques for nondestructive assessment of micro damage in material: A review. *International Journal of Precision Engineering and Manufacturing*, 10(1), 123-135.

47. McCall, K. R., & Guyer, R. A. (1994). Equation of state and wave propagation in hysteretic nonlinear elastic materials. *Journal of Geophysical Research: Solid Earth*, 99(B12), 23887-23897.

48. Guyer, R. A., & Johnson, P. A. (1999). Nonlinear mesoscopic elasticity: Evidence for a new class of materials. *Physics Today*, 52(1), 30-36.

49. Broda, D., Staszewski, W. J., Martowicz, A., Uhl, T., & Silberschmidt, V. V. (2014). Modelling of nonlinear crack–wave interactions for damage detection based on ultrasound - A review. *Journal of Sound and Vibration*, 333(4), 1097-1118.

50. Van Den Abeele, K. A., Johnson, P. A., & Sutin, A. (2000). Nonlinear elastic wave spectroscopy (NEWS) techniques to discern material damage, part I: nonlinear wave modulation spectroscopy (NWMS). *Journal of Research in Nondestructive Evaluation*, 12(1), 17-30.

51. Solodov, I. Y., Krohn, N., & Busse, G. (2002). CAN: an example of nonclassical acoustic nonlinearity in solids. Ultrasonics, 40(1-8), 621-625.

52. Solodov, I. (2009). Nonlinear acoustic NDT: approaches, methods, and applications. In *Proceedings NDT in Progress, 5th International Workshop of NDT Experts.* Prague.

53. Pecorari, C., & Solodov, I. (2006). Nonclassical nonlinear dynamics of solid surfaces in partial contact for NDE applications. In *Universality of Nonclassical Nonlinearity* (Vol. 1, p. 309-326). New York: Springer.

54. Meo, M., Polimeno, U., & Zumpano, G. (2008). Detecting damage in composite material using nonlinear elastic wave spectroscopy methods. *Applied Composite Materials*, 15(3), 115-126.

55. Novak, A., Bentahar, M., Tournat, V., El Guerjouma, R., & Simon, L. (2012). Nonlinear acoustic characterization of micro-damaged materials through higher harmonic resonance analysis. *NDT & E International*, 45(1), 1-8.

56. Soleimanpour, R., Ng, C. T., & Wang, C. H. (2017). Higher harmonic generation of guided waves at delaminations in laminated composite beams. *Structural Health Monitoring*, 16(4), 400-417.

57. Mandal, D. D., & Banerjee, S. (2019). Identification of breathing type disbonds in stiffened panels using non-linear lamb waves and built-in circular PWT array. *Mechanical Systems and Signal Processing*, 117(1), 33-51.

58. Korshak, B. A., Solodov, I. Y., & Ballad, E. M. (2002). DC effects, sub-harmonics, stochasticity and "memory" for contact acoustic non-linearity. *Ultrasonics*, 40(1-8), 707-713.

59. Moussatov, A., Gusev, V., & Castagnede, B. (2003). Self-induced hysteresis for nonlinear acoustic waves in cracked material. *Physical Review Letters*, 90(12), 124301.

60. Yamanaka, K., Mihara, T., & Tsuji, T. (2004). Evaluation of closed cracks by model analysis of subharmonic ultrasound. *Japanese Journal of Applied Physics*, 43(5S), 3082.

61. Semperlotti, F., Wang, K. W., & Smith, E. C. (2009). Localization of a breathing crack using nonlinear subharmonic response signals. *Applied Physics Letters*, 95(25), 254101.

62. Park, C. S., Kim, J. W., Cho, S., & Seo, D. C. (2016). A high resolution approach for nonlinear sub-harmonic imaging. *NDT & E International*, 79(1), 114-122.

63. Ohara, Y., Mihara, T., & Yamanaka, K. (2019). Subharmonic phased array for crack evaluation (SPACE). In *Nonlinear Ultrasonic and Vibro-Acoustical Techniques for Nondestructive Evaluation* (Vol. 1, p. 419-469). Cham: Springer.

64. Lim, H. J., & Sohn, H. (2019). Online fatigue crack prognosis using nonlinear ultrasonic modulation. *Structural Health Monitoring*, 18(5-6), 1889-1902.

65. Malfense Fierro, G. P., Ciampa, F., & Meo, M. (2020). Phase symmetry analysis for nonlinear ultrasonic modulated signals. *Structural Control and Health Monitoring*, 27(5), 2516.

66. Johnson, P. A., Zinszner, B., & Rasolofosaon, P. N. (1996). Resonance and elastic nonlinear phenomena in rock. *Journal of Geophysical Research: Solid Earth*, 101(B5), 11553-11564.

67. Van Den Abeele, K. A., Carmeliet, J., Ten Cate, J. A., & Johnson, P. A. (2000). Nonlinear elastic wave spectroscopy (NEWS) techniques to discern material damage, Part II: Single-mode nonlinear resonance acoustic spectroscopy. *Journal of Research in Nondestructive Evaluation*, 12(1), 31-42.

68. Polimeno, U., & Meo, M. (2009). Detecting barely visible impact damage detection on aircraft composites structures. *Composite Structures*, 91(4), 398-402.

69. Jeong, H., & Barnard, D. (2015). Experimental studies on NRUS behavior of impact-damaged composite laminates. In *AIP Conference Proceedings* (Vol. 1650, No. 1, p. 1275-1279). AIP Publishing.

70. Hogg, S. M., Anderson, B. E., Le Bas, P. Y., & Remillieux, M. C. (2019). Nonlinear resonant ultrasound spectroscopy of stress corrosion cracking in stainless steel rods. *NDT & E International*, 102(1), 194-198.

71. Johnson, P., & Sutin, A. (2005). Slow dynamics and anomalous nonlinear fast dynamics in diverse solids. *The Journal of the Acoustical Society of America*, 117(1), 124-130.

72. Bentahar, M., & Guerjouma, R. E. (2009). Monitoring progressive damage in polymer-based composite using nonlinear dynamics and acoustic emission. *The Journal of the Acoustical Society of America*, 125(1), 39-44.

73. Yu, X., Bentahar, M., Mechri, C., & Montrésor, S. (2019). Passive monitoring of nonlinear relaxation of cracked polymer concrete samples using acoustic emission. *The Journal of the Acoustical Society of America*, 146(4), 323-328.

74. Yoritomo, J. Y., & Weaver, R. L. (2020). Slow dynamic nonlinearity in unconsolidated glass bead packs. *Physical Review E*, 101(1), 012901.

75. Tenek, L. H., Henneke II, E. G., & Gunzburger, M. D. (1993). Vibration of delaminated composite plates and some applications to non-destructive testing. *Composite Structures*, 23(3), 253-262.

76. Solodov, I., Bai, J., Bekgulyan, S., & Busse, G. (2011). A local defect resonance to enhance acoustic wave-defect interaction in ultrasonic nondestructive evaluation. *Applied Physics Letters*, 99(21), 211911.

77. Hettler, J., Tabatabaeipour, M., Delrue, S., & Van Den Abeele, K. (2017). Detection and characterization of local defect resonances arising from delaminations and flat bottom holes. *Journal of Nondestructive Evaluation*, 36(1), 2.

78. Segers, J., Hedayatrasa, S., Poelman, G., Van Paepegem, W., & Kersemans, M. (2020). Probing the limits of full-field linear Local Defect Resonance identification for deep defect detection. *Ultrasonics*, 106130.

79. Ostrovsky, L. A., & Johnson, P. A. (2001). Dynamic nonlinear elasticity in geo materials. Rivista del Nuovo Cimento della Societa Italiana di Fisica, 24(7), 1-46.

80. Zaitsev, V. Y., & Matveev, L. A. (2006). Strain-amplitude dependent dissipation in linearly dissipative and nonlinear elastic microinhomogeneous media. *Geologiya i Geofizika*, 47(5), 695-710.

81. Breazeale, M. A., & Thompson, D. O. (1963). Finite-amplitude ultrasonic waves in aluminum. *Applied Physics Letters*, 3(5), 77-78.

82. Breazeale, M. A., & Ford, J. (1965). Ultrasonic studies of the nonlinear behavior of solids. *Journal of Applied Physics*, 36(11), 3486-3490.

83. Hikata, A., Chick, B. B., & Elbaum, C. (1963). Effect of dislocations on finite amplitude ultrasonic waves in aluminum. *Applied Physics Letters*, 3(11), 195-197.

84. Hikata, A., Chick, B. B., & Elbaum, C. (1965). Dislocation contribution to the second harmonic generation of ultrasonic waves. *Journal of Applied Physics*, 36(1), 229-236.

85. Gedroits, A., & Krasilnikov, V. (1963). Finite-amplitude elastic waves in solids and deviations from Hooke's law. *Soviet Physics JETP*, 16(5), 1122-1126.

86. Gedroitz, A. A., Krasilnikov, V. A., & Zarembo, L. K. (1963). Elastic waves of finite amplitude in solids and anharmonicity of the lattice. *Acta Acustica united with Acustica*, 13(2), 108-110.

87. Yost, W. T., & Cantrell, J. H. (1993). The effects of artificial aging of aluminum 2024 on its nonlinearity parameter. In *Review of Progress in Quantitative Nondestructive Evaluation* (Vol. 12A-12B, pp. 2067-2073). Boston: Springer.

88. Kim, J. Y., Jacobs, L. J., Qu, J., & Littles, J. W. (2006). Experimental characterization of fatigue damage in a nickel-base superalloy using nonlinear ultrasonic waves. *The Journal of the Acoustical Society of America*, 120(3), 1266-1273.

89. Matlack, K. H., Kim, J. Y., Jacobs, L. J., & Qu, J. (2015). Review of second harmonic generation measurement techniques for material state determination in metals. *Journal of Nondestructive Evaluation*, 34(1), 273.

90. Gebrekidan, S. B., Kang, T., Kim, H. J., & Song, S. J. (2018). Nonlinear ultrasonic characterization of early degradation of fatigued Al6061-T6 with harmonic generation technique. *Ultrasonics*, 85(1), 23-30.

91. Kim, J., Zhu, B., & Cho, Y. (2019). An experimental study on second harmonic generation of guided wave in fatigued spring rod. *Journal of Mechanical Science and Technology*, 33(9), 4105-4109.

92. Cai, Z., Liu, S., & Zhang, C. (2017). Measurement of ultrasonic nonlinear parameter by using electromagnetic acoustic transducer. In *AIP Conference Proceedings* (Vol. 1806, p. 050015). AIP Publishing.

93. Wang, R., Wu, Q., Yu, F., Okabe, Y., & Xiong, K. (2019). Nonlinear ultrasonic detection for evaluating fatigue crack in metal plate. *Structural Health Monitoring*, 18(3), 869-881.

94. Shui, G., Wang, Y. S., Huang, P., & Qu, J. (2015). Nonlinear ultrasonic evaluation of the fatigue damage of adhesive joints. *NDT & E International*, 70(1), 9-15.

95. Shui, G., Song, X., Xi, J., & Wang, Y. S. (2017). Experimental characterization of impact fatigue damage in an adhesive bonding using the second harmonics. *Journal of Nondestructive Evaluation*, 36(2), 23.

96. Kim, J., Jhang, K. Y., & Kim, C. (2018). Dependence of nonlinear ultrasonic characteristic on second-phase precipitation in heat-treated Al 6061-T6 alloy. *Ultrasonics*, 82(1), 84-90.

97. Choi, S., Lee, P., & Jhang, K. Y. (2019). A pulse inversion-based nonlinear ultrasonic technique using a single-cycle longitudinal wave for evaluating localized material degradation in plates. *International Journal of Precision Engineering and Manufacturing*, 20(4), 549-558.

98. Kim, J., Kim, J. G., Kong, B., Kim, K. M., Jang, C., Kang, S. S., & Jhang, K. Y. (2020). Applicability of nonlinear ultrasonic technique to evaluation of thermally aged CF8M cast stainless steel. *Nuclear Engineering and Technology*, 52(3), 621-625.

99. Zhong, F., Zhang, C., Li, W., Jiao, J., & Zhong, L. (2016). Nonlinear ultrasonic characterization of intergranular corrosion damage in super 304H steel tube. *Anti-Corrosion Methods and Materials*, 63(2), 145-152.

100. Climent, M. A., Miro, M., Carbajo, J., Poveda, P., de Vera, G., & Ramis, J. (2019). Use of Non-Linear Ultrasonic Techniques to Detect Cracks Due to Steel Corrosion in Reinforced Concrete Structures. *Materials*, 12(5), 813.

101. Zhu, W., Xiang, Y., Xuan, F. Z., Liu, C. J., Deng, M., & Zhang, H. (2017). Creep damage evaluation of P92 steels using nonlinear Lamb waves. In *2017 IEEE International Ultrasonics Symposium (IUS)* (Vol. 1, p. 1-4). IEEE.

102. Wang, X., Wang, X., Luo, B., Hu, X. L., & Yuan, T. B. (2019). Creep degradation assessment in 9% Cr heat-resistant steel welded joints using ultrasonic methods. *Results in Physics*, 12(1), 307-320.

103. Metya, A. K., Das, A., & Balasubramaniam, K. (2019). Nonlinear Lamb wave for the evaluation of creep damage in modified 9Cr–1Mo steel. *NDT & E International*, 107(1), 102130.

104. Ciampa, F., Onder, E., Barbieri, E., & Meo, M. (2014). Detection and modelling of nonlinear elastic response in damaged composite structures. *Journal of Nondestructive Evaluation*, 33(4), 515-521.

105. Rauter, N., & Lammering, R. (2015). Impact damage detection in composite structures considering nonlinear lamb wave propagation. *Mechanics of Advanced Materials and Structures*, 22(1-2), 44-51.

106. Hong, M., Mao, Z., Todd, M. D., & Su, Z. (2017). Uncertainty quantification for acoustic nonlinearity parameter in Lamb wave-based prediction of barely visible impact damage in composites. *Mechanical Systems and Signal Processing*, 82(1), 448-460.

107. Tie, Y., Zhang, Q., Hou, Y., & Li, C. (2020). Impact damage assessment in orthotropic CFRP laminates using nonlinear Lamb wave: Experimental and numerical investigations. *Composite Structures*, 111869.

108. Mattei, C., & Marty, P. (2003). Imaging of fatigue damage in CFRP composite laminates using nonlinear harmonic generation. In *AIP Conference Proceedings* (Vol. 657, p. 989-995). AIP Publishing.

109. Rauter, N., Lammering, R., & Kuhnrich, T. (2016). On the detection of fatigue damage in composites by use of second harmonic guided waves. *Composite Structures*, 152(1), 247-258.

110. Patra, S., Ahmed, H., Saadatzi, M., & Banerjee, S. (2019). Evidence of dissipative and growing nonlinearity in Lamb waves due to stress-relaxation and material degradation in composites. *Ultrasonics*, 96(1), 224-231.

111. Li, W., Cho, Y., & Achenbach, J. D. (2012). Detection of thermal fatigue in composites by second harmonic Lamb waves. *Smart Materials and Structures*, 21(8), 085019.

112. Zhou, C., Hong, M., Su, Z., Wang, Q., & Cheng, L. (2012). Evaluation of fatigue cracks using nonlinearities of acousto-ultrasonic waves acquired by an active sensor network. *Smart Materials and Structures*, 22(1), 015018.

113. Wang, K., Cao, W., Liu, M., Li, Y., Zhou, P., & Su, Z. (2020). Advancing elastic wave imaging using thermal susceptibility of acoustic nonlinearity. *International Journal of Mechanical Sciences*, 175(1), 105509.

114. Liu, M., Wang, K., Lissenden, C. J., et al. (2017). Characterizing hypervelocity impact (HVI)-induced pitting damage using active guided ultrasonic waves: From linear to nonlinear. *Materials*, 10(5), 547.

115. Ciampa, F., Scarselli, G., Pickering, S., & Meo, M. (2015). Nonlinear elastic wave tomography for the imaging of corrosion damage. *Ultrasonics*, 62(1), 147-155.

116. Li, W., & Cho, Y. (2016). Combination of nonlinear ultrasonics and guided wave tomography for imaging the micro-defects. *Ultrasonics*, 65(1), 87-95.

117. Ciampa, F., Pickering, S. G., Scarselli, G., & Meo, M. (2017). Nonlinear imaging of damage in composite structures using sparse ultrasonic sensor arrays. *Structural Control and Health Monitoring*, 24(5), 1911.

118. Boccardi, S., Calla, D. B., Ciampa, F., & Meo, M. (2018). Nonlinear elastic multi-path reciprocal method for damage localisation in composite materials. *Ultrasonics*, 82(1), 239-245.

119. Liu, X., Bo, L., Yang, K., et al. (2018). Locating and imaging contact delamination based on chaotic detection of nonlinear Lamb waves. *Mechanical Systems and Signal Processing*, 109(1), 58-73.

120. Sutin, A. M., & Johnson, P. A. (2005). Nonlinear elastic wave NDE II. Nonlinear wave modulation spectroscopy and nonlinear time reversed acoustics. In *AIP Conference Proceedings* (Vol. 760, p. 385-392). AIP Publishing.

121. Korotkov, A. S., & Sutin, A. M. (1994). Modulation of ultrasound by vibrations in metal constructions with cracks. *Acoustics Letters*, 18(4), 59-62.

122. Korotkov, A. S., Slavinskij, M. M., & Sutin, A. (1994). Variations of acoustic nonlinear parameters with the concentration of defects in steel. *Akusticheskij Zhurnal*, 40(1), 84-87.

123. Sutin, A. M., & Nazarov, V. E. (1995). Nonlinear acoustic methods of crack diagnostics. *Radiophysics and Quantum Electronics*, 38(3-4), 109-120.

124. Zaitsev, V. Y., Sutin, A. M., Belyaeva, I. Y., & Nazarov, V. E. (1995). Nonlinear interaction of acoustical waves due to cracks and its possible usage for cracks detection. *Modal Analysis*, 1(3), 335-344.

125. Donskoy, D. M., & Sutin, A. M. (1998). Vibro-Acoustic Modulation Nondestructive Evaluation Technique. *Journal of Intelligent Material Systems and Structures*, 9(9), 765–771.

126. Zaitsev, V., & Sas, P. (2000). Nonlinear response of a weakly damaged metal sample: a dissipative modulation mechanism of vibro-acoustic interaction. *Journal of Vibration and Control*, 6(6), 803-822.

127. Ryles, M., Ngau, F. H., McDonald, I., & Staszewski, W. J. (2008). Comparative study of nonlinear acoustic and Lamb wave techniques for fatigue crack detection in metallic structures. *Fatigue & Fracture of Engineering Materials & Structures*, 31(8), 674-683.

128. Amerini, F., & Meo, M. (2011). Structural health monitoring of bolted joints using linear and nonlinear acoustic/ultrasound methods. *Structural Health Monitoring*, 10(6), 659-672.

129. Klepka, A., Staszewski, W. J., Jenal, R. B., Szwedo, M., Iwaniec, J., & Uhl, T. (2012). Nonlinear acoustics for fatigue crack detection–experimental investigations of vibro-acoustic wave modulations. *Structural Health Monitoring*, 11(2), 197-211.

130. Donskoy, D., Sutin, A., & Ekimov, A. (2001). Nonlinear acoustic interaction on contact interfaces and its use for nondestructive testing. *NDT & E International*, 34(4), 231-238.

131. Duffour, P., Morbidini, M. and Cawley, P., 2006. A study of the vibro-acoustic modulation technique for the detection of cracks in metals. *The Journal of the Acoustical Society of America*, 119(3), 1463-1475.

132. Van Damme, B., & Van Den Abeele, K. (2012). Defect localization using the nonlinear impact modulation technique. In *Emerging Technologies in Non-Destructive Testing V-Proceedings of the 5th Conference on Emerging Technologies in NDT* (Vol. 1, p. 301-306). Boca Raton: CRC Press.

133. Meyer, J. J., & Adams, D. E. (2015). Theoretical and experimental evidence for using impact modulation to assess bolted joints. *Nonlinear Dynamics*, 81(1-2), 103-117.

134. Meyer, J. J., & Adams, D. E. (2019). Using impact modulation to quantify nonlinearities associated with bolt loosening with applications to satellite structures. *Mechanical Systems and Signal Processing*, 116(1), 787-795.

135. Yoder, N. C., Adams, D. E., & Triplett, M. (2008). Multidimensional sensing for impact load and damage evaluation in a carbon filament wound canister. *Materials Evaluation*, 66(7), 756-763.

136. Zagrai, A., Donskoy, D., & Lottiaux, J. L. (2004). N-Scan: New Vibro-Modulation System for Crack Detection, Monitoring and Characterization. In *AIP Conference Proceedings* (Vol. 700, No. 1, p. 1414-1421). AIP Publishing.

137. Yoder, N. C., & Adams, D. E. (2010). Vibro-acoustic modulation utilizing a swept probing signal for robust crack detection. *Structural Health Monitoring*, 9(3), 257-267.

138. Donskoy, D., Zagrai, A., Chudnovsky, A., Golovin, E., & Agarwala, V. (2006). Nonlinear vibro-acoustic modulation technique for life prediction of aging aircraft components. In *Proceedings of the Third European Workshop on Structural Health Monitoring* (Vol. 1, p. 251-258). DEStech Publications.

139. Zagrai, A., Donskoy, D., Chudnovsky, A., & Golovin, E. (2008). Micro-and macroscale damage detection using the nonlinear acoustic vibro-modulation technique. *Research in Nondestructive Evaluation*, 19(2), 104-128.

140. Parsons, Z., & Staszewski, W. J. (2006). Nonlinear acoustics with low-profile piezoceramic excitation for crack detection in metallic structures. *Smart Materials and Structures*, 15(4), 1110-1118.

141. Jiao, J. P., Drinkwater, B. W., Neild, S. A., & Wilcox, P. D. (2009). Low-frequency vibration modulation of guided waves to image nonlinear scatterers for structural health monitoring. *Smart Materials and Structures*, 18(6), 065006.

142. Sheppard, K., Zagrai, A., & Donskoy, D. (2007). A non-linear acoustic, vibro-modulation technique for the detection and monitoring of contact-type defects, including those associated with corrosion. *Corrosion Reviews*, 25(1-2), 81-96.

143. Aymerich, F., & Staszewski, W. J. (2010). Experimental study of impact-damage detection in composite laminates using a cross-modulation vibro-acoustic technique. *Structural Health Monitoring*, 9(6), 541-553.

144. Klepka, A., Pieczonka, L., Staszewski, W. J., & Aymerich, F. (2014). Impact damage detection in laminated composites by non-linear vibro-acoustic wave modulations. *Composites Part B: Engineering*, 65, 99-108.

145. Dao, P. B., Staszewski, W. J., Klepka, A., & Aymerich, F. (2014) Impact Damage Detection in Composites using Nonlinear Vibro-Acoustic Wave Modulations and Cointegration Analysis. In *11th European Conference on Non-Destructive Testing* (Vol. 1 p. 6-10). European Federation for Non-Destructive Testing.

146. Klepka, A., Staszewski, W. J., Di Maio, D., & Scarpa, F. (2013). Impact damage detection in composite chiral sandwich panels using nonlinear vibro-acoustic modulations. *Smart Materials and Structures*, 22(8), 084011.

147. Ooijevaar, T., Rogge, M. D., Loendersloot, R., Warnet, L., Akkerman, R., & Tinga, T. (2016). Vibro-acoustic modulation–based damage identification in a composite skin–stiffener structure. *Structural Health Monitoring*, *15*(4), 458-472.

148. Zhang, Z., Xu, H., Liao, Y., Su, Z., & Xiao, Y. (2017). Vibro-acoustic modulation (VAM)-inspired structural integrity monitoring and its applications to bolted composite joints. *Composite Structures*, 176, 505-515.

149. Zhang, Z., Liu, M., Liao, Y., Su, Z., & Xiao, Y. (2018). Contact acoustic nonlinearity (CAN)-based continuous monitoring of bolt loosening: Hybrid use of high-order harmonics and spectral sidebands. *Mechanical Systems and Signal Processing*, 103(1), 280-294.

150. Hillis, A. J., Neild, S. A., Drinkwater, B. W., & Wilcox, P. D. (2006). Bispectral Analysis of Ultrasonic Inter-Modulation Data for Improved Defect Detection. In *AIP Conference Proceedings* (Vol. 820, No. 1, p. 89-96). AIP Publishing.

151. Klepka, A., Dziedziech, K., Mrowka, J., & Gorski, J. (2019). Experimental investigation of modulation effects for contact-type interfaces in vibro-acoustic modulation tests. *Structural Health Monitoring*, 1475921719857624.

152. Straka, L., Yagodzinskyy, Y., Landa, M., & Hanninen, H. (2008). Detection of structural damage of aluminum alloy 6082 using elastic wave modulation spectroscopy. *NDT & E International*, 41(7), 554-563.

153. Sohn, H., Lim, H. J., DeSimio, M. P., Brown, K., & Derriso, M. (2014). Nonlinear ultrasonic wave modulation for online fatigue crack detection. *Journal of Sound and Vibration*, 333(5), 1473-1484.

154. Lim, H. J., Sohn, H., DeSimio, M. P., & Brown, K. (2014). Reference-free fatigue crack detection using nonlinear ultrasonic modulation under various temperature and loading conditions. *Mechanical Systems and Signal Processing*, 45(2), 468-478.

155. Fierro, G. P. M., & Meo, M. (2018). IWSHM 2017: Structural health monitoring of the loosening in a multi-bolt structure using linear and modulated nonlinear ultrasound acoustic moments approach. *Structural Health Monitoring*, 17(6), 1349-1364.

156. Zhao, N., Huo, L., & Song, G. (2020). A nonlinear ultrasonic method for real-time bolt looseness monitoring using PZT transducer–enabled vibro-acoustic modulation. *Journal of Intelligent Material Systems and Structures*, 31(3), 364-376.

157. Chrysochoidis, N. A., Barouni, A. K., & Saravanos, D. A. (2011). Delamination detection in composites using wave modulation spectroscopy with a novel active nonlinear acousto-ultrasonic piezoelectric sensor. *Journal of Intelligent Material Systems and Structures*, 22(18), 2193-2206.

158. Pieczonka, L., Ukowski, P., Klepka, A., Staszewski, W. J., Uhl, T., & Aymerich, F. (2014). Impact damage detection in light composite sandwich panels using piezo-based nonlinear vibro-acoustic modulations. *Smart Materials and Structures*, 23(10), 105021.

159. Chrysochoidis, N. A., Assimakopoulou, T. T., & Saravanos, D. A. (2015). Nonlinear wave structural health monitoring method using an active nonlinear piezoceramic sensor for matrix cracking detection in composites. *Journal of Intelligent Material Systems and Structures*, 26(15), 2108-2120.

160. Dao, P. B., Klepka, A., Pieczonka, L., Aymerich, F., & Staszewski, W. J. (2017). Impact damage detection in smart composites using nonlinear acoustics - cointegration analysis for removal of undesired load effect. *Smart Materials and Structures*, 26(3), 035012.

161. Pieczonka, L., Zietek, L., Klepka, A., Staszewski, W. J., Aymerich, F., & Uhl, T. (2018). Damage imaging in composites using nonlinear vibro-acoustic wave modulations. *Structural Control and Health Monitoring*, 25(2), 2063.

162. Haupert, S., Renaud, G., & Schumm, A. (2017). Ultrasonic imaging of nonlinear scatterers buried in a medium. *NDT & E International*, 87(1), 1-6.

163. Haupert, S., Ohara, Y., Carcreff, E., & Renaud, G. (2019). Fundamental wave amplitude difference imaging for detection and characterization of embedded cracks. *Ultrasonics*, 96(1), 132-139.

164. Fierro, G. P. M., & Meo, M. (2019). Nonlinear phased array imaging of flaws a modulation technique. In *Nondestructive Characterization and Monitoring of Advanced Materials, Aerospace, Civil Infrastructure, and Transportation XIII* (Vol. 10971, p. 1097116). International Society for Optics and Photonics.

165. Alston, J., Croxford, A., Potter, J., & Blanloeuil, P. (2018). Nonlinear non-collinear ultrasonic detection and characterisation of kissing bonds. *NDT & E International*, 99(1), 105-116.

166. Hufenbach, B., Habinc, S., & Vuillenmier, P. (1999). Space applications for smart sensors. In *Keynote lecture, Proceedings of the Eurosensors XIII, 13th European Conference on Solid-State Transducers* (Vol. 1, p. 3-6).

167. Dragan, K., Dziendzikowski, M., Kurnyta, A., Leski, A., & Bienias, J. (2014). Structural health monitoring of composite structures with use of embedded PZT piezoelectric sensors. In *ECCM-16th European Conference on Composite Materials.*

168. Meyer, Y., Lachat, R., & Akhras, G. (2019). A review of manufacturing techniques of smart composite structures with embedded bulk piezoelectric transducers. *Smart Materials and Structures*, 28(5), 053001.

169. Yang, S. M., & Chiu, J. W. (1993). Smart structures - vibration of composites with piezoelectric materials. *Composite Structures*, 25(1-4), 381-386.

170. Yang, S. M., Hung, C. C., & Chen, K. H. (2005). Design and fabrication of a smart layer module in composite laminated structures. *Smart Materials and Structures*, 14(2), 315.

171. De Rosa, I. M., & Sarasini, F. (2010). Use of PVDF as acoustic emission sensor for in situ monitoring of mechanical behaviour of glass/epoxy laminates. *Polymer Testing*, 29(6), 749-758.

172. Dezfouli, M. M. S., Ruslan, M. H., Karami, M., Sopian, K., & Bakhtyar, B. (2013). Calibration of impact localization of a passive smart composite plate fabricated by embedded pzt patch. *Recent Advances in Electrical Engineering Series*, 326713.

173. Tang, H. Y., Winkelmann, C., Lestari, W., & La Saponara, V. (2011). Composite structural health monitoring through use of embedded PZT sensors. *Journal of Intelligent Material Systems and Structures*, 22(8), 739-755.

174. Masmoudi, S., El Mahi, A., Turki, S., & El Guerjouma, R. (2014). Mechanical behavior and health monitoring by Acoustic Emission of unidirectional and cross-ply laminates integrated by piezoelectric implant. *Applied Acoustics*, 86(1), 118-125.

175. Holeczek, K., Starke, E., Winkler, A., Dannemann, M., & Modler, N. (2016). Numerical and experimental characterization of fiber-reinforced thermoplastic composite structures with embedded piezoelectric sensor-actuator arrays for ultrasonic applications. *Applied Sciences*, 6(3), 55.

176. Masmoudi, S., El Mahi, A., & Turki, S. (2017). Effect of piezoelectric implant on the structural integrity of composite laminates subjected to tensile loads. *Applied Composite Materials*, 24(1), 39-54.

177. Chen, X., Meyer, Y., Lachat, R., & Ouisse, M. (2017). Laminates with integrated piezoelectric transducers: influence of the transducers location along the thickness-axis on the structural performance. In *CIMNE, VIII ECCOMAS Thematic Conference on Smart Structures and Materials* (Vol. 1 p. 594-605).

178. Lampani, L., & Gaudenzi, P. (2018). Innovative composite material component with embedded self-powered wireless sensor device for structural monitoring. *Composite Structures*, 202(1), 136-141.

179. Lampani, L., Sarasini, F., Tirillo, J., & Gaudenzi, P. (2018). Analysis of damage in composite laminates with embedded piezoelectric patches subjected to bending action. *Composite Structures*, *202*, 935-942.

180. Crawley, E. F., & De Luis, J. (1987). Use of piezoelectric actuators as elements of intelligent structures. *AIAA Journal*, 25(10), 1373-1385.

181. Bronowicki, A. J., McIntyre, L. J., Betros, R. S., & Dvorsky, G. R. (1996). Mechanical validation of smart structures. *Smart Materials and Structures*, 5(2), 129.

182. Lin, M., & Chang, F. K. (1999). Composite structures with built-in diagnostics. *Materials Today*, 2(2), 18-22.

183. Mall, S., & Coleman, J. M. (1998). Monotonic and fatigue loading behavior of quasi-isotropic graphite/epoxy laminate embedded with piezoelectric sensor. *Smart Materials and Structures*, 7(6), 822.

184. Paget, C. A., & Levin, K. (1999). Structural integrity of composites with embedded piezoelectric ceramic transducers. In *Smart Structures and Materials 1999: Smart Structures and Integrated Systems* (Vol. 3668, p. 306-313). International Society for Optics and Photonics.

185. Mall, S., & Hsu, T. L. (2000). Electromechanical fatigue behavior of graphite/epoxy laminate embedded with piezoelectric actuator. *Smart Materials and Structures*, 9(1), 78.

186. Mall, S. (2002). Integrity of graphite/epoxy laminate embedded with piezoelectric sensor/actuator under monotonic and fatigue loads. *Smart Materials and Structures*, 11(4), 527.

187. Paradies, R., & Ruge, M. (2000). In situ fabrication of active fibre reinforced structures with integrated piezoelectric actuators. *Smart Materials and Structures*, 9(2), 220.

188. Lin, M., & Chang, F. K. (2002). The manufacture of composite structures with a built-in network of piezoceramics. *Composites Science and Technology*, 62(7-8), 919-939.

189. Sala, G., Olivier, M., Bettini, P., & Sciacovelli, D. (2004). Embedded piezoelectric sensors and actuators for control of active composite structures. *Mechanical and Thermal Engineering Department, Carlo Gavazzi Space ESTEC, European Space Agency*.

190. Su, Z., Wang, X., Chen, Z., Ye, L., & Wang, D. (2006). A built-in active sensor network for health monitoring of composite structures. *Smart Materials and Structures*, 15(6), 1939.

191. Ramos, C. A., De Oliveira, R., Marques, A. T., & Frazao, O. (2011). Measurement of dynamic strain using an optic fibre system in adaptive composite laminates with an integrated piezoelectric sensor/actuator. *Optica Applicata*, 41(1), 79-87.

192. Arellano, M. T., Crouzeix, L., Collombet, F., Douchin, B., & Grunevald, Y. H. (2012). Mechanical characterization of an alternative technique to embed sensors in composite structures: the monitoring patch. *Applied Composite Materials*, 19(3-4), 379-391.

193. Chilles, J. S., Croxford, A., & Bond, I. P. (2015). Design of an embedded sensor, for improved structural performance. *Smart Materials and Structures*, 24(11), 115014.

194. Zhong, C. H., Croxford, A. J., & Wilcox, P. D. (2015). Remote inspection system for impact damage in large composite structure. *Proceedings of the Royal Society A: Mathematical, Physical and Engineering Sciences*, 471(2173), 20140631.

195. Salloum, R. (2016). *Optimization of shunt damped composite structures using negative capacitances*. Thesis (Doctoral), Technische Universitat Darmstadt.

196. Yelve, N. P., Mitra, M., & Mujumdar, P. M. (2017). Detection of delamination in composite laminates using Lamb wave based nonlinear method. *Composite Structures*, 159(1), 257-266.

197. Clausen, J., Specht, U., Busse, M., Lang, A., & Sanders, J. (2013). Integration of glass fibre structures in aluminium cast parts for CFRP aluminium transition structures. *Procedia Materials Science*, 2(1), 197-203.

198. De Simone, M. E., Andreades, C., Hilmi, A. M., Meo, M., & Ciampa, F. (2019). Proof of concept for a smart composite orbital debris detector. *Acta Astronautica*, 160(1), 499-508.

199. Coles, A., De Castro, B. A., Andreades, C., Baptista, F. G., Meo, M., & Ciampa, F. (2020). Impact Localization in Composites Using Time Reversal, Embedded PZT Transducers, and Topological Algorithms. *Frontiers in Built Environment*, 6(1), 27.

200. Boccardi, S. (2019). *Structural Health Monitoring and Power Harvesting Systems for Aerospace Applications*. Thesis (Doctoral), University of Bath.